

This item was submitted to Loughborough's Institutional Repository (<https://dspace.lboro.ac.uk/>) by the author and is made available under the following Creative Commons Licence conditions.



For the full text of this licence, please go to:  
<http://creativecommons.org/licenses/by-nc-nd/2.5/>

POLY(2,5-BENZIMIDAZOLE) BASED POLYMER  
ELECTROLYTE MEMBRANES FOR HIGH  
TEMPERATURE FUEL CELL APPLICATIONS

by

QINGTING LIU

A Doctoral Thesis

Submitted in partial fulfilment of the requirements  
for the award of  
Doctor of Philosophy of Loughborough University

September 2010

Supervisor: Dr. XUJIN BAO

© by Qingting LIU 2010

# ABSTRACT

Polymer electrolyte membrane fuel cells (PEMFCs) are one of the most promising clean technologies under development. However, the main obstacles for commercialising PEMFCs are largely attributed to the technical limitations and cost of current PEM materials such as Nafion. Novel poly(2,5-benzimidazole) (ABPBI)/POSS based polymer composite electrolyte membranes with excellent mechanical and conductivity properties were developed in this project including (I) ABPBI, polybenzimidazole (PBI) and their copolymers were synthesised by solution polymerisation and their chemical structures were confirmed by FTIR and elemental analysis. ABPBI/OctaAmmonium POSS (ABPBI/OA) and ABPBI/TriSilanolPhenyl POSS (ABPBI/TSO) composites were also synthesised in situ. High quality polymer and composite membranes were fabricated by a direct cast method; and (II) The mechanical and thermal properties, microstructure and morphology, water and  $\text{H}_3\text{PO}_4$  absorbility and proton conductivity of phosphoric acid doped and undoped ABPBI and ABPBI/POSS composite membranes were investigated. SEM/TEM micrographs showed that a uniform dispersion of POSS nano particles in ABPBI polymer matrix was achieved. The best performances on both mechanical properties and proton conductivities were obtained from the ABPBI/OA composite membrane with 3 wt% of POSS (ABPBI/3OA). It was found that both the water and  $\text{H}_3\text{PO}_4$  uptakes were increased significantly with the addition of POSS due to formation of hydrogen bonds between the POSS and  $\text{H}_2\text{O}/\text{H}_3\text{PO}_4$ , which played a critical role in the improvement of the conductivity of the composite membranes at temperatures over  $100^\circ\text{C}$ . ABPBI/3OA membranes with  $\text{H}_3\text{PO}_4$  uptake above 117% showed best proton conductivities at both hydrous and anhydrous conditions from room temperature to  $160^\circ\text{C}$ , which is comparable with the conductivity of commercial Nafion 117 at  $20^\circ\text{C}$  in water-saturated condition, indicating that these composite membranes could be excellent candidates as a polymer electrolyte membrane for high temperature applications. A new mechanism for illustrating the improved proton conductivity of composite membranes was also developed.

**Key words:** PEMFC, polymer electrolyte membrane, poly(2,5-benzimidazole), ABPBI, TriSilanolPhenyl POSS, OctaAmmonium POSS, synthesis in-situ, direct casting, phosphoric acid doping, proton conductivity.

# ACKNOWLEDGEMENTS

First I would like to thank my supervisor, Dr. Xujin Bao, for his guidance and support during the course of my doctoral work at Loughborough University. I am highly impressed by his knowledge and approach to solve problems, his penchant for reading and learning and his persistence as a research scholar. What I have got from him is invaluable and unparalleled. The comments and suggestions from his research group members represented by Dr. Chaoying Wan, Dr. Dongxin Wang, Feng Zhao, Michael Young, Guanyan Xie from all the time are greatly appreciated.

I would also like to thank the students who have participated in this project, including Moifuai Soon, Siqin Zou, Jinxian Deng, Andrew J. Wilson and Daniel M. Rogers. Many thanks go to the department staff their support and help during last four years. I would also like to thank Prof. Rui Chen, Dr. Pratap Rama and Samuel Cruz-Manzo in Department of Aeronautical and Automotive providing the conductivity measurement apparatus and technical supports. Dr. Xiao Li is greatly acknowledged for guiding me into the world of electrochemistry. His knowledge within the field of PEMFC technology and modelling skills has undoubtedly been invaluable for the project. I would also thank Prof. Dizhen Wang and Dr. Zhaohui Chen in South China University of Technology for their supports on the characterisation of polymer samples.

The comments and suggestions of Dr Leslie Dix and Dr Steve Edmondson during the thesis writing-up and revision are greatly appreciated.

Appreciations also go to all friends in Loughborough for their friendship, kind help and all the fun my family had. Many thanks go to the families of Helen and Patrick, Judith and Clive, Jennet and Bill, Barbara and Neale. Special thanks also go to Dr Yi Zhang, Dr Li Wang, Dr Xiaoyun Cui, PhD student Jian Huang, Yi Qin, Yingtao Tian etc., who help me and my family a lot.

I would like to thank my parents for their support throughout my life. My life is indebted to them for their support and efforts for providing me with the best possible life and education. I also want to thank my wife Junzhen Xiong and son Tiancheng Xiong for their love. Many thanks also go to my parents-in-law, who have taken care of my son for many years, as well as my brothers for their support and encouragement.

**Dedicated to my father died two years ago.**

Qingting Liu

# ABBREVIATIONS

ABPBI	Poly(2,5-benzimidazole)	
ABPBI-53PA	ABPBI with 53% H <sub>3</sub> PO <sub>4</sub> uptake	
ABPBI/AM	AM-POSS embedded ABPBI composite	
ABPBI/1AM-88PA	ABPBI/1% AM-POSS composite with 88% H <sub>3</sub> PO <sub>4</sub> uptake	
ABPBI/SO	SO-POSS embedded ABPBI composite	
AFC	Alkaline fuel cell	
ATR	Attenuated total reflectance	
CPE	Constant phase element	
DAB (TAB)	3,3'-Diaminobenzidine	or
	3,3',4,4'-tetraaminobiphenyl	
DABA	3,4-Diaminobenzoic acid	
DMAc	N,N-dimethylacetamide	
DMF	Dimethylformamide	
DMFC	Direct methanol fuel cell	
DMSO	Dimethylsulfoxide	
DSC	Differential scanning Calorimetry	
DTG	Derivative thermogravimetric	
ECI	Electrochemical interface	
EDX	Energy dispersive X-ray	
EIS	Electrochemical impedance spectroscopy	
EW	Equivalent weight	
FAFC	Formic acid fuel cell	
FC	Fuel cell	
FEG-SEM	Field emission gun scanning electron microscopy	
FEP	Poly(tetrafluoroethylene-hexafluoropropylene)	
FTIR	Fourier transform infrared spectroscopy	
FRA	Frequency response analyser	
HPA	Heteropolyacid	
ICE	Internal combustion engine	
ICP-AES	Inductively coupled plasma atomic emission spectroscopy	
IEC	Ion exchange capacity	

## ABBREVIATIONS

IPA	Isophthalic acid
MCFC	Molten carbonate fuel cell
MEA	Membrane electrode assembly
MPPBBI	Poly( <i>m</i> -phenylenebenzobisimidazole)
MSA	Methanesulphonic acid
NMP	N-methylpyrrolidone
OA(AM)-POSS	OctaAmmonium POSS
ORR	Oxygen reduction reaction
PA	Phosphoric acid
PAA	Poly(acrylic acid)
PAFC	Phosphoric acid fuel cell
PBI	Poly[2,2'-( <i>m</i> -phenylene)-5,5'-bibenzimidazole] or polybenzimidazole
PBIs	Polybenzimidazoles (PBI and its derivatives)
PBI-BS	N-butanesulfonate grafted PBI
PBI-BzS	N-benzylsulfonate grafted PBI
PBI-PS	N-propanesulfonate grafted PBI
PEEK	Polyetheretherketone
PEFC	Polymer electrolyte fuel cell
PEM	Polymer electrolyte membrane or proton exchange membrane
PEMFC	Polymer electrolyte membrane fuel cell or proton exchange membrane fuel cell
PEI	Polyethyleneimine
PEO	Polyethylene oxide
PFSA	Perfluorosulfonic acid
PMoA	Polymolybdic acid
POSS	Polyhedral oligomeric silsesquioxane
PP	Poly- <i>p</i> -phenylene
PPA	Polyphosphoric acid
PPBP	Poly(4-phenoxybenzoyl-1,4-phenylene)
PPO	Poly( <i>p</i> -phenylene oxide)
PSF	Polysulfone
PSSA	Poly(styrene sulfonic acid)
PSU	Polysulfone
PTA (PWA)	Phosphotungstic acid



## ABBREVIATIONS

PTFE	Polytetrafluoroethylene	
PVA	Poly(vinyl alcohol)	
PVDF	Poly(vinylidene fluoride)	
PVPA	Poly(vinylphosphonic acid)	
P4VP	Poly(4-vinylpyridine)	
RHE	Reversible hydrogen electrode	
SDs	Degree of sulphonation	
SEM	Scanning electron microscopy	
SMPPBBI	Poly[m-(5-sulfo)-phenylenebenzobisimidazole]	
SPEEK	Sulphonated polyetheretherketone	
SPES	Sulphonated polyethersulfone	
SPFC	Solid polymer fuel cell	
SPOP	Sulphonated poly[bis(phenoxy)phosphazene]	
SPSF	Sulphonated polysulfone	
SO-POSS	TriSilanolPhenyl POSS	
SOFC	Solid oxide fuel cell	
STA (SiWA)	Silicotungstic acid	
TAB (DAB)	3,3',4,4'-Tetraaminobiphenyl 3,3'-diaminobenzidine	or
TBAC	Tetra- <i>n</i> -butylammonium chloride	
TPP	Triphenyl phosphite	
TFA	Trifluoroacetic acid	
TG	Thermogravimetric	
TGA	Thermogravimetric analysis	
WAXD	Wide angle X-ray diffraction	
XRD	X-ray diffraction	
ZPP	Zirconium pyrophosphate	
ZrP	Zirconium phosphates	

# SYMBOLS

$\alpha$	Reciprocal number of all possible proton hopping directions
$\eta$	Efficiency of energy conversion
$[\eta]$	Intrinsic viscosity
$\eta_{inh}$	Inherent viscosity
$\eta_{red}$	Reduced viscosity
$\theta$	Diffraction angle in XRD pattern Phase angle in Nyquist plots
$\lambda$	Hydration number
$\delta$	Constant of dependent on the diffusion coefficient and concentration of the electro-active species
$\sigma$	Proton conductivity
$\sigma_0$	Pre-exponential factor of proton conductivity
$\sigma_T$	Proton conductivity at temperature $T$
$\nu_0$	Proton hopping frequency
$\Delta G$	Gibbs free energy
$\Delta H$	Enthalpy Enthalpy of proton defect migration
$\Delta H_f$	Enthalpy of proton defect pair formation
$\Delta S$	Entropy Activation entropy of proton defect migration
$\Delta S_f$	Activation entropy of proton defect formation
$A$	Testing area of membrane Absorbance of infrared
$ac$	Alternative current
$b$	Tafel slope
$c$	Concentration of polymer solution
$c_0$	Concentration of monomer
$C$	Concentration of mobile species
$C_d$	Double-layer capacitance
$d$	Thickness of membrane Proton hopping distance
$dc$	Direct current

# SYMBOLS

$t$	Polymerisation reaction time
	Flow time of a polymer solution in an Ubbelohde viscometer
$t_0$	Flow time of a solvent in an Ubbelohde viscometer
$D_{CL}^{eff}$	Effective diffusion coefficient of O <sub>2</sub> through Catalyst Layer
$D_{GDL}^{eff}$	Effective diffusion coefficient of O <sub>2</sub> through Gas Diffusion Layer
$E$	Electrode potential
$E_a$	Activation energy
$E_c$	Modulus of composite
$E_f$	Modulus of filler
$E_m$	Modulus of polymer matrix
$E_{rev}$	Reversible electrode potential
$F$	Faraday constant
$i$	Current density
$\tilde{I}$	Current
$i_0$	Exchange current density
$i_c$	Double-layer charging current
$i_f$	Faradic current
$k'$	Rate constant of catalysed reaction
$M$	Molar concentration
$M(M_w)$	Molecular weight
$\overline{M}_n$	Number-average molecular weight
$n$	Transferred electron number in the hopping model
$p$	Fractional monomer conversion
	Extent of step-growth reaction
	Conversion of function groups of step-growth
$R$	Gas constant
	Bulk resistance ( $\Omega$ )
$R_{\Omega} (R_{ohm})$	Ohmic resistance
$R_{ct}$	Charge transfer resistance
$R_m$	Membrane resistance
$\Delta S$	Entropy
	Activation entropy of proton defect migration
$\Delta S_f$	Activation entropy of proton defect formation

# SYMBOLS

$t$	Flow time of a polymer solution in an Ubbelohde viscometer Reaction time of step-growth polymerisation
$t_0$	Flow time of the solvent in Ubbelohde viscometer
$T$	Absolute temperature (K) Transmittance of infrared (%)
$T_g$	Glass transition temperatures
$V$	Volume
$\tilde{V}$	Voltage
$V_f$	Volume fraction of filler
$V_m$	Volume fraction of polymer matrix
$\bar{x}_n$	number-average degree of polymerisation
$W_{doped}$	Weight of anhydrous membrane after doped in $H_3PO_4$
$W_{dry}$	Weight of anhydrous membrane
$W_{undoped}$	Weight of anhydrous membrane before doped in $H_3PO_4$
$W_{wet}$	Weight of hydrous membrane
$z$	Charge number in the hopping model
$Z$	Impedance
$Z'$	Real part of impedance
$Z''$	Imaginary part of impedance
$ Z $	Absolute magnitude of impedance
$Z_f$	Faradic impedance
$Z_w$	Warburg (mass transfer) impedance

# LIST OF FIGURES

Figure 2-1 Scheme of a PEMFC <sup>3</sup> .....	11
Figure 2-2 Proton transfer according to Grotthuss mechanism .....	19
Figure 2-3 Proton transfer according to Vehicle mechanism .....	20
Figure 2-4 Microstructure of Nafion <sup>9</sup> .....	23
Figure 2-5 Reactions happened on the anodic platinum catalyst.....	27
Figure 2-6 A diagram of different water movements in a PEMFC .....	29
Figure 2-7 Proton conducting in a sulphonated polymer membrane at high temperature and low humidity via 1, acid to acid; 2, H <sub>2</sub> O to acid.....	33
Figure 2-8 Structures of fluoropolymers and silicone polymers for PEMs.....	34
Figure 2-9 Structures of aromatic hydrocarbons for PEMs.....	36
Figure 2-10 Proton transport in polymer/nanoparticle composite membranes <sup>74</sup> .....	38
Figure 2-11 Proton transport in H <sub>3</sub> PO <sub>4</sub> doped PBI.....	43
Figure 2-12 Scheme of PBI by melt polycondensation .....	44
Figure 2-13 Synthesis of PBI with stable salt of the tetraamine and derivatives of isophthalic acid in polyphosphoric acid.....	44
Figure 2-14 Synthesis of PBI in a. PPA/TPP and b. TFA/MSA/P <sub>2</sub> O <sub>5</sub> .....	45
Figure 2-15 Synthesis of ABPBI in a. PPA and b. MSA/P <sub>2</sub> O <sub>5</sub> .....	46
Figure 2-16 Sulphonation of benzimidazole group .....	53
Figure 2-17 Scheme of chemically grafted PBI.....	55
Figure 2-18 Sulphonated PBI by synthesis from monomers containing sulphonic groups.....	55
Figure 2-19 Scheme of cross-linked acid based membranes: a. ionically cross-linked and b. covalently cross-linked blends .....	56
Figure 2-20 General structure of POSS .....	58
Figure 3-1 A procedure of polymer synthesis .....	61
Figure 3-2 Polymer synthesis set.....	61
Figure 3-3 Flow chart of the purification of DABA.....	62
Figure 3-4 Methods of membrane fabrications: a. casting; b. direct casting.....	66
Figure 4-1 FTIR spectra of (a) DABA monomer, (b) ABPBI synthesised in MSA and (c) ABPBI synthesised in PPA .....	74

Figure 4-2 Intrinsic viscosity and molecular weights as a function of the amount of $P_2O_5$ .....	79
Figure 4-3 Intrinsic viscosity and molecular weights as a function of reaction temperature .....	80
Figure 4-4 Intrinsic viscosity and molecular weights as a function of reaction time	81
Figure 4-5 Intrinsic viscosity and molecular weights as a function of string rate .....	82
Figure 4-6 Intrinsic viscosity and molecular weights as a function of amount of DABA .....	83
Figure 4-7 DSC curve of commercial and purified DABA .....	84
Figure 4-8 Mechanical properties of ABPBI with various molecular weights.....	85
Figure 4-9 XRD pattern of ABPBI .....	86
Figure 4-10 DSC curve of ABPBI.....	87
Figure 4-11 TGA/DSC curves of ABPBI .....	88
Figure 4-12 FTIR spectra of ABPBI at various temperatures .....	89
Figure 4-13 Synthesis of PBI in (a): PPA; (b): MSA / $P_2O_5$ .....	90
Figure 4-14 FTIR spectra of (a) DAB, (b) IPA, (c)PBI synthesised in MSA and (d) PBI synthesised in PPA. ....	91
Figure 4-15 Synthesis of copolymers of ABPBI and PBI .....	92
Figure 4-16 FTIR spectra of copolymers of ABPBI and PBI: (b) copolymer with 3:1 of mol ratio of DABA/DAB, (c) copolymer with 1:1 of mol ratio of DABA/DAB, (d) copolymer with 1:3 of mol ratio of DABA/DAB (a. ABPBI and e. PBI are as references).....	92
Figure 4-17 XRD patterns of ABPBI, PBI and their copolymers .....	97
Figure 4-18 DSC curves of PBI and copolymers operated under 350°C.....	98
Figure 4-19 TGA curves of PBI and copolymers of ABPBI and PBI.....	99
Figure 4-20 Intrinsic viscosities of PBI and copolymers.....	100
Figure 4-21 Structures of a. SO-POSS and b. AM-POSS .....	101
Figure 4-22 FTIR spectra of a. SO-POSS powder and b. ABPBI/5SO composite .	102
Figure 4-23 Condensation reaction between SO-POSS and DABA monomer .....	103
Figure 4-24 TGA curves of SO-POSS powder.....	104
Figure 4-25 SO-POSS degradation mechanisms .....	104
Figure 4-26 Thermostability of ABPBI/5SO-POSS composite .....	105
Figure 4-27 FTIR spectra of AM-POSS and ABPBI/AM-POSS composite.....	106
Figure 4-28 TGA/DSC curves of AM-POSS .....	107

Figure 4-29 Degradation mechanisms of AM-POSS .....	108
Figure 4-30 TGA/DTG/DSC curves of ABPBI and ABPBI/5%OA-POSS membranes .....	109
Figure 5-1 Comparison of $H_3PO_4$ uptake of ABPBI and ABPBI/AM .....	111
Figure 5-2 Models proposed for $H_3PO_4$ absorption in an ABPBI/AM composite membrane.....	112
Figure 5-3 Comparison of $H_3PO_4$ uptake of ABPBI and ABPBI/SO-POSS.....	113
Figure 5-4 Water and moisture absorptilities of ABPBI and Nafion 117 membranes .....	115
Figure 5-5 Models proposed for the water absorption in the pristine and $H_3PO_4$ doped ABPBI membranes at ambient atmosphere .....	118
Figure 5-6 Models of water absorption for ABPBI/POSS composite membranes..	119
Figure 5-7 Mechanical properties of dry $H_3PO_4$ doped ABPBI membrane .....	121
Figure 5-8 Mechanical properties of saturated $H_3PO_4$ doped ABPBI membranes..	122
Figure 5-9 Mechanical strength of $H_3PO_4$ doped ABPBI/ISO at dry and saturated condition .....	123
Figure 5-10 Mechanical properties of undoped ABPBI/AM-POSS composite membranes .....	125
Figure 5-11 Mechanical properties of undoped ABPBI/SO-POSS composite membranes .....	125
Figure 5-12 Schematic drawing showing a polymer matrix bridged by POSS particles .....	126
Figure 5-13 SEM image of ABPBI membrane under the heating conditions of evaporating solvent: A. 180°C for 24 hours, B. 200°C for 24 hours, C. 220°C for 24 hours, D. the temperature varied from 150~220°C with 10°C intervals per hour then hold at 220°C for over 10 hours.....	127
Figure 5-14 XRD pattern of ABPBI membrane .....	128
Figure 5-15 SEM images (left) and EDAX images (right) of samples without treatment of dissolving in ethanol before synthesis in-situ: a. ABPBI/3SO, b. ABPBI/3AM .....	129
Figure 5-16 SEM images of samples without ultrasonication treatment before synthesis in-situ: A. ABPBI/3SO, B. ABPBI/3AM.....	129
Figure 5-17 SEM images of a. SO-POSS powder, b. ABPBI/ISO, c. ABPBI/3SO, d. ABPBI/5SO .....	131

Figure 5-18 SEM images of A. AM-POSS powder, B. ABPBI/1AM, C. ABPBI/3AM, D. ABPBI/5AM .....	131
Figure 5-19 EDX map of 10M H <sub>3</sub> PO <sub>4</sub> doped ABPBI/5SO (left) and ABPBI/3AM (right) .....	132
Figure 5-20 SEM images of a. 10M H <sub>3</sub> PO <sub>4</sub> doped ABPBI/5SO, b. 12M H <sub>3</sub> PO <sub>4</sub> doped ABPBI/5SO, c. 10M H <sub>3</sub> PO <sub>4</sub> doped ABPBI/5AM, d. 12M H <sub>3</sub> PO <sub>4</sub> doped ABPBI/5AM dry membranes .....	132
Figure 5-21 TEM images (left) and EDX images (right) of (A) undoped ABPBI, (B) undoped ABPBI/5AM, (B) 4M H <sub>3</sub> PO <sub>4</sub> doped ABPBI/1AM and (D) 4M H <sub>3</sub> PO <sub>4</sub> doped ABPBI/3AM.....	133
Figure 5-22 XRD patterns of undoped ABPBI/AM composite membranes: B. ABPBI/1AM, C. ABPBI/3AM, D. ABPBI/5AM (A. ABPBI and E. AM-POSS powder are as references) .....	135
Figure 5-23 XRD patterns of H <sub>3</sub> PO <sub>4</sub> doped ABPBI/AM composite membranes: a. ABPBI/1AM-92PA, b. ABPBI/3AM-241PA and c. ABPBI/5AM-94PA .....	135
Figure 5-24 XRD patterns of a. SO-POSS powder, c. ABPBI/3SO and d. ABPBI/3SO-84PA .....	136
Figure 5-25 FTIR spectra of a. undoped ABPBI, b. ABPBI-47PA, c. ABPBI-77PA, d. ABPBI-91PA membranes and e. 85% H <sub>3</sub> PO <sub>4</sub> solution .....	137
Figure 5-26 Models proposed for protonation of the benzimidazole group by phosphoric acid .....	139
Figure 5-27 FTIR spectra of a. ABPBI/3SO-49PA, b. ABPBI/3SO-62PA and c. ABPBI/3SO-70PA .....	140
Figure 5-28 FTIR spectra of a. undoped ABPBI/3AM, b. ABPBI/3AM-89PA, c. ABPBI/3AM-117PA, d. ABPBI/3AM-153PA and e. ABPBI/3AM-194PA membranes .....	141
Figure 5-29 TG curve of 85% H <sub>3</sub> PO <sub>4</sub> solution .....	144
Figure 5-30 TGA curves of 10M H <sub>3</sub> PO <sub>4</sub> doped membranes: a. ABPBI-79PA, b. ABPBI/3SO-94PA and c. ABPBI/3AM-194PA.....	144
Figure 6-1 A Nyquist plot of imaginary impedance ( $Z''$ ) against real impedance ( $Z'$ ) to define electrical impedance ( $Z$ ) and phase angle ( $\theta$ ) .....	146
Figure 6-2 A typical equivalent circuit often used for an electrochemical cell: a. the equivalent circuit, b. the subdivision of the Faradic impedance.....	147



Figure 6-3 A Nyquist plot of the impedance for an electrochemical cell <sup>214</sup> .....	148
Figure 6-4 Conductivity measurement unit used in this work.....	152
Figure 6-5 Equivalent circuit of the membrane impedance measurement system (a) at high frequency; (b) in this experiment.....	153
Figure 6-6 Nyquist plot of ABPBI-94PA measured in a frequency range of 20kHz~100Hz at 20°C and saturated condition) .....	155
Figure 6-7 Simulated Nyquist plot of ABPBI-94PA in the frequency range of $10^{10}$ Hz~ $10^{-3}$ Hz .....	156
Figure 6-8 Fitted Nyquist plot of ABPBI-94PA in the measuring frequency range (20kHz~100Hz) .....	156
Figure 6-9 Simulated Nyquist plot of Nafion 117 in the frequency range of $10^{10}$ Hz~ $10^{-3}$ Hz .....	157
Figure 6-10 Nyquist plot of the impedance of saturated Nafion 117 membrane at various bias voltages .....	159
Figure 6-11 Nyquist plot of the impedance of anhydrous ABPBI-74PA at 160°C and various bias voltages .....	159
Figure 6-12 Nyquist plot of the impedance of saturated Nafion 117 membrane at 20°C and ambient atmosphere .....	161
Figure 6-13 Nyquist plot of the impedance of saturated ABPBI-47PA at 20°C and ambient atmosphere .....	161
Figure 6-14 Nyquist plot of the impedance of saturated ABPBI/3SO-92PA measured at 20°C and ambient atmosphere .....	162
Figure 6-15 Variation of conductivity of anhydrous H <sub>3</sub> PO <sub>4</sub> doped ABPBI with temperature .....	164
Figure 6-16 Variation of conductivity of anhydrous H <sub>3</sub> PO <sub>4</sub> doped ABPBI/1AM with temperature .....	164
Figure 6-17 Variation of conductivity of anhydrous H <sub>3</sub> PO <sub>4</sub> doped ABPBI/3AM with temperature .....	165
Figure 6-18 Variation of conductivity of anhydrous H <sub>3</sub> PO <sub>4</sub> doped ABPBI/5AM with temperature .....	165
Figure 6-19 Variation of conductivity of anhydrous H <sub>3</sub> PO <sub>4</sub> doped ABPBI/3SO with temperature .....	166
Figure 6-20 Arrhenius plot of conductivity of H <sub>3</sub> PO <sub>4</sub> doped ABPBI.....	166

Figure 6-21 Arrhenius plot of conductivity of anhydrous $\text{H}_3\text{PO}_4$ doped ABPBI/1AM	167
Figure 6-22 Arrhenius plot of conductivity of anhydrous $\text{H}_3\text{PO}_4$ doped ABPBI/3AM	167
Figure 6-23 Arrhenius plot of conductivity of anhydrous $\text{H}_3\text{PO}_4$ doped ABPBI/5AM	168
Figure 6-24 Arrhenius plot of conductivity of anhydrous $\text{H}_3\text{PO}_4$ doped ABPBI/3SO	168
Figure 6-25 Hydrogen bonding forms proposed in a $\text{H}_3\text{PO}_4$ doped ABPBI membrane	172
Figure 6-26 Conductivity of ABPBI-53PA and Nafion 117 at 20°C and ambient atmosphere against various exposure times	173
Figure 6-27 Conductivity of $\text{H}_3\text{PO}_4$ doped hydrous ABPBI and Nafion 117 at various temperatures	173
Figure 6-28 Conductivity of $\text{H}_3\text{PO}_4$ doped hydrous ABPBI/AM composites at various time	174
Figure 6-29 Conductivity of $\text{H}_3\text{PO}_4$ doped hydrous ABPBI/3SO composites at various temperatures	174
Figure 6-30 Comparison of conductivities of anhydrous and hydrous ABPBI/60PA, ABPBI/1AM-77PA and ABPBI/5AM-76PA samples measured above 100°C	175
Figure 6-31 Comparison of conductivities of anhydrous and hydrous ABPBI/3AM samples measured above 100°C	175

# LIST OF TABLES

Table 2-1 Type of fuel cells .....	8
Table 2-2 Energy density comparison for several kinds of fuels .....	13
Table 2-3 Structure of PFSA polymer and typical properties of commercial PFSA membranes .....	21
Table 2-4 Main properties of Nafion® membranes.....	22
Table 2-5 Summary of modifications of Nafion membranes .....	32
Table 2-6 Summary of inorganic-organic composites used as PEM under development.....	39
Table 2-7 Polymerisation conditions and molecular weights achieved by different laboratories.....	46
Table 2-8 Sulphonation of PBI membrane and its properties.....	53
Table 3-1 Chemicals used in this project.....	60
Table 3-2 Amount of monomers for synthesis of copolymers .....	64
Table 3-3 Weight of monomers for synthesis of ABPBI/OctaAmmonium POSS composite .....	64
Table 3-4 Weight of monomers for synthesis of ABPBI/TriSilanolPhenyl POSS composite .....	65
Table 3-5 Preparation of different concentrations of phosphoric acid solutions.....	67
Table 4-1 Element contents of ABPBI synthesised in MSA/P2O5 .....	76
Table 4-2 Assignments of ABPBI infra-red spectra .....	94
Table 4-3 Element contents of PBI synthesised in PPA and MSA respectively .....	95
Table 4-4 Element contents of copolymers synthesised in MSA .....	96
Table 5-1 Water uptake of ABPBI, ABPBI/POSS and Nafion 117 membranes.....	115
Table 5-2 Water uptake of H <sub>3</sub> PO <sub>4</sub> doped ABPBI membrane .....	116
Table 5-3 Moisture absorptivity of dry H <sub>3</sub> PO <sub>4</sub> doped ABPBI membrane.....	117
Table 5-4 Water uptake of H <sub>3</sub> PO <sub>4</sub> doped ABPBI/AM-POSS membranes .....	119
Table 5-5 Water uptake of H <sub>3</sub> PO <sub>4</sub> doped ABPBI/SO-POSS membranes .....	120
Table 5-6 FTIR spectra assignment of phosphoric acid and phosphate ions (solid state).....	142
Table 6-1 Activation energy of conductivity of H <sub>3</sub> PO <sub>4</sub> doped ABPBI membrane .	169

Table 6-2 Activation energy of conductivity of H <sub>3</sub> PO <sub>4</sub> doped ABPBI/3SO composite membrane.....	169
Table 6-3 Activation energy of conductivity of H <sub>3</sub> PO <sub>4</sub> doped ABPBI/AM composite membrane.....	169

# CONTENTS

ABSTRACT.....	I
ACKNOWLEDGEMENTS .....	II
ABBREVIATIONS .....	V
SYMBOLS.....	VIII
LIST OF FIGURES .....	XI
LIST OF TABLES .....	XVII
CONTENTS .....	XIX
CHAPTER 1 INTRODUCTION.....	1
1.1 BACKGROUND .....	1
1.2 MOTIVATION AND OBJECTIVES .....	3
1.3 OUTLINE OF THESIS .....	4
CHAPTER 2 LITERATURE SURVEY.....	6
2.1 A BRIEF INTRODUCTION OF FUEL CELLS .....	6
2.1.1 <i>Brief history of fuel cells development</i> .....	7
2.1.2 <i>Classification of fuel cells</i> .....	8
2.2 INTRODUCTION OF PEMFC.....	11
2.2.1 <i>Hydrogen PEMFC</i> .....	12
2.2.2 <i>Direct Methanol Fuel Cells (DMFC)</i> .....	14
2.2.3 <i>Other fuels for PEMFC</i> .....	16
2.2.4 <i>Advantages and disadvantages of PEMFCs</i> .....	17
2.3 DEVELOPMENT OF POLYMER ELECTROLYTE MEMBRANES .....	17
2.3.1 <i>Mechanism of proton conducting in PEM</i> .....	18
2.3.2 <i>Perfluorinated ionomer membranes</i> .....	21
2.3.3 <i>Reasons for developing high temperature polymer electrolyte membranes</i> .....	25
2.4 APPROACHES FOR HIGH TEMPERATURE PEM.....	31
2.4.1 <i>Modifications of PFSA polymer membranes</i> .....	31
2.4.2 <i>Alternative sulphonated polymer membranes</i> .....	33
2.4.3 <i>Acid-based polymer electrolyte membranes</i> .....	39
2.5 DEVELOPMENT OF POLYBENZIMIDAZOLES (PBIs) BASED PEM .....	41
2.5.1 <i>Proton conducting routes in PBIs membranes</i> .....	42
2.5.2 <i>Synthesis of PBIs</i> .....	44
2.5.3 <i>Fabrication of PBIs membranes</i> .....	47
2.5.4 <i>Properties of acid doped PBIs PEMs</i> .....	48
2.5.5 <i>Modified PBIs Membranes</i> .....	51
2.6 BRIEF INTRODUCTION OF POSS .....	57

2.7 SUMMARY .....	59
<b>CHAPTER 3 EXPERIMENTAL DETAILS.....</b>	<b>60</b>
3.1 CHEMICALS .....	60
3.2 SYNTHESIS OF POLYMERS .....	61
3.2.1 <i>Synthesis of poly(2,5-benzimidazole) (ABPBI)</i> .....	62
3.2.2 <i>Synthesis of polybenzimidazole (PBI)</i> .....	63
3.2.3 <i>Synthesis of copolymers of ABPBI and PBI in MSA</i> .....	64
3.3 SYNTHESIS OF ABPBI/POSS COMPOSITES .....	64
3.3.1 <i>Synthesis of ABPBI/OctaAmmonium POSS composite</i> .....	64
3.3.2 <i>Synthesis of ABPBI/TriSilanolPhenyl POSS composite</i> .....	65
3.4 FABRICATION OF MEMBRANES .....	65
3.5 PREPARATION OF PHOSPHORIC ACID DOPED MEMBRANES .....	67
3.6 PREPARATION OF NAFION MEMBRANE .....	67
3.7 CHARACTERISATION .....	68
3.7.1 <i>Characterisation of chemical structures of the polymers</i> .....	68
3.7.2 <i>Characterisation of mechanical properties</i> .....	70
3.7.3 <i>Characterisation of thermal properties of the polymers</i> .....	70
3.7.4 <i>Characterisation of morphologies of membranes</i> .....	70
3.7.5 <i>Characterisation of water and phosphoric acid uptakes of polymer and composite membranes</i> .....	71
3.7.6 <i>Characterisation of conductivity of membrane</i> .....	72
<b>CHAPTER 4 RESULTS AND DISCUSSION: SYNTHESIS AND CHARACTERISATION OF POLYMERS AND POLYMER COMPOSITES</b>	<b>73</b>
4.1 SYNTHESIS AND CHARACTERISATION OF ABPBI POLYMER .....	73
4.1.1 <i>Chemical structure of poly(2,5-benzimidazole) (ABPBI)</i> .....	73
4.1.2 <i>Optimisation of reaction conditions for ABPBI synthesis</i> .....	77
4.1.3 <i>Properties of ABPBI polymer</i> .....	85
4.2 SYNTHESIS AND CHARACTERISATION OF PBI AND COPOLYMERS.....	90
4.2.1 <i>Chemical structures of PBI and copolymers</i> .....	90
4.2.2 <i>Properties of PBI and copolymers</i> .....	97
4.3 SYNTHESIS OF ABPBI/POLYHEDRAL OLIGOMERIC SILSEQUIOXANES COMPOSITES (ABPBI/POSS) .....	101
4.3.1 <i>Synthesis of ABPBI/SO-POSS composites</i> .....	101
4.3.2 <i>Synthesis of ABPBI/AM-POSS composites</i> .....	106
<b>CHAPTER 5 RESULTS AND DISCUSSION: FABRICATION AND CHARACTERISATION OF ABPBI AND ABPBI/POSS COMPOSITE MEMBRANES .....</b>	<b>110</b>
5.1 PHOSPHORIC ACID AND WATER ABSORBILITY OF ABPBI AND ITS COMPOSITE MEMBRANES.....	110
5.1.1 <i>Comparison of H<sub>3</sub>PO<sub>4</sub> absorptivity of ABPBI and ABPBI/POSS composite membranes</i> .....	110
5.1.2 <i>Investigation of water absorptivity of undoped membranes</i> .....	114
5.1.3 <i>Comparison of water absorptivity of H<sub>3</sub>PO<sub>4</sub> doped membranes</i> .....	116
5.2 MECHANICAL PROPERTIES OF ABPBI AND ITS COMPOSITE MEMBRANES .....	120

5.2.1 Effect of phosphoric acid and water on the mechanical properties of ABPBI membrane .....	120
5.2.2 Effect of POSS particles on the mechanical properties of ABPBI/POSS composite membrane .....	123
5.3 MORPHOLOGIES OF ABPBI AND COMPOSITE MEMBRANES .....	126
5.3.1 Effect of the casting procedure on the morphologies of ABPBI membranes .....	126
5.3.2 Evaluation of ABPBI/POSS composite morphology.....	128
5.4 FTIR ANALYSIS .....	136
5.4.1 FTIR analysis of phosphoric acid doped ABPBI membrane .....	136
5.4.2 FTIR analysis of $H_3PO_4$ doped ABPBI/SO composite membrane .....	140
5.4.3 FTIR analysis of $H_3PO_4$ doped ABPBI/AM composite membrane .....	141
5.5 THERMOSTABILITY OF $H_3PO_4$ DOPED MEMBRANES.....	143
<b>CHAPTER 6 RESULTS AND DISCUSSION: PROTON CONDUCTIVITY OF ABPBI BASED POLYMER ELECTROLYTE MEMBRANES.....</b>	<b>146</b>
6.1 BACKGROUND AND THEORY OF IMPEDANCE SPECTROSCOPY .....	146
6.1.1 Introduction of impedance spectroscopy .....	146
6.1.2 Introduction of measurement techniques of electrochemical impedance spectroscopy (EIS) .....	149
6.2 EXPERIMENTAL DETAILS .....	150
6.2.1 Experimental apparatus.....	150
6.2.2 Calculation of the proton conductivity .....	152
6.3 EVALUATION OF MEASUREMENT TECHNOLOGY .....	154
6.3.1 Verification of the equivalent circuit and calculation of conductivity....	154
6.3.2 Effect of bias voltage on the proton conductivity .....	157
6.3.3 Effect of pressure on the proton conductivity .....	160
6.4 PROTON CONDUCTIVITY OF PHOSPHORIC ACID DOPED MEMBRANES .....	162
6.4.1 Effect of temperature on proton conductivity .....	162
6.4.2 Effect of $H_3PO_4$ on proton conductivity .....	170
6.4.3 Effect of water on proton conductivity.....	172
<b>CHAPTER 7 CONCLUSIONS AND RECOMMENDATIONS FOR FUTURE WORK .....</b>	<b>178</b>
7.1 CONCLUSIONS .....	178
7.2 RECOMMENDATIONS FOR FUTURE WORK .....	180
<b>REFERENCES.....</b>	<b>181</b>
<b>PUBLICATIONS .....</b>	<b>195</b>

# Chapter 1 INTRODUCTION

## **1.1 Background**

As the natural resource depletion is accelerated, new energy sources are needed more urgently. The conventional and renewable energy industries are currently experiencing dramatic changes, especially in the last few years because of the price fluctuations of fossil energy sources.<sup>1</sup> It is a consensus that the future global energy supply can only be secured by increasing the share of renewable energy. Development of the fuel cell (FC) technology has obtained huge support and interest around the world in the past decade due to its huge market potential, positive impact on air quality and radically different nature, which makes it better than currently available power sources, and is considered one of the promising substitutes for new energy supply. Based on the latest fuel cell industry analysis report, the fuel cell market had a high growth in the global cumulative shipments at a compound annual growth rate of around 49% during 2005-2008 and will grow by over 75% during 2010-2012.<sup>2</sup>

There are several different kinds of fuel cells in terms of the operation temperature, electrolytes and conducting ions transferring through the electrolytes, including polymer electrolyte membrane fuel cell (PEMFC), alkaline fuel cell (AFC), phosphoric acid fuel cell (PAFC), molten carbonate fuel cell (MCFC) and solid oxide fuel cell (SOFC) etc.<sup>3</sup> Among these fuel cells, the PEMFC is highlighted because of its broad potential applications for portable electrical devices, automobiles and residential use.<sup>4</sup>

A basic single PEMFC consists of a proton conducting membrane, sandwiched between two catalyst impregnated porous electrodes. The combination of membrane and electrodes, called the membrane electrode assembly (MEA), is the core component of a PEMFC. Meanwhile, the membrane is also regarded as the core component for a MEA.<sup>5</sup> The current well-developed PEMFC technology is based on the perfluorosulfonic acid (PFSA) polymer membrane (e.g., Nafion® produced by DuPont Company) as the electrolyte.<sup>6</sup> However, the operational temperature for this



kind of polymer membrane is limited to below 100°C at atmospheric pressure as the conductivity is dependent on the presence of water<sup>6-8</sup>. The current research on PEMFC is focused on the optimisation of a device working at operational temperatures above 100°C and at very low humidity levels. Such operative conditions offer the advantages, including an enhanced catalyst stability towards the fuel impurities, a faster electrode kinetic and, crucially a simplified water management design, which is particularly important in the case of stationary applications.<sup>9</sup>

To improve the operating temperature to above 100°C, modified PFSA membranes, alternative sulphonated polymers and their composite membranes, and acid-based complex membranes are under investigation. Acid-doped polybenzimidazoles (PBIs, including polybenzimidazole and its derivatives) are particularly appealing as electrolyte membranes because of their high proton conductivities with no or low humidification and promising fuel cells performances.<sup>10</sup> In addition, phosphoric acid doped PBIs are the only type of polymer membranes which can work up to 200°C so far.<sup>11</sup> Due to containing alkaline functional groups (i.e. NH groups in benzimidazole rings) which can easily interact with strong acids, such as H<sub>3</sub>PO<sub>4</sub> and H<sub>2</sub>SO<sub>4</sub>, poly[2,2'-(m-phenylene)-5,5'-bibenzimidazole], generically referred to as polybenzimidazole (PBI), allows proton migration along the anionic chains via Grotthuss mechanism<sup>12-14</sup>. In particular, PBI has been widely investigated including synthetic approaches and casting processes<sup>15</sup>, membrane thermal stability<sup>16</sup>, methanol crossover<sup>17</sup>, acid doping procedure, proton transport<sup>14, 18-20</sup>, and fuel cells performances<sup>17, 21-25</sup>. High-temperature, PBI-based membrane electrolyte assemblies (MEAs) for PEMFC were commercially developed by the Celanese Ventures GmbH, Germany.<sup>26</sup> However, the under developing PBI membranes are still far from the PEMFC applications. Therefore, more researches of PBI polymer electrolyte membranes have been focusing on alternative acid impregnation, inorganic fillers composites, cross-linked blends etc.<sup>11, 27</sup>

Since the productivity of a PBI based polymer membrane is mainly supported by the proton migration along the anionic chains, and the anionic groups can easily be attached or grafted to the imidazole rings via N-H bonds, therefore it is a useful approach to enhance the productivity by increasing the numbers of imidazole groups

in the PBI based polymer membrane. Poly(2,5-benzimidazole) (ABPBI) is another benzimidazole polymer having better thermal and conductance properties than that of PBI as it has more rigid backbones and higher percentages of imidazole rings in the backbones.<sup>28-30</sup> Additionally, ABPBI can be synthesised from commercially available, cheap, single monomer, which could reduce the cost of synthesis of ABPBI and make ABPBI one of the most suitable polymers for PEMFC.

## **1.2 Motivation and Objectives**

To date, most of the energy that we use is converted via heat engines, which causes a significant waste of energy due to their low efficiency, and massive pollution, such as carbon dioxide, nitrogen and sulfur oxides etc. Driven by reducing greenhouse gas emissions, any technology with potentially improved energy efficiency to meet these aims should be developed and investigated.

As a sustainable, efficient and environmentally friendly energy converter, a fuel cell has a broad range of applications, such as for portable and mobile applications, stationary use etc; particularly, as an alternative to internal combustion engines in the transport section. Therefore, the development of fuel cell technology is of paramount importance in public and private life.

As mentioned before, one of the main challenges in PEMFCs is to develop the polymer electrolyte membrane (PEM) used at high temperatures with low humidification for improving the efficiencies which is also the main objective of this project including understanding the scientific research through the investigation of the development of PEMFC, exploring new methods and/or materials to produce higher operational temperature membranes and measuring their various properties. The details of the objectives are as follow:

- ❖ to synthesise ABPBI with adequate molecular weights for pristine and modified membranes fabrication;
- ❖ to synthesise in situ and characterise ABPBI/polyhedral oligomeric silsesquioxane (POSS) composite membranes;

- ❖ to understand the proton conducting mechanisms of phosphoric acid, water and POSS on the proton conductivity of phosphoric acid doped ABPBI and ABPBI/POSS composite membranes;

### **1.3 Outline of Thesis**

After the short introduction to this project, a more detailed introduction of fuel cells is included in Chapter 2. In Chapter 2, the specific topics include the background knowledge of fuel cell technology especially PEMFCs and a review of the development of PEM. As the main purpose of this project is to develop a PEM for high temperature applications, the fundamental theory of proton conducting and the approaches of achieving high temperature PEM materials are discussed in considerable detail.

Chapter 3 lists the main chemicals used in the project, providing the details of synthesis of polymers, membrane fabrication techniques and characterisation.

The results and discussion of the synthesis and characterisation of polymers are presented in Chapter 4. The synthesised polymers include ABPBI, copolymers of ABPBI and PBI, two different types of POSS respectively embedded ABPBI composites. The characterisation of these polymers includes their chemical structures, morphologies and thermal stabilities. Additionally, the evaluation of the reaction conditions of ABPBI synthesis is illustrated.

The fabrication and properties of membranes are described in Chapter 5. Effects of fabricating processes on the morphology of membranes and the relationship between the chemical structure and property of the membrane are discussed.

Chapter 6 presents the results and discussion of proton conductivity for ABPBI and ABPBI/POSS composite membranes. For a better understanding of the conductivity measurement, a brief introduction of the background and theory of impedance spectroscopy is reviewed followed by the details of conductivity measurement apparatus.

Finally, the conclusions are summarised in Chapter 6. The contribution and limitations of this work are also discussed followed by the suggestions with regards to the further work.

# Chapter 2 LITERATURE SURVEY

## 2.1 A Brief Introduction of Fuel Cells

As a promising alternative power source, fuel cells have the potential to play a significant role as they displays several advantages in future energy resources, including low emissions, high efficiency, low noise and simplicity and so on.<sup>3, 31</sup>

### a. Low emissions

Fuel cells can produce electrical and thermal power with lower emissions of greenhouse gases compared to more conventional power systems. Zero emission can be achieved if hydrogen is used as the fuel and produced from a renewable energy source.

### b. High efficiency

The highest efficiency that a heat engine can achieve is subject to the Carnot Cycle. In the Carnot cycle, a thermodynamic cycle occurs when a system is taken through a series of different states, and finally returned to its initial state. In the process of going through this cycle, the system may perform work on its surroundings, thereby acting as a heat engine. In an ICE, the engine accepts heat from a source at a high temperature ( $T_1, K$ ), converts part of the energy into mechanical work and rejects the remainder to a low temperature ( $T_2, K$ ). The maximum efficiency ( $\eta, \%$ ) can be expressed as:

$$\eta = \frac{T_1 - T_2}{T_1} \quad 2-1$$

Therefore, the greater efficiency can be achieved in an ICE when the temperature difference is greater. However, increasing temperature difference adds immense costs and inconvenience. As one of the main competitors of fuel cells, the internal combustion engine (ICE) is still only capable of converting less than 20% of the energy from the fuel though after continuous development in 20<sup>th</sup> century.<sup>31</sup> A fuel cell is not constrained by the maximum Carnot cycle efficiency as the combustion engine is, because it relies on an electrochemical reaction instead of a thermal cycle. In other words, it is just like an electrochemical energy conversion device which

converts the chemical energy directly into electrical energy. Consequently, this engine converter can have very high efficiency. Theoretically, a fuel cell can achieve an energy efficiency of 85 to 90% if the rejected heat is harnessed.<sup>31</sup> Current energy conversion efficiency for a power generation is about 30% depending on the fuel and process used, and fuel cell energy efficiency is currently 40% to 55% for electrical power generation, and potentially up to 70% for a fuel cell/gas turbine hybrid system.<sup>31</sup>

### **c. Low noise and simplicity**

The essentials of fuel cells are very simple. Unlike an ICE, fuel cells run very quietly owing to no moving parts and minimisation of noise and vibration levels caused by auxiliary equipments, therefore, fuel cells are highly reliable and long-lasting.<sup>32</sup>

Besides these benefits mentioned above, to consider the full advantages of a hydrogen economy-sustainability and increased energy security, fuel cells are seen as one of the future key enabling technologies for high efficiency, integrated electrical power and heat generation.<sup>31</sup>

## **2.1.1 Brief history of fuel cells development**

In 1838 a German-Swiss scientist Christian Friedrich Schönbein discovered the principle of fuel cells. The following year, based on his work, William Grove<sup>33</sup> invented the first fuel cell. He inserted platinised electrodes into two bottles filled with hydrogen and oxygen respectively. After adding diluted sulfuric acid solution, he noticed a small current flow between the two electrodes. Following on from that, Ludwig Mond and Dr. Charles Langer<sup>33</sup> developed fuel cells by using a thin porous diaphragm soaked with electrolyte and two porous electrodes containing perforated platinum or gold leaf as a current collector. In terms of the structure, it was very close to a modern fuel cell. However, because of the rapid development and wide application of heat engines at that time, the research and development on fuel cells stagnated for many years.

At the end of 1950s, Pratt and Whitney<sup>34</sup> developed an Alkaline Fuel Cell (AFC) system employed by U.S. Apollo space program. Subsequently, in 1962 a Polymer Electrolyte Membrane Fuel Cell (PEMFC) invented by the General Electric company

was deployed in the U.S. Gemini program.<sup>34</sup> The successful application of fuel cells in the space program again brought this technology to public attention.

Since 1990, the research and development of fuel cells has met a boom period due to the increasingly serious global energy crisis. In this century, because of another issue of global warming and waste gas emission, fuel cells are exciting the minds of not only theoretical scientists and practical technologists, but also most governments. It is believed that fuel cells will soon become a major competitor and eventually replace conventional energy devices.

### 2.1.2 Classification of fuel cells

**Table 2-1 Type of fuel cells**

Fuel Cell	Electrolyte /Catalyst	Operat. Temp./ Electric Power	Electrochemical Reaction
PEMFC	Polymer membrane/ Pt	80°C / Up to 250kW	Anode (A): $2H_2 \rightarrow 4e^- + 4H^+$ Cathode (C): $O_2 + 4e^- + 4H^+ \rightarrow 2H_2O$
AFC	Liquid KOH (immobilized)/ Pt	200°C / Up to 20kW	A: $2H_2 + 4OH^- \rightarrow 4H_2O + 4e^-$ C: $O_2 + 4e^- + 2H_2O \rightarrow 4OH^-$
PAFC	Liquid $H_3PO_4$ (immobilized)/ Pt	200 °C / >200kW	A: $2H_2 \rightarrow 4e^- + 4H^+$ C: $O_2 + 4e^- + 4H^+ \rightarrow 2H_2O$
MCFC	Molten carbonate/ Nickel	650 °C / >1MW	A: $2H_2 + 2CO_3^{2-} \rightarrow 2H_2O + 2CO_2 + 4e^-$ C: $O_2 + 2CO_2 + 4e^- \rightarrow 2CO_3^{2-}$
SOFC	Ceramic/ Ceramic	1000 °C / >50kW	A: $2H_2(CO) + 2O^{2-} \rightarrow 2H_2O(CO_2) + 4e^-$ C: $O_2 + 4e^- \rightarrow 2O^{2-}$

Note: PEMFC-Polymer electrolyte membrane fuel cell; PAFC-Phosphoric acid fuel cell; AFC-Alkaline fuel cell; MCFC-Molten carbonate fuel cell; SOFC-Solid oxide fuel cell

Fuel cell systems can be classified according to the working temperature: very high (over 1000°C), high (500-1000°C), intermediate (100-500°C) and low (25-100°C) temperature systems, or referring to the (atmospheric) pressure of operation: high, medium and low pressure system. They may be further distinguished by the fuels and/or the oxidants used: gaseous reactants (such as hydrogen, ammonia, air and oxygen), liquid fuels or solid fuels. For practical reasons fuel cell systems are simply distinguished by the type of electrolyte used (Table 2-1). The electrolyte can be solid polymer, liquid acid, ceramic, or molten ionic salt.<sup>31</sup>

**Alkaline fuel cell (AFC)**

The Alkaline Fuel Cell (AFC) was the first modern fuel cell developed intensively at the beginning in 1960. In an AFC, the electrolyte is concentrated KOH whilst hydroxyl ions are the conducting species transferring in the electrolyte.

There are two main advantages for the AFC<sup>35</sup>. Both anode and cathode reactions allow the application of non-precious metal nickel or its alloys as electro-catalysts, thus the cost can be relatively low. Furthermore, compared to other types of fuel cell, the AFC exhibits relatively high efficiency of up to 70%, which is mainly due to the rapid kinetics of oxygen reduction in the alkaline environment.

However, the AFC's performance is greatly affected by CO<sub>2</sub> from reformed fuels at the anode and air at the cathode. On the one hand, the reaction between CO<sub>2</sub> and OH<sup>-</sup> causes a reduced OH<sup>-</sup> concentration; on the other hand, KOH is gradually diluted by water which is generated during operation, both leading to a reduced conductivity of the electrolyte. As a result, water must be ejected immediately and CO<sub>2</sub> must be eliminated at both electrodes. However, to solve these problems would bring to the complexity of the fuel cell structure and increasing cost, thereby these defects limit the AFC's wide applications.

**Phosphoric acid fuel cell (PAFC)**

The PAFC was the first commercialised fuel cell technology owing to its stability, low volatility, and tolerability to CO.<sup>3</sup> The PAFC is working in a similar way to a PEMFC, i.e. the concentrated H<sub>3</sub>PO<sub>4</sub> is used as a proton-conducting electrolyte and the electrochemical reactions take place on highly dispersed electro-catalysts particles (i.e. Pt) supported on carbon black.

Although phosphoric acid electrode/electrolyte technology has now reached a level of commercialisation, to further improve carbon monoxide and sulphur tolerance, the research into catalysts is still focusing on evaluating Pt alloy, transition metal organic macrocycles etc. as cathode electro-catalysts. However, these technologies are still too expensive compared with alternative power generation systems, therefore, increasing the power density of the cells whilst reducing costs are still the key issues<sup>3</sup>.



**Molten carbonate fuel cell (MCFC)**

Similar to a PAFC, a MCFC also use a liquid electrolyte which is immobilised in a porous matrix. The electrolyte of a MCFC is a molten mixture of alkali metal carbonates. It operates at a relatively high temperature (typically 600-700°C) where the alkali carbonates form a highly conductive molten salt, with carbonate ions ( $\text{CO}_3^{2-}$ ) providing ionic conductivity. From the reactions (in Table 2-1), carbon dioxide acts as a reactant at the cathode and product at the anode. To make the cell work more efficiently, the  $\text{CO}_2$  generated from the anode is usually recycled to the cathode where it is consumed. Due to the high working temperature, non precious nickel and nickel oxide are used as the catalysts to promote the anode and cathode reactions. However, the MCFC operating temperature poses a great challenge to the stability and life of the cell components.<sup>3</sup>

**Solid oxide fuel cell (SOFC)**

In a SOFC, an oxide ion-conducting ceramic material (i.e. zirconia) is used as the electrolyte and the device is completely solid-state device<sup>3</sup>. Similar to the MCFC, in the SOFC a negatively charged ion ( $\text{O}^{2-}$ ) is transferred from the cathode through the electrolyte to the anode. Hydrogen or carbon monoxide can be used as a fuel.

In terms of principle and structure, the SOFC is an ideal choice with some distinct advantages over other types of fuel cell.<sup>31</sup> Because of no containing the liquid electrolyte, it can operate without worrying about electrolyte loss and material corrosion. Furthermore, non-precious metal electro-catalysts (such as Zr, Ni and Sr and so on) are used due to their high working temperature. However, successful candidates for electrolyte must be able to conduct  $\text{O}^{2-}$  which requires high operating temperatures and, while running at that high temperature, relative components must be thermally stable with closely matched thermal expansion coefficients which are the same as MCFC.<sup>3</sup>

**Polymer electrolyte membrane fuel cell (PEMFC)**

The polymer electrolyte membrane fuel cell (PEMFC), also known as proton exchange membrane fuel cell, was first developed for use by NASA in 1960s, and is now being developed for applications of transport as well as stationary and portable power. More details are given in following sections.

## 2.2 Introduction of PEMFC

A PEMFC uses a polymer membrane as the electrolyte. Therefore, it is also called the polymer membrane fuel cell (PMFC) or the solid polymer fuel cell (SPFC). A basic single PEMFC consists of a proton conducting membrane sandwiched between two catalyst (usually platinum or its alloys) impregnated porous electrodes (Figure 2-1a)<sup>3</sup>. This combination of membrane and electrodes is the core component of a PEMFC, called the membrane electrode assembly (MEA) (Figure 2-1b). Generally, an electrolyte attached to either side of the electrolyte physically separates the two reactants, and also prevents electronic conduction, while allowing ions to pass through; the electrons travel through an external loop to supply the load. The diffusion layers (Figure 2-1.a) provide a path for oxidant, electrons and fuel diffusion to the catalyst layers where the electrochemical reactions occur. At the anode, the fuel (i.e.  $H_2$  shown in Figure 2-1a and b) crosses the diffusion layer and produces protons and electrons at the catalyst layer. Protons then transfer through the membrane, while electrons go through the external circuit. Both finally reach the catalyst layer at the cathode to participate in the cathode reaction with oxygen.

Hydrogen was the initial option to be used as a fuel. Since then, several other fuels have been developed in the PEMFC. With different fuels, a PEMFC can be classified into hydrogen-PEMFC ( $H_2$ -PEMFC), direct methanol fuel cell (DMFC), formic acid fuel cell (FAFC) and so on.

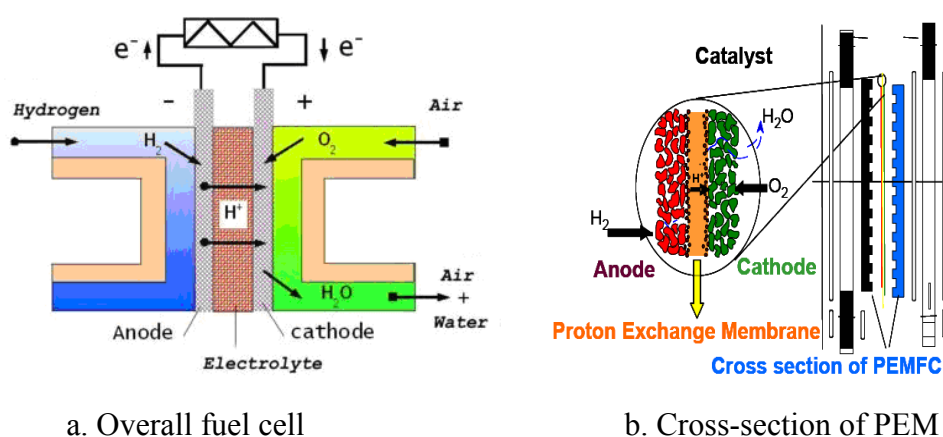


Figure 2-1 Scheme of a PEMFC<sup>3</sup>

### 2.2.1 Hydrogen PEMFC

As shown in the scheme of a PEMFC in Figure 2-1 and electrochemical reactions in Table 2-1, with hydrogen feeding at the anode, the hydrogen is oxidized. Electrons pass through the load to provide the desired current and end up at the cathode, where the matching reduction reaction occurs. Electrostatic balance is reached as the hydrogen ions diffuse through the electrolyte to get to the cathode. Therefore, with fuel continuously supplied, electricity is produced.

This technology has drawn the most attention because of its simplicity, viability, quick start-up, and it has been demonstrated in almost any conceivable application. After nearly half a century of development, this device has reached the test and demonstration phase<sup>36</sup>. An application of PEMFC as a primary power source in electric vehicles has received increasing attention in the last decade. Current commercial PEMFC, operating in the temperature range from 25°C to 80°C, can achieve power densities in the range of 0.35-0.7W/cm<sup>2</sup> in hydrogen-air systems at pressure levels between ambient pressure and 2.5 bar, which has brought the power density at stack level above the 1kW/l target that was set for automotive applications.<sup>37</sup>

Hydrogen is the most widely used fuel for fuel cells for various reasons:

#### a) Rich resource

The usage of fossil fuels (i.e. coal, oil and natural gas) has lasted over 200 years. It is believed that the fossil fuel can support human activities for less than 100 years.<sup>38</sup>

Fortunately, hydrogen is the most abundant element in the universe and can be easily produced from water and hydrocarbon compounds. A hydrogen-based energy system is regarded as a viable and advantageous option for delivering high-quality energy services in a wide range of applications in an efficient, clean and safe manner while meeting sustainability goals<sup>37, 39</sup>. In 2004, the worldwide hydrogen production was about 40 billion standard cubic feet per day, which is equivalent to about 75,000 MW of electrical power<sup>38</sup>. Barreto<sup>40</sup> also indicates that the aggregate share of fuel cells in global transportation market will be over 50% in the year 2050 and will rise to 71%

at the end of the 21<sup>st</sup> century. Hydrogen will account for a quarter of global final energies consumption in 2050 and half in 2100.

### b) Cleanness

Unlike fossil fuels, the final emission of hydrogen PEMFC is only water, without any greenhouse gas or nitric oxides, sulphur oxides etc.

### c) Large energy density

The energy density of fuel is defined as the amount of energy stored in a given amount of fuel:

$$\text{Energy density, MJ/kg} = -\Delta G/M \quad 2-2$$

where  $\Delta G$  represents the change in molar Gibbs free energy of formation at standard condition (298K, 1atm), and  $M$  is the molecular weight of the fuel.

Compared with other fuels, hydrogen has the highest energy density (Table 2-2).

**Table 2-2 Energy density comparison for several kinds of fuels**

<b>Fuel</b>	<b>Energy density, MJ/kg</b>
Hydrogen	113.68
Natural gas	49.9
Gasoline	47.5
Propane	47.0
Ethanol	28.3
Methanol	21.5
Formic acid	5.9

Note: All the data of Gibbs free energy are taken from Yaws<sup>41</sup>, the energy density of gasoline is from Caldirola<sup>42</sup>.

However, the wide application of hydrogen is technically limited by its generation, transportation and storage.<sup>43</sup>

### i. Hydrogen generation

Hydrogen is the clean energy only if all the moves (i.e. production and transportation) cause minimal environmental impact. Hydrogen in the free form is unavailable in

nature and the generation of hydrogen from fossil fuels in order to attain the same amount of energy is obviously not good for the environment, therefore, hydrogen generation from renewable energy has become a popular research area. Currently, hydrogen is mostly produced from fossil fuels in industry, and only 5% of hydrogen is produced from renewable sources.<sup>44</sup>

## **ii. Hydrogen transportation**

Currently, the infrastructures for hydrogen transportation are needed desperately and using the paved pipelines designed for natural gas has been proposed. However, the volumetric energy density of hydrogen is only one third of that of natural gas, which means that, in order to obtain the same amount of energy, hydrogen has to be transported at a much higher rate, thus leading to more significant pumping losses<sup>43</sup>. Also new fittings, pipe specifications, and more powerful compressors are required for hydrogen carrying<sup>43</sup>. In other words, a completely new distribution system for hydrogen transportation may be needed.

## **iii. Hydrogen storage**

It's a big challenge to store hydrogen as a liquid like other liquid hydrocarbons. The liquefaction of hydrogen is also expensive and inefficient.<sup>43</sup> However, progress has been made in the use of metal hydrides, and carbon-based hydrogen storage materials.

### **2.2.2 Direct Methanol Fuel Cells (DMFC)**

The operation of a DMFC is very similar to that of a H<sub>2</sub>-PEMFC, apart from the use of methanol as fuel and the production of carbon dioxide at the anode. In a DMFC, the hydrogen ions travel through the electrolyte and react with oxygen from the air and the electrons from the external circuit to form water at the anode completing the circuit. Although the gravimetric energy density of methanol is average (Table 2-2), it is the most electro-active organic fuel for fuel cells.<sup>45</sup>

Compared to a PEMFC relying on on-board reforming of hydrocarbons as its hydrogen source, a DMFC uses methanol directly as its fuel, without complex reforming components, thus the fuel cell system is significantly simplified. Unlike the usage of hydrogen suffers from storage and transportation, a DMFC does not

bear these drawbacks. Methanol is liquid at room temperature, thus it is much safer and more convenient to transport and store than gaseous hydrogen. In addition, methanol can be readily produced via manufacturing processes from plentiful raw materials such as coal and methane<sup>46</sup>. The DMFC can work at higher efficiency than conventional energy devices so that the emission of carbon dioxide can be effectively reduced. Moreover, no sulphur oxide, nitrous oxide or other pollutants are produced, thus DMFC is still environmentally acceptable.

However, a DMFC still suffers from two main drawbacks: lower efficiency and lower power density than H<sub>2</sub> PEMFC, due to the slower electrochemical methanol oxidation and methanol permeation through the polymer membrane.<sup>47</sup> The reaction rate of methanol oxidation at the anode is at least 3 to 4 orders of magnitude lower (even with high Platinum loading) than the electro-oxidation of hydrogen with a low Pt catalyst<sup>48</sup>. When using methanol as a fuel, part of methanol tends to permeate through the electrolyte membrane, which is known as methanol crossover. The diffusion driven by a methanol concentration gradient and electro-osmosis are mainly responsible for the methanol crossover. However, methanol diffusion occurs all the time in a DMFC as long as a concentration gradient is present, whilst electro-osmosis only takes place when current is being drawn, and the rate varies with membrane materials, e.g. the electro-osmotic drag coefficient (the number of water molecules taken by each proton whilst it is moving) of the Nafion polymer membrane is 2~3 at room temperature, but polybenzimidazole has an electro-osmotic drag coefficient near zero<sup>49</sup>. Methanol crossover has several disadvantageous effects on the cell performance<sup>3</sup>:

- ✧ **Reducing the fuel efficiency.** The methanol which crosses over produces no electrical energy, and is therefore essentially wasted.
- ✧ **Resulting in a ‘mixed potential’.** When methanol gets to the cathode, undesirable methanol oxidation may occur. This competes with oxygen reduction for catalytic sites, resulting in a ‘mixed potential’. This adverse effect leads to a lower open circuit voltage than the thermodynamic value.

- ✧ **Increasing the mass transport over potential.** To facilitate the cathode reaction, oxygen needs to readily diffuse to the catalyst layer, but crossed-over methanol consumes oxygen at the catalyst, thereby increasing the mass transport over potential.

### 2.2.3 Other fuels for PEMFC

Besides methanol and hydrogen, formic acid<sup>50-52</sup>, ethanol<sup>53, 54</sup> and hydrazine<sup>55</sup> etc., can also be employed as fuels for using in PEMFC.

Formic acid features a high theoretical open circuit potential (1.45 V) and is widely available in nature. Differing from proton transferred via sulphonic acid ions (e.g. Nafion®) or phosphoric acid (e.g. PBI membranes) in many membranes, in a formic acid (FAFC), formic acid partially dissociates into formate anions ( $\text{HCOO}^-$ ) which transfer proton<sup>50</sup>. Although the utilization of high concentrations of formic acid enhances the anode electrochemical kinetics, facilitates fuel cell design and raises the energy density of FAFC devices, the anode oxidation kinetics is still slow and current research is focused on the development of a more efficient anode catalyst.

An ethanol fuel cell has some advantages such as low toxicity and abundant availability in nature, but also suffers the fuel crossover problem similar to a DMFC.. Compared to methanol, ethanol has lower permeation rates probably due to its larger molecular size<sup>53</sup>. In addition, the ethanol permeation exhibited a less serious effect on the cell performance at the cathode compared to methanol due to its slower electrochemical oxidation kinetics on the Pt/C cathode<sup>54</sup>. However, the biggest disadvantage of ethanol fuel cells still comes from the slow ethanol oxidation at the anode.

Yamada et al<sup>55</sup> explored the hydrazine ( $\text{N}_2\text{H}_4$ ) as the fuel for PEMFC. Although the theoretical open circuit voltage for hydrazine is high (1.56 V), the performance of the hydrazine fuel cell is compromised by fuel crossover problems and permeation of by-product  $\text{NH}_3$  decomposed from hydrazine through the membrane.

### 2.2.4 Advantages and disadvantages of PEMFCs

Based on the brief description of different types of fuel cells in the above sections, the relative merits of PEMFC can be summarised. Usually, the advantages<sup>31</sup> of PEMFC against other fuel cells include:

- ✓ No free corrosive liquid in the cell;
- ✓ Simplified fabrication of the cell;
- ✓ Ability to withstand large pressure differentials;
- ✓ Minimal material corrosion problems;
- ✓ Long-life in operation etc.

However, the disadvantages<sup>31, 56</sup> of PEMFC exist in:

- Traditionally expensive fluorinated polymer electrolyte membrane (e.g. Nafion®) and high cost cells;
- Poor carbon monoxide (CO) tolerance of PFSA-based polymer membranes;
- Intricate water management and dehydration of polymer membranes when high humidification is needed;
- Difficulties in using reformat gases (such as methanol);
- Relative low energy efficiency owing to operating in low temperature etc.

## 2.3 Development of Polymer Electrolyte Membranes

Traditional electrolyte systems such as sulphuric acid and potassium hydroxide, used for their low cost and high ionic conductivity but saddled with their extreme corrosivity and challenging sealability, are giving way to new polymeric electrolyte systems. As early as in the 1940s scientists began to develop organic ion exchange resins which also were known as ionomers. Due to the interaction occurred between polymer and ions, these ionomeric polymers have many different properties compared to conventional polymers and are typically used as thermoplastics, fuel cell membranes, ion exchange membranes etc.<sup>57</sup>

As mentioned before, the first practical proton exchange membrane fuel cell developed by General Electric in the United States in the 1960s was used in manned space vehicles. This polystyrene sulphonate ion exchange membrane had a life time



of only 500h because of suffering from insufficient electrochemical stability under fuel cell operation conditions<sup>58</sup>.

The development of fluorocarbon based typically perfluorinated ionomers is regarded as one of the most important breakthroughs in the fields of ionomeric membranes. The state-of-the-art polymer electrolyte membrane fuel cell (PEMFC) technology is based on perfluorosulphonic acid (PFSA) polymer.<sup>59, 60</sup> A lifetime of over 60,000h under fuel cell conditions has been achieved with commercial Nafion membranes.<sup>6</sup>

However, the major shortcomings of PFSA polymer membranes include low operating temperature (typically 80°C) and extremely high cost.<sup>56, 61</sup> It is worthy to mention that most of the shortcomings related to the low temperature PEMFC technology based on PFSA polymer membranes can be solved or avoided by exploring alternative materials for operating at higher temperatures. Therefore, high temperature polymer electrolyte membranes, such as modified PFSA membranes, alternative polymers (e.g. sulphonated polyetheretherketone and sulphonated PBI etc.) and their composite membranes, and acid-based complex membranes (e.g. phosphoric acid doped PBI) for operation above 100°C are under active development.

To better understand the development of polymer electrolyte membranes, first of all, it is important to understand the mechanism of ion (or proton) transfer in or between these ionomeric polymers. The concise introduction of well developed PFSA membranes and the motivations for the purpose of high temperature PEMFC applications are also necessary to be reviewed.

### **2.3.1 Mechanism of proton conducting in PEM**

Proton conductivity is a key process in the production of electricity in a hydrogen fuel cell. The proton conducting phenomena have been studied extensively from different points of view by many scientists. Amongst of them, Grotthuss initially presented ‘hopping’ mechanism<sup>12</sup> in 1806, then Kreuer et al. presented ‘vehicle’ mechanism<sup>62</sup> in 1982. Although the transfer of protons in solid electrolyte polymer is widely studied and the precise mechanism is not completely known yet, the

‘hopping’ mechanism and ‘vehicle’ mechanism have been mostly accepted because they can well explain the proton conductivity phenomena in currently widely developed PEMFC.

The proton has no electron shell of its own therefore strongly interacts with the electron density of its environment. In non-metallic compounds, it strongly interacts with the valence electron density of its nearest neighbours. If this is a single oxygen, this results in the formation of an O-H bond which is less than 100pm in length compared to about 140pm for the ionic radius of the oxide ion. For the distance of oxygen with  $\sim 280\text{pm}$ , the proton may be involved in two bonds, i.e. a short and strong bond with the so-called proton donor and a longer but weak bond with a proton acceptor, which is the asymmetrical hydrogen bond (O-H $\cdots$ O).<sup>63</sup> Water is thought as the best solvent for protons and exhibits unusually high equivalent conductivity of protons. The proton transfers through hydrogen-bonded network of water molecules, which is so-called ‘Grotthuss mechanism’<sup>12, 13</sup>, or ‘hopping mechanism’ or ‘structure diffusion’.

In the ‘hopping’ mechanism, two steps are involved, i.e. polarisation of the hydrogen bond or the proton intermolecular transfer and the depolarisation or reorientation of water dipole (in Figure 2-2).<sup>13</sup> The current is realised through the protons fluctuating between proton donors and acceptors. This mechanism comprises features typical for both the solid and liquid state therefore is widely employed to explain the proton conductivity in a PEMFC at hydrous and/or anhydrous conditions.

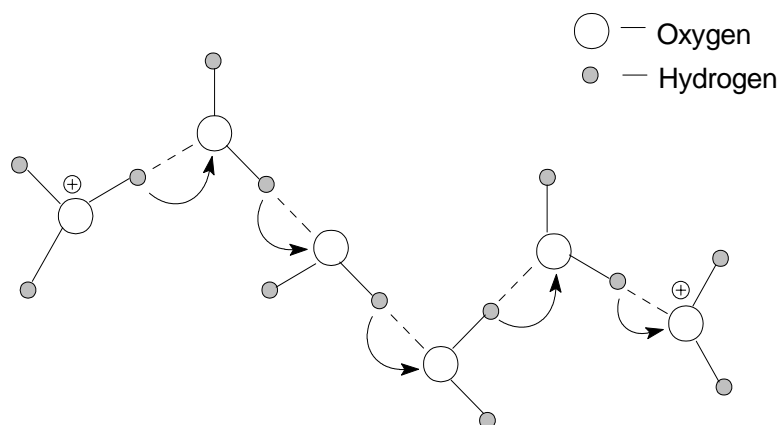


**Figure 2-2 Proton transfer according to Grotthuss mechanism**

Based on the ‘hopping’ mechanism, the free proton is regarded as having a momentary existence. However, in the late 1960s, Fischer et al.<sup>64</sup> suggested that the proton may remain shielded by some electron density along the entire diffusion path to explain the some phenomena of proton diffusivity. Obviously, in that case, the momentary existence of a free proton is not required. Kreuer et al. further proposed ‘vehicle’ mechanism which is also called molecular diffusion.<sup>9, 13, 62, 63, 65</sup>

The proton transfer via ‘vehicle’ mechanism in a hydrous Nafion membrane is illustrated in Figure 2-3. The proton loaded on a H<sub>2</sub>O molecule (as a ‘vehicle’ form H<sub>3</sub>O<sup>+</sup>) migrates through the channel and is unloaded to another H<sub>2</sub>O molecule, whilst, the unloaded ‘vehicle’ (H<sub>2</sub>O) move in the opposite direction. Gradually, the proton is transferred from the anode to the cathode. Obviously, unlike the ‘hopping’ mechanism, a hydrogen bond is not necessary for proton transport within this model and the proton does not migrate as H<sup>+</sup> but as H<sub>3</sub>O<sup>+</sup>.

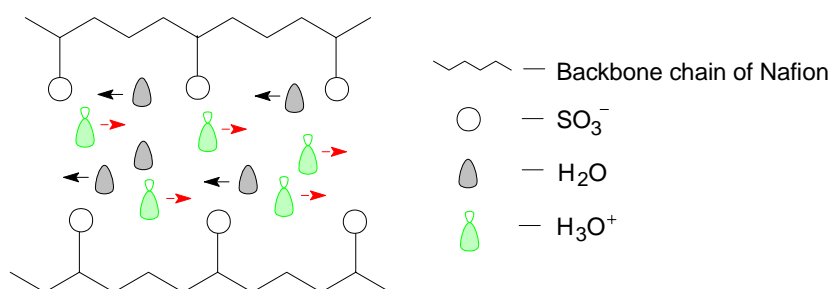


**Figure 2-3 Proton transfer according to Vehicle mechanism**

Generally, the ‘hopping’ mechanism can well explain the proton transfers in the anhydrous oxo-acids systems (i.e. H<sub>3</sub>PO<sub>4</sub><sup>66</sup>), whilst the ‘vehicle’ mechanism is prevalent in concentrated aqueous systems (i.e. Nafion). In some cases, Kreuer found that, these two mechanisms could work together as a mixed mechanism<sup>67</sup> and the dominated one can be either the ‘hopping’ mechanism or the ‘vehicle’ mechanism based on the various temperature and concentration of the system. To further distinguish the pivotal role between these two mechanisms, Kreuer proposed a method by measuring the relevant rates of the proton transfer and proton diffusion. For a example, if the rate of proton transfer is much larger than the rate of proton diffusion, which indicates the proton transfer rate successfully dominates over the vehicle diffusion, in other words, the character of conduction mechanism change from the ‘vehicle’ mode to ‘hopping’ mode.<sup>68</sup>

## 2.3.2 Perfluorinated ionomer membranes

### 2.3.2.1 The structure and properties of perfluorosulphonic (PFSA) polymer membranes

As mentioned before, the well-developed PEMFC technology is based on PFSA materials as PEMs. It is a common view that the future optimal membrane materials will not be a PFSA polymer. However, the PFSA based PEMFCs have become the standard against those membrane material candidates. To take in this sense, it is still necessary to know the properties of PFSA based membranes.

**Table 2-3 Structure of PFSA polymer and typical properties of commercial PFSA membranes**

$$\begin{array}{c} \text{---}(\text{CF}_2\text{---CF}_2)_x\text{---}(\text{CF}_2\text{---CF})_y\text{---} \\ | \\ (\text{O---CF}_2\text{---CF})_m\text{O---}(\text{CF}_2)_n\text{---SO}_3\text{H} \\ | \\ \text{CF}_3 \end{array}$$

Structure parameter	Trade name and types	Equivalent weight (IEC, mequiv.g <sup>-1</sup> )	Thickness (μm)
m=1;x=5-13.5; n=2;y=1	DuPont Co.		
	Nafion® 120	1200(0.83)	260
	Nafion® 117	1100(0.91)	175
	Nafion® 115	1100(0.91)	125
m=0,1;n=1-5	Nafion® 112	1100(0.91)	80
	Asahi Glass Co.		
	Flemion®-T	1000(1.00)	120
	Flemion®-S	1000(1.00)	80
m=0;n=2-5;X=1.5-14	Flemion®-R	1000(1.00)	50
	Asahi Chemicals		
	Aciplex®-S	1000-1200(0.83-1.00)	25-100
m=0;n=2;X=3.6-10	Dow Co.		
	Dow®	800(1.25)	125
	Solvay		
	Hyflon®-Ion	900(1.11)	

As one of typical fluorocarbon based ionomers, the PFSA polymer is composed of carbon-fluorine backbone chains with perfluoro side chains containing sulphonic acid groups at its end (in Table 2-3). The polytetrafluoroethylene (PTFE)-like molecular backbone provides PFSA polymer with excellent long-term stability in both oxidative and reductive environments whilst the sulphonic acid groups cause the

sulphonate polymer to swell in various organic solvents and be suspended for further formations of membranes or MEAs. Since DuPont Company commercialised the polymer membrane based on PFSA with the trade name of Nafion in 1968, Nafion has become the industry standard PEM and widely used in almost all current PEMFC development.<sup>6</sup> Other companies such as Dow, Asahi and Solvay, have also developed their membranes based on similar PFSA structures. Some typical commercial PFSA membranes and their structures are listed in Table 2-3.<sup>56, 69</sup>

Basically, to determine a qualified PEM when fuel cell system tests are absent, ion exchange capacity (or equivalent weight), water content and proton conductivity are regarded as the key parameters.

**Table 2-4 Main properties of Nafion® membranes**

Property	Typical Value
<b>Physical Properties</b>	
Tensile modulus, MPa	(ASTM D 882)
50% RH, 23°C	249
Water soaked, 23°C	114
Tensile strength, MPa	(ASTM D 882)
50% RH, 23°C	43 <sup>a</sup>
Water soaked, 23°C	34 <sup>a</sup>
Elongation at break, %	(ASTM D 882)
50% RH, 23°C	225
Water soaked, 100°C	200
Density, g/cm <sup>3</sup>	1.98
<b>Hydrolytic Properties</b>	
Water content, %water	5 (ASTM D570)
Water uptake, %water	38 <sup>b</sup> (ASTM D570)
Thickness change, %increase	
from 50%RH to water soaked, 23°C	10 (ASTM D 756)
Linear expansion, %increase	
from 50%RH to water soaked, 23°C	10 (ASTM D 756)
Conductivity, S.cm <sup>-1</sup>	
Measurement cell submersed in 25°C D.I. water during experiment	$8.3 \times 10^{-2}$

Note: a, measured in machine direction; b, water uptake from dry membrane soaked in water at 100°C for 1 hour.

The ion-exchange capacity (*IEC*) is defined as the moles of exchangeable acidic protons per gram of dry polymer. Another common term used to describe the ionic content is the equivalent weight (*EW*) which is the inverse of *IEC*. Obviously, the

higher the value of *IEC* leads to higher proton conductivity. The water content in a membrane is represented by the water uptake (calculated by weighing the membrane under both hydrated and dry conditions) or the number of water molecules per acid unit, also referred to as the hydration number ( $\lambda$ ) (calculated from water uptake and *IEC*). Via the hopping or vehicle mechanism, the water molecules always act as the very important proton carriers, resulting in higher conductivity if the higher water content existed in the membrane. The proton conductivity of a membrane is particularly important since it plays a significant role in the performance of the PEMFC. Higher levels of proton conductivity result in higher power densities. Although there are many other properties of PEMs that have important correlations to fuel cell performance (thermal stability, methanol crossover, electro-osmotic drag, etc.), the parameters of *IEC*, water uptake and proton conductivity are essential when it comes to evaluating membranes as the candidates for PEMFCs<sup>70</sup>. The main properties of Nafion membranes are given in Table 2-4.<sup>71</sup>

### 2.3.2.2 Proton transfer routes in PFSA polymer membranes

Water is always essential for the proton transfer in a PFSA based membrane. Kreuer<sup>9</sup> provided a classical explanation about the proton transfer routes in the case of Nafion membrane (in Figure 2-4).

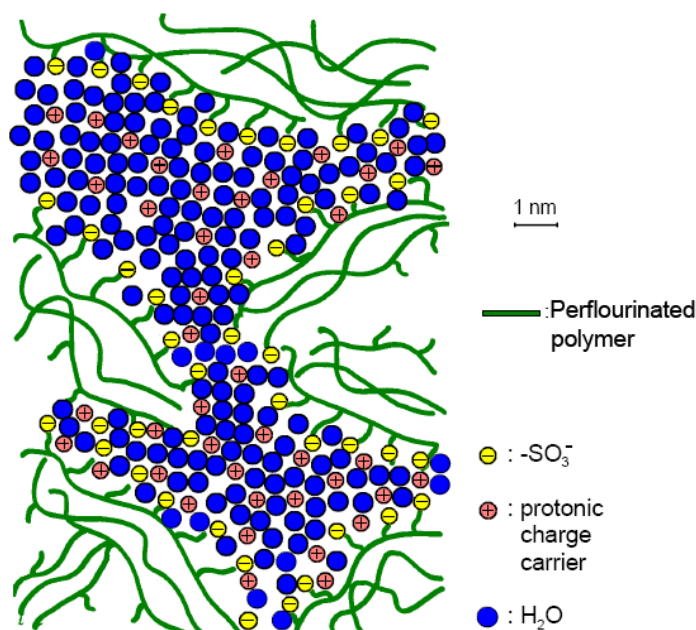


Figure 2-4 Microstructure of Nafion<sup>9</sup>

The structure of Nafion involves the extremely high hydrophobicity of the PTFE-like polymer backbone with the extremely high hydrophilicity of grafted sulphonic acid functional end groups, which results in a hydrophilic/hydrophobic nano-separation especially in the presence of water. The hydrophilic domains which are formed by the aggregation of sulfonic acid groups spontaneously absorb water and then swell to form nano-channels. These nano-channels are well connected each other and responsible for water and protons transporting. In the nano-channels, charge carriers are formed by dissociation of the hydrated acidic functional groups whilst protons transfer through the hydrophilic channels via ‘hopping’ and/or ‘vehicle’ forms. Additionally, the hydrophobic domains provide the polymer membrane with morphological stability and prevent its dissolution in water.

### 2.3.2.3 Limitations of PFSA polymer membranes

Compared to these currently developing electrolytes, Nafion membrane performed some unique characteristics. For example, compared with  $\text{H}_3\text{PO}_4$ , the catalytic activity of carbon-supported noble metal catalysts for oxygen reduction is high in the PFSA electrolyte, owing to the non-absorbing nature of sulphonic acid anions on the Pt catalyst surface. Solubility of  $\text{H}_2$ <sup>72</sup> and  $\text{O}_2$ <sup>73</sup> are also found to be 20-30 times higher than that in  $\text{H}_3\text{PO}_4$ . As a result of the fast electrode reaction kinetics, the performance of Nafion based PEMFC is high, especially at low noble metal loading.<sup>56</sup>

Although great success has been made with the PFSA membranes, some fatal or inherent shortcomings hindered their widely commercialised applications. The main disadvantages of the Nafion membrane include:

#### 1. Limited operational temperature;

Since the high proton conductivity of hydrated polymers relies on the presence of water in the hydrophilic domains as described above, the presence of water limits the operational temperature below 100°C under ambient atmosphere pressure, typically around 80°C. At 100% relative humidity (RH) the conductivity of Nafion is generally between  $1.0 \times 10^{-2}$  and  $1.0 \times 10^{-1} \text{ S.cm}^{-1}$  and drops by several orders of magnitude as the humidity is decreased.<sup>74</sup>

## 2. High cost;

Nafion membrane cost amounting to more than 100US\$ per kW makes its applications in cost critical situations such as fuel cells for electrical vehicles unlikely.<sup>56</sup>

## 3. Low CO tolerance;

The currently limited operation temperature leads to a low CO tolerance of the electrocatalyst.<sup>75</sup>

## 4. High crossover rate of methanol.

In the DMFC, when methanol is directly used as fuel, Nafion membrane suffers from a high crossover rate of methanol.<sup>76</sup>

### 2.3.3 Reasons for developing high temperature polymer electrolyte membranes

The term high temperature for a PEMFC refers to a temperature range from 100~200°C relative to the currently well-developed PFSA based PEMFC technology typically operating under 100°C. It is widely considered that, these shortcomings associated with the low temperature PEMFC technology based on PFSA membranes mentioned above, can be overcome by exploring alternative membranes operational at higher temperatures (i.e. >100°C). The advantages from the PEMFC operating at high temperatures have been broadly reviewed in some literatures<sup>56, 74, 77, 78</sup>. Generally, the driving forces of developing alternative membranes operational at higher temperatures are involved in benefits from electrode reactions, lifetime of catalyst, fuel feeding, structural design and overall system energy efficiency which are summarised as follows.

#### 2.3.3.1 Enhancing kinetics of electrodes reactions

The Tafel equation is normally used to represent the performance of a PEMFC in the kinetically controlled regime.<sup>78</sup>

$$E = E_{rev} + b \log i_0 - b \log i \quad 2-3$$

where  $E$ ,  $E_{rev}$ ,  $b$ ,  $i$  and  $i_0$  are the electrode potential, reversible potential, Tafel slope, current density and exchange current density, respectively.



Tafel slope  $b$  can be calculated by

$$b = -2.3 \times \frac{RT}{\alpha n F} \quad 2-4$$

where  $\alpha$  is the electron transfer coefficient and  $n$  the number of transferred electrons.

Electrode potential ( $E$ ) is the electromotive force of driving the electrodes reaction in a cell. The smaller the value  $E$  of is, the easier the electrodes reactions occur. From the Tafel equation,  $E$  is determined by  $E_{rev}$ ,  $b$ , and  $i_0$ . Theoretically, Tafel slope  $b$  varies linearly with temperature (equation 2-4) when assuming the electrochemical reaction mechanism is independent of the temperature.  $i_0$  is also found to increase with temperature<sup>78</sup>. The variation of  $E_{rev}$  with temperature is discussed as follows.

$E_{rev}$  is related to temperature according to equation below:

$$E_{rev} = E_{rev}^o + \left( \frac{\Delta S}{nF} \right)_p (T - 298) \quad 2-5$$

where  $\Delta S$ ,  $n$  and  $p$  is the entropy, the transferred electron number and partial pressure for  $H_2/O_2$  reactions respectively,  $F$  is the Faraday constant.

When the electrochemical reaction of  $H_2/O_2$  occurs under  $100^\circ\text{C}$ , the gaseous reactants ( $H_2$  and  $O_2$ ) transfer into the liquid product ( $H_2O$ ), thus the entropy ( $\Delta S$ ) for the  $H_2/O_2$  reaction is negative. Therefore,  $E_{rev}$  decreases with increasing temperature under  $100^\circ\text{C}$ . However, this effect is less judged above  $100^\circ\text{C}$  because the product  $H_2O$  becomes gaseous.

In the electrochemical reaction, the term thermodynamic open circuit voltage (OCV) is another factor for determining the workability of electrochemical reactions. The OCV decreases with increasing temperature, especially above  $100^\circ\text{C}$  resulting from the increase of partial pressure of the gaseous product  $H_2O$ , which is confirmed by Xu et al.<sup>79</sup>

To sum up, the kinetics for both electrode reactions is enhanced with the operational temperature increasing. Additionally, in a DMFC, because the methanol oxidation rate is at least three to four orders of magnitude lower than hydrogen oxidation<sup>48</sup> and the overall kinetics is determined by the relatively slow oxidation reaction, thus, the enhanced kinetic with increasing temperature is especially important for the direct oxidation of methanol in DMFC.

### 2.3.3.2 Increasing CO tolerance

As discussed before, the pure hydrogen is not yet a viable option due to lack of availability and impractical storage technique, though PEMFC generally performs best by using pure hydrogen. On-site generation of hydrogen by steam reforming of various organic fuels is the obvious choice, but these reformed gases contain carbon monoxide. It was found that, however, at the conventional PEMFC operating temperature of 80°C, a CO content as low as 10-20ppm in the fuel feed results in a significant loss in cell performance due to CO poisoning of the electrode catalyst.<sup>80</sup> Figure 2-5 shows the mechanism of CO poisoning Pt electrode catalyst.<sup>22</sup>

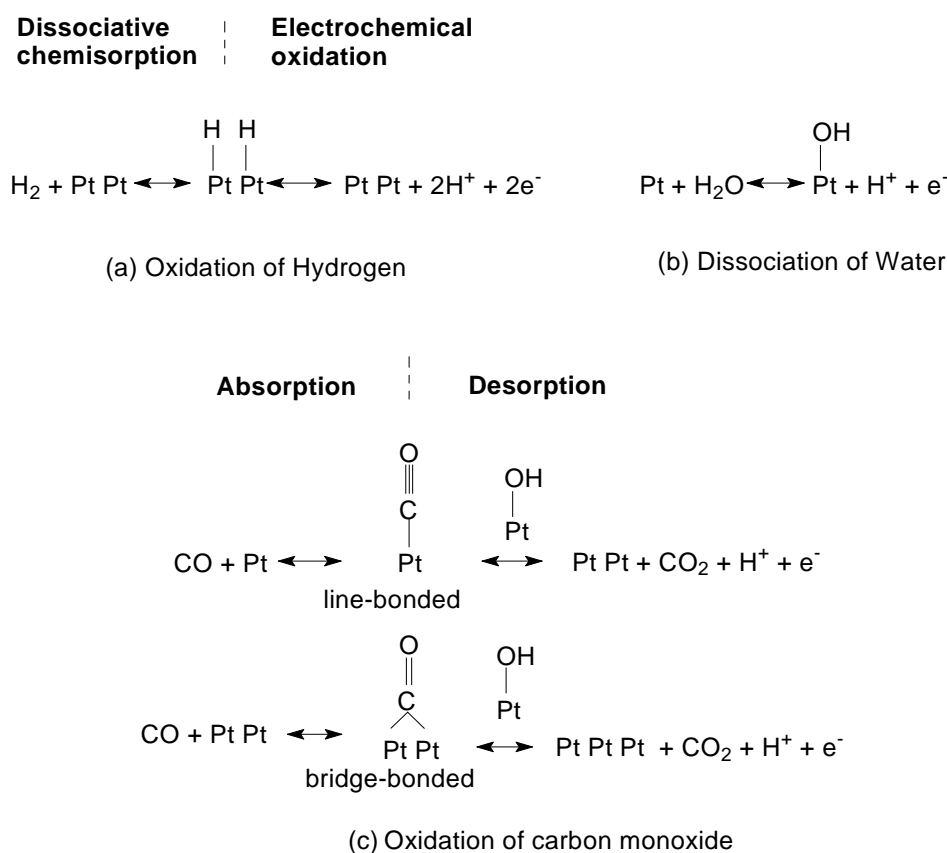


**Figure 2-5** Reactions happened on the anodic platinum catalyst

As shown in Figure 2-5a, oxidation of  $H_2$  on Pt takes place in two steps, i.e. dissociative chemisorption and electrochemical oxidation. The former step requires two free adjacent sites of Pt surface atoms and the latter produces two free Pt sites instead.

When CO is contained in  $H_2$  fuel, it competes with  $H_2$  for the adsorption sites of Pt with two types of bonding models (line-bonded and bridge-bonded shown in Figure 2-5c). With the attendance of O atoms from the dissociation of water (Figure 2-5b), it will be easy to desorb CO from the site of Pt via CO to  $CO_2$ . However, the rate-determining step for sequences of CO adsorption and desorption is the formation of the oxygen-containing adsorbate, or the dissociation of water. Additionally, the desorption of the adsorbed CO occurs at around 0.5V vs. RHE (reversible hydrogen electrode) of an anode potential whilst the anode potential is under 0.1V vs. RHE under operational conditions in a PEMFC. In other words, CO is an inert adsorbate on the Pt surface, resulting in the dramatically reduction of the Pt activity.

The considerable efforts have been made to reduce the effect of CO, including feeding oxidant into the fuel, further purifying the fuel and exploring CO-tolerant electro-catalyst etc. However, these lead to other drawbacks such as high cost and safety issues.

It is well known that, however, the adsorption of CO on Pt is strongly favoured at low temperature and disfavoured at higher temperature<sup>81, 82</sup>. Therefore, it is valuable to improve CO tolerance by increasing operational temperatures. Compared with the CO tolerance of 10-20ppm at 80°C, Pt based catalysts can tolerate up to 1,000ppm at 130 °C and up to 30,000ppm at 200 °C<sup>56</sup>. Obviously, such a high CO tolerance makes it possible to use the simply reformed  $H_2$  fuel.

### **2.3.3.3 Improving water management and gas diffusion**

In most cases, the proton conductivity of a membrane is dependent on its level of hydration and the performance of a PEMFC is greatly affected by the operational environmental humidity. Figure 2-6 gives a basic view of the water balance in a PEMFC: i) the anodic oxidation consumes water at the anode; ii) the cathodic reduction produces water which may diffuse back to the anode; iii) the protons

associated with water molecules (electro-osmotic drags) transport from the anode to the cathode; iv) water at the cathode may evaporate into the air; v) water may be delivered if the supplied air is humidified and, vi) the supplied fuel contains water that may diffuse into the anode.<sup>3</sup>

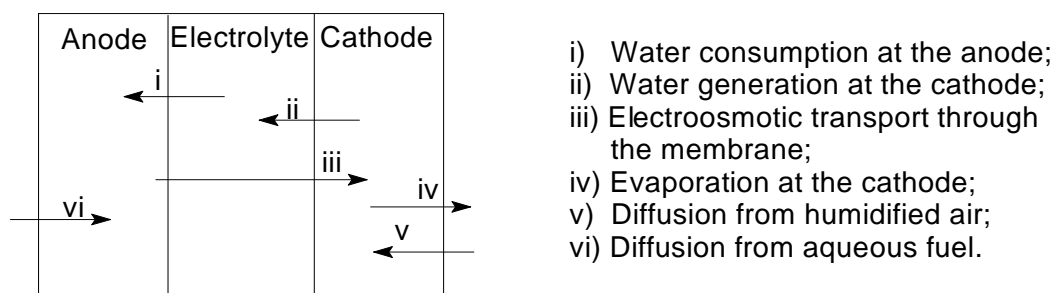


**Figure 2-6 A diagram of different water movements in a PEMFC**

It is well known that the proton conductivity significantly decreases with a lack of water in the membranes and gas diffusion electrodes in a PEMFC below 100°C. However, the excessive water in the cathode causes ‘flooding’, which also leading to restrict oxygen transport through the porous gas diffusion electrode.<sup>78</sup> These problems can be relieved by operating a PEMFC above 100°C because at that condition, only a single phase of gaseous water exists, therefore the water management system can be largely simplified.

The performance of a PEMFC is also greatly affected by gas diffusion. Basically, the more or rapider the gas (e.g. H<sub>2</sub> and O<sub>2</sub>) is transported to participate the electrochemical reaction at the anode and cathode, the higher the current density can be achieved. Gas diffusion through a MEA is characterised by the gas diffusion coefficient. Generally, with the operational temperature increasing the gas diffusion coefficient increases whereas the gas solubility decreases, for example, the gas diffusion coefficient of O<sub>2</sub> through water vapour is several orders of magnitude larger than through liquid water. Therefore, high operational temperature facilitates gas transporting through the MEA and should lead to an increased PEMFC performance in the mass transport controlled regime.<sup>78</sup>

#### **2.3.3.4 Increasing overall system energy efficiency**

Due to the thermodynamically irreversible reaction, changes in entropy and Joule heating, nearly half of the energy produced in a PEMFC operated at 80°C has to be

dissipated through the cooling system.<sup>56</sup> Obviously, it is very inefficient for a PEMFC operating below 100°C.

When a PEMFC operates above 100°C, the heat rejection is much easier because the temperature in a fuel cell system is great different from the ambient environment, leading to the simplified cooling system and the increased power density of the fuel cell system. In addition, the waste heat produced at higher temperature can also be recovered and in turn used either for direct heating, steam reforming, or pressurised operation. Thus, the overall system efficiency is significantly increased under higher temperature operating conditions.<sup>78</sup>

### **2.3.3.5 Other benefits of high temperature operation**

Besides the benefits listed above, there are other advantages<sup>78</sup> of high operational temperature as follows.

- 1) Because of little or even no liquid water presented in the fuel cell above 100°C, the flow field which is to provide a uniform reactant distribution over electrode surface area can be simplified and flow fields may be simplified without having to consider two-phase flow.
- 2) The high operational temperature i.e. 100-200°C can provide the heat for H<sub>2</sub> desorption at the anode which is favourable for developing the higher hydrogen storage materials.
- 3) High operational temperature is also very important for a direct methanol fuel cell. As we know, one of the main technical challenges for the direct use of methanol as fuel is the insufficient activity of anodic catalyst which leads to a high anodic over-potential loss. The insufficient activity of the anode catalyst results from the slow kinetics of the methanol oxidation and the strong poisoning effect of the intermediate species (CO) from methanol oxidation. Both negative effects could be lightened by increasing the operational temperature of DMFC. Additionally, when DMFC operates at 200°C, the temperature close to that of methanol reforming, will allow for an integration of the fuel cell with a high-capacity hydrogen storage tank or a methanol reformer. The integration is expected to give the overall power system

advanced features including higher efficiency, smaller size, lighter weight, simple construction and operation, and power capital and operational cost.<sup>83</sup>

## **2.4 Approaches for High Temperature PEM**

The essential requirements for operational high temperature polymer membrane electrolyte materials of PEMFC include<sup>56</sup>:

- High proton conductivity;
- Good chemical stability and thermal stability;
- Good mechanical properties (strength, flexibility, and processability);
- Low gas permeability and low water drag;
- Fast kinetics for electrode reactions;
- Low cost and commercial availability.

In order to meet the requirements of the high operating temperature (above 100°C), modified PFSA membranes, alternative sulphonated polymer and their composite membranes, and acid-based complex membranes are under investigation.

### **2.4.1 Modifications of PFSA polymer membranes**

Since the conductivity of PFSA membrane will decrease at the temperature approaching 100°C because of the water loss, many research studies have been carried out to modify the PFSA membranes for operating at high-temperature with low humidification. Generally, the routes for modifying the PFSA membranes include<sup>56</sup>:

- 1) Replacing water by swelling the membranes with nonaqueous and low volatile solvent to replace water. The difficulties for those PFSA membranes swollen in these media may arise from the immobilisation of liquids especially in the presence of water, and adsorption of the solvent on the catalyst surface.
- 2) Exploring thin and reinforced PFSA membranes. Although the thickness has been successfully reduced down to 5~30 $\mu\text{m}$  with good conducting, one of the challenges is to maintain the good mechanical strength under swelling and high temperatures.

3) Composites with single-functional particles (as the water absorber) and bi-functional particles (both as the water absorber and proton conductor) to enhance water absorbability and/or proton conductivity.

Table 2-5 summarised the efforts as well as other modifications of PFSA-based membranes.<sup>56</sup> However, they are constrained by PFSA polymer's glass transition temperature (160°C for a completely dry sample and 99°C for a fully hydrated sample<sup>77</sup>).

**Table 2-5 Summary of modifications of Nafion membranes**

Modifiers	Remarks
H <sub>3</sub> PO <sub>4</sub>	$5.0 \times 10^{-2} \text{ S.cm}^{-1}$ at 150°C
PTA-acetic acid	H <sub>2</sub> /O <sub>2</sub> , 110°C, 660mA.cm <sup>-2</sup> at 0.6V, 1/1atm, humidifier 50/50°C
PTA-TBAC	H <sub>2</sub> /O <sub>2</sub> , 120°C, 700mA.cm <sup>-2</sup> at 0.6V, 1/1atm, humidifier 50/50°C
SiO <sub>2</sub>	$>2.0 \times 10^{-1} \text{ S.cm}^{-1}$ , 100°C, 100%RH
SiO <sub>2</sub>	DMFC, 145°C, 4.5/5.5 atm(air), 350mA.cm <sup>-2</sup> at 0.5V
SiO <sub>2</sub> /siloxane	H <sub>2</sub> /O <sub>2</sub> , 130°C, 3/3atm
Teflon + PTA	H <sub>2</sub> /O <sub>2</sub> , 120°C, 400mA.cm <sup>-2</sup> at 0.6V, 1/1atm, humidifier 90/84°C
ZrP	DMFC, 150°C, 4/4atm, 350mW.cm <sup>-2</sup> (O <sub>2</sub> ), 260mW.cm <sup>-2</sup> (air)
ZrP	H <sub>2</sub> /O <sub>2</sub> , 130°C, 1.5A.cm <sup>-2</sup> at 0.45V, 3atm
di-isopropyl phosphate	$4.0 \times 10^{-2} \text{ S.cm}^{-1}$ at 25°C
SiP-PMoA/PTA	$5.0 \times 10^{-3} \text{ S.cm}^{-1}$ at 23°C, fully hydrated
SiWA( + thiophene)	Fuel cell test at 80°C
SiO <sub>2</sub> ,PTA-SiO <sub>2</sub> , SiWA-SiO <sub>2</sub>	DMFC, 140°C, 3/4atm, 400mW.cm <sup>-2</sup> (O <sub>2</sub> ), 250mW.cm <sup>-2</sup> (air)
PMoA+SiO <sub>2</sub>	$>3.0 \times 10^{-1} \text{ S.cm}^{-1}$ , 90°C

## 2.4.2 Alternative sulphonated polymer membranes

Development of sulphonated polymer membranes as alternatives to PFSA is principally motivated by reducing the material cost for low-temperature operation. Sulphonation can be performed mainly in three ways: 1) Direct sulphonation in concentrated sulfuric acid;; 2) Chemically grafting a group containing a sulphonic acid onto a polymer or by graft copolymerisation using high energy radiation followed by sulphonation of the aromatic component; and 3) Synthesis from monomers bearing sulphonic acid groups.

Since the high chemical and thermal stabilities are the basic requirements for a PEM material at high operating temperature, two main groups of polymers, inorganic elements (i.e. F, Si etc.) contained polymers and aromatic polymers with phenylene backbones, respectively, have been widely investigated for these purposes.

Some of these materials show interesting features for a possibility of operating at high temperatures. More efforts are also undertaken to develop organic-inorganic composites based on these alternative polymers in order to achieve high operational temperatures.

### 2.4.2.1. Proton transfer routes in sulphonated polymer membranes

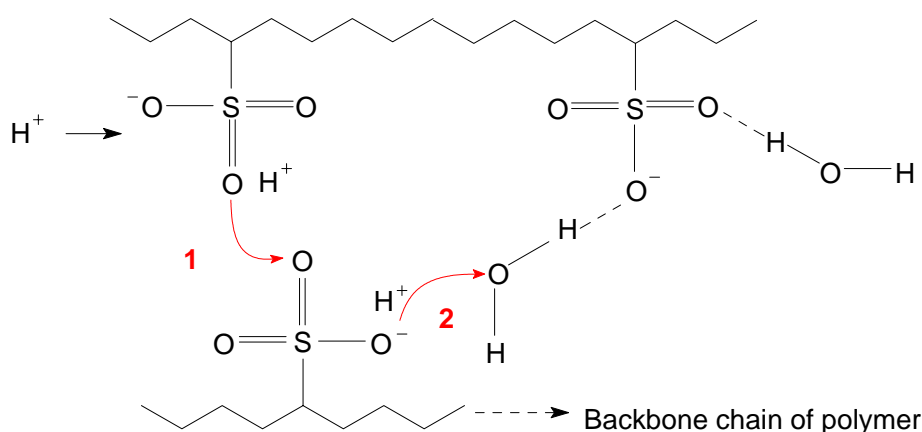


**Figure 2-7 Proton conducting in a sulphonated polymer membrane at high temperature and low humidity via 1, acid to acid; 2,  $\text{H}_2\text{O}$  to acid**

In a sulphonated PEM operated at a high temperature with low humidity, it was found that the conductivity of the membranes depends directly on the concentration of acid groups and the strength of the acids<sup>77</sup>. There are two main routes for proton



migration (in Figure 2-7). When the sulphonic groups are closely enough, the proton will transfer through O-O atoms in acid groups via the ‘hopping’ mechanism (route 1 in Figure 2-7). Due to the hydrophilicity of sulphonic groups, there are water existed even at very low humidity. The water molecules are hydrogen-bonded with sulphonic groups to bridge ionic inclusions. Thus, the protons transfer through acid-water-acid via the ‘hopping’ mechanism or by the immigration of hydroniums via the ‘vehicle’ mechanism (route 2 in Figure 2-7).

#### 2.4.2.2. Fluoropolymers and silicone polymers

The chemical bond strength of C-F is about  $485 \text{ kJ.mol}^{-1}$  and Si-O  $445 \text{ kJ.mol}^{-1}$ . Both of them are higher than that of C-H ( $350\text{-}435 \text{ kJ.mol}^{-1}$ ) and C-C ( $350\text{-}410 \text{ kJ.mol}^{-1}$ ). Therefore, these fluoropolymers and silicone polymers (e.g. polysiloxanes) (Figure 2-8) provide high thermal and chemical stabilities.

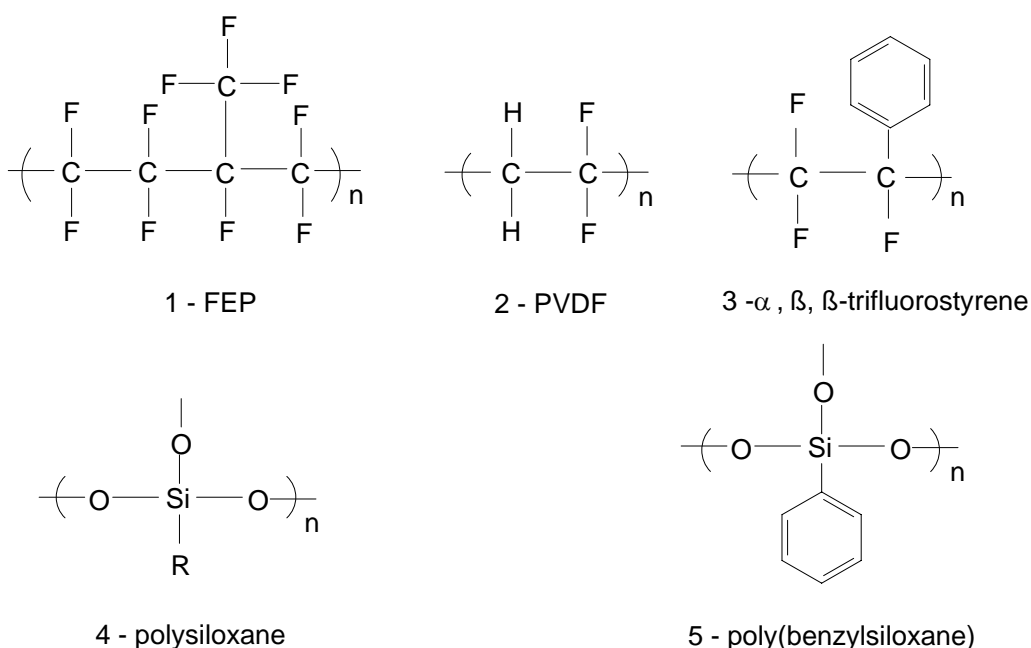


**Figure 2-8 Structures of fluoropolymers and silicone polymers for PEMs**

Fluoropolymers have been studied extensively for using as fuel cell membranes as the fluorine atoms can bring interesting properties<sup>69</sup> including

- Improvement of the thermal, chemical and oxidizing stabilities of the resulting (co)polymers and, to some extent, the mechanical properties;

- Enhancing the acid behaviour of a sulphonic acid function when a fluorinated group is adjacent to it, leading good protonic conductivities.

Besides the perfluoropolymers such as PFSA polymers, partially fluorinated polymer membranes have also been studied for the preparation of PEM. Silicone polymers normally are synthesised by grafting functional organic groups (i.e. arylsulphonic anions or alkylsulphonic anions etc.) onto the inorganic Si-O backbones and further forming cross-linked network via hydrosilylation therefore exhibiting high thermal and chemical stabilities, optical transparency and proton conductivities for the PEMFC applications. These information can be traced in the reviews by Li et al.<sup>56</sup> and Souzy et al.<sup>69</sup>

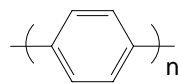
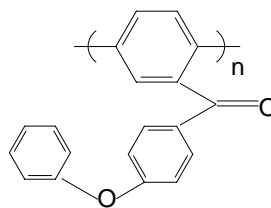
However, only the promising performance of these fluoropolymer and silicone polymer membranes as opposed to Nafion membranes can be achieved at low temperature fuel cell test, and no properties at high operational temperature were reported which might be due to the water loss at high temperature.

#### **2.4.2.3. Aromatic hydrocarbons as polymer electrolyte membranes**

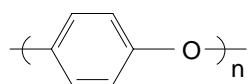
The aromatic hydrocarbons appear as the outstanding candidates for using as PEM, mainly owing to their

- a) Good oxidation resistance due to C-H bonds strength in the benzene ring ( $\sim 435 \text{ kJ} \cdot \text{mol}^{-1}$ ) and excellent mechanical properties due to their benzene ring contained repeat units in backbones;
- b) Practicability of commercialisation;
- c) Low cost.

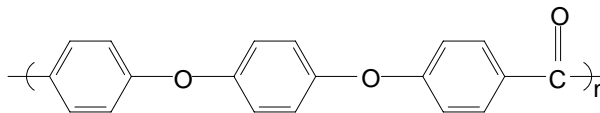
They can be classified into three types by different repeat units in their backbones including, Type A: repeat unit only consisted of a benzene ring; Type B: repeat unit consisted of benzene ring(s) and other element(s) or group(s); and Type C: repeat unit consisted entirely of heteroaromatic ring(s) and/or benzene ring(s) (Figure 2-9).

**Type A:**A-1 : poly-*p*-phenylene

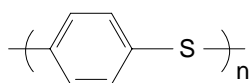
A-2 : PPBP

**Type B:**

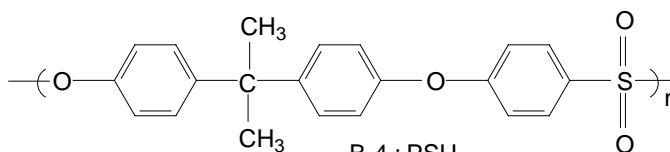
B-1 : PPO



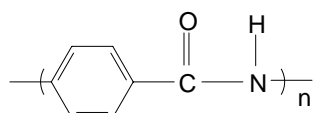
B-3 : PEEK



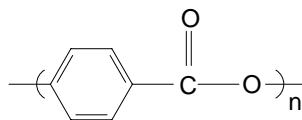
B-2 : PPS



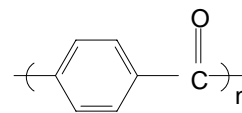
B-4 : PSU



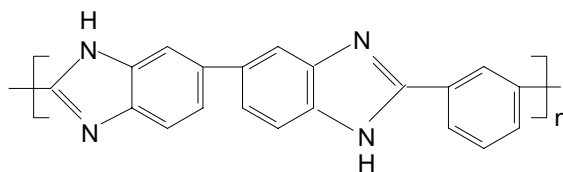
B-5 : Polyamides



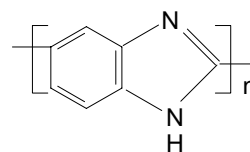
B-6 : Polyesters



B-7 : Polyketones

**Type C:**

C-1 : PBI



C-2 : ABPBI

**Figure 2-9 Structures of aromatic hydrocarbons for PEMs**

Type A polymers exhibit super resistance and extreme rigidity due to only the benzene ring in the repeat units of the backbones and meet the difficulty of processability. By introducing flexible and high thermo-stable ether groups into main chains of Type A polymers, the obtained Type B polymers have favourable processability with good thermal and chemical stabilities. Among of Type B polymers, sulphonated polysulphone (PSF) and polyetheretherketone (PEEK) were investigated extensively and Zhang et al.<sup>78</sup> and Li et al.<sup>56</sup> gave good reviews. In type C, the representative polymers are PBI and its derivatives, i.e. ABPBI, which will be discussed in the late section.

For the purpose of high temperature (>100°C) operating PEM, the proton conductivities based on these aromatic hydrocarbon PEM are far from satisfaction to

be used at high temperatures with low humidity, mainly due to water loss at high temperature. Therefore, some hygroscopic materials were introduced to improve the water retention and/or second proton conducting species were embedded to improve the conductivity. These kinds of modifications will be discussed in the following inorganic-organic composites section.

#### **2.4.2.4. Inorganic-organic composites**

The advantages of inorganic-organic composites may include the following<sup>56</sup>:

- ◆ Improvement of the water retaining ability. The finely dispersed hydrophilic inorganic particles can absorb water which is particularly important at the anode side since the water will carry proton and traverse the membrane from anode to cathode, resulting in the drying-out of the membrane at the anode side;
- ◆ Reduction of the electro-osmotic drag. The larger sized inorganic particles can retard the migration of smaller sized hydroniums, leading to reducing the electro-osmotic drag;
- ◆ Decrease of the fuel crossover. Obviously, the particles can hinder the permeation of the fuel since the sizes of inorganic particles are normally larger than that of fuel molecules;
- ◆ Enhancement of the conductivity. The advantages mentioned above can improve proton conductivity of the membrane. Besides, the proton conductivity can also be enhanced by introducing other proton conductors, for example, when the inorganic fillers are also proton conductors;
- ◆ Improving the mechanical and thermal properties. The homogeneously dispersed inorganic particles can reinforce the membrane and improve its thermostability;

The proton transport in composite membranes is the result of a complex process dominated by the surface and chemical properties of the composites. There are two general approaches to increase the proton transport. One is to introduce a hygroscopic material (e.g. silica) into the polymer matrix. The hygroscopic

composite, on the one hand, effectively retains water in the membranes at lower relative humidity, on the other hand, hinder the fuel permeation. The migration of protons is mainly through the hydroniums from the hygroscopic fillers (in Figure 2-10).

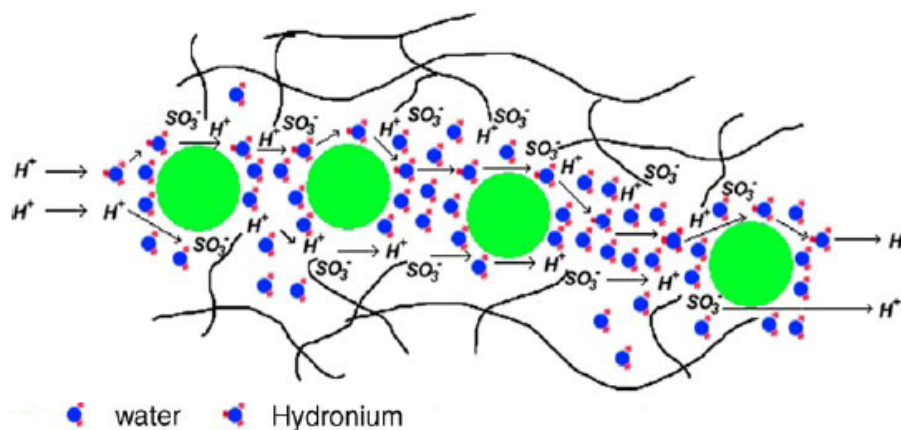


**Figure 2-10 Proton transport in polymer/nanoparticle composite membranes<sup>74</sup>**

Another is to add a second proton conductor (solid particles) into the polymer to enhance proton conductivity whilst reduce the methanol and water permeability of the membranes.<sup>84-86</sup> Due to their larger sizes, the finely dispersed particles can be the hindrances for the unwanted species migration. The introduced conductive species (e.g.  $\alpha$ -ZrP) is assumed to make up for conduction losses due to the reduced water within the membrane, in which the protons migrate through functional acid ions. Sulphonated hydrocarbon polymers were also used as a host matrix for preparation of inorganic-organic composites for high temperature PEMFC applications. Generally, high sulphonation of a membrane leads to high conductivity and also results in poor mechanical properties. Hence, the addition of inorganic materials into the polymers for both enhancing the proton conductivity and maintaining the mechanical properties is a very effective approach.

A summary of inorganic-organic composites used as PEM above 100°C is given in Table 2-6<sup>56</sup>. It can be seen that some of these inorganic-organic composite membranes exhibited a promising conductivity at the temperature above 100°C.

**Table 2-6 Summary of inorganic-organic composites used as PEM under development**

<b>Organic component</b>	<b>Inorganic component</b>	<b>Remarks</b>
SPEK, SPEEK	ZrP+(SiO <sub>2</sub> , TiO <sub>2</sub> , ZrO <sub>2</sub> )	Reduced methanol crossover <sup>87</sup>
SPEEK	SiO <sub>2</sub> , ZrP, Zr-SPP	$9.0 \times 10^{-2}$ S.cm <sup>-1</sup> at 100°C, 100%RH <sup>88</sup>
SPEEK	HPA	$10^{-1}$ S.cm <sup>-1</sup> above 100°C <sup>89</sup>
SPEEK	BPO <sub>4</sub>	$5.0 \times 10^{-1}$ S.cm <sup>-1</sup> , 160°C, fully hydrated <sup>90</sup>
PBI	ZrP+H <sub>3</sub> PO <sub>4</sub> ;	$9.0 \times 10^{-2}$ S.cm <sup>-1</sup> , 200°C, 5%RH
	PWA/SiWA+H <sub>3</sub> PO <sub>4</sub>	$3.0 \sim 4.0 \times 10^{-2}$ S.cm <sup>-1</sup> , 200°C, 5%RH <sup>91</sup>
PBI	SiWA+SiO <sub>2</sub>	$2.2 \times 10^{-3}$ S.cm <sup>-1</sup> , 160°C, 100%RH <sup>85</sup>
PBI	PWA+SiO <sub>2</sub> +H <sub>3</sub> PO <sub>4</sub>	$1.5 \times 10^{-3}$ S.cm <sup>-1</sup> , 150°C, 100%RH <sup>84</sup>
PVDF	CsHSO <sub>4</sub>	$10^{-2}$ S.cm <sup>-1</sup> , >150°C, 80%RH <sup>92</sup>
GPTS	SiWA+; SiWA+ZrP	$1.9 \times 10^{-2}$ S.cm <sup>-1</sup> , 100°C, 100%RH <sup>93</sup>
Polysilsesquioxanes	PWA	$3 \times 10^{-2}$ S.cm <sup>-1</sup> , 140°C <sup>94</sup>
PEO	Tungsten acid	$10^{-2}$ S.cm <sup>-1</sup> , 120°C <sup>95</sup>
PEO, PPO, PTMO	PWA	$10^{-2}$ S.cm <sup>-1</sup> , 140°C <sup>96, 97</sup>

### 2.4.3 Acid-based polymer electrolyte membranes

Acid-based complexation is regarded as an effective approach of developing proton conducting membranes.<sup>98</sup> The basic sites such as ether, alcohol, amine, or imide groups in a polymer can react with strong acids (typically sulfuric acid or phosphoric acid) to form ionic bonds. Once the acid is added, the complexation polymer acts both as a donor and an acceptor in proton transfer and therefore allows for the proton migration.

H<sub>3</sub>PO<sub>4</sub> and H<sub>2</sub>SO<sub>4</sub> can be self-ionised and self-dehydrated thereby exhibit unique proton conductivity even in an anhydrous.<sup>99</sup> When a basic polymer is present, the interaction between these acids and the polymer through hydrogen bonding or protonation would increase the acid dissociation, compared to that of anhydrous acids. Therefore, most acid-based PEMs have been prepared by combining sulfuric acid or phosphoric acid with basic polymers.

Sulphonation of hydrocarbon polymers, briefly reviewed above, is regarded as one of the main methods for the preparation of acid-based polymer membranes preparation including ionic cross-linking polymers. In addition, the ionic cross-linking polymer matrix can enhance the membrane mechanical stability. The flexible ionomer networks were prepared from acid-based polymers by ionic cross-linking of polymeric acids and polymeric bases. The acidic polymers used are sulphonated polysulphone (SPSF), sulphonated polyethersulphone (SPES), or sulphonated polyetheretherketone (SPEEK). Some basic polymers are commercially available, such as PBI, polyethyleneimine (PEI), and poly(4-vinylpyridine) (P4-VP) whilst new basic polymers by modifying the PSF backbones with  $\text{NH}_2$ - or  $\text{N}(\text{CH}_3)_2$ - groups have also been reported. Combinations of these acidic and basic polymers such as SPEEK/PBI, SPEEK/P4VP, SPSF/PBI, SPEEK/PSF( $\text{NH}_2$ )<sub>2</sub> and SPSF/P4VP have been explored. These information can be traced from the works by Ma<sup>100</sup> and Li et al.<sup>56</sup>

It is worth mentioning that high conductivity can be obtained at high acid contents, however, the mechanical properties will decrease greatly especially at high temperature. To enhance the membrane mechanical properties, besides the development of ionic cross-linking polymers, adding inorganic filler or/and plasticizer is another effective approach. When the higher acid content is added, the plasticisation effect of the excessive acid would lead to the formation of a soft paste, resulting in the difficulty of processability, so that the inorganic filler such as high-surface-area  $\text{SiO}_2$  was added into such as PEI<sup>101</sup> and Nylon<sup>102</sup> to reinforce the membrane materials.

Besides the sulphonation of polymers, acid doping is another important method for preparing acid-based membranes. Of these, most investigations were focused on the phosphoric acid doped PBIs. Because of its outstanding properties,  $\text{H}_3\text{PO}_4$ -doped PBIs have received much attention in the past few years. As this project is mainly focusing on phosphoric acid doped ABPBI and its composite membranes, more details about the development of PBIs based PEMs are given in the next section.

## **2.5 Development of Polybenzimidazoles (PBIs) Based PEM**

Poly[(2,2'-(m-phenylene)-5,5'-bibenzimidazole] (polybenzimidazole, PBI) which is commercially available from Hoechst-Celanese primarily since 1960s, have applications as thermally stable textile fabrics, high temperature matrix resins, adhesives and foams, due to its excellent thermal and chemical stability and mechanical properties.<sup>103, 104</sup> Owing to its all-aromatic structure (type C-1 in Figure 2-9), PBI has a glass transition temperature of above 420°C and melting point of above 600°C.<sup>105</sup> Pure PBI is an electronic and ionic insulator, which, however, can be a very good ionic conductor when it is modified by acids under proper conditions. In the form of a membrane, PBI has received much attention mainly for use in blood dialysis and reverse osmosis at high temperatures and in harsh environments.<sup>106</sup>

PBI was primarily and deeply investigated as an electrolyte material by Litt, Savinell, Wainright, etc.<sup>16, 19, 21, 107-109</sup> Compared with PFSA polymer membranes, acid-based PBI membranes possess the following advantages<sup>14, 103</sup>:

1. Good proton conductivity at elevated temperature (up to 200°C);<sup>19, 107</sup>
2. Almost zero electro-osmotic drag number for water and methanol<sup>108</sup> compared to the drag number of 0.6-2.0 for the Nafion® membrane. This unique feature of the acid-doped PBI membrane allows the PBI fuel cell to be operated at elevated temperature and low gas humidity without membrane dehydration.
3. Low methanol vapour permeability.<sup>110</sup>

In addition, acid-doped PBI membranes have excellent oxidative and thermal stability<sup>16</sup> and good mechanical flexibility at high temperature<sup>111</sup>, which makes it a promising candidate electrolyte for high temperature PEMFC.

ABPBI is another benzimidazole polymer possessing comparable thermal and conducting properties as that of PBI.<sup>28, 30</sup> It is particularly important that the ABPBI is synthesised from a commercially available, cheap, single monomer and hence will



be cheaper than PBI. It is believed that ABPBI is one of the best choices for applying in PEMFC.

Beside phosphoric acid doping, other studies of PBIs based polymer electrolyte membranes have been focusing on impregnation with different acid or base, composites with inorganic particles, grafting functional groups onto PBI, copolymers included benzimidazole repeated unit, polymer blends etc.. In this section, the mechanisms of proton conduction, synthesis and modifications of PBIs, their membranes fabrication and their performances as polymer membranes will be mainly reviewed.

### 2.5.1. Proton conducting routes in PBIs membranes

As discussed in section 2.3.1, hopping and vehicle mechanisms are addressed to explain proton transfer through PEM, and, at some conditions, these two mechanisms work together and can also change from one to another model depending on various temperatures and concentrations of acid in the system. The proton transfer in acid doped PBI can be well explained by these mechanisms together.

Since phosphoric acid doped PBI was proposed to be used as a PEM, the proton transfer routes have been investigated by different researchers. Through the characterisation of a solid-state nuclear magnetic resonance (SS-NMR), Wasmus et al.<sup>112</sup> found that the phosphoric acid absorbed by the PBI membrane was relatively immobile compared to free phosphoric acid, indicating that there was an interaction between imidazole groups of PBI and phosphoric acid. Schechter et al.<sup>113</sup> further found that the free or mobile acid shared some characteristics of liquid acid solution and the water activity influenced the concentration of this free acid by adsorption and release into the polymer matrix. By the measurement of IR spectroscopy, Glipa et al.<sup>114</sup> thought that protons transferred from  $\text{H}_3\text{PO}_4$  to the imino groups of PBI<sup>114</sup>, whilst Kawahara et al.<sup>115</sup> thought that  $\text{H}_3\text{PO}_4$  did not protonate the imidazole groups of PBI but interacted by hydrogen bonding between the OH and N groups. The presence of  $\text{HPO}_4^{2-}$  and  $\text{H}_2\text{PO}_4^-$  anions implied that the proton conduction occurred according to the Grotthuss mechanism. Bouchet et al.<sup>20</sup> suggested that the nitrogen of the imidazole was protonated by the acids and proton transfer from one imidazole site to another in which the anionic species participate through the Grotthuss

mechanism. Moreover, the anions were linked to the polymer by rather strong hydrogen bonding. Pu et al.<sup>116</sup> proposed that proton transport in phosphoric acid blended PBI was the consequence of the two contributions: one was based on rapid proton exchange (hopping) via hydrogen bonds between solvent molecules, which could be the phosphate, N-heterocycles of PBI and water molecules; and the other was based on the self-diffusion of phosphate moieties and water molecules (vehicle mechanism).

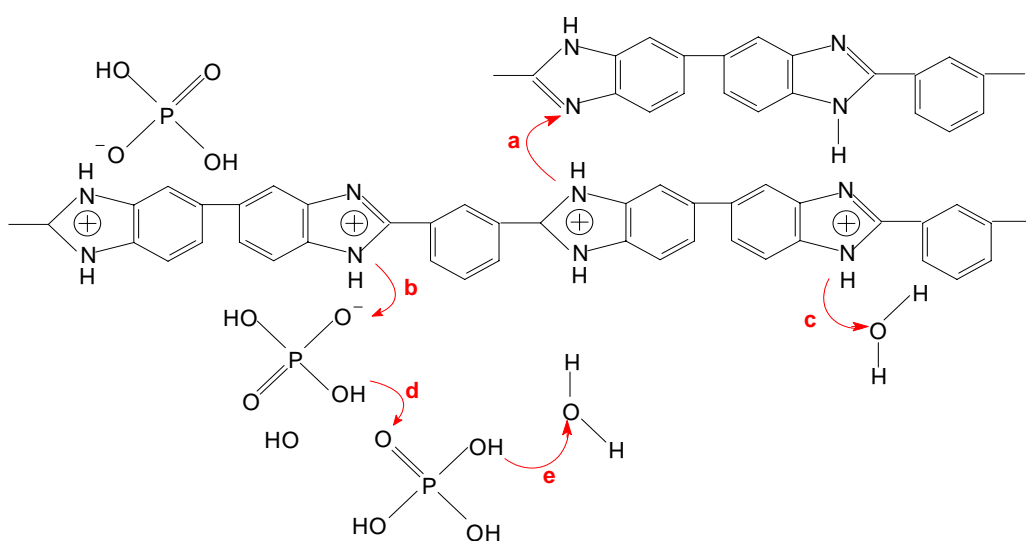


**Figure 2-11 Proton transport in  $\text{H}_3\text{PO}_4$  doped PBI**

Although the mechanisms of proton transfer in acid doped PBIs are still debatable, the main proton transfer routes in Figure 2-11<sup>14, 18</sup> are widely accepted. Protons may transfer between benzimidazole (BI) and BI (Figure 2-11a), BI and phosphoric acid (Figure 2-11b), BI and water (Figure 2-11c), acid molecules (Figure 2-11d), and acid and water (Figure 2-11e). The dominated proton transfer routes will be various according to different conditions. Generally, at no acid and/or a very low acid doping level, the proton mainly transfer between polymer chains (i.e. BI and BI), resulting in a poor conductivity. With the acid doping level increasing, the proton transfer between polymer chains and phosphoric acid becomes significant, leading to rapid increase of conductivity. When the acid doping level is above the saturation level of polymer chain protonation, i.e., the acid acts a ‘solvent’ whilst the polymer chains like ‘solute’, the proton transfer is dominated by transporting through acid to acid, resulting in the crucial improvement of conductivity. If water exists, the more routes for proton transfer also lead to the increase of conductivity.

## 2.5.2 Synthesis of PBIs

### 2.5.2.1 Synthesis of polybenzimidazole (PBI)

PBIs were first synthesised by melt polycondensation of suitable aromatic tetraamines and aromatic dicarboxylic acids (i.e. heating the 3,3'-diaminobenzidine and 1,2,4,5-tetraaminobenzene with diphenyl isophthalate in an inert atmosphere at high temperature) in 1961.<sup>117</sup> This melt polycondensation proceeds by two consecutive nucleophilic reactions (a nucleophilic substitution to form an amine-amide followed by cyclization via nucleophilic addition) (Figure 2-12). The disadvantages of this melt polycondensation include: (i) oxidation sensitive since the trace of oxygen can oxidize the tetraamine impeding the production of the polymer; (ii) toxic by-product of the reaction-phenol; (iii) vacuum required for the polymerisation process.

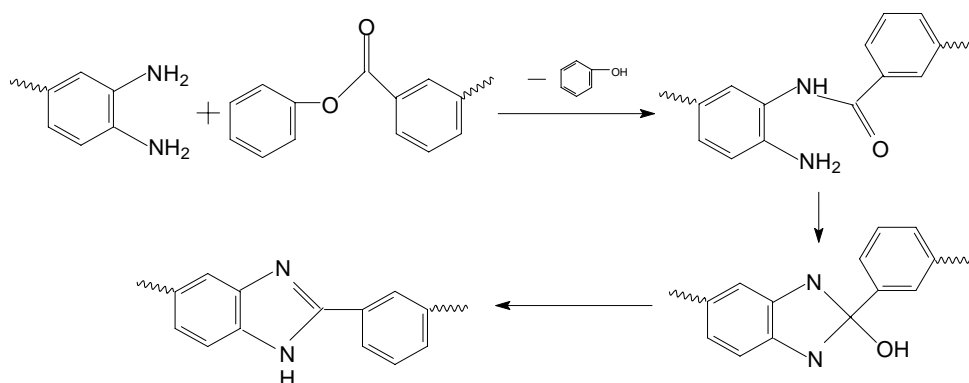


Figure 2-12 Scheme of PBI by melt polycondensation

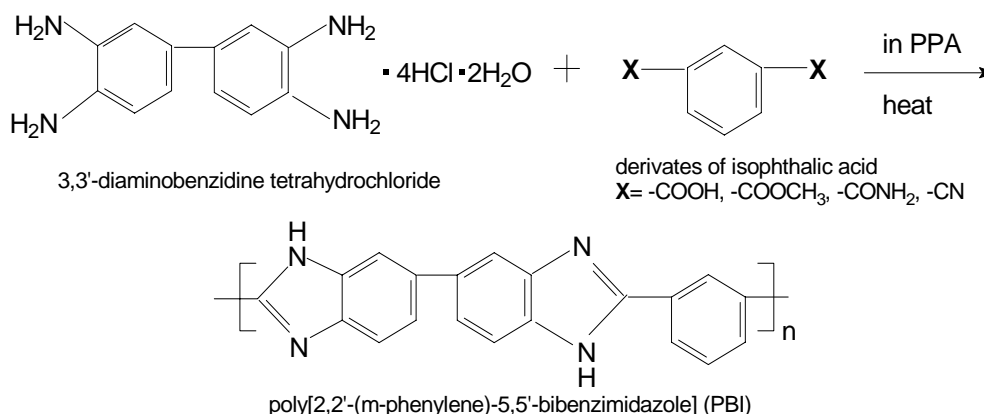


Figure 2-13 Synthesis of PBI with stable salt of the tetraamine and derivatives of isophthalic acid in polyphosphoric acid

In order to avoid the above disadvantages, a more stable salt of the tetraamine and derivatives of isophthalic acid in polyphosphoric acid (PPA) were used<sup>118, 119</sup>, which

acted as polycondensation agent and solvent (Figure 2-13). However, this synthesis process required a rather long reaction time (200°C for 12 hours). The polymer molecular weight was also extremely sensitive in this reaction condition. Thus low molecular weight molecules had to be eliminated for the purpose of achieving polymer with high molecular weights.

Choe et al.<sup>120, 121</sup> obtained high molecular weight PBI by using arylhalo phosphorus compound catalyst. However, these processes required quite harsh conditions such as temperatures as high as 480°C, and an absolutely inert reaction environment. Also phenol was generated as the by-product of the reaction when biphenyl isophthalate was used as the monomer.

A new method to synthesise PBI was proposed by adding an amount of triphenyl phosphate as the catalyst (Figure 2-14.a) and the molecular weights between 115,000 and 190,000 were obtained.<sup>122</sup> PBI and a series of polybenzimidazoles (PBIs) incorporating main chain pyridine groups were synthesised by using PPA as both solvent and polycondensation reagent.<sup>123, 124</sup> In these synthesis processes, the typical reaction conditions are under 220°C for less than 24 hours at nitrogen atmosphere. Therefore, PBI can be easily synthesised in PPA medium at lab scale. Kim et al.<sup>125</sup> developed a new route by using a mixture of trifluoromethanesulphonic acid (CF<sub>3</sub>SO<sub>3</sub>H, TFA), methanesulphonic acid (CH<sub>3</sub>SO<sub>3</sub>H, MSA) and phosphorous pentoxide (P<sub>2</sub>O<sub>5</sub>) as reaction medium, and 3,3'-diaminobenzidine and isophthalic acid as monomers (Figure 2-14.b). In their work, PBI with suitable molecular weight were achieved by adjusting the ratio of TFA and MSA.

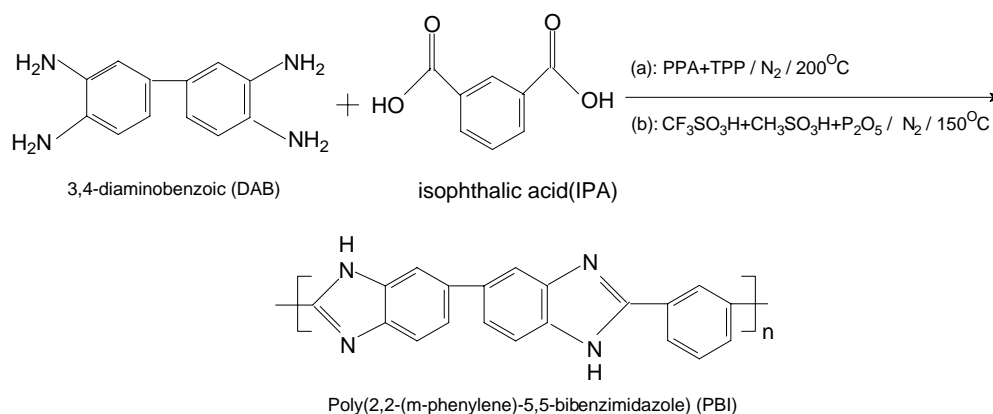


**Figure 2-14 Synthesis of PBI in a. PPA/TPP and b. TFA/MSA/P<sub>2</sub>O<sub>5</sub>**



When new reaction media (TFA/MSA for PBI & MSA/P<sub>2</sub>O<sub>5</sub> for ABPBI) were employed, the newly developed method had these advantages:

- ✓ Reaction temperature was quite low (150°C);
- ✓ Reaction time was extremely short (less than 1 hour);
- ✓ Molecular weights of the polymers could be controlled simply by changing the ratio of the solvents;
- ✓ Membranes fabrication can be directly cast.

### 2.5.3 Fabrication of PBIs membranes

Because of the structural rigidity, PBIs can only be dissolved in strong acids (i.e. H<sub>2</sub>SO<sub>4</sub>, H<sub>3</sub>PO<sub>4</sub>, HNO<sub>3</sub>, HCl ect.), strong bases (i.e. KOH or NaOH/ethanol etc.), and in a small number of organic solvents, such as dimethylsulfoxide(DMSO), N,N-dimethylacetamide (DMAc), N,N- dimethylformamide (DMF), N-methylpyrrolidone(NMP).<sup>118</sup> Thus there are a very limited number of solutions employed for the fabrication of PBIs membranes, using two main methods i.e. casting and direct casting.

As a typical procedure of a membrane made by the casting method, firstly the pristine polymer is dissolved in a solvent to form a homogeneous solution. Then the membrane is formed by pouring the homogeneous solution onto a glass plate (or petri dish), which normally needs to be boiled in an acid or basic solution and washed with deionised water to remove the solvent. Finally, the purified membrane is immersed in different concentrations of H<sub>3</sub>PO<sub>4</sub> solutions to achieve acid-doped membranes with various acid doping levels. PBIs membranes were initially cast from a NaOH/Ethanol solution under N<sub>2</sub> environment<sup>111, 129</sup>. Currently most of PBI membranes were typically prepared by forming a 3-5wt% suspension of PBI in the DMAc/LiCl solution followed by heating and filtration to obtain concentrated 20wt% PBI solution then casting onto a glass plate.<sup>10, 16, 19, 21, 49, 107, 108, 114, 130</sup>

For a direct casting method, once the synthesis of polymer is finished, the hot solution is poured onto a glass plate and cools to form a membrane followed by purification and dryness processes. ABPBI membranes were produced easily by direct casting with use of MSA/P<sub>2</sub>O<sub>5</sub> solvents.<sup>28, 30</sup> PBI membranes with a well

controlled acid doping level were also reported by direct casting from TFA/P<sub>2</sub>O<sub>5</sub> and a mixture media of TFA/MSA/P<sub>2</sub>O<sub>5</sub>, respectively.<sup>131</sup> The main benefits of using the direct casting method include the fact that the later method saves a step of purification of the polymer after synthesis and before fabrication of membrane and the membrane is obtained with a controlled acid doping level (acid molecule per polymer repeat unit). Particularly, the direct casting method is more convenient since the nitrogen atmosphere is not necessary. Asensio et al.<sup>132</sup> reported that, with the same doping level, the direct acid casting ABPBI membrane had higher crystallinity but lower conductivity compared to the acid soaking ABPBI membranes, which was attributed to the dehydration of the phosphoric acid during MSA evaporation at 150~200°C.

A sol-gel process was described as producing PA-doped PBI membranes.<sup>124</sup> After polymerisation, the PBI solution in PPA was directly cast without isolation or re-dissolution of the polymers. The solution temperature also dropped from the casting temperature to room temperature. The hydrolysis of the solvent from PPA (a good solvent for PBI) to H<sub>3</sub>PO<sub>4</sub> (a poor solvent for PBI) combined with the temperature drop induced a transition from the solution state to the gel state that produced PBI membranes doped with H<sub>3</sub>PO<sub>4</sub> in one step. Upon casting, hydrolysis of the PPA to H<sub>3</sub>PO<sub>4</sub> induced a sol-gel transition which produced membranes with a desirable suite of physicochemical properties. In fact, during the overall membrane fabrication process, a direct casting was followed by the sol-gel process.

## **2.5.4 Properties of acid doped PBIs PEMs**

### **2.5.4.1 Properties of Phosphoric acid doped PBIs membranes**

As a PEM for operating at high temperatures, the acid doping level and proton conductivity are the key parameters for estimating its performance if a fuel cell system test is absent. The proton conductivity of PBI was first studied more than 35 years ago.<sup>129</sup> For phosphoric acid doped PBI membranes, the conductivity has been measured by several groups.

The influence of temperature, humidity and acid doping level (the number of acid molecule in per repeat unit of PBI) were studied from a lot of works. Typically, Li et

al.<sup>10</sup> measured conductivity as a function of temperature and 3.0~16.0 of acid doping levels (the number of acid molecule in per repeat unit of PBI) at RH (relative humidity) between 80%~85%. A conductivity of  $4.6 \times 10^{-2} \text{ S.cm}^{-1}$  at 165°C was obtained. In their work,  $\text{H}_3\text{PO}_4$  doping level between 3.5~7.5 was suggested for an appropriate quality membrane to have both conductivity and mechanical strength. Kawahara et al.<sup>115</sup> prepared  $\text{H}_3\text{PO}_4$  doped PBI membranes by immersing the PBI membranes into a mixed solution of acid and methanol. The conductivity of the anhydrous  $\text{PBI} \cdot 2.9\text{H}_3\text{PO}_4$  (i.e. PBI with 2.9 of  $\text{H}_3\text{PO}_4$  doping level) reached  $10^{-4} \text{ S.cm}^{-1}$  at 160°C. Different acid doping levels are relative to different route of proton transfer. To improve acid absorptivity, a porous PBI with a high doping level up to 14.6 was prepared by Mecerreyes et al.<sup>133</sup> The porous structure was formed by leaching out a low-molecular-weight porogen (such as phthalates or triphenyl phosphate) using a selective solvent of the porogen from polymer/porogen mixtures. The proton conductivity of these acid doped porous membranes with high doping levels was up to  $10^{-2} \text{ S.cm}^{-1}$  at 140°C and 0%RH. However, the mechanical properties were greatly affected due to up to 70% of the porosity of the membranes. Ma et al.<sup>14, 100</sup> proposed that the order of the proton transfer rate between different species were:  $\text{H}_3\text{PO}_4$  to  $\text{H}_2\text{O} > \text{H}_3\text{PO}_4$  to  $\text{H}_2\text{PO}_4^- > \text{N}^+ \text{-H} > \text{H}_2\text{PO}_4^- > \text{N}^+ \text{-H} > \text{H}_2\text{O} > \text{N}^+ \text{-H}$  to  $\text{N-H}$ . Broadly speaking, at the low acid-doping level i.e. lower than 2, proton exchange most like happens between protonated and unprotonated imino nitrogen groups on the neighbouring polymer chains; at the high doping level, i.e. between 4-6, the proton transfer is proposed to happen mainly along the acid and anion chain or the acid and water; at the higher doping level, i.e. above 6.3, the environment for proton transport is similar to concentrated phosphoric acid and the proton conductivity is mainly contributed by molecular phosphoric acid.<sup>11, 100</sup>

The influence of pressure on the conductivity and activation volume of phosphoric acid doped PBI membranes was also studied. Fontanella et al.<sup>19</sup> measured the proton conductivity at compression of up to 0.25GPa. At room temperature the conductivity decreases with increasing pressure due to the viscosity increase. Based on the estimation of activation volume values ( $4 \sim 7 \text{ cm}^3/\text{mol}$ ) of acid doped PBI, it was proposed that proton transport in the acid-doped PBI was mediated by segmental motions of the polymer. Bouchet et al.<sup>20, 130</sup> proposed an activated mechanism (Grotthuss mechanism) for the proton migration from conductivity data as a function



of temperature (30~90°C) and isostatic pressure (1~4000 bars). They suggested that the proton migrates from a protonated imide site to a neighbouring unprotonated one. Pu et al.<sup>116</sup> also studied the temperature and pressure dependence of the conductivity of PBI·xH<sub>3</sub>PO<sub>4</sub> membranes. They reported that the activation energies of proton migration in PBI membranes with phosphoric acid doping levels of 1.8~3.8 were 70~85 kJ/mol and the activation volume decreased with increasing temperature. A negative activation volume for 85% phosphoric acid at 75°C was observed by Fontanella<sup>19</sup>, which suggested that only a small charge carrier and a solvent-free proton transported through the membrane.

Additionally, the influence of membrane morphology and processing on the proton conductivity were studied by Jayakody et al.<sup>134</sup> They found the proton diffusivity is about an order of magnitude higher in PBI membranes cast from polyphosphoric acid (PPA) than in which cast from DMAc, indicating an additional proton transfer mechanism existed involving rapid exchange between phosphoric acid and pyrophosphoric acid species.

#### **2.5.4.2 Properties of Phosphoric acid doped ABPBI membranes**

Asensio et al.<sup>132</sup> found that ABPBI·3H<sub>3</sub>PO<sub>4</sub> membrane with a direct casting procedure had a conductivity of  $1.5 \times 10^{-2}$  S.cm<sup>-1</sup> at 180°C in dry conditions compared to a conductivity of  $2.5 \times 10^{-2}$  S.cm<sup>-1</sup> at the same condition from ABPBI·2.7H<sub>3</sub>PO<sub>4</sub> membrane with a casting procedure. The relative lower conductivity and larger activation energies were considered due to the dehydration of H<sub>3</sub>PO<sub>4</sub> during MSA evaporation at 150-200°C. They also found that the higher crystallinity of the acid membrane caused the reduction of the proton conductivity. Uchida et al.<sup>135</sup> reported that, under 100% RH, ABPBI·1.4H<sub>3</sub>PO<sub>4</sub> showed conductivity as high as  $1.2 \times 10^{-1}$  S.cm<sup>-1</sup> at temperatures below 120°C, but decreased to  $2.5 \times 10^{-2}$  S.cm<sup>-1</sup> above 150°C, which was also ascribed to a dehydration of the doped acid. Kim et al.<sup>28</sup> reported higher conductivities of  $2.6 \times 10^{-2}$  S.cm<sup>-1</sup> for ABPBI·1.6H<sub>3</sub>PO<sub>4</sub>,  $4.1 \times 10^{-2}$  S.cm<sup>-1</sup> for ABPBI·2.4H<sub>3</sub>PO<sub>4</sub> and  $6.0 \times 10^{-2}$  S.cm<sup>-1</sup> for ABPBI·3.7H<sub>3</sub>PO<sub>4</sub> at 110°C without external humidification.

### 2.5.4.3 Other acid doped PBIs membranes

It is worthwhile highlighting that a comprehensive work of comparing the conductivity of PBI membranes doped with various acids has been carried out by Xing and Savadogo et al.<sup>136</sup> In their work, the conductivity measurements were made across the membrane in an acid solution using four-point probe technique and the conductivity was changed in the order of  $\text{H}_2\text{SO}_4 > \text{H}_3\text{PO}_4 > \text{HClO}_4 > \text{HNO}_3 > \text{HCl}$  for high doping levels.

Various strong acids (i.e.  $\text{H}_2\text{SO}_4$ ,  $\text{CH}_3\text{SO}_3\text{H}$ , or  $\text{C}_2\text{H}_5\text{SO}_3\text{H}$ ) doped PBI have been studied by Sanui et al.<sup>8, 115</sup> The onsets of thermal decompositions for PBI/ $\text{H}_2\text{SO}_4$ ,  $\text{CH}_3\text{SO}_3\text{H}$ , and  $\text{C}_2\text{H}_5\text{SO}_3\text{H}$  complexes started from 330, 240, and 220°C, respectively, indicated the complexes bearing a loss of thermal stability. In addition, poor proton conductivities ( $10^{-6} \sim 10^{-9} \text{ S.cm}^{-1}$  at 100°C) were thought far from applications in a PEMFC.

As mentioned before, one of the shortcomings for phosphoric acid doped PBI membranes with high acid doping levels is bearing the acid leaching out when the environmental humidity is high. To avoid that, aromatic mono- and di-esters of phosphoric acid were developed by Akita et al.<sup>128</sup> Their work showed that the novel acid based PBI membranes had excellent stabilities in the presence of water and methanol but low water absorbability due to the substitution of at least one hydroxyl group.

## 2.5.5 Modified PBIs Membranes

### 2.5.5.1 Composite membranes of PBIs with inorganic fillers

Several groups have been studying on the composite membranes of PBI containing inorganic fillers in order to improve proton conductivity, reactant crossover resistance, mechanical properties at high temperatures etc.<sup>77, 100, 137, 138</sup>

PBI composites have been prepared by blending with inorganic proton conductors, such as heteropolyacids and hygroscopic moiety etc. Xing et al.<sup>136</sup> reported that phosphotungstic acid (PTA or PWA,  $\text{H}_3\text{PW}_{12}\text{O}_{40} \cdot n\text{H}_2\text{O}$ ) doped PBI membranes bearing very low proton conductivity (of the order of  $10^{-6} \text{ S.cm}^{-1}$ ) were due to the

leach-out of the acid, which has low interaction with the polymer, as well as the micro-sized dispersion of fillers in the PBI matrix. To retain the acid in PBI membrane, sol-gel process prepared silica-immobilized phosphotungstic acid (PTA/SiO<sub>2</sub>)<sup>84</sup> and silica-immobilised silicotungstic acid (STA or SWA, H<sub>4</sub>SiW<sub>12</sub>O<sub>40</sub>·nH<sub>2</sub>O) (STA/SiO<sub>2</sub>)<sup>85, 139</sup> were used as fillers in PBI membranes. It was found that PBI-PTA/SiO<sub>2</sub> membranes were chemically stable in boiling water and thermally stable in air up to 400°C. The highest conductivities of  $3 \times 10^{-3}$  S.cm<sup>-1</sup> at 100°C and 100%RH atmosphere and  $1.4 \times 10^{-3}$  S.cm<sup>-1</sup> at 150°C and 100%RH atmosphere were obtained from PBI-60wt% PTA/SiO<sub>2</sub> (PTA/SiO<sub>2</sub> weight ratio of 30/70) composite membranes. Similarly, PBI-50wt% STA/SiO<sub>2</sub> (STA/SiO<sub>2</sub> weight ratio of 45/55) composite membranes had up to  $3 \times 10^{-3}$  S.cm<sup>-1</sup> of conductivity at 160°C and 100%RH atmosphere. However, these conductivities were still too low for PEMFC applications.

Since phosphoric acid have an excellent performance in proton conducting and those heteropolyacids composited PBI membranes have very low conductivity, PBI composite membranes prepared by incorporating with inorganic heteropolyacid followed by H<sub>3</sub>PO<sub>4</sub> doping process were developed. The inorganic fillers, including zirconium phosphate (ZrP, Zr(HPO<sub>4</sub>)<sub>2</sub>·nH<sub>2</sub>O), PTA and STA, were reported by He et al.<sup>91</sup> Compared to H<sub>3</sub>PO<sub>4</sub> doped PBI membranes with same acid doping level, PBI composite -15wt% ZrP/H<sub>3</sub>PO<sub>4</sub> gave higher conductivities over the whole temperature and RH range, whilst PBI-30wt%PTA/H<sub>3</sub>PO<sub>4</sub> and PBI-30wt%STA/H<sub>3</sub>PO<sub>4</sub> gave a higher or comparable conductivity only below 110°C, and lower conductivity above 110°C due to the water loss. Recently, a CsPOM/PBI/H<sub>3</sub>PO<sub>4</sub> (CsPOM, Cs<sub>2.5</sub>H<sub>0.5</sub>PMo<sub>12</sub>O<sub>40</sub>) composite membrane was prepared by Li et al.<sup>140</sup> The composite membrane, doped with H<sub>3</sub>PO<sub>4</sub> had a higher proton conductivity ( $>1.5 \times 10^{-1}$  S.cm<sup>-1</sup>) than that of a phosphoric acid doped PBI membrane and was thermally stable above 200°C.

Several heteropolyacid, such as phosphomolybdic acid (PMo<sub>12</sub>, H<sub>3</sub>PMo<sub>12</sub>O<sub>40</sub>)<sup>141, 142</sup> and Zirconium pyrophosphate (ZPP)<sup>143</sup> have been used for preparation of ABPBI composite membranes as well. Compared to the pure ABPBI membrane, the ABPBI-PMo<sub>12</sub> hybrid membrane promoted the uptake of H<sub>3</sub>PO<sub>4</sub> and therefore increased the proton conductivity under the same conditions. The highest proton

conductivity of  $\text{H}_3\text{PO}_4$  doped ABPBI-45wt%  $\text{PMo}_{12}$  hybrid membrane is up to  $3.0 \times 10^{-2} \text{ S.cm}^{-1}$  at  $185^\circ\text{C}$  in air<sup>141</sup>. ABPBI/ZPP composite membranes were prepared by PPA direct casting method. The incorporation of 10-20wt% ZPP into membranes improved thermal and dimensional stabilities; meanwhile ABPBI/ZPP/ $\text{H}_3\text{PO}_4$  membranes had high conductivities above  $1.2 \times 10^{-1} \text{ S.cm}^{-1}$  at  $180^\circ\text{C}$ .

### 2.5.5.2 Sulphonated PBIs membranes

In section 2.4.2, three different methods for preparing sulphonated polymer membranes, i.e. sulphonation, grafting and synthesis of derivatives and copolymers, have been mentioned. Those methods have also been used to modify PBI membranes.

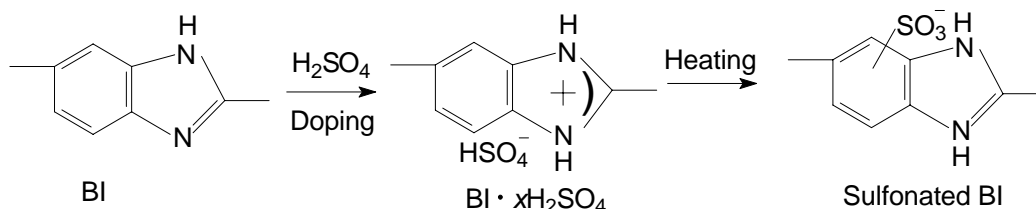


Figure 2-16 Sulphonation of benzimidazole group

Table 2-8 Sulphonation of PBI membrane and its properties

Sulphonation conditions		Remarks	
Immersion	Heating	Sulphonation degree ( $x\text{SO}_3\text{H}/\text{PBI}$ , $x=$ )	Conductivity
96% $\text{H}_2\text{SO}_4$ , 48 hrs at $40^\circ\text{C}$	$200^\circ\text{C}$ $300^\circ\text{C}$	$0.95\text{-}1.46$ <sup>109</sup>	-
96% $\text{H}_2\text{SO}_4/\text{P}_2\text{O}_5$ 2-24hrs, $150\text{-}200^\circ\text{C}$		$1.9\text{-}2.2$ <sup>100</sup> ( $-\text{SO}_3$ detected by IR)	-
10% $\text{H}_2\text{SO}_4$ , 24 hrs at $25^\circ\text{C}$	5 min at $450^\circ\text{C}$ in air	0.6 after immersion, 41% $-\text{SO}_3$ after heating	$3.5 \times 10^{-2} \text{ S.cm}^{-1}$ at $185^\circ\text{C}$ <sup>141</sup>
2.5% $\text{H}_2\text{SO}_4$ , 2 hrs at $50^\circ\text{C}$	0.5-1 min at $450^\circ\text{C}$	$0.93$ <sup>144</sup>	-
5-20% $\text{H}_2\text{SO}_4$ , 1 hr at $50^\circ\text{C}$	2 min at $475^\circ\text{C}$ 2 min at $350^\circ\text{C}$	- No $-\text{SO}_3$ group	$7.5 \times 10^{-5} \text{ S.cm}^{-1}$ at $160^\circ\text{C} \& 100\% \text{RH}$ <sup>145</sup>
2.5% $\text{H}_2\text{SO}_4$ , 2 hrs at $50^\circ\text{C}$	0.5-2 min at $450^\circ\text{C}$	24% of PBI repeated units sulphonated	$2.3 \times 10^{-6} \text{ S.cm}^{-1}$ at $40^\circ\text{C} \& 100\% \text{RH}$ <sup>146</sup>

Kuder and Chen<sup>144</sup> described the process for direct sulphonation of PBIs (Figure 2-16). When immersed in a dilute sulphuric acid solution, the imidazole group in a PBI repeat is protonated by the sulphuric acid to form a sulphate-ionic salt. After heating, the ionic bond is converted to a permanent, covalent C-S bond. The conditions and results of sulphonated PBI by different groups are summarized in Table 2-8<sup>100</sup>. Obviously, the sulphonation degree is greatly changed with various sulphonation conditions.

Compare to sulphonation introduced above, the degree of sulphonation (SDs) or numbers of sulphonic groups can be well controlled by using grafting and copolymerisation methods.

For the method of grafting, the presence of the N-H group allows the PBI to be treated with a sulphonated side chain reagent to form an water soluble N-substituted alkyl- or arylsulphonated polymer.<sup>147</sup> The degree of sulphonation can be controlled by the extent of activation of the polymer (number of N-H groups ionised) and the degree of grafting on to the activated sites<sup>148</sup>. Chemically grafted benzyulsulphonic acid PBI (Figure 2-17.a) was developed mainly by Gieselmann et al.<sup>147, 149</sup> and Glipa et al.<sup>148, 150</sup> It was reported that the conductivity of  $1.0 \times 10^{-2} \text{ S.cm}^{-1}$  at 50°C and 100% RH of the membrane with a sulphonation level of 75% was close to that of Nafion 117 under the same conditions.<sup>148</sup> However, one major disadvantage of these water soluble membranes is that they tend to shrink and loose their flexibility and conductivity at low levels of humidity.<sup>150</sup> Ogata et al. mainly developed sulphoalkylation of PBI with a similar method.<sup>151, 152</sup> PBI-PS (propanesultone) (Figure 2-17.b)<sup>151</sup> showed proton conductivity in the order of  $10^{-3} \text{ S.cm}^{-1}$  in the temperature range from 100~140°C at low humidity. Compared to PBI-PS, PBI-BS (butanesultone) (Figure 2-17.c)<sup>152</sup> provided higher conductivity at high temperatures with low RH (close to  $10^{-3} \text{ S.cm}^{-1}$ , at 100~160°C, RH<100%) which was attributed to the relatively longer length of -SO<sub>3</sub> parts of PBI-PS, which might result in relative free movement of the hydrophilic parts. Ethylphosphorylated PBI (Figure 2-17.d)<sup>8</sup> was also synthesised with the same procedure. But the resulting polymer was insoluble in organic solvents. However, this membrane showed a high proton conductivity of  $10^{-3} \text{ S.cm}^{-1}$  even as a compressed pellet.

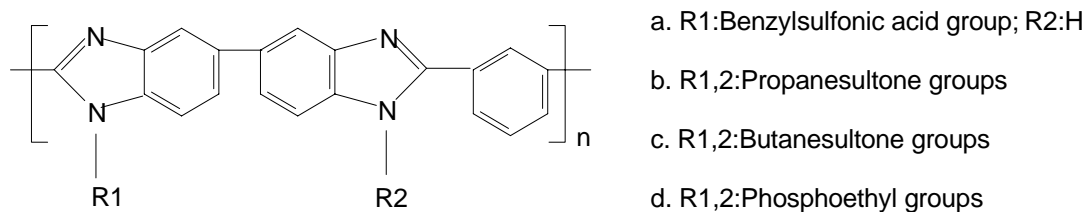


Figure 2-17 Scheme of chemically grafted PBI

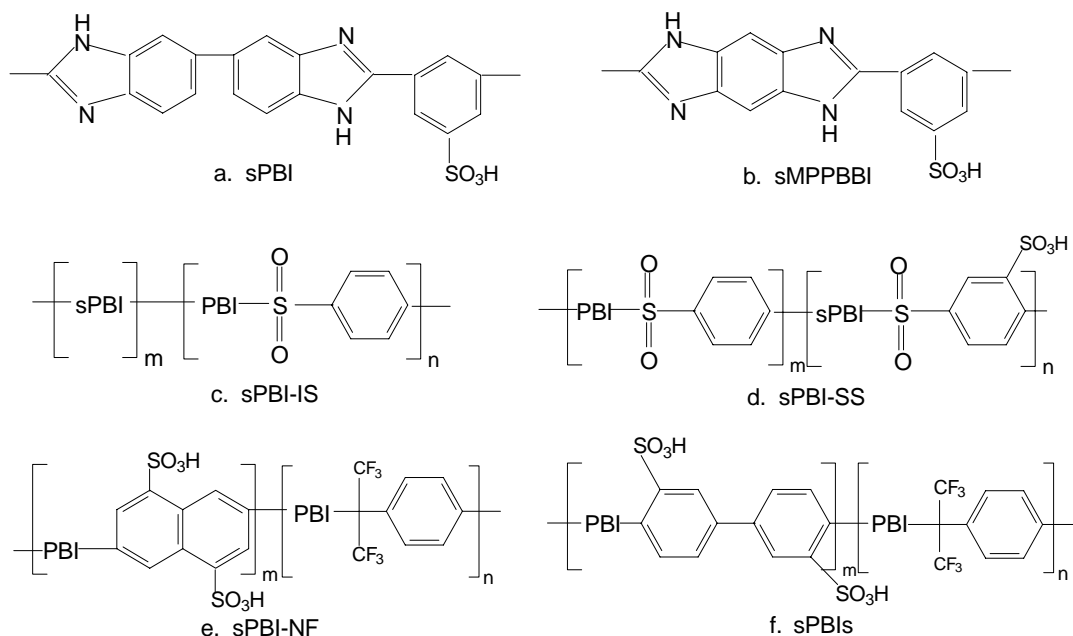


Figure 2-18 Sulphonated PBI by synthesis from monomers containing sulphonic groups

The method of synthesis with monomers bearing sulphonic groups, was mainly used for PBI derivatives<sup>153</sup> and copolymers<sup>154-156</sup>. Asensio et al. found that the maximum conductivity of poly[*m*-(5-sulfo)-phenylenebezobisimidazole] (SMPPBBI)<sup>153</sup> (Figure 2-18.b) with H<sub>3</sub>PO<sub>4</sub> doping level of 3.6 was  $2.0 \times 10^{-6} \text{ S.cm}^{-1}$ , which was higher than that of poly(*m*-phenylenebezobisimidazole) (MPPBBI) with same doping level ( $9.0 \times 10^{-8} \text{ S.cm}^{-1}$ ). Qing et al. synthesised sPBI-IS<sup>155</sup> (Figure 2-18.c) and sPBI-SS<sup>154</sup> (Figure 2-18.d) by solution copolycondensation in PPA. The resulting polymer membranes with high hygroscopicity show potential application as the high temperature PEM in fuel cell. Recently, they copolymerised sPBI-NF<sup>156, 157</sup> (Figure 2-18.e&f) and the highest conductivity of this copolymer reached up to  $2.7 \sim 2.8 \times 10^{-3} \text{ S.cm}^{-1}$  at 90°C and 100%RH. Recently Bai and Winston<sup>158</sup> synthesised sulphonated PBI copolymers and prepared PEMs through an in-situ phase inversion technique,

which showed extremely high conductivities ( $>1.0 \times 10^{-1} \text{ S.cm}^{-1}$ ) at high temperatures ( $>120^\circ\text{C}$ ), presenting a potential for high temperature application.

### 2.5.5.3 Polymer blends of PBIs with other polymers

A high degree of sulphonation leads to poor mechanical properties of the membranes and a high acid doping level has a potential problem of acid leaking from the membranes. Therefore, ionic cross-linking structures have been introduced into the preparation of polymer membranes. Flexible ionomer networks can be prepared from acid-based polymers by ionically and/or covalently cross-linking (Figure 2-19) of polymeric acids and polymeric bases,<sup>159-162</sup> as reviewed by Kerres<sup>163</sup> and recently by Li et al.<sup>11</sup>

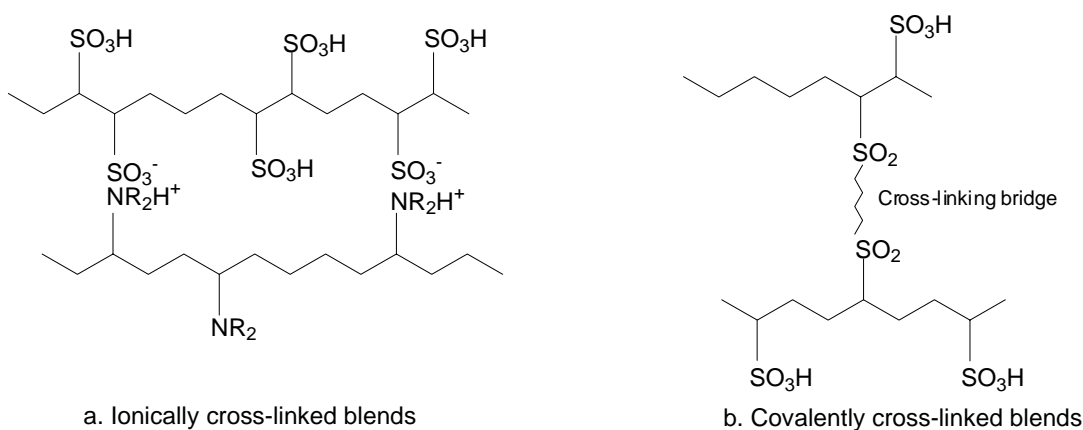


**Figure 2-19 Scheme of cross-linked acid based membranes: a. ionically cross-linked and b. covalently cross-linked blends**

The commercially available acidic polymers used to be blended with basic PBI polymer include sulphonated polysulphone (SPSF)<sup>164</sup>, sulphonated polyetheretherketone (SPEEK)<sup>165</sup>, sulphonated poly(arylene thioether)s<sup>166</sup>, and sulphonated poly[bis(phenoxy)phosphazene] (SPOP)<sup>167</sup> etc. Based on FTIR, FT-Raman spectra and IEC results<sup>17, 159, 161, 168</sup>, a strong interaction between the N-H bonds of PBI and sulphonated or/and sulphone groups of the polymer acids in the polymer blend was suggested.

In order to enhance chemical stability and improve the flexibility of cross-linking polymer membranes, sulphonated partially fluorinated arylene main chain polymers have recently been synthesised and blended with PBI which were demonstrated on fuel cells by Kerres and Li et al.<sup>169-172</sup> These PBI blended membranes exhibit

excellent thermal stability. Phosphoric acid-doping levels as high as 11~12 have been achieved with high proton conductivities (above  $1.0 \times 10^{-1} \text{ S.cm}^{-1}$ ), less acid swelling, reasonable mechanical strength and therefore better fuel cell performance.

Recently, blends of ABPBI-Poly(vinylphosphonic acid)(PVPA) were prepared.<sup>173, 174</sup> Acar et al.<sup>173</sup> reported that the conductivity of ABPBI/PVPA blends increased with elevated ratio of PVPA and the highest conductivity of  $4.0 \times 10^{-3} \text{ S.cm}^{-1}$  was achieved at 20°C and 50%RH. In Akbey et al.'s work<sup>174</sup>, the complex with a 1:1 mixing ratio had the lowest activation energy for proton mobility, and at the same time contained the most structured hydrogen bonded protons. Very recently, Acar et al.<sup>175</sup> also prepared the blends of ABPBI-poly(styrene sulfonic acid) (PSSA). The blended membrane of ABPBI/PSSA with molecular ratio of 1:2 showed the proton conductivity of  $2.0 \times 10^{-2} \text{ S.cm}^{-1}$  (ambient temperature, RH=50%) which was at least five-order of magnitude higher than that of anhydrous material.

However, ionically cross-linked membranes normally suffered from poor thermal stability in aqueous media as the ionic cross-link breaks at higher temperatures.<sup>163</sup> The covalent cross-linked membranes showed good chemical stability in the aqueous acidic environment and mainly developed by Kerres et al.<sup>176-178</sup> However, no covalently cross-linked membranes based on PBI are reported so far.

## **2.6 Brief Introduction of POSS**

Compared to macroscopic composites, nanocomposites present non-linear changes in properties.<sup>179</sup> Generally, the properties of organic/inorganic hybrid nanocomposites are higher than the sum of the individual contributions of both phases. The improved properties of organic/inorganic hybrid nanocomposites result from the interfacial interactions between individual components and have been arousing great interest.<sup>180, 181</sup> The polyhedral oligomeric silsesquioxanos (POSS) belong to the family of these new hybrid materials.<sup>182, 183</sup> Oligomeric silsesquioxanes were first synthesised in 1946<sup>184</sup>, but only in the last decade have been developed in several applications.

POSS are produced by sol-gel techniques through hydrolytic condensation of tri-functional monomers  $\text{RSiX}_3$  (X presents a highly reactive substituent, such as Cl or alkoxy) with a diameter around 0.53 nm of an inorganic central core surrounded



by eight organic groups or hydrogen, R, providing the empirical formula of  $(\text{RSiO})_{1.5}$  (Figure 2-20).<sup>185</sup> In a POSS hybrid composite, POSS cages can be introduced into polymer systems via physical blending or chemical reactions (i.e. copolymerisation). Currently, the method of copolymerisation is mostly employed because it involves the formation of chemical bonds between POSS cages and polymer matrices, resulting in the fine dispersion of POSS in the polymer matrices. However, nanocomposites obtained by physical blending were less frequently reported, which might be possibly due to the unfavourable miscibility of silsesquioxanes with polymers.<sup>186, 187</sup>

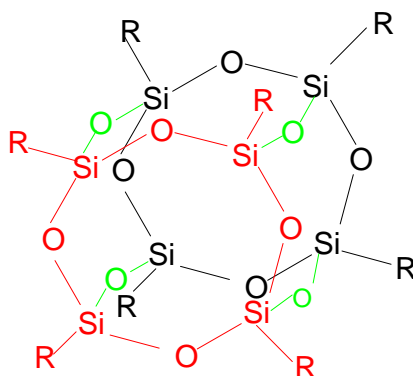


**Figure 2-20 General structure of POSS**

Owing to the hybrid organic/inorganic structure and therefore possessing unique properties, the great interest is focused on POSS building blocks in the nanocomposites. For example, POSS were used in from low dielectric constant materials to new resists for electron beam lithography materials and high temperature lubricants.<sup>185</sup> To achieve multifunctional materials with intermediate properties between organic polymer matrices and inorganic ceramics, the preparations of novel polymeric compositions, polymer nanocomposites and hybrids are greatly highlighted among the various applications of POSS.<sup>185, 188</sup>

Recently, Eshel et al.<sup>189</sup> prepared nanocomposite hydrogels containing epoxy functionalised POSS. In their work, with less than 5% epoxy functionalised POSS incorporated into the hydrogel, water swelling increased by more than 120% and storage modulus by 300% compared to the neat hydrogel, which was due to the large surface area of the nanosize POSS particles affecting water-swelling behaviour and mechanical properties of hydrogel. Very recently, Subianto et al.<sup>190</sup> prepared Nafion/POSS composite PEM. Due to the hygroscopic POSS cores and the

functional groups from sulphonated POSS, the proton conductivity and mechanical properties have been greatly improved.

## **2.7 Summary**

PEMFCs are receiving increasing attention due to their abilities as power generators for both stationary and transportation applications. The main features of PEMFCs are high power density, pollution free operation and all-solid construction; and, therefore, less corrosion. The most successful membrane, i.e. Nafion membrane, can only offer reasonable performance below 90°C under fully hydrated conditions. The potential operation of PEMFCs at high temperatures (i.e. >100°C) can provide many advantages therefore are focused on by many researchers.

To achieve high temperature operation of PEMFC, acid-based polymer membranes represent an effective approach. The phosphoric acid doped PBI membrane seems so far the most successful system in the field. However, the acid leaching prevents the phosphoric acid doped PBI membrane from using at low temperatures and causes problems of long-term stability. Therefore, to retain phosphoric acid in the membrane at various temperatures and humidity is extremely important for the acid-based membrane. The chemically bonded functional groups onto the polymer exhibit a promising way to solve the problem, as well as composite membranes of PBI with other functional fillers, which can lessen this problem to some extent. Both of these membranes show lower conductivity and higher dependence on humidity and need further optimisation. Even so, it is important to understand the mechanism of proton conduction in these membranes in a fundamental molecular-based point in order to design new membranes.

# Chapter 3 EXPERIMENTAL DETAILS

## 3.1 Chemicals

The main chemicals used in this project are listed in Table 3-1.

**Table 3-1 Chemicals used in this project**

Chemicals	Main Properties	Manufacturer
3,3'-diaminobenzidine (DAB)	Purity: 99% Mw: 214.27 g/mol Melting point: 175-177°C	Sigma-Aldrich Co. Ltd
Isophthalic acid (IPA)	Purity: 99% Mw: 166.13 g/mol Melting point: 341-343°C	Sigma-Aldrich Co. Ltd
3,4-Diaminobenzoic acid (DABA)	Purity: 97% Mw: 152.15 g/mol Melting point: 215-218°C	Sigma-Aldrich Co. Ltd
Polyphosphoric acid (85% P <sub>2</sub> O <sub>5</sub> ) (PPA)	Density: 2.050 g/mL	Sigma-Aldrich Co. Ltd
Phosphorus pentoxide (P <sub>2</sub> O <sub>5</sub> )	Purity: 99+% Melting point: 340°C	Sigma-Aldrich Co. Ltd
Methanesulphonic acid (MSA)	Purity: 99+% Mw: 96.11 g/mol Density: 1.481g/mL Boiling point: 167°C	Fisher Scientific UK
Sodium hydroxide (NaOH)	Mw: 40.00g/mol Density: 2.13g/mL	Sigma-Aldrich Co. Ltd
Phosphoric acid (PA)	Purity: 84% Boiling point: 158°C	Fisher Scientific UK
96-98% Sulphuric acid	Purity: 96-98%	Fisher Scientific UK
Hydrazine hydrate	1.005g/mL	Sigma-Aldrich Co. Ltd
Activated Carbon	/	Sigma-Aldrich Co. Ltd
Acetic acid	Density: 1.463g/mL	Sigma-Aldrich Co. Ltd
TriSilanolPhenyl POSS (SO-POSS, SO1458)	Mw: 931.34 Solvent solubility: Ethanol	Hybrid Plastic, Inc., USA
OctaAmmonium POSS (AM-POSS, AM0285)	Mw: 1173.18 Solvent solubility: water	Hybrid Plastic, Inc., USA
H <sub>2</sub> O <sub>2</sub>	Density: 1.463g/mL	Fisher Scientific UK
Nafion 117	Thickness: 175µm IEC: 1100 mequiv.g <sup>-1</sup>	DuPont Co. USA

### 3.2 Synthesis of Polymers

A general procedure of synthesis is showed in Figure 3-1. The synthesis was carried out in the media of methanesulphonic acid (MSA) and phosphorus pentoxide ( $P_2O_5$ ), a two-neck round flask (250mL, Fisher Co.) with a magnetic oval stir bar (35mm×10mm, Fisher Co.) was used as shown in Figure 3-2. For the purpose of investigating the effect of different stirring styles (i.e. magnetic and mechanical stirring) on the molar mass of ABPBI, a PTFE stir rod was used instead of magnetic stir bar. When ABPBI and PBI were synthesised in the medium of polyphosphoric acid (PPA) respectively, a smaller set including a reaction tube (50mL, Fisher Co.) and a magnetic stir bar (25mm×6mm, Fisher Co.) was used instead of the above set. All the synthesis was carried out at a nitrogen ( $N_2$ ) atmosphere by purging  $N_2$  gas through two needles inserted into the rubber plugs. Before synthesis, the synthesis set was purged with  $N_2$  stream for 1 hour to empty air.

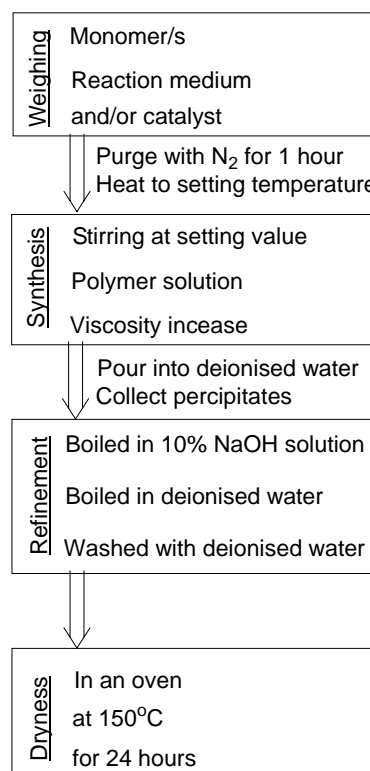


**Figure 3-1 A procedure of polymer synthesis**



**Figure 3-2 Polymer synthesis set**

### 3.2.1 Synthesis of poly(2,5-benzimidazole) (ABPBI)

#### 3.2.1.1 Purification of 3,4-diaminobenzoic acid (DABA)

The purification procedure<sup>28</sup> of the monomer 3,4-diaminobenzoic acid (DABA) is illustrated in Figure 3-3. 20.0g of commercial DABA was dispersed in 250mL of water at 70°C. Hydrazine hydrate was added until a homogeneous solution was obtained. Activated carbon black (10 g) was added to the reaction mixture which was heated at 70°C for 30 minutes. The mixture was filtered through a filtrator whilst hot.

After cooling the filtrate to room temperature, acetic acid was added slowly until the precipitation had formed. It was placed under an ambient condition for 24 hours. The precipitates were then collected and dried under reduced pressure for 36 hours at 70°C in a vacuum oven.

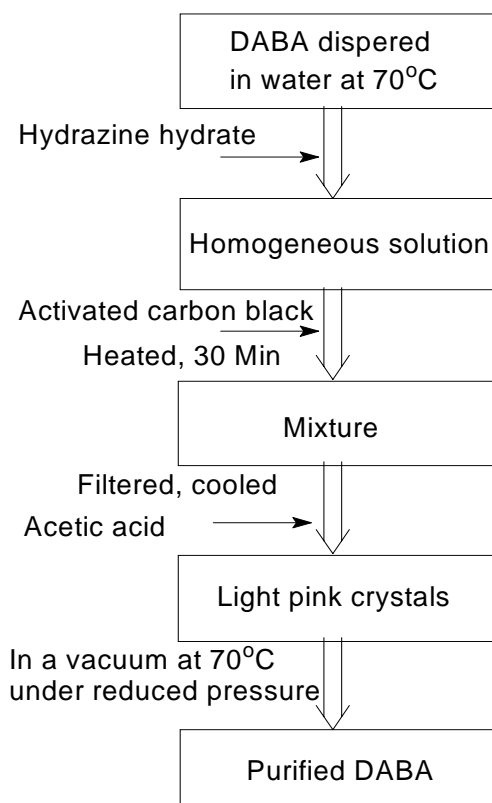


Figure 3-3 Flow chart of the purification of DABA

### **3.2.1.2 Synthesis of ABPBI in polyphosphoric acid (PPA)**

6.6mmol (1.000g) of DABA was added into 20.0g of the reaction medium of polyphosphoric acid (PPA) in a 50mL reaction tube. The synthesis procedure was shown in Figure 3-1. The synthesis was carried out at 200°C under N<sub>2</sub> atmosphere for 5 hours<sup>127</sup>. The hot polymer solution was slowly poured into the deionised water (500mL) to get fibre-like polymers. The obtained polymers were boiled in a beaker with 500mL 10% NaOH solution at 100°C for 2 hour to remove phosphoric acid and the solvent, subsequently boiled in 500mL deionised water for one hour to remove NaOH. After that, the polymers were washed with deionised water for several times to remove residual NaOH. Finally, the polymers were dried in an oven at 150°C for 24 hours. The obtained brown fibre-like polymers were placed in a sealed flask.

### **3.2.1.3 Synthesis of ABPBI in methanesulphonic acid (MSA)**

26.6mmol (4.183g) of DABA was mixed with 40mL of methanesulphonic acid (MSA) and 4.0~6.0g of phosphorus pentoxide (P<sub>2</sub>O<sub>5</sub>). The synthesis and refinement procedures were the same as that in PPA medium, except the synthesis was carried out at 140~160°C from 20 minutes to 3 hours. The commercial and purified DABA, mechanical and magnetic stirring styles were used, respectively.

## **3.2.2 Synthesis of polybenzimidazole (PBI)**

### **3.2.2.1 Synthesis of PBI in PPA**

1.5mmol (0.320g) of DAB and 1.5mmol (0.250g) of IPA were mixed with 20.0g of PPA in a 50mL reaction tube. The synthesis worked at 200°C for 9 hours.<sup>122</sup> The obtained dark purple liquids were poured into the 500mL deionised water to precipitate the polymer. During the precipitation process, a centrifuge was used to hasten the precipitation. After refinement and dryness treatments which were the same as that of ABPBI, the dark purple polymer powders were sealed in a flask.

### **3.2.2.2 Synthesis of PBI in MSA/P<sub>2</sub>O<sub>5</sub>**

26.7mmol (5.891g) of DAB and 26.7mmol (4.430g) of IPA were mixed with 40mL of MSA and 6.0g of P<sub>2</sub>O<sub>5</sub>. The synthesis condition was at 150°C for 3 hours whilst the synthesis processes were the same as synthesised in PPA.

### 3.2.3 Synthesis of copolymers of ABPBI and PBI in MSA

The copolymers of ABPBI and PBI were synthesised in the media of MSA/P<sub>2</sub>O<sub>5</sub> with the amounts of monomers given in Table 3-2. These syntheses were carried out at 150°C for 3 hours. During the refinement, a centrifuge was used. The other processes were the same as that of PBI synthesised in the media of MSA/P<sub>2</sub>O<sub>5</sub>.

**Table 3-2 Amount of monomers for synthesis of copolymers**

Monomer	Molar ratio of monomers		
	75:25	50:50	25:75
DABA (97%), <i>mmol</i> (g)	20.0(3.137)	13.3(2.091)	6.7(1.046)
DAB (99%), <i>mmol</i> (g)	6.7(1.473)	13.3(2.945)	20.0(4.418)
IPA, <i>mmol</i> (g)	6.7(1.108)	13.3(2.215)	20.0(3.323)

### 3.3 Synthesis of ABPBI/POSS Composites

The ABPBI/POSS composites were synthesised in situ in the media of 40mL of MSA and 6.0g of P<sub>2</sub>O<sub>5</sub>. The reaction ran at 150°C for 3 hours with magnetic bar stirring at 400rpm.

#### 3.3.1 Synthesis of ABPBI/OctaAmmonium POSS composite

The ABPBI/OctaAmmonium POSS (ABPBI/AM or ABPBI/OA-POSS) composites with different percentage of AM-POSS were synthesis. The amounts of AM-POSS and monomer DABA were given in Table 3-3.

**Table 3-3 Weight of monomers for synthesis of ABPBI/OctaAmmonium POSS composite**

Chemical	Percentage of AM-POSS		
	1.0 wt.% (ABPBI/1AM)	3.0 wt.% (ABPBI/3AM)	5.0 wt.% (ABPBI/5AM)
DABA (97%), g	1.021	1.000	0.979
AM-POSS, g	0.010	0.030	0.050

AM-POSS was added into 10mL of MSA followed by ultrasonication for 30 minutes in an ultrasonic bath to obtain a homogeneous transparent solution. Subsequently, DABA and 1.5g of P<sub>2</sub>O<sub>5</sub> were added, followed by another 30 minutes of

ultrasonication treatment. Finally, the mixtures were synthesis at 150°C for 2 hours with a magnetic bar stirring at the rate of 400rpm. The procedures of synthesis and refinement were the same as described above.

### 3.3.2 Synthesis of ABPBI/TriSilanolPhenyl POSS composite

The amounts of TriSilanolPhenyl (SO-POSS) and monomer DABA for the synthesis of ABPBI/TriSilanolPhenyl POSS (ABPBI/SO) composites were shown in Table 3-4.

**Table 3-4 Weight of monomers for synthesis of ABPBI/TriSilanolPhenyl POSS composite**

Chemical	Percentage of SO-POSS		
	1.0 wt. %	3.0 wt. %	5.0 wt. %
	(ABPBI/1SO)	(ABPBI/3SO)	(ABPBI/5SO)
DABA, g	1.021	1.000	0.979
SO-POSS, g	0.010	0.030	0.050

The TriSilanolPhenyl POSS (SO-POSS) was dissolved first in 0.5~1.0mL of ethanol then added into 10mL of MSA followed by an ultrasonication until an even-distributed suspension obtained (around 1~2 hours). After that, DABA and 1.5g of P<sub>2</sub>O<sub>5</sub> were added for synthesis. The synthesis process was the same as described above.

### 3.4 Fabrication of Membranes

In this project, two different methods for membrane fabrication, casting and direct casting, were employed (Figure 3-4).

In the casting method (Figure 3-4a), 0.5g of polymer or composite material was dissolved in 10mL of MSA at 130°C for 2 hours to form a homogeneous solution. After that, the hot solution was poured onto a Petri dish, which was then put into a fume cupboard and heated up to 200°C for 24 hours to form a membrane. During the heating process, the temperature increased from 100~200°C gradually to avoid forming pin holes. With the time elapse, the Petri dish with the membrane was cooled down then immersed in the deionised water so that the membrane was peeled off from the Petri dish. The membrane was boiled in 10% NaOH solution at 100°C



for 1 hour to remove phosphoric acid and residual solvent then boiled in deionised water for another hour to remove NaOH. The membrane was rinsed by deionised water several times to remove the possible residual NaOH on the surface. Finally, the membrane was dried in an oven at 150°C for 24 hours. The obtained dry membrane was kept in a sealed glass container.

In the direct casting (Figure 3-4b), the as-synthesised hot polymer or composite mixtures were poured onto a Petri dish and heated up to 200°C gradually for 24 hours to obtain a membrane. The subsequent purification of the membrane was the same as that used in casting method. Differing from that in the casting method, the time-consuming procedures i.e. the purification of polymer and the re-dissolution were avoided in direct casting.

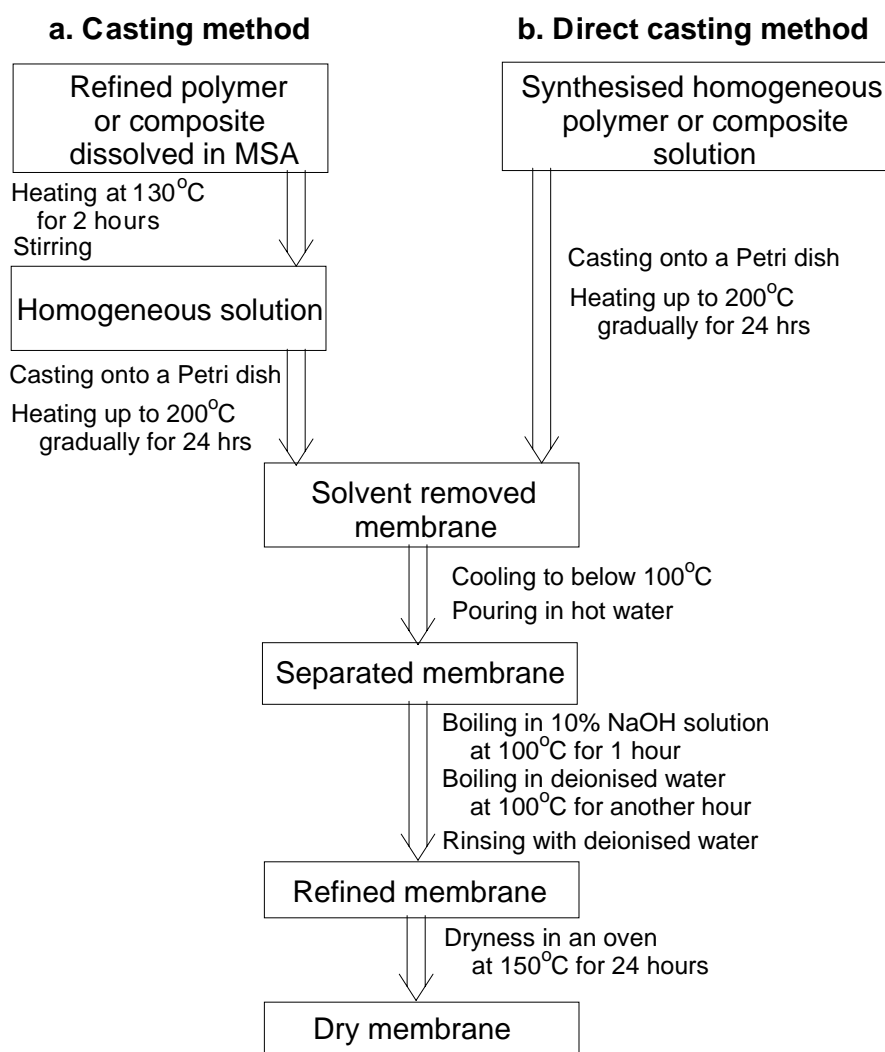


**Figure 3-4 Methods of membrane fabrications: a. casting; b. direct casting**

### 3.5 Preparation of Phosphoric Acid doped membranes

A series of phosphoric acid solutions from 2 to 12 M were prepared (Table 3-5). The molar concentration of phosphoric acid solution can be calculated by the following equation:

$$M_{PA}, mol/L = \frac{(V_{PA} \times 1.680 g/mL \times 85\%)/(98.0 g/mol)}{(V_{PA} + V_{H_2O}) \times 10^{-3}} \quad 3-1$$

where,  $M_{PA}$  is the molar concentration of phosphoric acid solution,  $V_{PA}$  is the volume of phosphoric acid (85wt.%), and  $V_{H_2O}$  the volume of deionised water.

**Table 3-5 Preparation of different concentrations of phosphoric acid solutions**

$M_{PA}, M$	2	4	6	8	10	12
$V_{PA}, mL$	10.0	20.0	30.0	40.0	50.0	60.0
$V_{H_2O}, mL$	62.7	52.7	42.7	32.7	22.7	12.7

Phosphoric acid doping was carried out by immersing a dry membrane in a specified concentration of  $H_3PO_4$  solutions for certain period of time (i.e. 7 days) at room temperature reaching equilibrium then the phosphoric acid doped membrane was rinsed with plenty of deionised water to remove free phosphoric acid on the membrane surface. Finally the surface water of the membrane was absorbed by filter papers. At that time, the membrane was considered as a saturated membrane. When the membrane was then placed at ambient atmosphere to reach equilibrium, the membrane was looked upon as a membrane at ambient atmosphere. Correspondingly, the membrane subsequently dried in an oven was defined as a dry membrane. For the purpose of measurements, it is necessary to identify these membranes at three different states, i.e. saturated, ambient atmosphere and dry conditions.

### 3.6 Preparation of Nafion Membrane

The pre-treatment of commercial Nafion 117 membrane employed the wide-used method<sup>191</sup>. Firstly, the Nafion 117 membrane was boiling in 3%  $H_2O_2$  for at least 1 hour, subsequently rinsing with boiling water for several times, then boiling in 0.5M  $H_2SO_4$  solution for 1 hour, next to boil in deionised water for another 1 hour. Finally, the membrane was rinsing with deionised water several times. Those procedures

were purposed to remove the impurities. The obtained transparent Nafion membrane was kept in the deionised water before further characterisations and use.

### **3.7 Characterisation**

#### **3.7.1 Characterisation of chemical structures of the polymers**

##### **3.7.1.1 Fourier transform infrared (FTIR) spectroscopy**

A FT-infra-red spectrometer (FTIR-8400, Shimadzu corp., Japan) was used with a resolution of  $4\text{cm}^{-1}$  and 64 scans in the region of  $4000\text{-}400\text{cm}^{-1}$ . The polymer powders and POSS powders were measured with the transmission mode by preparing a thin film pressured with potassium bromide (KBr) pellets. The polymer membranes cast from a solution were measured by attenuated total reflectance (ATR) mode. For convenience of comparing the FTIR spectra of polymer powders and polymer membranes, the FTIR data based on transmission and ATR modes can be converted by the following equation<sup>192</sup>:

$$A = 2 - \log_{10} T \quad 3-2$$

where  $T$  is the transmittance, %;  $A$  is the absorbance, AU.

##### **3.7.1.2 Elemental analysis**

A vario EL elemental analyser (ELEMENTAL Vario corp., German) was used to detect the content of carbon (C), hydrogen (H) and nitrogen (N).

An ICP-AES (IRIS Advantage Thermo Jarrell Ash Co., USA) was used to determine the content of phosphorus (P) and sulphur (S) in samples.

##### **3.7.1.3 Characterisation of molecular weights of the polymers**

An Ubbelohde viscometer (Shanghai Qihang Analytical Instrument Company, China) with the diameter of 1.03 mm was used to measure the flow times in order to determine the molecular weight of synthesised PBI and ABPBI.

Five concentrations of 0.2, 0.4, 0.6, 0.8, and 1 g/dl of PBI and ABPBI solutions were prepared, respectively. The polymers with specified weight (0.2, 0.4, 0.6, 0.8 and

1.0g) were dissolved in 100mL 98% H<sub>2</sub>SO<sub>4</sub> and stirred for 24 hours to form homogeneous polymer solutions. Afterwards, flow times of all the solutions and the solvent were measured. All the measurements of flow times were carried out at 30±0.1°C water bath. Before measuring, the viscometer containing a polymer solution was kept in 30±0.1°C water bath over 30 minutes to approach equilibrium. The inherent viscosities and the reduced viscosities were calculated by the following equations:

$$\eta_{inh} = \frac{\ln(t/t_0)}{c} \quad 3-3$$

$$\eta_{red} = \frac{(t-t_0)/t_0}{c} \quad 3-4$$

where  $\eta_{inh}$  and  $\eta_{red}$  are the inherent and the reduced viscosities, respectively, dl/g;  $t$  is the flow time for each solution and  $t_0$  is the corresponding time for the solvent or 98% H<sub>2</sub>SO<sub>4</sub>, s;  $c$  is the concentration of the polymer solution, g/dl.

The intrinsic viscosity (or limiting viscosity number,  $[\eta]$ ) can be calculated from  $[\eta] = \lim_{c \rightarrow 0} \eta_{inh} = \lim_{c \rightarrow 0} \eta_{red}$ . In other words a straight line can be obtained from the plot of  $\eta_{inh}$  or  $\eta_{red}$  (Y axis) against  $c$  (X axis) and an intercept of the straight line extrapolated to zero concentration is the value of  $[\eta]$ .

The intrinsic viscosity can be readily related to the molecular weight of polymer,  $M_w$ , through a semi-empirical equation (Mark-Houwink equation). By light scattering and intrinsic viscometry, Kojima et al.<sup>193, 194</sup> and Wang et al.<sup>109, 195</sup> studied the dilute solution properties of PBI and ABPBI, and found that the characteristic parameters depend on molecular weight distribution, respectively. The Mark-Houwink equations for PBI and ABPBI polymers are

$$\text{For PBI}^{122}: [\eta] = 1.35326 \times 10^{-4} \times M_w^{0.7328} \quad 3-5$$

$$\text{For ABPBI}^{127}: [\eta] = 8.7 \times 10^{-3} \times (M_w/116)^{1.10} \quad 3-6$$

### 3.7.2 Characterisation of mechanical properties

Tensile strength was measured according to ASTM D638 by the universal testing machines (Model LR50K Plus, Lloyd Instrument, UK) with a dumbbell type specimen under the conditions: gauge length=10mm; width=2.5mm; crosshead speed=50 mm/min; load cell=1.0 kN.

### 3.7.3 Characterisation of thermal properties of the polymers

#### 3.7.3.1 Differential scanning calorimetry (DSC)

Two differential scanning calorimetry (DSC) instruments were used in this work. The DSC (Model 2010, TA instrument, Inc.) was used to measure the heat flow of materials (such as the DABA monomer, membranes etc.) with the temperature increasing from 25°C to around 350°C. Another DSC was assembled with TGA which can reach higher temperatures (>800°C). Samples of 5-10mg were examined in a nitrogen atmosphere. As for the measuring of the melting temperature of DABA monomer before and after purification, the heated rate was of 1°C/min, for other samples the heated rate was 10°C/min.

#### 3.7.3.2 Thermogravimetric analysis (TGA)

A simultaneous TGA/DSC (2960 SDT V3.0F, TA Instruments Inc., USA) was used to trace the thermal degradation of the polymers and/or phosphoric acid, residual solvents and moistures. The glass transition temperatures ( $T_g$ ) of polymers were also detected with DSC mode. Samples of 8-12mg were examined in a nitrogen atmosphere from room temperature to 900°C with a heated rate of 10°C/min.

### 3.7.4 Characterisation of morphologies of membranes

#### 3.7.4.1 Scanning electron microscopy (SEM)/Transmission electron microscopy (TEM)

A Field Emission Gun Scanning Electron Microscope (FEG-SEM) with electron high tension of 5.00 kV and working distance of 5~9mm was used to characterise the morphologies of polymer membranes. For conventional imaging in the SEM, samples must be electrically conductive at least at the surface, all the samples were coated by gold in this experiment. The energy dispersive X-ray (EDX) analysis was used to illustrate the distribution of elements (C, N, O, P and/or Si etc.).

The TEM investigation of POSS particles dispersion in the ABPBI/POSS composite membrane was performed with a JEOL 2000FX microscope and LINK analytical X-ray spectrometer.

#### 3.7.4.2 X-ray diffraction (XRD)

A range of 5-75° with a Cu K $\alpha$  radiation source operating at 40 kV and 40 mA was used for X-Ray diffraction (XRD) characterisation. The sample membrane was scanned under ambient conditions. The sample POSS powders were kept at refrigerated temperature for at least 24 hours prior to the measurement and spread on a microscope slide without further preparation, then scanned under ambient conditions.

### 3.7.5 Characterisation of water and phosphoric acid uptakes of polymer and composite membranes

#### 3.7.5.1 Water uptake

The dry sample membrane was immersed in deionised water to reach equilibrium (i.e. 3 days) followed by absorbing the surface water by filter papers. At this stage the membrane was viewed at saturated condition. When continuously placed at ambient atmosphere to reach equilibrium, the membrane was considered as at ambient condition. Before drying in an oven, the sample membrane was regarded as a wet (hydrous) membrane. After dried at an oven at 150°C for 24 hours, the membrane was regarded as a dry (anhydrous) membrane.

The water absorptivity of undoped (no acid doped) membrane is represented by the water uptake which is calculated by following equation

$$\text{Water uptake, \%} = \frac{W_{\text{wet}} - W_{\text{dry}}}{W_{\text{dry}}} \times 100\% \quad 3-7$$

where  $W_{\text{wet}}$  and  $W_{\text{dry}}$  are the weight of wet and dry membrane, respectively, g.

The water uptake of phosphoric acid doped membrane is calculated by

$$\text{Water uptake, \%} = \frac{W_{\text{wet}} - W_{\text{dry}}}{W_{\text{undoped}}} \times 100\% \quad 3-8$$

where  $W_{\text{wet}}$  and  $W_{\text{dry}}$  are the weight of wet and dry membrane after acid doping, respectively,  $W_{\text{undoped}}$  is the weight of dry membrane before acid doping.

It is noteworthy that, for the purpose of measuring the water uptake at saturated condition and ambient atmosphere, the relative weight of the wet membrane was measured from at saturated condition and the equilibrium condition at ambient atmosphere respectively. Whilst measuring the moisture absorptivity,  $W_{\text{wet}}$  was the weight of an original dry membrane placed at ambient atmosphere for certain period of time (i.e. 7 days) reaching equilibrium.

### 3.7.5.1 Phosphoric acid uptake

The dry membrane sample was soaked in phosphoric acid solution for certain period of time (i.e. 7 days) to reach equilibrium. The phosphoric acid absorptivity of a polymer membrane can be characterised by acid doping level or acid uptake. Here, the former is defined as the phosphoric acid molecule per repeat unit of ABPBI polymer:

$$\text{PA doping level} = \frac{(W_{\text{doped}} - W_{\text{undoped}})/98}{W_{\text{undoped}}/116} \quad 3-9$$

where  $W_{\text{doped}}$  and  $W_{\text{undoped}}$  were the weight of dried membrane after and before doped in phosphoric acid.

The later is defined as the weight ratio of phosphoric acid and polymer:

$$\text{PA uptake, \%} = \frac{W_{\text{doped}} - W_{\text{undoped}}}{W_{\text{undoped}}} \times 100\% = 0.845 \times \text{PA doping level} \quad 3-10$$

### 3.7.6 Characterisation of conductivity of membrane

A Solartron Analytical 1280 Electrochemical Measurement Unit (1280 EMU, Solartron Analytical Ltd.) was used to measure the impedance of membranes. The details are described in Chapter 6.

# **Chapter 4 RESULTS AND DISCUSSION:**

## **SYNTHESIS AND CHARACTERISATION OF POLYMERS AND POLYMER COMPOSITES**

### ***4.1 Synthesis and Characterisation of ABPBI Polymer***

#### **4.1.1 Chemical structure of poly(2,5-benzimidazole) (ABPBI)**

##### **4.1.1.1 FTIR analysis of ABPBI**

Infra-red (IR) spectroscopy is a chemical analysis technique, which measures the infra-red intensity versus wave-number of light. The infra-red spectroscopy detects the vibration characteristics of chemical functional groups in a sample. When infra-red light interacts with the matter, chemical bonds will stretch, contract and bend. As a result, a chemical functional group tends to adsorb infra-red radiation in a specific wave-number range regardless of the structure of the rest of the molecule. Hence, the correlation of the band wave-number position with the chemical structure is used to identify a functional group in a sample. In this work the reactant or monomer 3,4-diaminobenzoic (DABA) and the polymer product were measured by FTIR to trace the changes of IR spectra of latent reactive groups and then confirm the typical structure of the product.

The FTIR spectra of the commercial monomer DABA and synthesised polymers are shown in Figure 4-1. In the spectrum of the monomer DABA (Figure 4-1a), two sharp bands assigned to asymmetric and symmetric vibrations of primary amine  $\text{NH}_2$  group are observed at  $3320$  and  $3198\text{cm}^{-1}$ , respectively; the dissociated two peaks at  $3443$  and  $3419\text{cm}^{-1}$  are attributed to vibration of hydrogen bonded  $\text{NH}_2$  group; the bending and twisting modes of  $\text{NH}_2$  groups are seen at  $1582$  and  $833\text{cm}^{-1}$ , respectively; whilst the vibration of  $\text{C-NH}_2$  appears at  $1306\text{cm}^{-1}$ . The most characteristic features of the carboxylic group are the two bands recognised at  $1620$  and  $1368\text{cm}^{-1}$  which are due to asymmetric and symmetric stretching vibrations of  $\text{COO}$  group; two other characteristic carboxylic group vibrations are  $\text{C-O}$  stretching



and C-OH bending. However, these bands are overlapped by those of aromatic chain vibrations<sup>196</sup>, i.e. the peaks of C-OH in-plane (at  $1152\text{cm}^{-1}$ ) and out-of-plane bending (at  $763\text{cm}^{-1}$ ) are overlapped by that of C-H in-plane and out-of-plane bending, respectively; the peak at  $1306\text{cm}^{-1}$  is contributed to C-O stretching and C-H in-plane bending. In the aromatic structure, C-H stretching vibration is centred at  $3073\text{cm}^{-1}$ ; C-H wagging is at  $934$  and  $912\text{cm}^{-1}$ ; the regions of the out-of-plane bending of C-H ( $900\text{-}800\text{cm}^{-1}$ ) and in-plane bending ( $1080\text{-}1250\text{cm}^{-1}$ ) are found to be contaminated by C-O and C-OH stretching.<sup>196</sup> The peak at  $1439\text{cm}^{-1}$  is attributed to C-C stretching and C-H in-plane bending.<sup>196</sup>

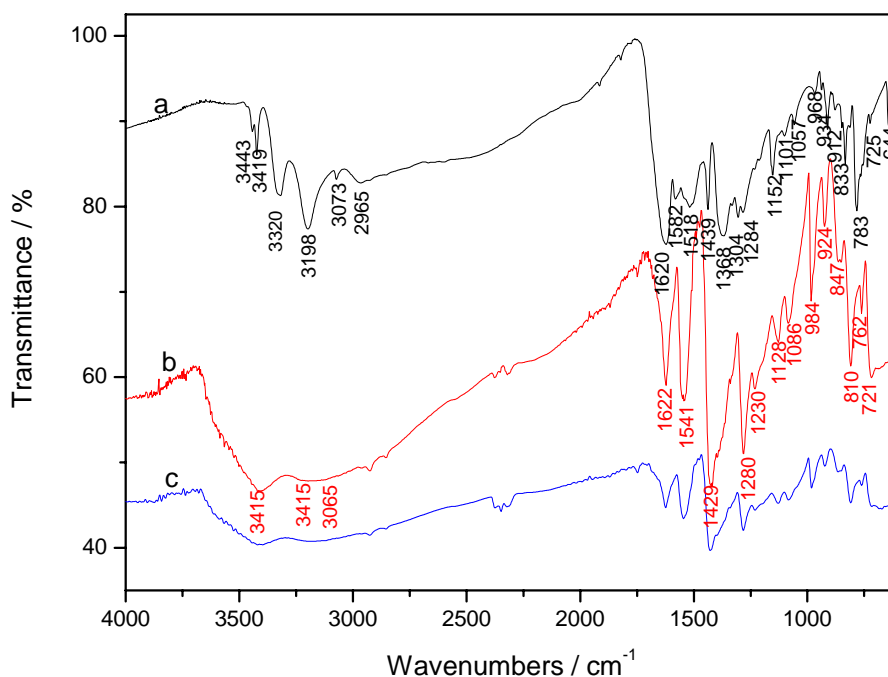


**Figure 4-1** FTIR spectra of (a) DABA monomer, (b) ABPBI synthesised in MSA and (c) ABPBI synthesised in PPA

When ABPBI is synthesised from the monomer DABA, in the region  $4000\text{-}2000\text{cm}^{-1}$ , the vibration of N-H in benzimidazole groups is expected to occur; benzimidazole ring vibrations as well as in-plane CH, NH and CN deformation modes are expected to appear in the region  $2000\text{-}1000\text{cm}^{-1}$ ; below  $1000\text{cm}^{-1}$ , cycle vibrations and out-of-plane NH and CH deformations are expectant as well.

The FTIR spectrum shown in Figure 4-1b is of the polymer synthesised in MSA/P<sub>2</sub>O<sub>5</sub> media. In the high wave-number region, the sharp peak centred at 3415cm<sup>-1</sup> is attributed to the stretching vibration of isolated, non-hydrogen bonded N-H group, and the very broad, asymmetric absorption, approximately centred at 3145cm<sup>-1</sup>, is assigned to self-associated, hydrogen bonded N-H group.<sup>105, 197</sup> C-H stretching in benzene ring assigned at 3065cm<sup>-1</sup> overlaps to the broad absorption of N-H group. The region from 1650 to 1500cm<sup>-1</sup> is regarded as a very characteristic range for benzimidazole groups. The band at 1622cm<sup>-1</sup> is for the C=C/C=N stretching whilst a strong absorption at 1541cm<sup>-1</sup> is resulted from in-plane deformation of benzimidazole ring. Moreover, the breathing mode of the imidazole ring can also be seen at around 1281cm<sup>-1</sup>.<sup>105</sup> It is noteworthy, compared to that of DABA, the reduction of 10cm<sup>-1</sup> of C-C stretching (1429 vs. 1439cm<sup>-1</sup>) should be due to the effect from the adjacent imidazole ring, and the characteristic in-plane and out-of-plane C-H deformation vibrations also slightly shift due to the same reason. The assignments of ABPBI are listed in Table 4-2. Compared to the IR spectra of monomer DABA, the disappearance of characteristic bands of amino and carboxylic groups in the DABA monomer and appearance of typical bands representing benzimidazole structures indicate ABPBI polymer are synthesised successfully according to the reaction equation in Figure 2-15. As described in the chapter of literature review, ABPBI was generally synthesised from PPA medium in the lab scale. ABPBI was also synthesised from PPA medium in this work. Compared to that in MSA/P<sub>2</sub>O<sub>5</sub>, the similar IR curve (Figure 4-1c) shows ABPBI was successfully obtained by synthesising in PPA medium.

#### 4.1.1.2 Elemental analysis of ABPBI

Elemental analysis is a process whereby a sample of some material is analysed for its elemental and sometimes isotopic composition. There are many different experimental methods for determining elemental composition. The most common type of elemental analysis is for carbon, hydrogen, and nitrogen (CHN analysis). This type of analysis is especially useful for organic compounds (compounds containing carbon-carbon bonds). The analysis of results is performed by determining the ratio of elements from within the sample, and working out a chemical formula that fits with those results. This process is useful as it helps determine if a sample is a desired compound and confirms the purity of a compound.

Inductively coupled plasma atomic emission spectroscopy (ICP-AES) is an analytical technique used for the detection of elements. It is a type of emission spectroscopy that uses the inductively coupled plasma to produce excited atoms and ions that emit electromagnetic radiation at wavelengths characteristic of a particular element. The intensity of this emission is indicative of the concentration of the element within the sample. Here it was used to trace the possible residuals of by determining the content of phosphorus (P) and sulphur (S) in samples.

The polymer synthesised from DABA monomer in MSA medium was characterised by elemental analysis. As shown in Table 4-1, no phosphorus and sulphur were found, indicating the solvent of MSA and catalyst of  $P_2O_5$  or  $H_3PO_4$  were completely removed from the sample.

**Table 4-1 Element contents of ABPBI synthesised in MSA/ $P_2O_5$**

Elements	Calculated contents, wt%	Measured contents, wt%
C	72.40	52.40
N	24.12	17.50
H	3.47	5.56
P	0	Not found
S	0	Not found
O	0	(24.54)
C/N/H (mol ratio)	7/2/4	6.98/2.00/8.82

In theory, the repeat unit of ABPBI is  $C_7N_2H_4$ , or the calculated molar ratios of C/N/H 7/2/4. The found element molar ratios of C/N/H are 6.98/2.00/8.82, which is not the same as the calculated molar ratios. In another word, more hydrogen is found in the sample. Because of the hydrophilicity of ABPBI sample, it is reasonable to assume that the excess hydrogen might be from water and the remaining amount, 24.54% ( $24.54\% = 100\% - 52.40\% - 17.50\% - 5.56\%$ ) oxygen from water as well. Thereby, the content of water is 26.61% ( $26.61\% = 24.54\% \times 18/16$ ), the content of hydrogen from water is 3.07% ( $3.07\% = 2 \times 24.54\% / 16$ ) and that of hydrogen from polymer 2.49% ( $2.49\% = 5.56\% - 3.07\%$ ). As a result, the molar ratios of C/N/H assigned to the sample are 6.98/2.00/3.98, which is fairly accordant with theoretical values.

### 4.1.2 Optimisation of reaction conditions for ABPBI synthesis

In this work the method of homogeneous solution polymerisation was used for ABPBI synthesis. The monomer DABA was added into the MSA solution with  $P_2O_5$  as catalyst and after synthesis the obtained ABPBI polymer dissolved in the reaction media and formed a homogeneous solution. Since the condensation reactions take place between bi-functional monomer molecules and small molecules (i.e. water) is the by-product, the ABPBI synthesis is catalogued to condensation polymerisation (or polycondensation) or step-growth polymerisation.

Sufficient molecule weights are essential for a polymer to possess the appropriate mechanical properties. The number-average molecular weight of ABPBI polymer can be predicted by following Carothers' equation<sup>198</sup>

$$\overline{M}_n = \frac{M_{DABA} - pM_{H_2O}}{1 - p} \quad 4-1$$

where  $\overline{M}_n$  is number-average molecular weight of ABPBI,  $M_{DABA}$  is the molecular weight of monomer DABA and  $M_{H_2O}$  the molecular weight of by-product water,  $p$  is conversion of function groups.

Since the by-product water is absorbed by catalyst  $P_2O_5$  and equimolar monomer (i.e. equal numbers of functional groups) is used in this case, the above equation is simplified to

$$\overline{x}_n = \frac{1}{1 - p} \quad 4-2$$

where  $\overline{x}_n$  is the number average degree of polymerisation,  $p$  is the extent of reaction. The parameter  $p$  is related to the kinetics of step-growth polymerisation by the following equation<sup>198</sup>

$$c_0 k' t = \frac{1}{1 - p} - 1 \quad 4-3$$

where  $c_0$  is the concentration of monomer DABA,  $k'$  is the rate constant of catalysed reaction and  $t$  the reaction time.

According to Carothers' equation (4-1, 4-2), to achieve ABPBI polymer with high molecular weight, the main routes are to remove by-product (i.e. water) in time and improve the value of  $p$ . Based on the reaction kinetics equation (4-3), the improvement of the value of  $p$  can be realised through increasing the values of  $c_0$ ,  $k'$  and  $t$ . Therefore, the factors effected on these parameters, i.e. catalyst, reaction temperature, reaction time and purification of monomers were investigated.

The techniques that have been described so far to measure the molecular weights of polymers in solution depend on the equilibrium properties of the polymer solution.<sup>199</sup> It is possible to relate the molecular weight of the polymer to the solution properties by studying the transport properties of polymer solutions (e.g. solution viscosity) through semi-empirical approaches, and the measurements are normally extrapolated to zero concentration where the solution exhibits ideal behaviour. In fact, solution viscosity is widely considered to provide a quick and simple method of determining the molecular weight of a synthetic polymer. Hence, the molecular weights of ABPBI were calculated from the intrinsic viscosities of polymer solutions through the Mark-Houwink equation which were given in detail in the chapter on experimental work.

#### 4.1.2.1 Effect of the amount of catalyst $P_2O_5$ on polymer molecular weight

Synthesis of ABPBI polymer was carried out at 150°C with an atmospheric pressure. The removal of by-product of water was mainly through the absorbance of catalyst  $P_2O_5$  and evaporation at high temperature. The viscosities and molecular weights of polymers obtained with the various amount of  $P_2O_5$  are shown in Figure 4-2.

It can be seen that with the amount of  $P_2O_5$  increased from 2.0 to 4.0g, the intrinsic viscosity of ABPBI increased linearly. Normally, the polycondensation reactions of linear polymers are reversible. However, it is often assumed that, during the polymerisation process, there is no mutual interference of end groups in the same molecule especially when these groups attach to aromatic rings<sup>198</sup>. In other word, the

polycondensation reactions from single bi- or multi-functional monomers (especially aromatic rings contained) are assumed irreversible. Thus the polycondensation reaction of ABPBI is considered as irreversible. Therefore, the elimination of the by-product of water by  $P_2O_5$  to form phosphoric acid drives the step-growth reactions forward resulting in the growth of polymer chains, and the incremental  $P_2O_5$  enhances the eliminating process. The increase of the intrinsic viscosity of the polymer was slowed down when more than 4.0g of  $P_2O_5$  was added. With excess  $P_2O_5$  added, the viscosity of synthesis system increased greatly, leading to the difficulty of movement of growing polymer chains and then reducing the reaction probability between the functional groups, consequently affecting the continuous growth of polymer chains.

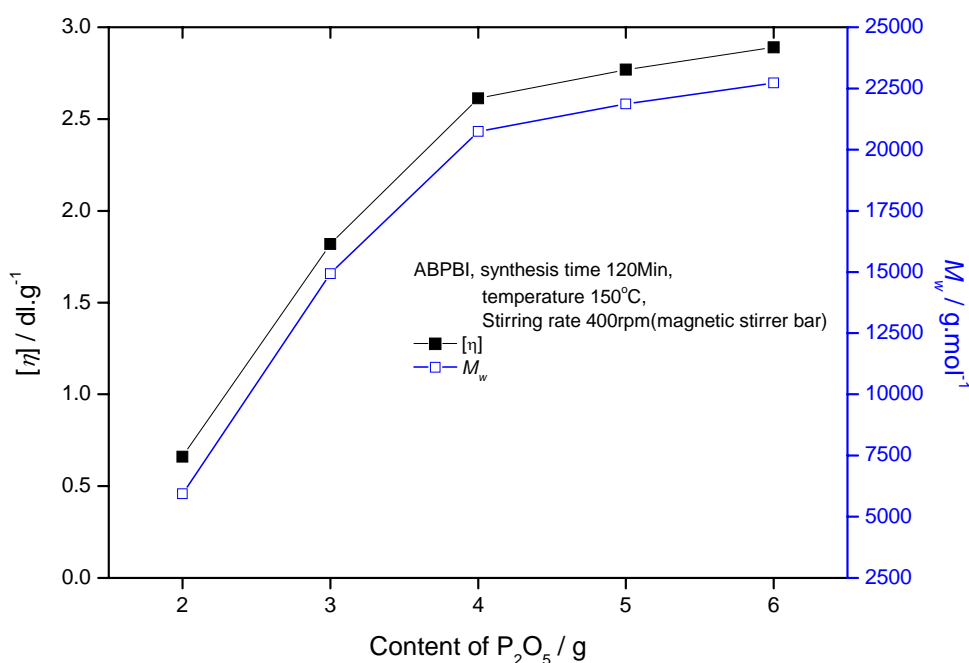


**Figure 4-2 Intrinsic viscosity and molecular weights as a function of the amount of  $P_2O_5$**

#### 4.1.2.2 Effect of the reaction temperature on polymer molecular weight

The intrinsic viscosities and molecular weights of ABPBI polymers which were synthesised at various temperatures were given in Figure 4-3.

From Figure 4-3, the polymer molecular weight increases with the elevated reaction temperatures, i.e. from 3700g/mol at 130°C to 18,010g/mol at 160°C, which is due to

the enhancement of step-growth polymerisation kinetics with the increased reaction temperatures. When the reaction temperature increased from 150 to 160°C, the polymer molecular weight increased slowly but the yield decreased. It was also noticed that the needle for nitrogen outflow was blocked by the volatile matters during polymerisation above 150°C which was probably due to the evaporation of solvent. Because the reaction temperature is close to the boiling point of solvent MSA (158°C), the evaporation of solvent MSA results in a great increase of polymer concentration, leading to a dramatic increase of viscosity thereby hindering the growing reaction of polymer chains.

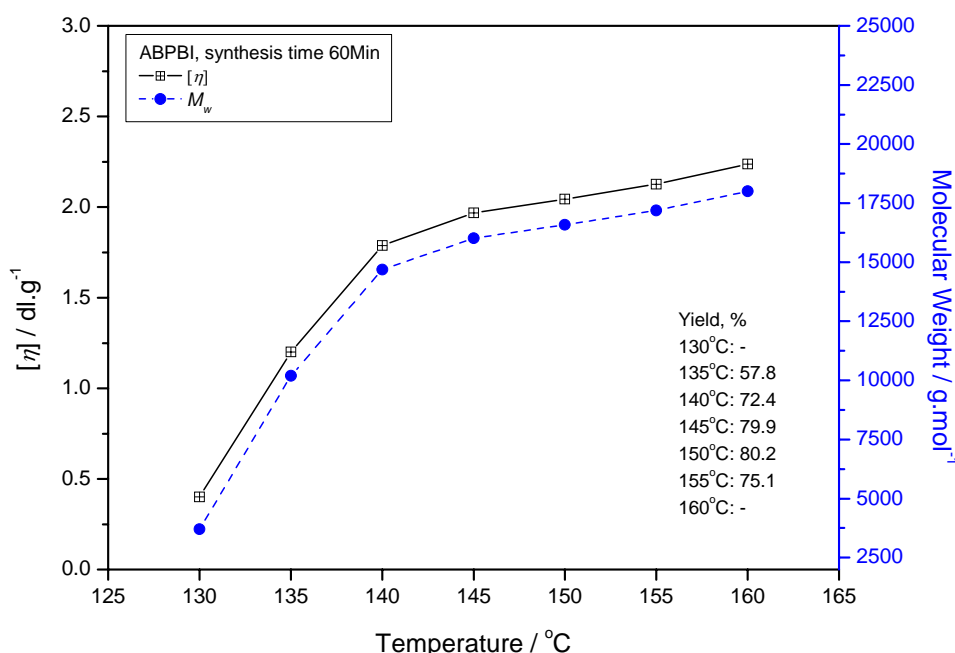


**Figure 4-3 Intrinsic viscosity and molecular weights as a function of reaction temperature**

#### 4.1.2.3 Effect of the reaction time on polymer molecular weight

The intrinsic viscosities and molecular weights of ABPBI synthesised at various reaction times were given in Figure 4-4.

With the increase of reaction time from 20 to 100 minutes, the polymer molecular weight apparently increased from 11,640 to 19,710g/mol. When the reaction time was prolonged to 120 minutes, the molecular weight slightly increased to 20,460g/mol. However, no factual increase of the molecular weight was observed

when the reaction time increased further to 180 minutes, which should be due to viscous solution resulting in the difficulty of the movement of polymer chains thereby hindering their further chain growth reactions.

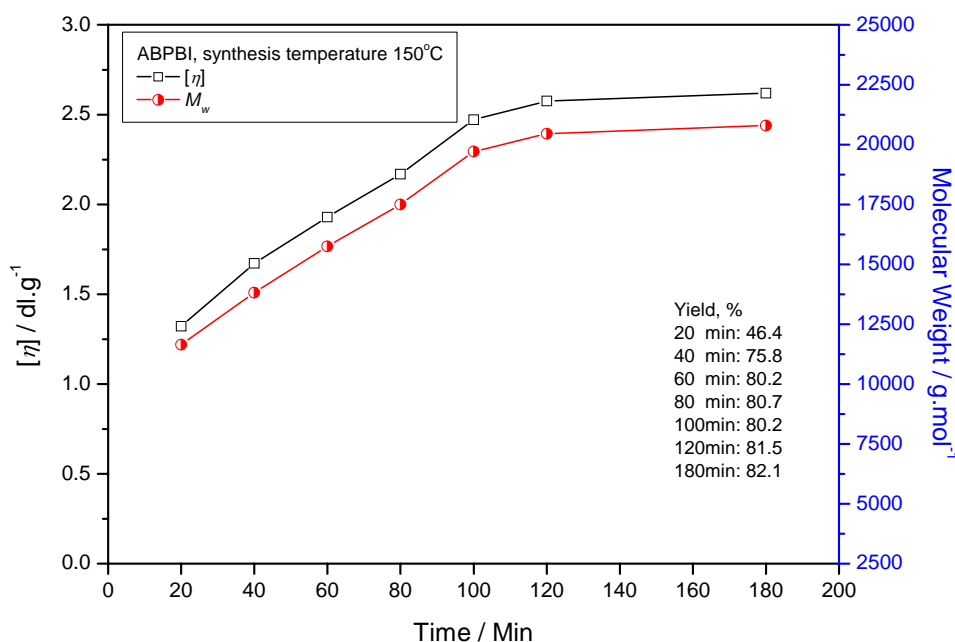


**Figure 4-4 Intrinsic viscosity and molecular weights as a function of reaction time**

#### 4.1.2.4 Effect of stirring conditions on polymer molecular weight

The effect of stirring conditions including stirring method (mechanical and magnetic) and stirring rate (from 100 to 400rpm) was investigated, and the results are shown in Figure 4-5. It can be seen that the molecular weight of ABPBI increased with the increase of the stirring rate and the mechanical stirring method showed more positive effect on the molecular weights of polymers. It was noticed that, during the synthesis process, the produced by-product of water forms bubbles. Stirring helps the formation of bubbles by cavitations and breaks existing bubbles, increasing interfacial area<sup>198</sup>. The increased interfacial area is in favour of the contact between functional groups, resulting in an acceleration of condensation reactions. Also, stirring helps the contact of  $P_2O_5$  and water and the consequent elimination of water, driving the reactions forward.



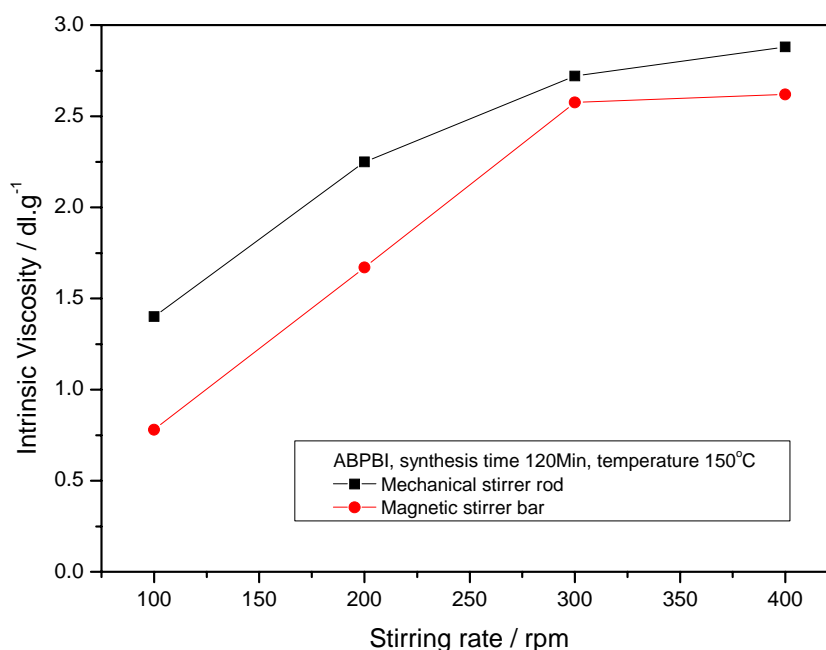


**Figure 4-5 Intrinsic viscosity and molecular weights as a function of string rate**

#### 4.1.2.5 Effect of the monomer concentration on polymer molecular weight

The various amounts of commercial DABA were employed to synthesise ABPBI. The results of intrinsic viscosities and molecular weights were shown in Figure 4-6. It can be seen that both the intrinsic viscosity and molecular weights grew with the increase of monomer concentration and then levelled off at higher concentration. The highest value of molecular weight of 22,660g/mol was obtained from 4.183g of DABA.

According to the reaction kinetics equation 4-3, the relationship between the concentration of monomers and the molecular weight is in direct proportion, indicating that higher molecular weight can be achieved from the increased concentration of monomers. It can also explain how the higher molecular weight was achieved from the purified monomer DABA compared to the same amount of commercial DABA. The commercial and purified DABA were measured by DSC (shown in Figure 4-7). The improved melting point (223.58°C) compared to that of commercial DABA (219.29°C) resulted from higher crystallinity, indicating that the purifier monomer were obtained through the purification process which agrees with the results from literature<sup>28</sup>.

When purified DABA monomer was used, the higher molecular weight polymers were achieved whilst the solution also became more viscous. Due to the viscosity as a limiting factor, the side reactions (i.e. ring-forming reactions) are preferred to occur in the solution with high viscosity<sup>198, 199</sup>. Therefore, polycondensation must be carried out in bulk or with a concentration of solvent as low as possible to avoid the ring-forming reactions. However, considering the ring-forming reactions are usually happened in reversible polycondensation in bulk<sup>198</sup>, and the polycondensation of ABPBI polymer is considered as irreversible as discussed before, the side reactions can be ignored in the synthesis of ABPBI polymer.

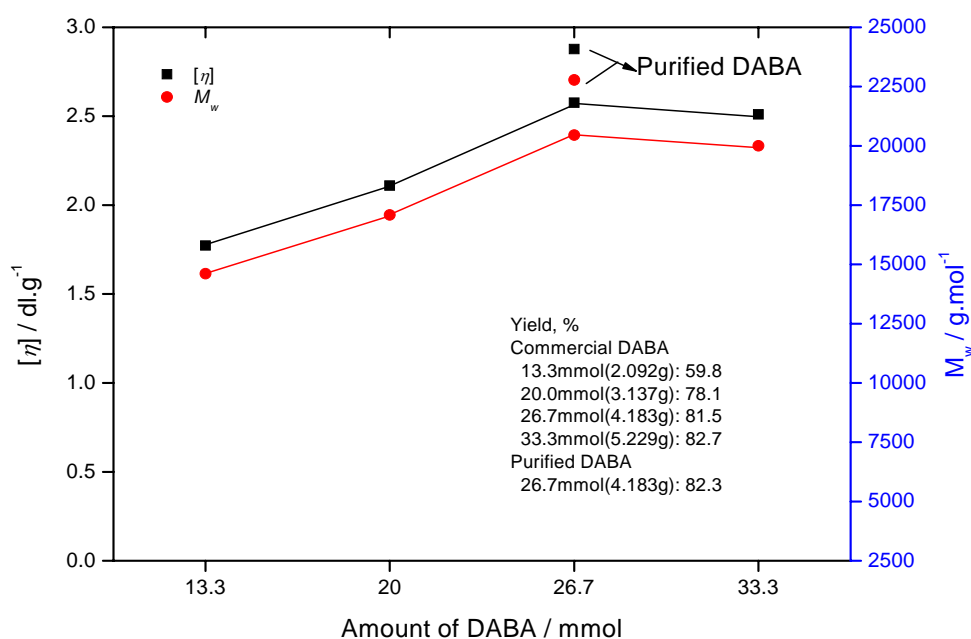


**Figure 4-6 Intrinsic viscosity and molecular weights as a function of amount of DABA**

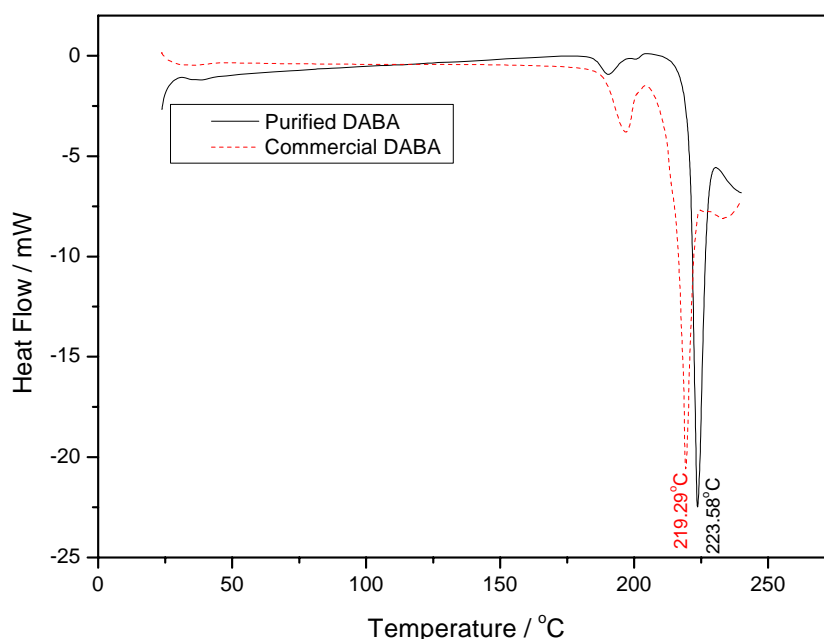


**Figure 4-7 DSC curve of commercial and purified DABA**

#### **4.1.2.6 Effect of the molecular weight on polymer mechanical properties**

The mechanical properties of dry ABPBI samples with different molecular weights were given in Figure 4-8. With the molecular weight increases from 10,200 to 22,660g/mol, the mechanical strength increases from 69.9 to 160.2MPa and Young's modulus from 1.0 to 3.2GPa, respectively. The increase of these values benefits by the contribution of long chains. However, the highest value of elongation (46.2%) is obtained from the sample with lowest molecular weight, which is probably due to the plasticisation of low molecular weight materials. When the molecular weight increases from 14,690g/mol, the elongation values do not change much. This might be explained as follows: the polymer chains do not entangle greatly due to their very rigid-rod molecular structures, resulting in a limited extension of polymer chains during the tensile test.

Based on the above analysis, the optimised reaction conditions are considered as 26.7mmol (4.184g) of monomer DABA synthesised in the reaction media of 40mL of MSA and 4~6.0g of  $P_2O_5$  at 150°C for above 100 minutes with 300~400rpm of the stirring rate. In practice, ABPBI polymer synthesised at these conditions with the

molecular weight of above 18,000g/mol was successful to fabricate high quality membranes for usages.

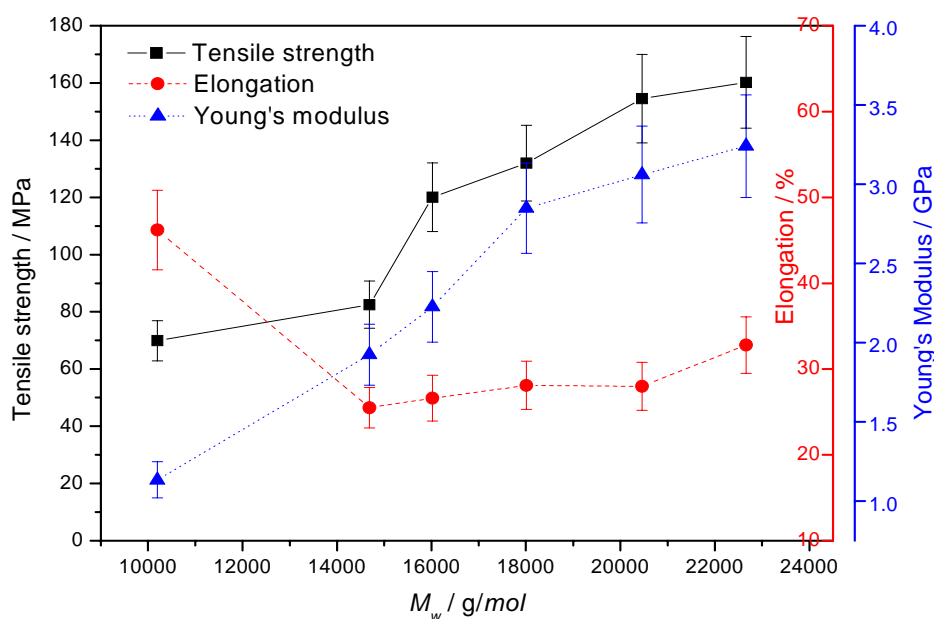


Figure 4-8 Mechanical properties of ABPBI with various molecular weights

### 4.1.3 Properties of ABPBI polymer

#### 4.1.3.1 Morphology of ABPBI polymer

X-ray diffraction techniques are the non-destructive analytical techniques which reveal information about the crystallographic structure, chemical composition, and physical properties of materials and thin films. These are based on observing the scattered intensity of an X-ray beam hitting a sample as a function of incident and scattered angle, polarisation, and wavelength or energy. In these techniques, wide angle X-ray diffraction (WAXD) is often used to determine the crystalline structure of polymers.

The XRD patterns of ABPBI in a wide range of  $2\theta$  degrees ( $5\sim 75^\circ$ ) are illustrated in Figure 4-9. No sharp peak for crystalline nature but a broad peak centred at  $2\theta \approx 11\sim 26^\circ$  is observed, indicating an amorphous structure of ABPBI.<sup>198</sup> The amorphous nature of ABPBI polymer are also considered as the attribution of its unsymmetrical structural unit.<sup>200</sup>

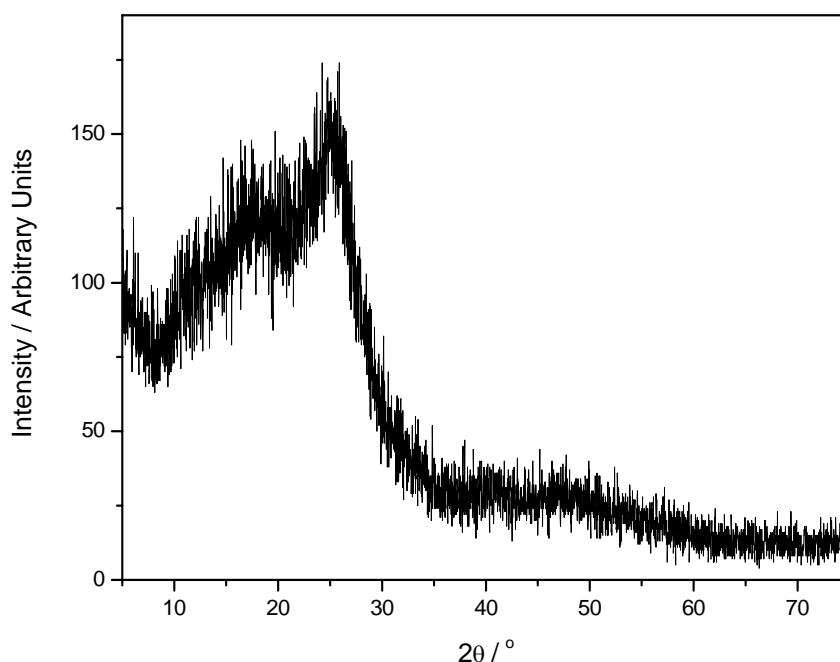


**Figure 4-9 XRD pattern of ABPBI**

#### **4.1.3.2 Thermostability of ABPBI polymer**

The thermostability of ABPBI polymer was measured by DSC, TGA and FTIR spectra from various temperatures, respectively.

The DSC result of ABPBI measured at the range of room temperature to 350°C is shown in Figure 4-10. A broad endothermic peak is observed before around 250°C in the first heating round, which is attributed to the evaporation of free and hydrogen bonded water. As ABPBI polymers tend to bond water through  $\text{N-H}\cdots\text{OH}_2$ . Therefore, water exists in the sample in two forms, i.e. free water and hydrogen bonded water. The elimination of water is confirmed by the disappearance of the peak instead of a horizontal line in the second heating round. It is noteworthy that the approximate peak after about 250°C in the first heating round might be due to the removal of residual low mass materials or oligomers, which is also confirmed to be evaporated before 350°C by the approximate horizontal line in the second heating round.

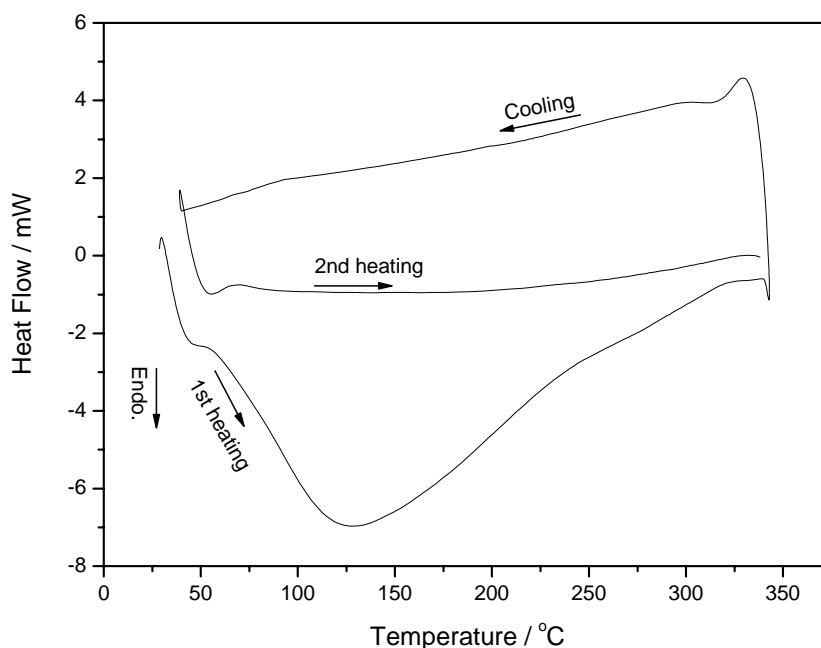


**Figure 4-10 DSC curve of ABPBI**

The thermostability of ABPBI was also traced by an integrated TGA/DSC. From the thermogravimetric (TG) curve in Figure 4-11, three stages of weight loss which are related to three peaks in the derivative thermogravimetric (DTG) curve are observed. The first peak corresponding to about 6.0% of weight loss occurred before 400°C is attributed to the evaporation of water and low molar mass materials or oligomers. The final weight loss after 580°C is assigned to the decomposition of ABPBI backbones.<sup>117</sup> The second stage with about 5.2% of weight loss was found at the range of 470~580°C which should include the decomposition of end groups in ABPBI backbones. However, the content of end groups in the ABPBI backbones should be less than 1.0% since the typical molecular weight of the used ABPBI sample is 18,000g/mol. Therefore, this stage of weight loss must involve in the decomposition and evaporation of low molar mass ABPBI molecules.

The thermal behaviours corresponding to three stages of weight loss were also recorded by relative endothermic and exothermic peaks in the DSC curve (in Figure 4-11). Normally, the rigid-rod polymers do not melt and do not possess a glass transition below the degradation temperature. However, an apparent glass transition is detected starting from around 425°C in the DSC curve which is overlapped by that

of degradation started from 460°C. This  $T_g$  value reflects the results of  $T_g=450^\circ\text{C}$  measured by dynamic mechanical analyser (DMA) from the research literature.<sup>143</sup>

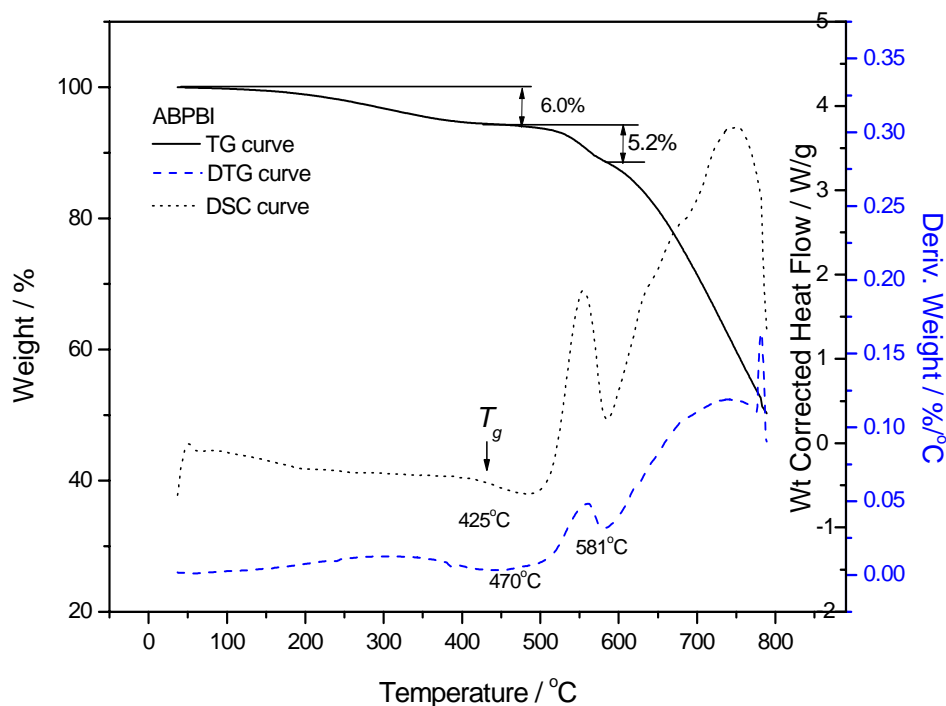


**Figure 4-11 TGA/DSC curves of ABPBI**

The thermal stability of ABPBI is also confirmed by FTIR spectra recorded at various temperatures. Since the mostly typical characteristic of ABPBI is located at the fingerprint region, the FTIR spectra of ABPBI measured at various temperatures at the region  $1700\sim 600\text{cm}^{-1}$  are shown in Figure 4-12.

With the temperature increased from room temperature to  $450^\circ\text{C}$ , the absorption peaks at  $1622$ ,  $1541$ ,  $1281$ ,  $1128$ ,  $984$ ,  $922$ ,  $849$ ,  $810$ ,  $762$  and  $721\text{cm}^{-1}$ , which belong to the typical characteristic of benzimidazole groups, remain unchanged - except for a minor decrease in intensity, indicating that the polymer has a good thermostability at this range of temperature. However, the peak at  $1429\text{cm}^{-1}$  assigned to C-C stretching and the peaks at below  $700\text{cm}^{-1}$  due to C-H and N-H wagging, decreases in intensity with the temperature increased from  $300$  to  $400^\circ\text{C}$  then remains unchanged between  $400$  to  $450^\circ\text{C}$ . This must be due to the elimination of low molar mass materials or oligomers resulting in the decrease of those peaks in intensity.

It is worthy to mention that, the water content measured from elemental analysis and TGA is different, which is due to the different exposed time of samples at the atmosphere. The water or moisture absorptibilities of ABPBI sample will be also discussed in the next chapter (i.e. section 5.1.2).

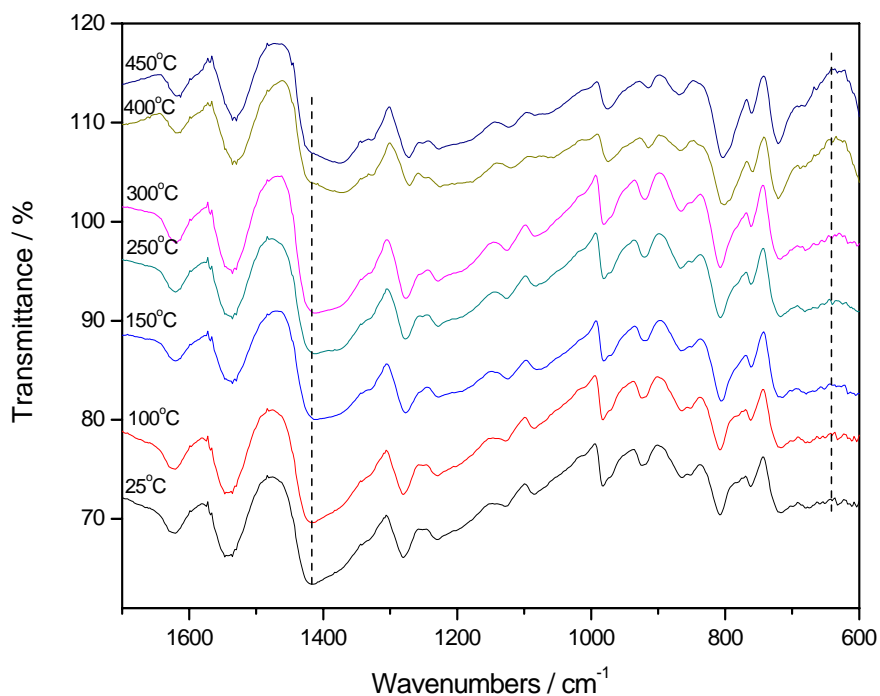


**Figure 4-12 FTIR spectra of ABPBI at various temperatures (curves have been vertically offset for clarity)**



## 4.2 Synthesis and Characterisation of PBI and copolymers

### 4.2.1 Chemical structures of PBI and copolymers

#### 4.2.1.1 FTIR analysis of PBI polymer

The chemical reactions involved in the polymerisation of PBI are as follows

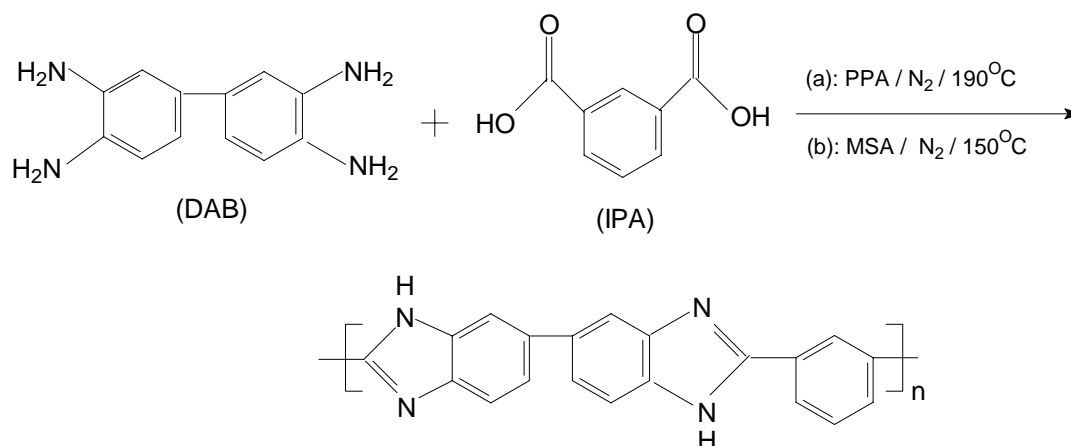


**Figure 4-13** Synthesis of PBI in (a): PPA; (b): MSA / P<sub>2</sub>O<sub>5</sub>

It is noteworthy that the synthesis of PBI carried out in MSA medium has not been reported so far. Compared to the structure of ABPBI, there is a meta-substituted benzene ring in a PBI repeat unit. Moreover, two imidazole groups link together to a biphenyl in a PBI repeat unit. Therefore, the vibrations of these unique characteristic bands recorded by infra-red spectra are expected to occur. The IR spectra of monomer DAB, monomer IPA and PBI synthesis in MSA and PPA solution respectively, are shown in Figure 4-14.

The curves of Figure 4-14a and Figure 4-14b represent the IR spectra of monomer DAB and monomer IPA, respectively; Figure 4-14c is the IR spectrum of PBI synthesis in MSA solution. The main band assignments of the benzimidazole group are similar to that of ABPBI. The absorbance centred at about 3602cm<sup>-1</sup> is due to residual bonded water, thereby the band at 3145cm<sup>-1</sup> assigned to hydrogen bonded N-H stretching becomes very broad and is partially overlapped by that of C-H stretching. The characteristic ring vibration due to conjugation between imidazole ring and benzene ring is observed at 1590cm<sup>-1</sup>.<sup>105</sup> The enhanced absorbance at 801cm<sup>-1</sup> is due to the overlay from C-H out-of-plane bending of the three adjacent

hydrogens in the substituted benzene ring<sup>105</sup>. The peak shoulder at  $1410\text{cm}^{-1}$  assigned to the stretching mode of C-C in biphenyl is observed. The observed typical characteristic of benzimidazole groups indicates PBI was successfully synthesised in MSA, which is also confirmed by the similar IR spectrum synthesised in PPA medium since PPA is widely used as the reaction medium for the synthesis of PBI as discussed before.

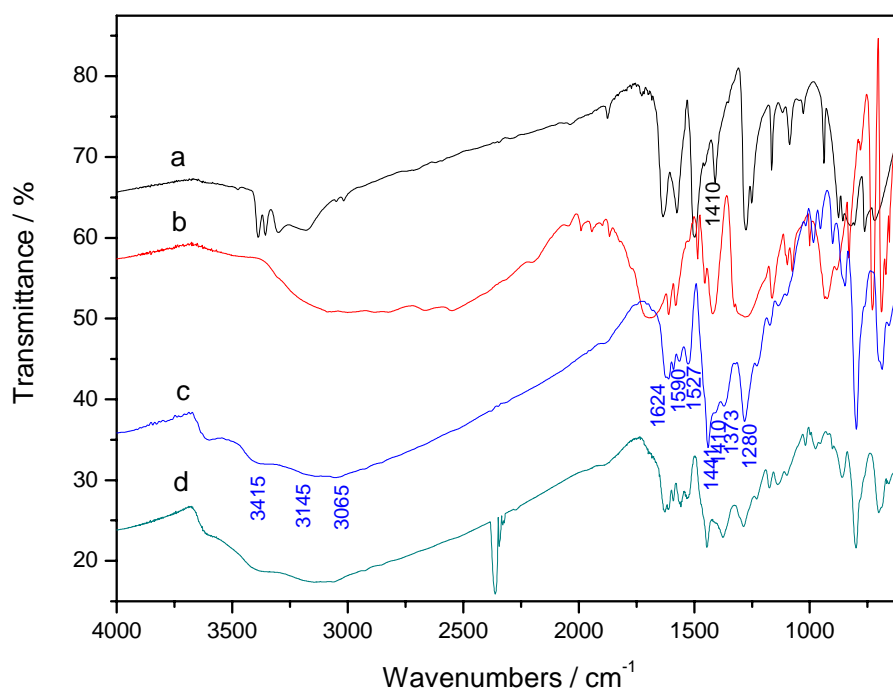


**Figure 4-14** FTIR spectra of (a) DAB, (b) IPA, (c)PBI synthesised in MSA and (d) PBI synthesised in PPA.

#### 4.2.1.2 FTIR analysis of copolymers of ABPBI and PBI

The copolymers of ABPBI and PBI with various ratios of monomers were synthesised in MSA medium (shown in Figure 4-15). The vibration frequency shifts in the FTIR spectra of these polymers resulted from the gradually increased content of benzene rings. Accordingly, the decreased content of benzimidazole rings from ABPBI via copolymers of ABPBI and PBI to PBI is expected to occur.

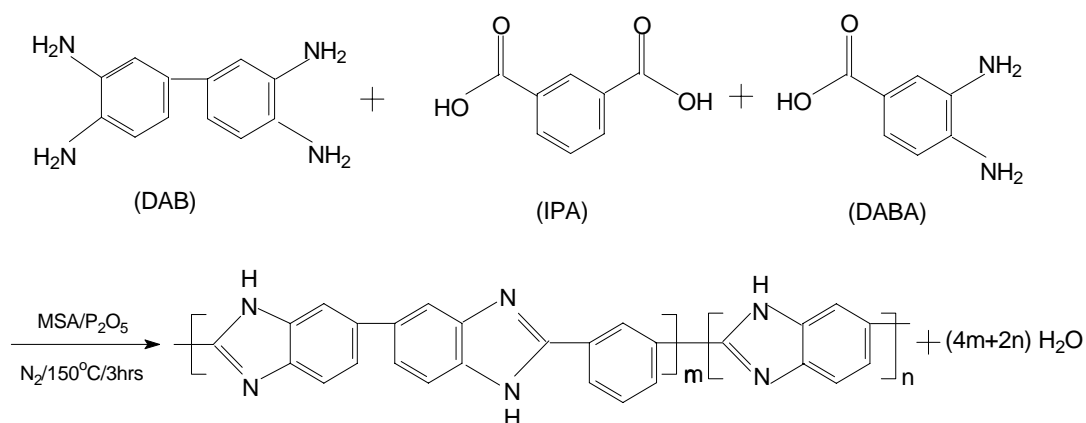


**Figure 4-15 Synthesis of copolymers of ABPBI and PBI**

The band assignments for copolymers (mol ratio of monomers for ABPBI and PBI: 3:1, 1:1 and 3:1, respectively) in the region  $4000\sim 2000\text{cm}^{-1}$  are the same as those for ABPBI and PBI. Therefore, more details will be discussed in the fingerprint region, i.e.  $1650\sim 600\text{cm}^{-1}$  (shown in Figure 4-16) (spectra of ABPBI and PBI are as shown in the references).

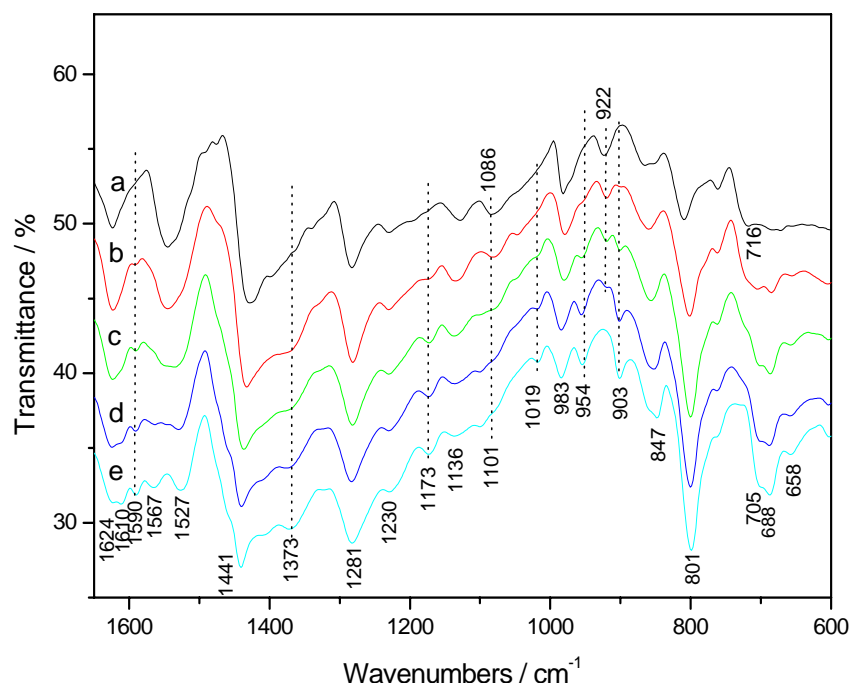


**Figure 4-16 FTIR spectra of copolymers of ABPBI and PBI: (b) copolymer with 3:1 of mol ratio of DABA/DAB, (c) copolymer with 1:1 of mol ratio of DABA/DAB, (d) copolymer with 1:3 of mol ratio of DABA/DAB (a. ABPBI and e. PBI are as references).**

The peak at  $1610\text{cm}^{-1}$  is assigned to  $\text{C}=\text{C}/\text{C}=\text{N}$  stretching in PBI<sup>105</sup>, which is also observed in the spectra of copolymers but absent in that of ABPBI, indicating it must belong to  $\text{C}=\text{C}$  stretching in the meta-substituted benzene ring. As described above, the band of  $1590\text{cm}^{-1}$  is due to the conjugation between benzene and imidazole rings in PBI. In fact, there are two different benzene rings connected to an imidazole ring, i.e. benzene in heterocyclic benzimidazole and meta-substituted benzene ring. Therefore, the nearby band of  $1567\text{cm}^{-1}$  might be due to the conjugation between the substituted benzene and imidazole. In the spectrum of ABPBI, the band at  $1541\text{cm}^{-1}$  is assigned to benzimidazole in-plane ring vibration. Because of the conjugation of the substituted benzene in PBI and copolymers, this peak shifts with a reduction of the peak intensity from  $1541$  to  $1527\text{cm}^{-1}$  from ABPBI via copolymers to PBI.

The band at  $1372\text{cm}^{-1}$  is attributed to C-H in-plane bending of three adjacent hydrogens in monomers<sup>196</sup>, therefore it appears in PBI and copolymers but is absent in ABPBI. It can be seen that C-H out-of-plane bending of three adjacent hydrogens in substituted benzene ring is located at  $801\text{cm}^{-1}$ , and increases in intensity with the increased content of substituted benzene rings. The peak at  $1173\text{cm}^{-1}$  in PBI assigned to C-H in-plane bending<sup>105</sup> is observed in copolymers but absent in ABPBI, thus it must belong to C-H in-plane bending of single hydrogen in substituted benzene. The bands at  $1019$  and  $983\text{cm}^{-1}$  were assigned to benzene ring in-plane bending in the literatures<sup>105, 197</sup>. Due to the absence of  $1019\text{cm}^{-1}$  in ABPBI, the band of  $1019\text{cm}^{-1}$  can be identified to substituted benzene in-plane bending whilst  $983\text{cm}^{-1}$  the benzene in benzimidazole in-plane ring bending. The peak at  $922\text{cm}^{-1}$  in ABPBI assigned to C-H out-of-plane bending of single hydrogen in benzene decreased intensively in copolymers and disappeared in PBI, whereas the new peaks at  $954$  and  $903\text{cm}^{-1}$  rose in copolymers and PBI. Therefore, they must be due to C-H out-of-plane bending of single hydrogen in two different benzene rings. Musto et al.,<sup>105</sup> Cordes<sup>197</sup> and Asensio et al.<sup>153</sup> also assigned  $762$  and  $703\text{cm}^{-1}$  to heterocyclic ring vibration and  $688\text{cm}^{-1}$  to C-H out-of-plane bending of 3,4-disubstituted biphenyl, respectively. The band assignments for ABPBI, PBI and their copolymers are summed up in Table 4-2.

**Table 4-2 Assignments of ABPBI infra-red spectra**

<b>Wavenumbers (cm<sup>-1</sup>)</b>			<b>Assignment</b>
<b>ABPBI</b>	<b>Copolymers</b>	<b>PBI</b>	
3415	3415	3415	Free non-hydrogen bonded N-H stretching
3145	3145	3145	Self-associated or hydrogen bonded N-H stretching
3065	3065	3065	C-H stretching
1622	1624	1624	C=C/C=N stretching
	1610	1610	C=C stretching in substituted benzene
	1590	1590	Ring vibration of conjugation between imidazole and benzene
	1567	1567	Ring vibration of conjugation between imidazole and benzene
1541	1527	1527	In-plane ring vibration of benzimidazole
1429	1441	1441	C-C stretching/Benzimidazole in-plane deformation
	1410	1410	C-C stretching in biphenyl
	1373	1373	In-pane C-H deformation of three hydrogens in substituted benzene
1281	1281	1281	Breathing mode of the imidazole ring
1230	1230	1230	In-pane C-H deformation of single hydrogen in benzimidazole
	1173	1173	In-pane C-H deformation of single hydrogen in benzene
1128	1136	1136	N-H in-plane bending
1086	1101	1101	In-pane C-H deformation of two adjacent H in benzimidazole
984	983	983	Benzene ring vibration
	954	954	Out-of-plane C-H bending of single hydrogen in benzene
922	922		Out-of-plane C-H bending of single hydrogen in benzimidazole
	903	903	Out-of-plane C-H bending of single hydrogen in benzimidazole
849	847	847	Out-of-plane C-H bending of two adjacent hydrogens in benzene
810	801	801	Benzimidazole in-plane vibration/Out-of-plane C-H bending of three adjacent hydrogens in substituted benzene
762	762	762	In-plane ring bending
721	688	688	C-H out-of-plane bending
	658	658	Out-of-plane C-H bending of benzimidazole

#### 4.2.1.3 Elemental analysis of PBI

The elemental analysis results of PBI synthesised in PPA and MSA/P<sub>2</sub>O<sub>5</sub> respectively, are given in Table 4-3. It can be seen that the found C/N molar ratios agree with the calculated molar ratio of C/N. The excessive amount of H should come from water. For example, in the sample synthesised from MSA, the amount of O is assumed to be 12.41% (=100%-67.47%-4.73%-15.39%). Thereby, H from water is 1.55% (=2×12.41%/16) and H in polymer equals to 3.18% (3.18%=4.73%-1.55%). Finally, the found molar ratios of C/N/H are 20.5/11.6/4.0, are close to the calculated ratios (20/12/4).

**Table 4-3 Element contents of PBI synthesised in PPA and MSA respectively**

Element	Calculated	Measured contents, wt%	
	contents, wt%	Synthesised in PPA	Synthesised in MSA/P <sub>2</sub> O <sub>5</sub>
C	78.18	61.86%	67.47%
H	3.52	4.42%	4.73%
N	18.24	13.84%	15.39%
P	0	Not found	Not found
S	0	Not found	Not found
C:H:N	20 : 12 : 4	20.9 : 17.9 : 4.0	20.5 : 17.2 : 4.0
(mol/mol)			

#### 4.2.1.4 Elemental analysis of copolymers of ABPBI and PBI

The elemental analysis results for the copolymers of ABPBI and PBI are listed in Table 4-4. From the chemical formula of the copolymer,  $(C_{20}N_4H_{12})_m(C_7N_2H_4)_n$ , the molar ratios of C/N/H are calculated by

$$C / N / H = (7n + 20m) / (2n + 4m) / (4n + 12m) \quad 4-4$$

where,  $n$  and  $m$  was the numbers of the repeat unit of ABPBI and PBI respectively.

In Table 4-4, the calculated molecular ratios of C/N/H are based on the assumption that all monomers were converted to the polymers. Amongst the measured results, the excessive hydrogen was attributed to the absorbed moisture as discussed above. Interestingly, the found amount of C was higher than that calculated in all samples.

In other words, the content of PBI fraction was higher than that of ABPBI fraction in those samples.

**Table 4-4 Element contents of copolymers synthesised in MSA**

Elements	Molar ratio of monomer DABA/DAB		
	3:1	1:1	1:3
C, wt%	69.42	64.56	66.50
N, wt%	19.34	15.78	15.72
H, wt%	4.33	4.51	4.72
P, wt%	Not found	Not found	Not found
S, wt%	Not found	Not found	Not found
Calculated C/N/H (mol/mol)	4.10/1.00/2.40	4.50/1.00/2.67	4.79/1.00/2.86
Found C/N/H (mol/mol)	4.19/1.00/3.14	4.77/1.00/4.00	4.93/1.00/4.21
ABPBI/PBI fraction (mol/mol)	2.35/1	0.36/1	0.32/1

It is clear that copolymerisation is a much more complex process than polymerisation using a single monomer. For example, in a copolymerisation, using two monomers, the tendency of each type of monomer to add to the growing chain may be different. This can lead to a variation of copolymer composition during the reaction even when equimolar amounts of two types of monomer are used initially. This phenomenon is known as composition drift and is a common feature in copolymerisation reactions<sup>199</sup>. In this work, the molar ratio of PBI fraction versus ABPBI fraction in each copolymer sample was found higher than original molar ratio of monomer DAB versus DABA, indicating a higher reactivity of monomer DAB and IPA than that of DABA, or a higher reaction rate or faster reaction kinetic of PBI self-propagation than that of ABPBI. The faster reaction kinetic could introduce more PBI fractions at the reaction beginning period. With the reactions continued, the reaction mixtures become viscous, which could limit the movement of active centres in monomer and growing chain units thereby hinder the chain propagation reactions. As a result, with 3:1, 1:1 and 1:3 of molar ratios of monomer DABA and DAB feeding, the molar ratios of ABPBI and PBI fractions in copolymers were 2.35/1, 0.36/1 and 0.32/1, respectively.

## 4.2.2 Properties of PBI and copolymers

### 4.2.2.1 Morphology of PBI and copolymers

The XRD patterns of PBI and copolymers of ABPBI and PBI in a range of  $5\sim 75^\circ$  are shown in Figure 4-17.

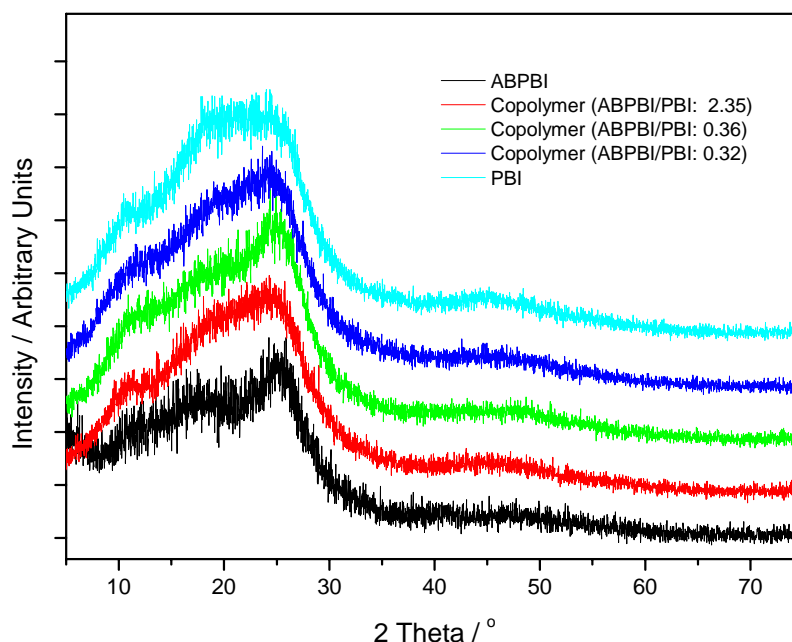


**Figure 4-17** XRD patterns of ABPBI, PBI and their copolymers

The broad peaks centred at  $2\theta \approx 18\sim 26^\circ$  resulted from a convolution of amorphous and crystalline scattering. The amorphous nature is attributed to their unsymmetrical structural units<sup>200</sup>. Compared to that of PBI and copolymers, the appearance of a narrower peak at  $2\theta = 26^\circ$  in the XRD pattern of ABPBI results from a more ordered regularity of ABPBI backbones since no substituted benzene group exists in the ABPBI repeat unit. This narrower peak in ABPBI is also regarded as a characteristic of quasi-amorphous<sup>142</sup> or semicrystalline<sup>201</sup> structure. The peak with  $2\theta = 26^\circ$  is corresponding to a d spacing between two parallel benzimidazole chains of  $3.3\text{\AA}$ , which was due to the stacking of ABPBI chains<sup>202</sup>. In general, the narrowing down peak at  $18\sim 26^\circ$  from PBI via copolymers to ABPBI, indicates a tendency of crystallinity with the increasing of ABPBI repeat units.



#### 4.2.2.2 Thermostability of PBI and copolymers

The thermostabilities of PBI and copolymers were measured by DSC and TGA, respectively.

The DSC curves of PBI and copolymers measured under 350°C are given in Figure 4-18. Similar to the analysis of ABPBI, the elimination of free and hydrogen bonded water is responsible for the very broad endothermic peak that appeared under 250°C in each sample when initially heating up to 350°C. The absorbed water is also confirmed by the second heating round in the curve of PBI sample (in Figure 4-18a).

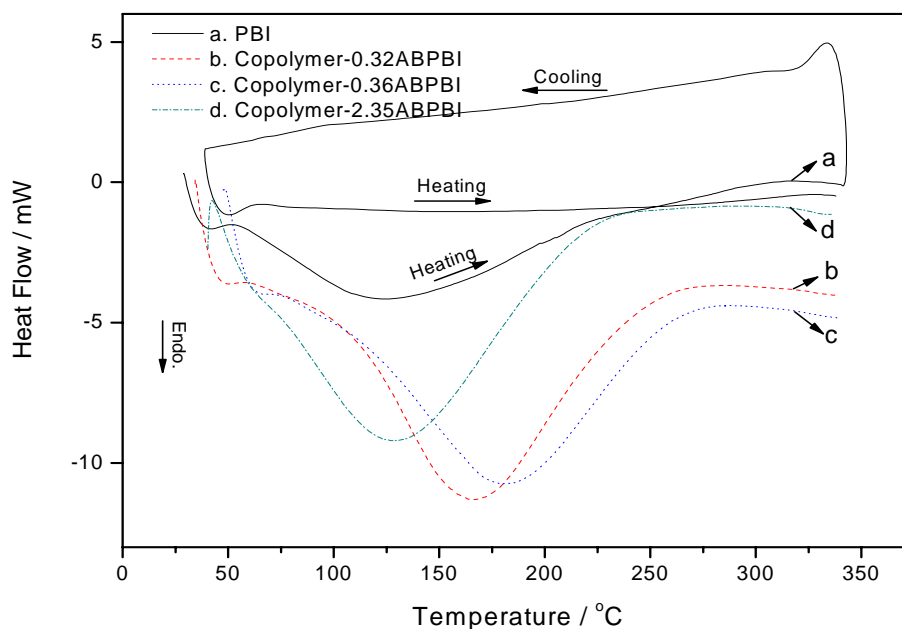


**Figure 4-18 DSC curves of PBI and copolymers operated under 350°C**

The TG and DTG curves of PBI and copolymers are shown in Figure 4-19d1-a1. Similar to ABPBI, three apparent weight-loss stages during the whole thermogravimetric process are observed in each sample. In DTG curves, the first peak appeared before 350°C is due to the release of water and low mass residuals; the second small peak observed between 350~420°C in PBI (Figure 4-19d2), copolymer-0.32ABPBI (Figure 4-19c2), copolymer-0.36ABPBI (Figure 4-19b2) and between 350~480°C in copolymer-2.35ABPBI (Figure 4-19a2) is attributed to the

decomposition of end groups of polymer chains. The subsequently appeared peak owes to the decomposition of polymer backbones. Compared to PBI and copolymer-0.32ABPBI and copolymer-0.36ABPBI, the lagged peak due to the decomposition of polymer chains appeared in the DTG curve and lower weight loss appeared in the TG curve of the copolymer-2.35ABPBI sample indicates that the copolymer with dominated ABPBI fractions possesses a higher thermal stability. The relative low thermostability of PBI and copolymers with dominated PBI fractions result from the decomposition starting at the broken of C-C in biphenyl groups<sup>117</sup>.

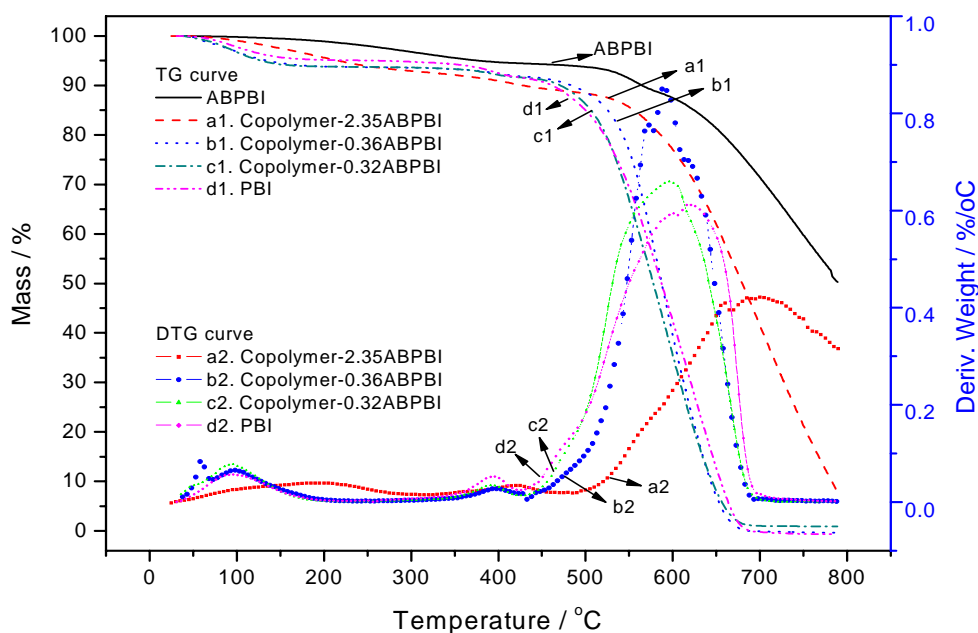


**Figure 4-19 TGA curves of PBI and copolymers of ABPBI and PBI**

#### 4.2.2.3 Viscosities of PBI and copolymers

The viscosities of PBI and copolymers were measured by an Ubbelohde viscometer and the molecular weights of PBI were calculated through the Mark-Houwink equation. In Figure 4-20, the obtained PBI has an intrinsic viscosity of 0.222dl/g with molecular weight ( $M_w$ ) of 24,330g/mol; the viscosities of copolymers slightly increase with the increased molar ratio of ABPBI/PBI fractions from 0.32/1 to 2.35/1. Compared to ABPBI composed of all benzimidazole groups, PBI and copolymers owns more flexible structures due to existed meta-substituted benzene ring groups and biphenyl groups, resulting in the apparent lower viscosity values of PBI and copolymers compared to 2.575dl/g of viscosity (20,460g/mol of  $M_w$ ) of ABPBI.

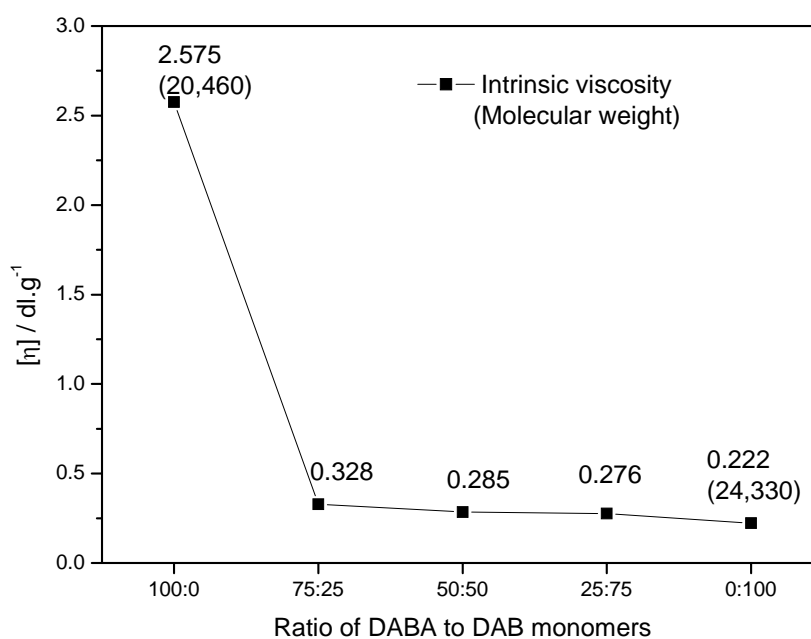
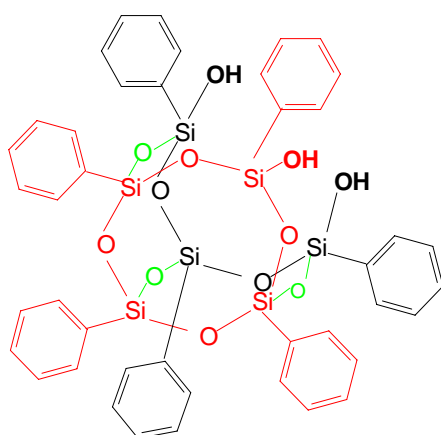


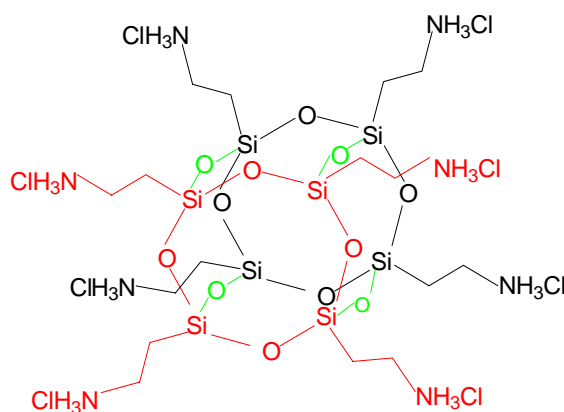
Figure 4-20 Intrinsic viscosities of PBI and copolymers

### 4.3 Synthesis of ABPBI/Polyhedral oligomeric silsequioxanes Composites (ABPBI/POSS)

TriSilanolPhenyl POSS (SO-POSS) and OctaAmmonium POSS (AM-POSS) were employed in order to synthesise ABPBI/POSS composites in-situ, respectively. As shown in Figure 4-21a, SO-POSS possesses a hybrid inorganic-organic three dimensional structures which contain three hydroxide groups and seven phenyl groups linked with the silicon-oxygen open cage framework, containing the formula  $C_{42}H_{38}O_{12}Si_7$ . AM-POSS contains an inorganic siloxane core linked by eight trialkylammonium chloride ( $-CH_2CH_2CH_2NH_3Cl$ ) groups possessing the formula  $C_{24}H_{72}Cl_8N_8O_{12}Si_8$  (shown in Figure 4-21b).



a. TriSilanolPhenyl POSS-SO1458



b. OctaAmmonium POSS-AM0285

**Figure 4-21 Structures of a. SO-POSS and b. AM-POSS**

#### 4.3.1 Synthesis of ABPBI/SO-POSS composites

##### 4.3.1.1 FTIR analysis of ABPBI/SO-POSS composite

The structures of SO-POSS particle and 1, 3 and 5% SO-POSS hybrid ABPBI composite (ABPBI/1SO, ABPBI/3SO and ABPBI/5SO) were recorded by FTIR spectra, respectively. The FTIR spectra of SO-POSS powder and ABPBI/5SO composite are shown in Figure 4-22. In the FTIR spectrum of SO-POSS powder (Figure 4-22a), the broad peak centred at  $3250\text{cm}^{-1}$  and the sharp peak at  $887\text{cm}^{-1}$  are assigned to the stretching and bending modes of Si-OH; the range of  $3100\sim3000\text{cm}^{-1}$

are related to stretching of C-H in a phenyl group whilst  $696$  and  $746\text{cm}^{-1}$  to the C-H out-of-plane deformations; the region of  $2000\text{-}1600\text{cm}^{-1}$  are typically characteristic of a benzene ring whilst the peak at  $1595\text{cm}^{-1}$  is attributed to the vibration of C=C in a benzene ring linked with a POSS core; the peak at  $1432\text{cm}^{-1}$  is due to the stretching of -Si-phenyl groups<sup>203</sup>; the typical characteristic of Si-O cage and network are located at the broad peak from  $1160$  to  $1060\text{cm}^{-1}$ . The in-plane and out-of-plane stretching of Si-O-Si groups are observed at  $1028$  and  $640\text{cm}^{-1}$ , respectively.<sup>185, 204</sup>

In the FTIR spectrum of in-situ synthesised ABPBI/5SO composite, the typical characteristic of benzimidazole group appears indicating ABPBI was existed. The observed characteristic peaks of Si-O cage and network at  $1140$  and  $1040\text{cm}^{-1}$  and the peak at  $696\text{cm}^{-1}$  attributed to C-H out-of-plane bending of five adjacent hydrogens in benzene ring, indicate that SO-POSS cage structure is retained in the composite. The increased intensity of the peak at  $1622\text{cm}^{-1}$  assigned to the C=C stretching is due to the overlay of phenyl groups from SO-POSS.

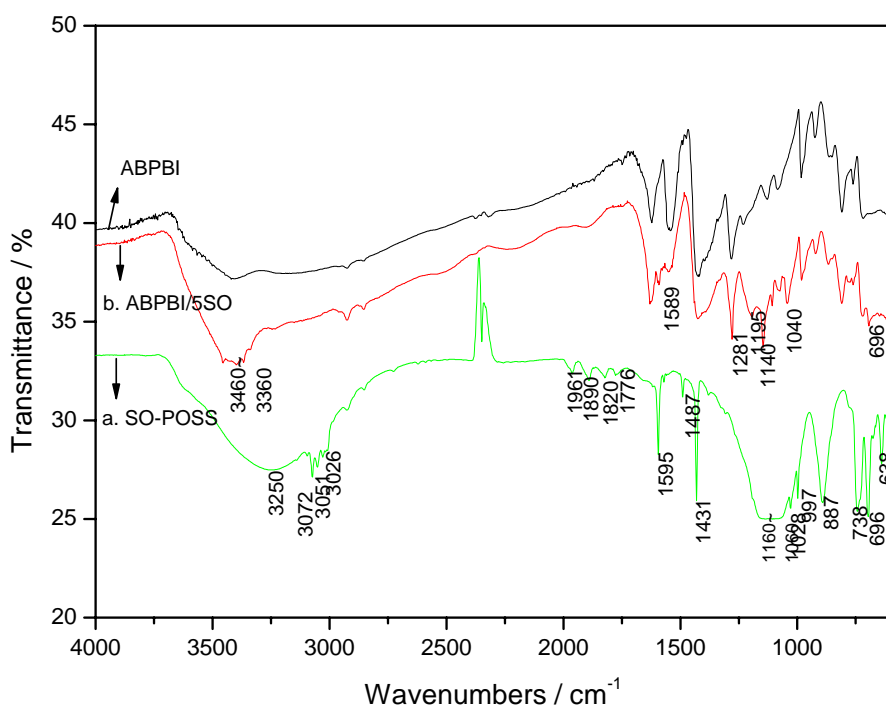
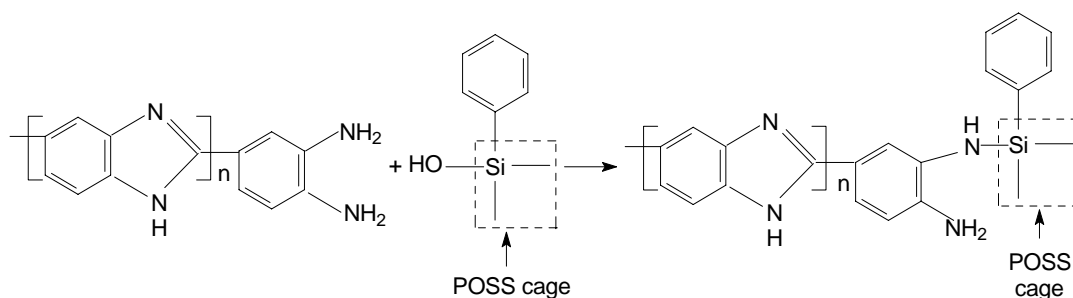


Figure 4-22 FTIR spectra of a. SO-POSS powder and b. ABPBI/5SO composite

It is assumed that a condensation reaction has happened between silanol (Si-OH) group in SO-POSS and amine group (NH<sub>2</sub>) in DABA monomer (shown in Figure 4-23). Based on this assumption, an unreacted primary amine group in the end of ABPBI polymer chain and -Si-NH- groups are expected in the FTIR spectrum. In Figure 4-22b, the increased broad peak at 3460-3360cm<sup>-1</sup> in intensity compared to that of ABPBI should be attributed to the vibration of hydrogen bonded NH<sub>2</sub> groups. Also, the vibration of -Si-NH- group is observed at 1195cm<sup>-1</sup> and the stretching of -NH in Si-NH- group is overlapped by the N-H stretching in benzimidazole groups at the range of 3200-3000cm<sup>-1</sup>.<sup>205</sup> In addition, the peak at 1281cm<sup>-1</sup> assigned to the breathing mode of imidazole intensively increases compared to that in ABPBI, which might be due to the effect from the grafted POSS.



**Figure 4-23** Condensation reaction between SO-POSS and DABA monomer

#### 4.3.1.2 Thermogravimetric analysis of ABPBI/SO-POSS composite

The thermostability of SO-POSS powder and ABPBI/SO-POSS composites were performed by the integrated TGA/DSC measurement.

In Figure 4-24, SO-POSS powder displays two weight loss stages which are related to two different degradation mechanisms, which are shown in Figure 4-25. The first stage of weight loss (around 2.0% of weight loss) takes place at the range of 190~250°C. Since SO-POSS can react with hydroxyl-terminated alkylsilicone resin by thermally induced SiOH-SiOH condensation<sup>179, 206</sup>, the Si-OH groups of SO-POSS can themselves cause condensation<sup>179</sup>. Therefore, it is due to the condensation reaction which occurred between two close Si-OH groups, resulting in 1.93% of calculated weight loss which is approximate to 2.0% of found value. This condensation reaction is also recorded by a small endothermic peak appearing in the relative DSC curve (Figure 4-24c). The second stage of weight loss which started at

about 350°C and ended at about 730°C is due to the oxygenolysis of grafted phenyl groups and decomposition of POSS cores. Finally 47.0% of SiO<sub>2</sub> remains in the crucible. The total 51.0% of found weight loss at second stage agrees well with the calculated value (52.81%).

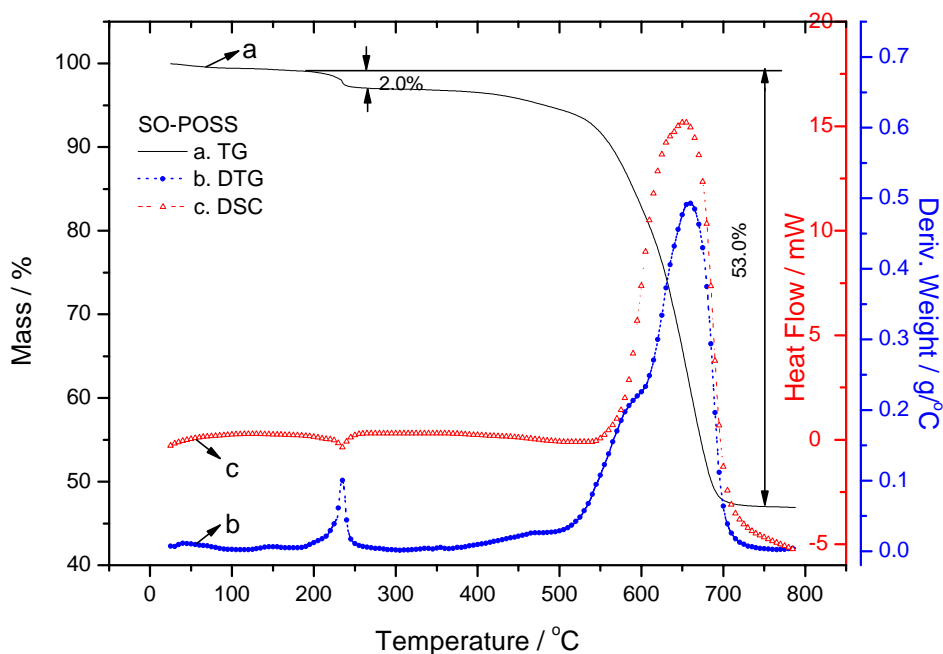


Figure 4-24 TGA curves of SO-POSS powder

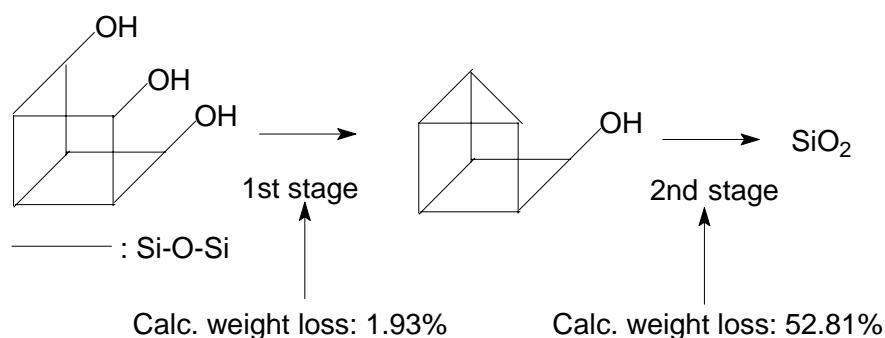
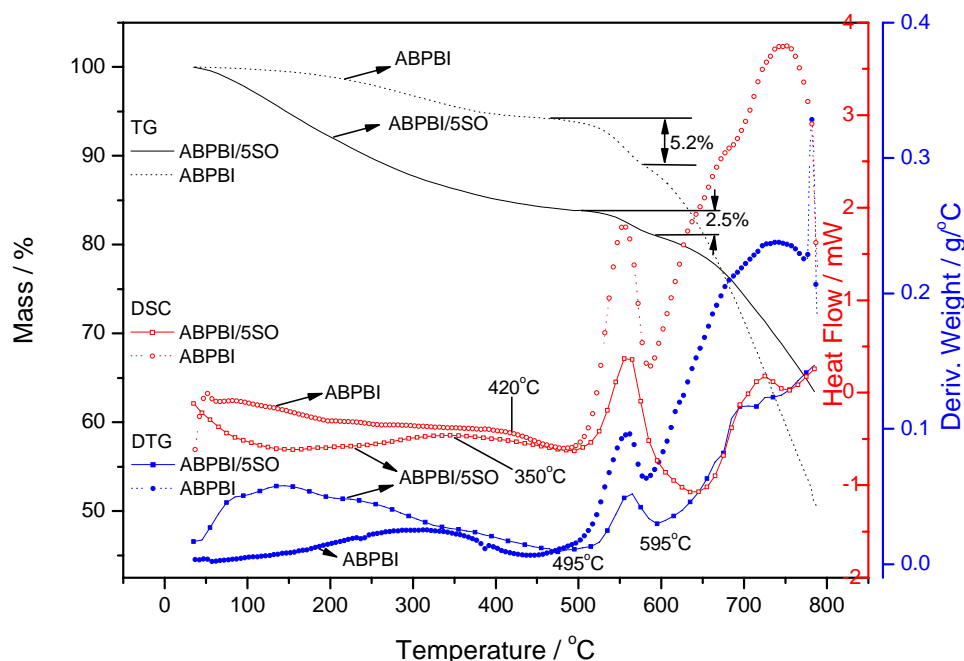


Figure 4-25 SO-POSS degradation mechanisms

ABPBI/5SO-POSS was taken as an example to investigate the thermostability of ABPBI/SO-POSS composites. The TG, DTG and DSC curves are shown in Figure 4-26 (pristine ABPBI as the reference). The weight loss before 200°C is due to the release of free and hydrogen bonded water; the weight loss at the range of 200~480°C owns to the continuous elimination of hydrogen bonded water, low mass

residuals and initial degradation of SO-POSS; the apparent oxygenolysis of SO-POSS particles and end groups of ABPBI polymer occurred after about 480°C; the decomposition of polymer chains is observed after 595°C.



**Figure 4-26** Thermostability of ABPBI/5SO-POSS composite

Compared to ABPBI, the broader and greater peak before 200°C in the DTG curve of the composite indicates that the composite owns enhanced hygroscopicity. The greater weight loss occurred between 250~350°C which should be mainly attributed to the elimination of the low mass residuals indicates the addition of SO-POSS particles affects the polycondensation reaction resulting in more low mass polymers. The value of 2.5% which is mainly due to the elimination of end groups of ABPBI polymer is much lower than that of 5.2% in pristine ABPBI polymer. This is probably due to the condensation reaction happening between the silanol group in SO-POSS and end groups ( $\text{NH}_2$ ) in ABPBI polymer, resulting in the reduction of end groups therefore improving its thermostability. The increased thermostability of composite also is confirmed by both the delayed starting temperatures (495°C and 595°C) of decomposition of end group and polymer chain respectively, and the slower decomposition rate that occurred in the decomposition course of polymer chains compared to that of ABPBI. It is noteworthy that a slight shift started at 350°C



in the DSC curve might indicate the glass transition of composite. Because of the impregnation of POSS particles, the distance between ABPBI polymer chains is enlarged, which is in favour of their free movements, resulting in the reduction of glass transition temperature compared to 420°C of pristine ABPBI.

### 4.3.2 Synthesis of ABPBI/AM-POSS composites

#### 4.3.2.1 FTIR analysis of ABPBI/AM-POSS composite

The FTIR spectra of AM-POSS and 5% AM-POSS hybrid ABPBI composite (ABPBI/5AM) is shown in Figure 4-27.

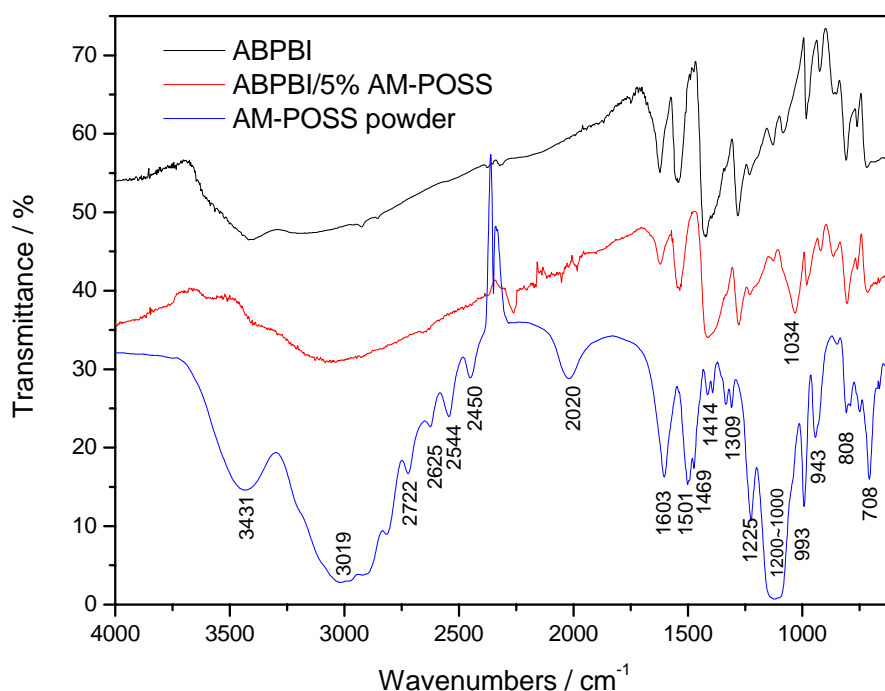


**Figure 4-27 FTIR spectra of AM-POSS and ABPBI/AM-POSS composite**

In the spectrum of AM-POSS powder, the peaks located at the range of 3400~2000cm<sup>-1</sup> are the typical characteristic of AM-POSS salt structure  $((Si_8O_{12})-(CH_2)_3-NH_3^+Cl^-)^{205}$ ; vibration of NH groups are located at 3431 and 1603cm<sup>-1</sup>; C-C stretching is observed at 1414cm<sup>-1</sup>; CH<sub>2</sub> in-plane and out-of-plane bending is seen at 1469 and 744cm<sup>-1</sup> respectively, whilst Si-CH<sub>2</sub>- stretching is at

$1225\text{cm}^{-1}$ ; the broad peak from  $1200\text{--}1000\text{cm}^{-1}$  is the characteristic of AM-POSS cage and network; the in-plane bending of Si-O-Si is performed at  $993\text{cm}^{-1}$ .<sup>205, 207</sup> In the FTIR spectra of ABPBI/5AM composite, the peak at  $1034\text{cm}^{-1}$  assigned to the POSS cage can be seen and the absorbance of moisture is found at around  $3600\text{cm}^{-1}$ , whilst other typical peaks of AM-POSS are overlapped by that of ABPBI polymer. In practice, the great hygroscopicity of ABPBI/5AM composite sample was also confirmed by the attached droplet when it was placed at ambient atmosphere for dozens of minutes.

#### 4.3.2.2 TGA/DSC of ABPBI/AM-POSS composite

The thermal stability of AM-POSS and ABPBI/5AM-POSS composite membranes were investigated by TGA/DSC (Figure 4-28 and Figure 4-30).

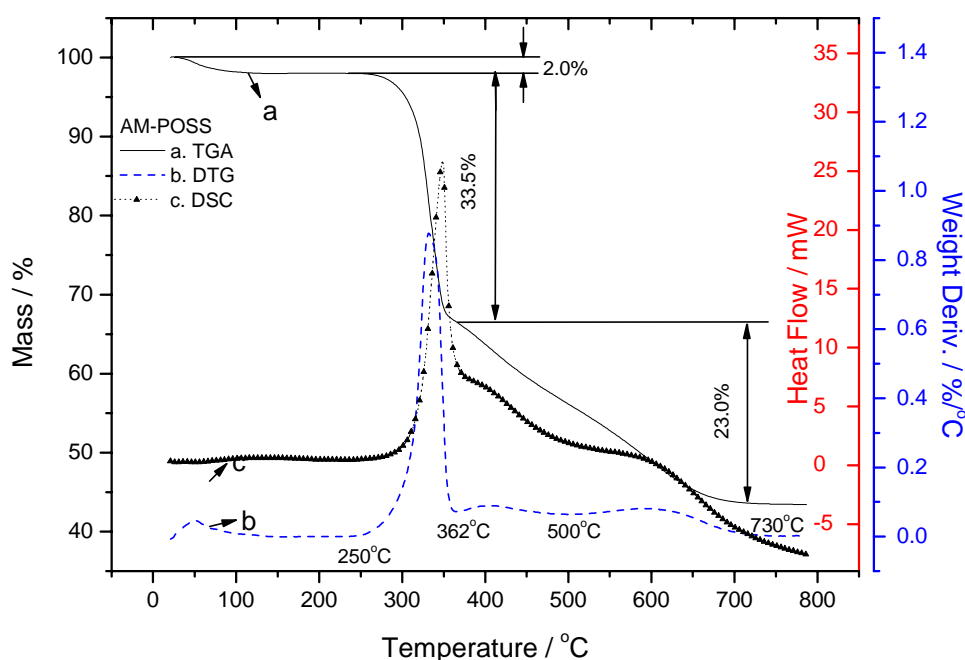


**Figure 4-28** TGA/DSC curves of AM-POSS

In Figure 4-28, four apparent peaks appearing in the DTG curve are assigned to different mechanisms of weight loss. Obviously, the weight loss before  $100^{\circ}\text{C}$  is due to the release of absorbed moisture. The other three stages of weight loss are attributed to the degradation of AM-POSS particles. The degradation mechanisms are tentatively explained as shown in Figure 4-29. The first stage located at the range

of 250~362°C is assigned to the oxygenolysis of terminal C-C bonds at the end groups of grafted organic side chains, resulting in 33.5% of weight loss which is roughly close to 35.1% of the calculated results. The second stage of weight loss, which can be identified by a hump, appeared between 362 and 500°C in the relative DTG curve, is due to the continuous oxidation of left terminal C-C bonds of organic side chains. The final stage of weight loss resulted from the decomposition of AM-POSS cage. The result is that, 43.5% of SiO<sub>2</sub> is found in the crucible. 23.0% of found weight loss covering the second and third stage is roughly in accord with the calculated value (24.6%). It is worth mentioning that the error between the calculated and found value should be due to the unstable oxidation intermediate products. In other words, the oxidations of terminal C-C bonds will product aldehyde which can be further oxidised to carboxylic acid. The calculated value is based on aldehydes regarded as the oxidation products, therefore higher than the found results.

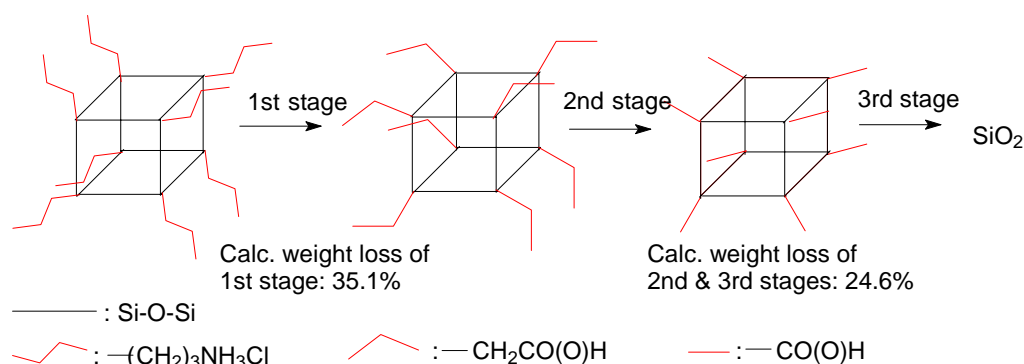


**Figure 4-29 Degradation mechanisms of AM-POSS**

Figure 4-30 traces the thermogravimetric course of ABPBI/5AM-POSS composite. The rapid evaporation of surface water is confirmed by the peak which appeared before 100°C in the DTG curve. Also this big peak results in the overlap of the subsequently appearing broad peak attributed to the continue release of hydrogen bonded water. A rapid weight loss occurred approximately between 250 and 350°C, which is identified by a dramatic step appearing at that temperature range. This should be mainly attributed to the degradation of AM-POSS. The weight loss after 500°C<sup>185</sup> is due to the decomposition of ABPBI polymer and OA-POSS cores.

Compared to ABPBI, ABPBI/AM-POSS composite owns a stronger hygroscopicity due to the introduction of hydrophilic AM-POSS particles. In practice, droplets

condensed on the surface of ABPBI/5AM-POSS composite were observed when exposed at the atmosphere for hours. It is also confirmed by the endothermic peak appeared in DTG curve before 100°C. An apparent glass transition started from 325°C is observed in the DSC curve of AM-POSS composite. The lower  $T_g$  (325°C) than that of ABPBI is attributed to the embedded AM-POSS between polymer chains, enlarging the these chain gaps thereby reducing  $T_g$ . The reduction of  $T_g$  can also be explained by the plasticisation since the POSS particles are distributed between polymer chains.

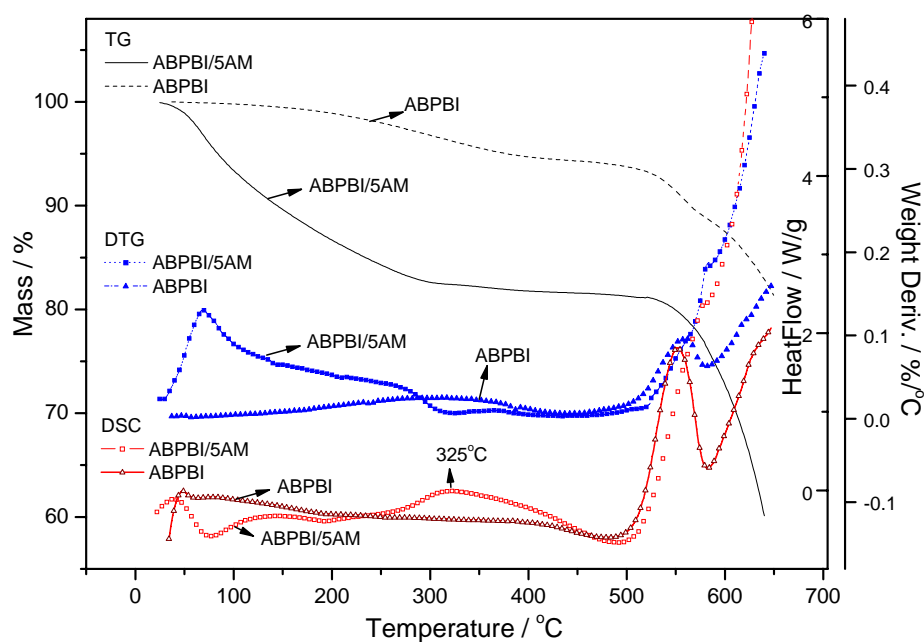


Figure 4-30 TGA/DTG/DSC curves of ABPBI and ABPBI/5%OA-POSS membranes

# **Chapter 5 RESULTS AND DISCUSSION:**

## **FABRICATION AND CHARACTERISATION**

### **OF ABPBI AND ABPBI/POSS**

#### **COMPOSITE MEMBRANES**

#### ***5.1 Phosphoric Acid and Water Absorbility of ABPBI and its Composite Membranes***

##### **5.1.1 Comparison of $H_3PO_4$ absorbility of ABPBI and ABPBI/POSS composite membranes**

In order to determine the phosphoric acid (PA) absorbility,  $H_3PO_4$  uptakes of ABPBI and ABPBI/POSS composite membranes were measured from the weights before and after being doped in phosphoric acid solution with various concentrations. The results are given in Figure 5-1 and Figure 5-3, for ABPBI and ABPBI/POSS composite membranes, respectively.

As shown in Figure 5-1,  $H_3PO_4$  uptake of ABPBI increases from 42.7% to 90.6% with the increase of  $H_3PO_4$  concentrations from 2 to 12M. When doped in  $H_3PO_4$  with higher concentration (i.e. 14M), the ABPBI membrane started to dissolve in the solvent. The  $H_3PO_4$  absorption of ABPBI membrane is mainly due to the hydrogen bonding or ionic reaction between alkaline imidazole group and  $H_3PO_4$  molecule. Theoretically, the degree of saturation of acid absorption or the maximum degree of protonation is 1.0, in another word, one imidazole groups can react with one  $H_3PO_4$  molecule. Thus, the excessive  $H_3PO_4$  should exist in the free form when  $H_3PO_4$  uptake is over 84.5% which equal to 1.0 of doping level.<sup>130</sup> The free  $H_3PO_4$  was confirmed by FTIR spectra from literatures<sup>130</sup> and also in this work which will be discussed in the later section. The dissolution of ABPBI membrane in high concentrated  $H_3PO_4$  solution was also reported by other researchers<sup>28, 127</sup>. In fact, high-concentration  $H_3PO_4$  tends to become polyphosphoric acid (PPA) which is used

widely as a solvent for ABPBI polymer. However, the values of  $\text{H}_3\text{PO}_4$  uptake were lower than that reported. For example, Asensio et al.<sup>127</sup> reported that around 3.0  $\text{H}_3\text{PO}_4$  molecules were absorbed by per repeat unit of ABPBI when the membrane was doped in 10M PA, whilst, in this research about 1.0  $\text{H}_3\text{PO}_4$  molecule was found probably due to different rinsing procedure were used. The excessive free  $\text{H}_3\text{PO}_4$  should and can be rinsed out by rinsing with a plenty of water. In fact, the excessive free  $\text{H}_3\text{PO}_4$  was believed to be the main reason leading to  $\text{H}_3\text{PO}_4$  leaching during a PEMFC operation<sup>11</sup>. In addition, the thickness of a membrane might be another factor. The membrane with 20 $\mu\text{m}$  of thickness was used by Asensio et al.<sup>127</sup>, whilst the thickness in the range of 70 to 190 $\mu\text{m}$  was employed in this work.

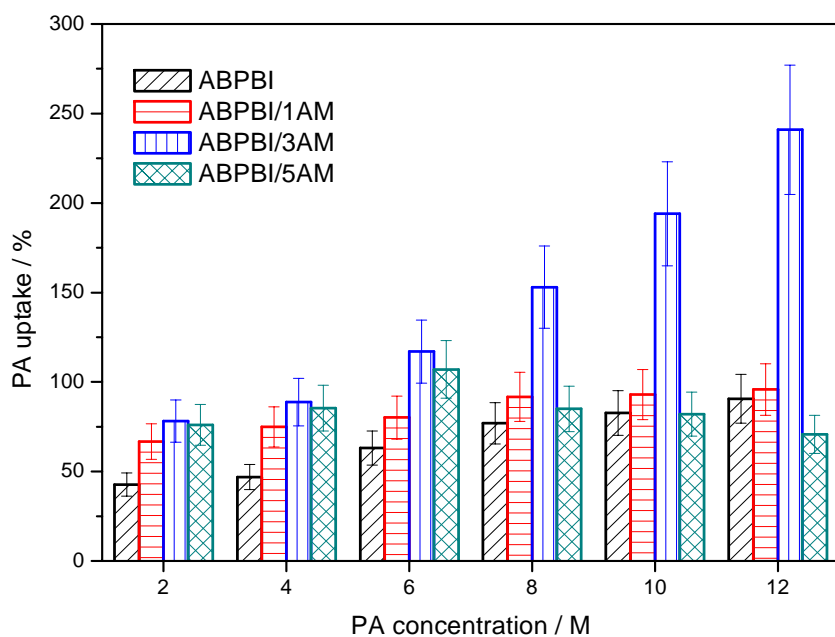


**Figure 5-1 Comparison of  $\text{H}_3\text{PO}_4$  uptake of ABPBI and ABPBI/AM**

$\text{H}_3\text{PO}_4$  uptakes for ABPBI/AM-POSS composite membranes are also shown in Figure 5-1. With the increase of  $\text{H}_3\text{PO}_4$  concentration from 2M to 12M,  $\text{H}_3\text{PO}_4$  uptake of ABPBI/1AM increased from 66.7 to 95.8%. Similar level of the increase in  $\text{H}_3\text{PO}_4$  uptake for ABPBI/5AM was observed. The most significant increase in  $\text{H}_3\text{PO}_4$  uptake was obtained for ABPBI/3AM composite membrane, in which, the maximum value of 241% was achieved in 12M  $\text{H}_3\text{PO}_4$ .

Compared to that of ABPBI, the increased  $\text{H}_3\text{PO}_4$  uptake for composite membranes should be mainly contributed to the embedding of AM-POSS particles in the polymer matrix. Figure 5-2 illustrates the  $\text{H}_3\text{PO}_4$  absorption in an ABPBI/AM composite membrane, in which, four different forms (form A~D) of  $\text{H}_3\text{PO}_4$  absorption are proposed. Imidazole groups in polymer backbones (form A) and amino groups in AM-POSS (form B) can be protonated by  $\text{H}_3\text{PO}_4$  and hydrophilic POSS core can absorb  $\text{H}_3\text{PO}_4$  via hydrogen bond (form C), resulting in the increase of  $\text{H}_3\text{PO}_4$  uptake. Additionally, one free  $\text{H}_3\text{PO}_4$  molecule can be hydrogen bonded by another  $\text{H}_3\text{PO}_4$  molecule (form D) when more free  $\text{H}_3\text{PO}_4$  molecules exist in. Also, the dispersed POSS particles enlarge the distance of polymer chains thereby providing more space for  $\text{H}_3\text{PO}_4$  molecules diffusing through the polymer chains and then reacting with functional groups in polymer chains and POSS particles.

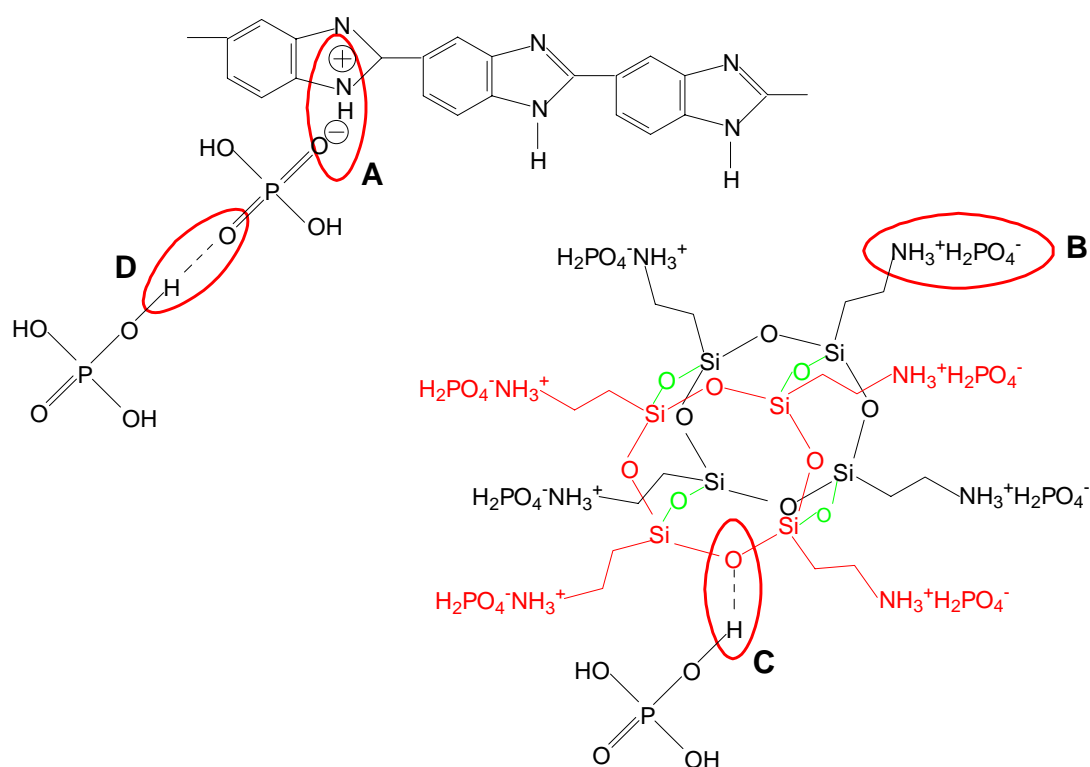


**Figure 5-2 Models proposed for  $\text{H}_3\text{PO}_4$  absorption in an ABPBI/AM composite membrane**

The slightly increased  $\text{H}_3\text{PO}_4$  uptake from 8M~12M  $\text{H}_3\text{PO}_4$  doped ABPBI/1AM sample (91.7% at 8M, 93.0% at 10M and 95.8% at 12M PA) might be due to a degree of saturation of  $\text{H}_3\text{PO}_4$  absorption reached. The significant increased  $\text{H}_3\text{PO}_4$  uptake in ABPBI/3AM sample indicates a fine dispersion of AM-POSS in the polymer matrix leading to the maximum surface area of POSS therefore resulting in

the maximum acid absorption. Compared to that of ABPBI/3AM, however, the value of  $\text{H}_3\text{PO}_4$  uptake of ABPBI/5AM was lower; additionally, it decreased with the  $\text{H}_3\text{PO}_4$  concentration increasing from 6M to 12M. The reduction of  $\text{H}_3\text{PO}_4$  uptake of ABPBI/5AM probably is due to the agglomeration of POSS, which results in the reduction of the surface area and the hindrance of interaction between the POSS and  $\text{H}_3\text{PO}_4$  molecules.

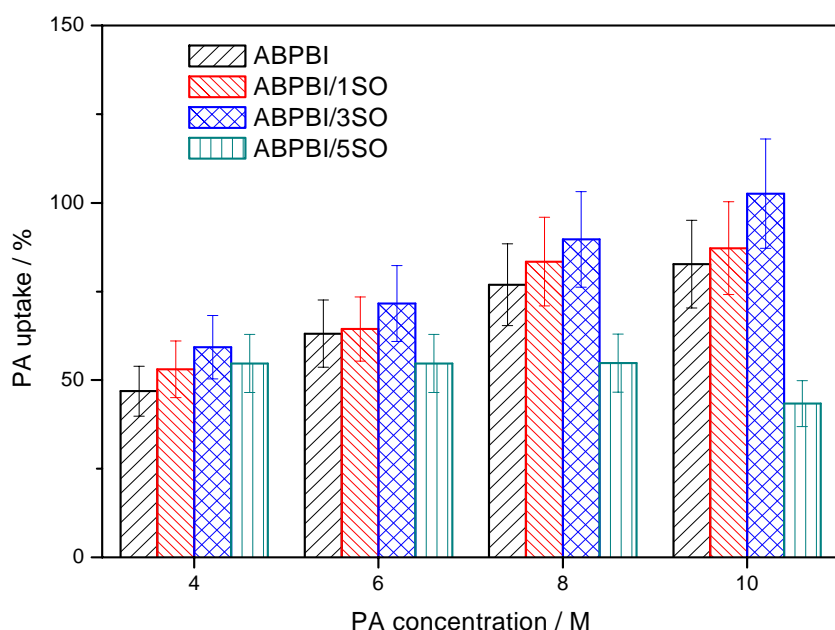


**Figure 5-3 Comparison of  $\text{H}_3\text{PO}_4$  uptake of ABPBI and ABPBI/SO-POSS**

The values of  $\text{H}_3\text{PO}_4$  uptake for ABPBI/SO composite samples are given in Figure 5-3. With the increase of  $\text{H}_3\text{PO}_4$  concentration from 4M to 10M,  $\text{H}_3\text{PO}_4$  uptake of ABPBI/1SO and ABPBI/3SO increases from 53.1 and 59.3 to 87.2% and 102.6%, respectively. The increased  $\text{H}_3\text{PO}_4$  uptake from ABPBI/1SO and ABPBI/3SO must be due to hydrogen bonding between SO-POSS cores and  $\text{H}_3\text{PO}_4$  molecules resulting in more  $\text{H}_3\text{PO}_4$  molecules being absorbed and the reduced values of  $\text{H}_3\text{PO}_4$  uptake from ABPBI/5SO should result from the agglomeration of POSS particles which is the same as that of ABPBI/5AM. It is also noticed that,  $\text{H}_3\text{PO}_4$  uptake of ABPBI/SO, in general, was lower than that of ABPBI/AM, which could be explained by the different chemical structures of two kinds of POSS. Since there are eight amino groups linked with a POSS core in AM-POSS particle but seven phenyl groups



linked with a POSS core in a SO-POSS particle, a  $\text{H}_3\text{PO}_4$  molecule can be linked with an amino group of AM-POSS via ionic bonds but not with the phenyl group of SO-POSS, resulting in the great difference of  $\text{H}_3\text{PO}_4$  uptake. Compared to that of pristine ABPBI and ABPBI/5AM composite doped in high-concentration  $\text{H}_3\text{PO}_4$  solution, the largely reduced  $\text{H}_3\text{PO}_4$  uptake of ABPBI/5SO in the same condition was mainly contributed to the agglomeration of SO-POSS particles.

### 5.1.2 Investigation of water absorptivity of undoped membranes

The results of water absorption of undoped membranes including Nafion 117 membrane are given in Figure 5-4.

As shown in Figure 5-4, the water uptake of a saturated ABPBI (31.6%) decreased with the exposure time in the air and reached to 23.2% at the equilibrium condition; whilst the dry ABPBI membrane was found to absorb the moisture from air, which reaches to 15.4% (1.0 mole ratio, or 1.0mol water in per repeat unit) in 50 hours and 18.08% (1.2 mole ratio) in 7 days at the ambient atmosphere. As a reference, the effect of the moisture on the water absorption of Nafion 117 was also investigated. The results showed that the water absorption of the saturated Nafion 117 membrane (30.3%) reduced to 7.1% at the ambient atmosphere in 120 minutes and no moisture absorption was observed for a dry Nafion membrane in this period.

The better water retaining ability and moisture absorptivity for the ABPBI membrane are attributed to hydrogen bonding formed between hydrophilic imidazole groups in polymer chains and water molecules. Although the hydrogen bonding form could occur between the hydrophilic sulphonic acid group and water molecule, the dominated hydrophobic PTFE main chains ( $\sim 87\text{mol}\%$ ) expels the water molecules from the membrane resulting in the rapid evaporation of water and hindering the moisture absorbing<sup>208, 209</sup>.

It can also be seen that the water absorptivity would be hugely affected by the humidity. In this work, the water uptake was evaluated in two conditions: a saturated and ambient atmosphere (i.e. 100%R.H. and 45~55%R.H.) respectively. Table 5-1 lists the water uptake values of no  $\text{H}_3\text{PO}_4$  doped ABPBI, ABPBI/POSS composites and Nafion membranes at those conditions.

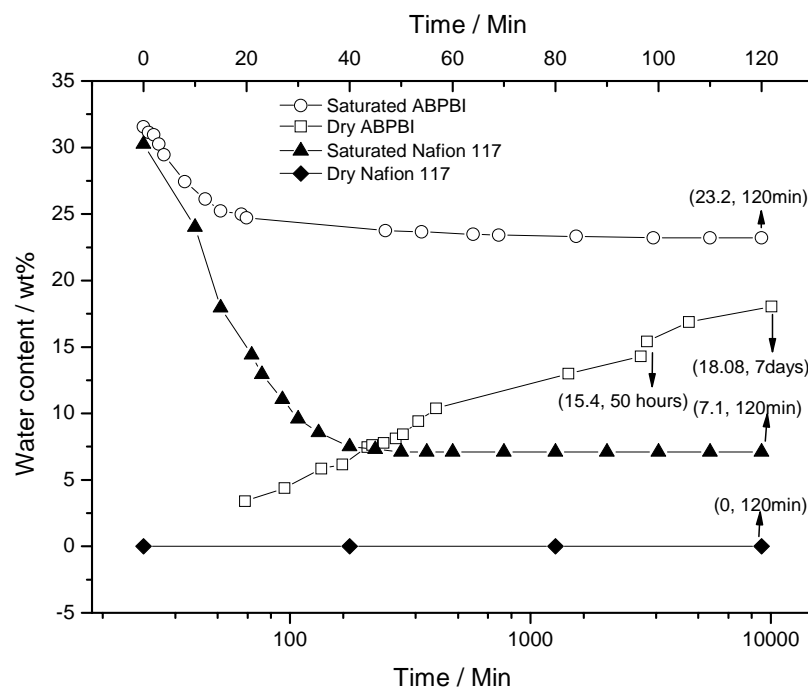


Figure 5-4 Water and moisture absorbilities of ABPBI and Nafion 117 membranes

Table 5-1 Water uptake of ABPBI, ABPBI/POSS and Nafion 117 membranes

Membrane	Water uptake, %	
	Saturated	Ambient atmosphere
ABPBI	$31.6 \pm 1.6$	$23.2 \pm 1.1$
ABPBI/1SO	$37.4 \pm 1.9$	$28.9 \pm 1.4$
ABPBI/3SO	$43.9 \pm 2.2$	$29.3 \pm 1.5$
ABPBI/5SO	$36.4 \pm 1.8$	$31.2 \pm 1.5$
ABPBI/1AM	$61.2 \pm 3.0$	$32.0 \pm 1.6$
ABPBI/3AM	$106.2 \pm 5.3$	$32.3 \pm 1.6$
ABPBI/5AM	$90.8 \pm 4.5$	$33.1 \pm 1.9$
Nafion 117	$30.3 \pm 1.5$	$7.1 \pm 0.3$

As seen in Table 5-1, compared to that of the pristine ABPBI, the increased water uptake of ABPBI/SO (4.8~12.3% at saturated and 5.7~8.0% at ambient atmosphere) should be contributed to the embedded POSS particles, as a hydrophilic SO-POSS cage core has three hydrophilic silanol groups and seven hydrophobic phenyl groups, although some of the silanol groups could be consumed by reacting with the monomer DABA during the synthesis in situ (which was confirmed by the FTIR analysis and discussed in the late section). Additionally, the water can also be

absorbed by hydrogen bonding through POSS core and water molecules ( $\text{Si-O(Si)}\cdots\text{H-O-H}$ ).

Accordingly, the significant increased value from ABPBI/AM (29.6~74.6% at saturated and 8.8~9.1% at ambient atmosphere) should be mainly attributed to the hydrophilic amino groups. The amino groups in AM-POSS enhance the water absorbability greatly through the hydrogen bonding between the amino groups and water molecules. In addition, the highest value appeared in 3% of POSS hybrid composite in either ABPBI/SO or ABPBI/AM implies that a uniform dispersion was achieved therefore resulting in greater surface area which provided more interaction between the POSS particles and  $\text{H}_3\text{PO}_4$  molecules.

### 5.1.3 Comparison of water absorbability of $\text{H}_3\text{PO}_4$ doped membranes

The water uptake of  $\text{H}_3\text{PO}_4$  doped ABPBI membranes is given in Table 5-2. It can be seen that the water absorbability of  $\text{H}_3\text{PO}_4$  doped ABPBI membrane was enhanced with the increased  $\text{H}_3\text{PO}_4$  uptakes either at a saturated condition or ambient atmosphere. This is due to the hydrogen bonds formed between  $\text{H}_3\text{PO}_4$  and water molecules i.e.  $(\text{HO})_2\text{OP-OH}\cdots\text{OH}_2$  or  $(\text{HO})_3\text{P=O}\cdots\text{H-O-H}$ . However, the water uptake of lower percentage  $\text{H}_3\text{PO}_4$  doped ABPBI membranes at ambient atmosphere was lower than that of undoped one (23.2% in Table 5-1) and the water uptake of ABPBI-36PA and ABPBI-53PA samples at saturated condition is lower than that of undoped at saturated condition (31.6% in Table 5-1). This implies a different mechanism of water absorption between polymer,  $\text{H}_3\text{PO}_4$  and water, which will be discussed in the analysis of the followed moisture absorption.

**Table 5-2 Water uptake of  $\text{H}_3\text{PO}_4$  doped ABPBI membrane**

ABPBI membrane	Water uptake, %	
	Saturated	Ambient atmosphere
ABPBI-36PA	17.2±1.7	9.4±0.2
ABPBI-53PA	24.2±2.4	12.6±0.3
ABPBI-60PA	34.7±3.5	13.7±0.4
ABPBI-79PA	40.1±4.0	14.1±0.4
ABPBI-84PA	53.0±5.3	15.0±0.5

The moisture absorptions of  $\text{H}_3\text{PO}_4$  doped ABPBI membrane are given in Table 5-3. It can be seen that, when the  $\text{H}_3\text{PO}_4$  doping level increased from 0.44 to 0.75, the moisture absorbance decreased but the sum of  $\text{H}_3\text{PO}_4$  and water absorption to per imidazole group or repeat unit is closed to 1.0 mole ratio. Theoretically, one repeat unit or imidazole group can absorb either one  $\text{H}_3\text{PO}_4$  or one water molecule. Therefore, the water molecules were hydrogen bonded with the spare imidazole groups in ABPBI polymer chains when the  $\text{H}_3\text{PO}_4$  doping level is less than 0.75. The moisture absorption increased with the rising of the  $\text{H}_3\text{PO}_4$  doping level, which might be mainly due to the absorption by  $\text{H}_3\text{PO}_4$  molecules via hydrogen bonding since the imidazole groups are fully occupied by  $\text{H}_3\text{PO}_4$  via hydrogen bonding. Based on the assumption of the water molecules hydrogen bonded to  $\text{H}_3\text{PO}_4$  molecules when the imidazole groups are fully occupied, it can be roughly calculated that one  $\text{H}_3\text{PO}_4$  molecule could absorb up to one water molecule at ambient atmosphere. For example, in the sample of ABPBI-84PA, 84.0wt% of  $\text{H}_3\text{PO}_4$  uptake equals to 1 mole ratio of  $\text{H}_3\text{PO}_4$  doping level or one  $\text{H}_3\text{PO}_4$  molecule bonds with one imidazole group; the water absorption of the membrane of 15.0wt%, or 1 mole ratio is mainly attributed to one  $\text{H}_3\text{PO}_4$  molecule absorbing one water molecule. The models shown in Figure 5-5 illustrate the absorption of water molecules with various forms.

**Table 5-3 Moisture absorptibility of dry  $\text{H}_3\text{PO}_4$  doped ABPBI membrane**

	PA doped ABPBI	Moisture absorption		PA + moisture
	PA mole ratio*	wt%	mole ratio	mole ratio
ABPBI-37PA	0.44	8.85	0.57	1.01
ABPBI-47PA	0.56	7.29	0.47	1.03
ABPBI-55PA	0.65	6.52	0.42	1.07
ABPBI-63PA	0.75	5.12	0.33	1.08
ABPBI-73PA	0.86	5.90	0.38	1.24
ABPBI-77PA	0.91	7.60	0.49	1.38
ABPBI-89PA	1.05	8.90	0.57	1.62

\*mole ratio: number of  $\text{H}_3\text{PO}_4$  or water molecule in per repeat unit

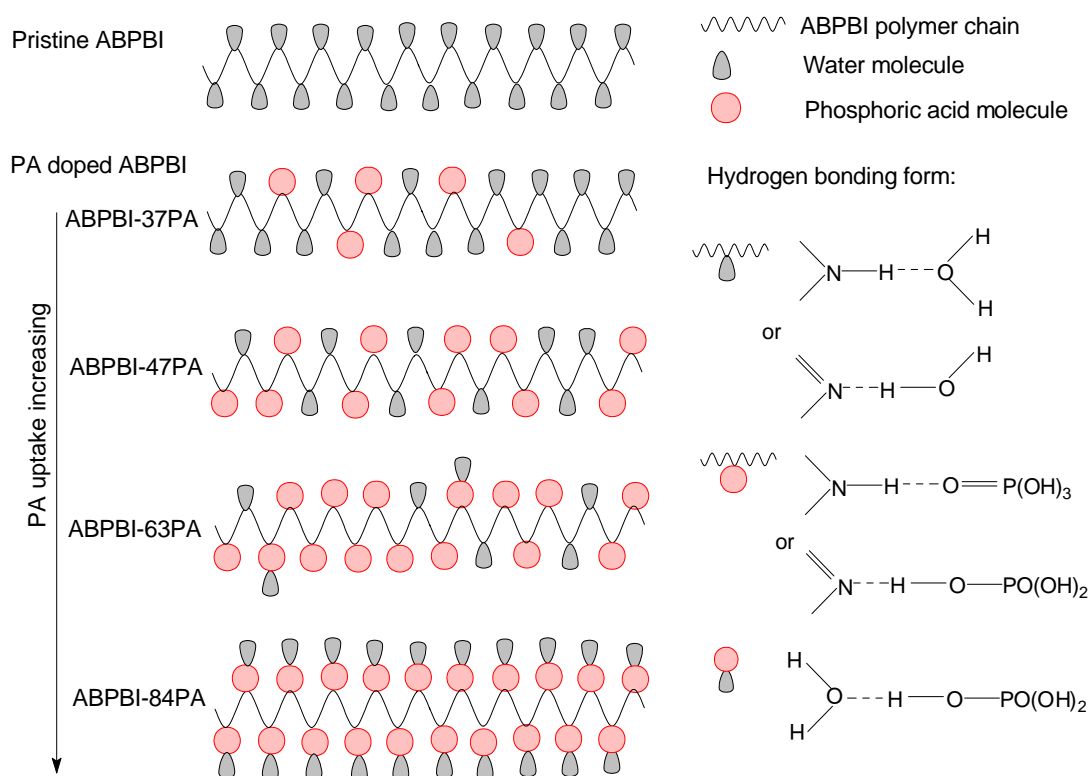


**Figure 5-5 Models proposed for the water absorption in the pristine and  $\text{H}_3\text{PO}_4$  doped ABPBI membranes at ambient atmosphere**

The water uptakes of ABPBI/AM and ABPBI/SO composite membranes are given in Table 5-4 and Table 5-5, respectively. With the increasing of  $\text{H}_3\text{PO}_4$  uptake, both the water uptakes at saturated and ambient atmosphere increased.

Compared to that of undoped ABPBI/POSS composite with the same amount of POSS addition (in Table 5-1) at ambient atmosphere, the values of  $\text{H}_3\text{PO}_4$  doped ABPBI/1AM, ABPBI/5AM, ABPBI/1SO and ABPBI/5SO composite samples at the same conditions were lower, which is the same as that of  $\text{H}_3\text{PO}_4$  doped and undoped ABPBI therefore owes the same explanation. The significant increase of water uptake is found in the sample of  $\text{H}_3\text{PO}_4$  doped ABPBI/3AM and ABPBI/3SO-102PA either at saturated or ambient atmosphere, indicating the dominant contribution of water uptake must result from the embedded POSS particles. In other words, the surface areas of POSS achieved from 3% addition of POSS particles must be larger than those with 1 or 5% addition, due to the fine dispersion of POSS in polymers which resulted in a great enhancement of water absorptivity. Figure 5-6 illustrates the water absorption in various additions of POSS embedded composites, of which, the highest surface areas for ABPBI/3% POSS led to the maximum water absorption.

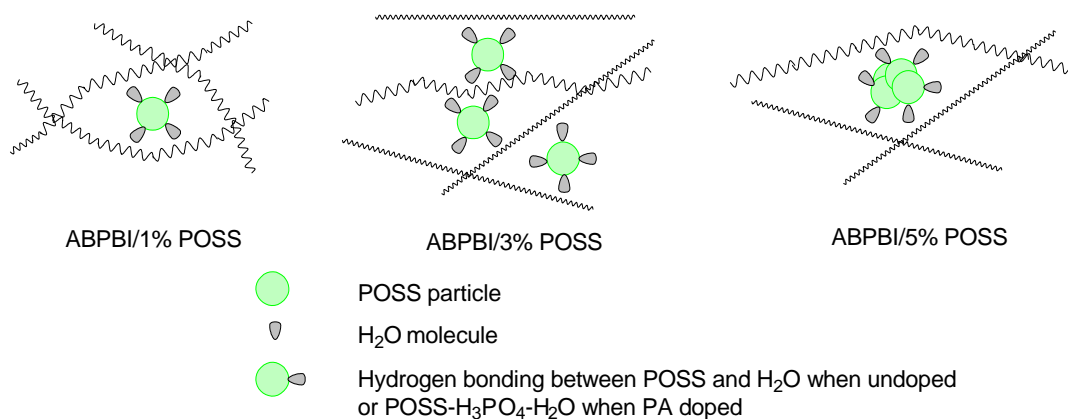


**Figure 5-6 Models of water absorption for ABPBI/POSS composite membranes**

**Table 5-4 Water uptake of H<sub>3</sub>PO<sub>4</sub> doped ABPBI/AM-POSS membranes**

ABPBI/AM-POSS Membrane	Water uptake, %	
	Saturated	Ambient atmosphere
ABPBI/1AM		
ABPBI/1AM-65PA	43.0±2.0	16.0±0.3
ABPBI/1AM-71PA	54.0±2.5	16.6±0.3
ABPBI/1AM-77PA	56.7±3.0	17.3±0.4
ABPBI/1AM-92PA	73.4±3.5	18.6±0.4
ABPBI/1AM-96PA	88.2±5.0	19.0±0.4
ABPBI/3AM		
ABPBI/3AM-88PA	108.0±5.5	36.1±0.7
ABPBI/3AM-117PA	114.9±5.5	41.3±0.8
ABPBI/3AM-153PA	133.2±6.5	47.8±1.0
ABPBI/3AM-194PA	145.4±7.0	53.3±1.1
ABPBI/3AM-241PA	153.6±7.5	58.2±1.2
ABPBI/5AM		
ABPBI/5AM-33PA	32.4±2.0	14.8±0.3
ABPBI/5AM-58PA	44.9±3.0	16.5±0.3
ABPBI/5AM-76PA	47.0±3.0	17.4±0.3
ABPBI/5AM-94PA	51.2±3.0	18.6±0.4
ABPBI/5AM-106PA	60.3±3.0	20.9±0.4

**Table 5-5 Water uptake of H<sub>3</sub>PO<sub>4</sub> doped ABPBI/SO-POSS membranes**

ABPBI/SO-POSS Membrane	Water uptake, %	
	Saturated	Ambient atmosphere
ABPBI/1SO		
ABPBI/1SO-33PA	47.2±2.5	15.2±0.3
ABPBI/1SO-71PA	55.4±3.0	16.3±0.3
ABPBI/3SO		
ABPBI/3SO-47PA	44.7±2.5	20.6±0.4
ABPBI/3SO-58PA	55.0±3.0	21.9±0.4
ABPBI/3SO-88PA	87.6±4.5	30.5±0.6
ABPBI/3SO-102PA	110.5±5.5	39.2±0.8
ABPBI/5SO		
ABPBI/5SO-43PA	28.5±1.5	13.5±0.3
ABPBI/5SO-55PA	34.3±2.0	15.7±0.3

## **5.2 Mechanical Properties of ABPBI and its Composite Membranes**

### **5.2.1 Effect of phosphoric acid and water on the mechanical properties of ABPBI membrane**

For ABPBI membranes with molecular weights of about 18,000g/mol, the mechanical properties of ABPBI membranes at dry and saturated conditions as a function of H<sub>3</sub>PO<sub>4</sub> uptake are shown in Figure 5-7 and Figure 5-8, respectively. In Figure 5-7, for the pristine (undoped) ABPBI membrane, the tensile strength is 135MPa, whilst it jumps to 173MPa for the 53% H<sub>3</sub>PO<sub>4</sub> doped ABPBI membrane. With H<sub>3</sub>PO<sub>4</sub> uptake continuously increasing, the tensile strength decreased. A similar variation tendency with the elevated H<sub>3</sub>PO<sub>4</sub> uptake is observed in Young's modulus and the maximum value of 7.0GPa was obtained from 53% H<sub>3</sub>PO<sub>4</sub> doped ABPBI. In contrast, the elongation at break is found to decrease firstly then increase with the elevated H<sub>3</sub>PO<sub>4</sub> uptake.

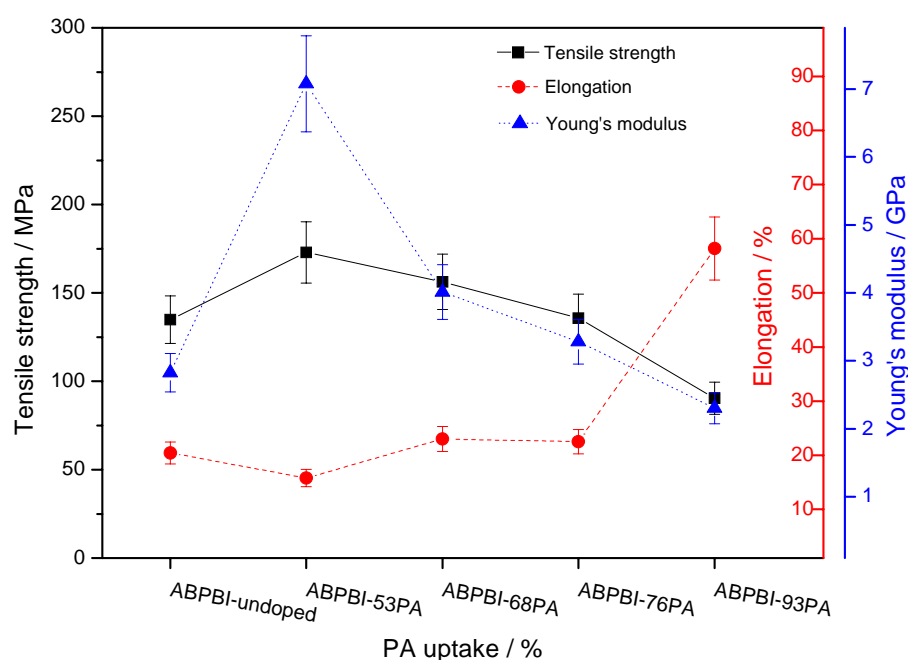


**Figure 5-7 Mechanical properties of dry H<sub>3</sub>PO<sub>4</sub> doped ABPBI membrane**

Generally, the mechanical strength of polymer membranes results from attraction forces between polymer molecules, which are dipole-dipole interaction (including hydrogen bonding), induction forces and dispersion between non-polar molecules. It may also result from ionic bonding and ion-dipole interactions with polymers containing ionic groups<sup>210</sup>. For pure ABPBI membrane, the hydrogen bonding between  $-N=$  and  $-NH-$  groups is the dominant force that determines its mechanical strength. When H<sub>3</sub>PO<sub>4</sub> is introduced, the intermolecular forces between ABPBI polymer chains could be weakened due to hydrogen bonds formed between  $-N=$  and H<sub>3</sub>PO<sub>4</sub> molecules. The doped phosphoric acid has two types of effect on the mechanical strength of the membranes: it improves the mechanical strength through hydrogen bonding when acid doping level is low (i.e. less than 1). Additionally, when the acid doping level is higher, the doped H<sub>3</sub>PO<sub>4</sub> the distance of polymer backbones which in turn would reduce intermolecular forces of polymer chains and consequently deteriorates the mechanical strength of the membranes<sup>210</sup>. Similar results from H<sub>3</sub>PO<sub>4</sub> doped PBI membranes were reported by He et al.<sup>211</sup> and Litt et al.<sup>111</sup> When the doping level was less than 1, one phosphoric acid could link with two different benzimidazole groups (or protonate benzimidazole rings) through ionic bonds to form cross-linking-like networks which can be seen in Figure 5-26 in the



late section. The formation of networks might be the dominant factor of resulting in the increase of mechanical strength and the decrease of elongation. The ionic bonds especially  $\text{HPO}_4^{2-}$  were confirmed by FTIR spectra which will be discussed in the later section. With more  $\text{H}_3\text{PO}_4$  absorbed, the ionic bonding form of one  $\text{H}_3\text{PO}_4$  molecule bonded with two imidazole groups could be replaced by that of one  $\text{H}_3\text{PO}_4$  molecule bonded with one imidazole group, resulting in the degeneration of cross-linking-like networks, therefore, decreased mechanical strength. In addition, the absorbed  $\text{H}_3\text{PO}_4$  can act as plasticiser resulting in the elongation increasing in the ABPBI membrane at high  $\text{H}_3\text{PO}_4$  uptake.

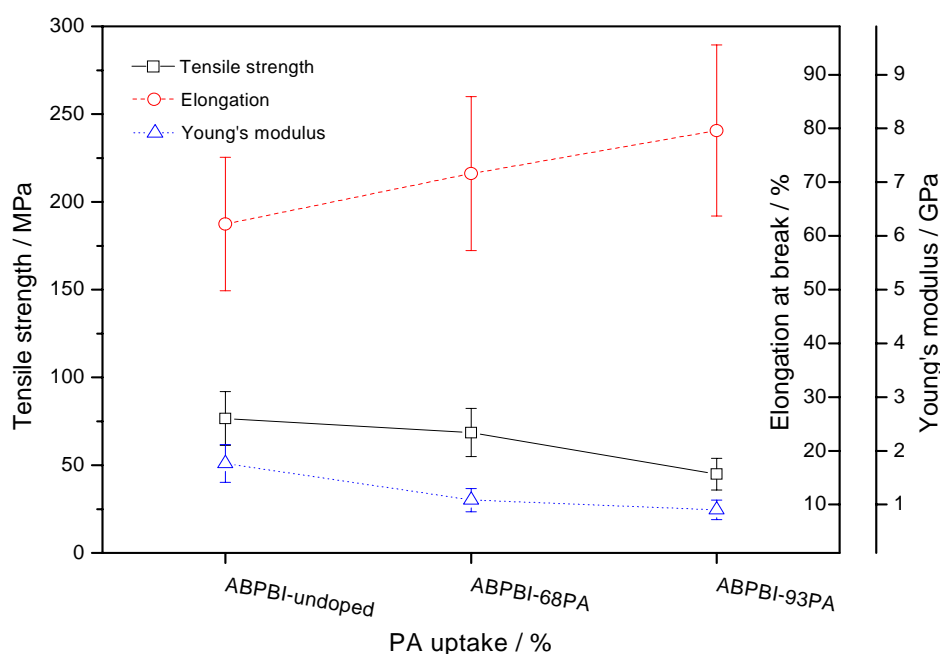


**Figure 5-8 Mechanical properties of saturated  $\text{H}_3\text{PO}_4$  doped ABPBI membranes**

The mechanical properties of  $\text{H}_3\text{PO}_4$  doped ABPBI membranes were also measured at water saturated condition. As shown in Figure 5-8, the mechanical strength and Young's modulus decrease with the increased  $\text{H}_3\text{PO}_4$  uptake, whilst the elongation increases. This is due to the absorbed water and  $\text{H}_3\text{PO}_4$  molecules, on one hand, resulting in the volume swelling therefore increases the distance of separation for ABPBI backbones, which would reduce intermolecular forces and deteriorate mechanical strength; on the other hand, plasticised polymers leading to increased elongation.

Similar to  $H_3PO_4$  doped ABPBI, the increased mechanical strength with low  $H_3PO_4$  uptake is also found in  $H_3PO_4$  doped ABPBI/POSS composite membranes. For example, in Figure 5-9, the tensile strength of ABPBI/ISO-70PA at the dry condition is 242MPa, whilst it is 165MPa from undoped ABPBI/ISO and 144MPa from ABPBI/ISO-87PA respectively. The increased mechanical strength should be due to the cross-linking-like network formed by phosphoric acid with low doping levels. Correspondingly, the decreased values at the saturated condition should result from the increased distance of the separation of polymer chains due to the increased absorbance of water compared to that of undoped ABPBI/ISO.

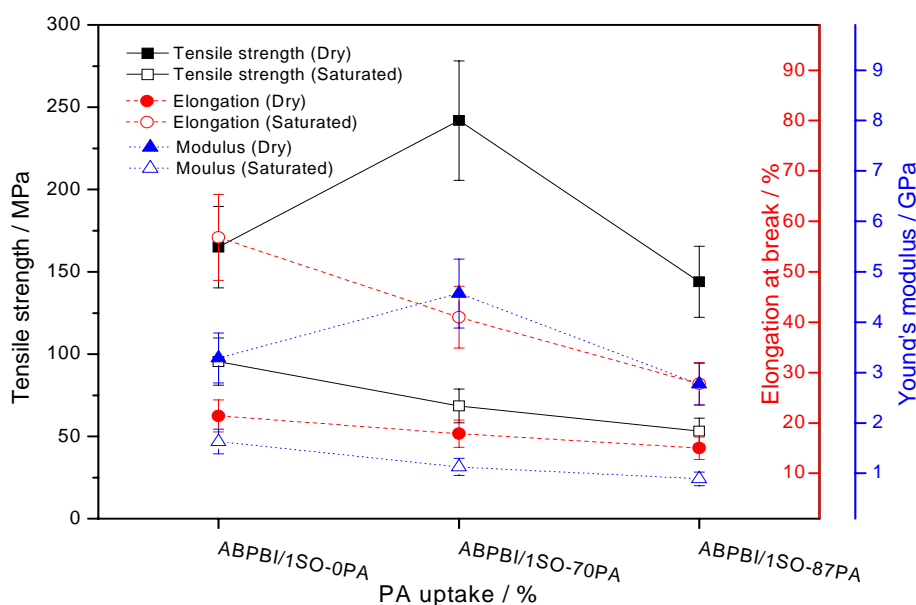


Figure 5-9 Mechanical strength of  $H_3PO_4$  doped ABPBI/ISO at dry and saturated condition

### 5.2.2 Effect of POSS particles on the mechanical properties of ABPBI/POSS composite membrane

The mechanical properties of undoped ABPBI/AM-POSS and ABPBI/SO-POSS composite membranes are shown in Figure 5-10 and Figure 5-11, respectively.

It can be seen that, in Figure 5-10, both the tensile strength and Young's modulus are increased with the addition of AM-POSS. Compared to the slight increase of that from ABPBI/1AM and ABPBI/5AM, significant increases i.e. around 92% of the

increase of tensile strength (258MPa) and 62% of the increase of Young's modulus (4.6GPa), respectively, are observed from dry ABPBI/3AM composite membrane.

The modulus of a composite can be expressed by the "Rule of Mixture"<sup>199</sup> as following

$$E_c = E_m V_m + E_f V_f \quad 5-1$$

where  $E$  is the modulus and  $V$  is the volume fraction ( $V_m + V_f = 1$ ),  $c$ ,  $m$  and  $f$  represents composite, matrix (polymer) and filler (POSS), respectively.

A model of the geometric configuration of POSS particles dispersed in ABPBI polymer matrix used in the present analysis is also proposed in Figure 5-12. For a 1% addition of POSS, the negligible volume fraction of POSS addition could not result in an obvious contribution to the composite modulus although the modulus of inorganic POSS particle is significantly higher than that of polymer ( $E_f \gg E_m$ ). Therefore, the increased modulus could be mainly due to the dipole-dipole interaction and induction forces between POSS particles and polymer chains. A 3% addition of POSS could enhance the composite modulus in two ways, i.e. on the one hand, a uniformly dispersed POSS could result in the increased volume fraction of fillers thereby enhancing the composite modulus; on the other hand, the stress could transport through the evenly and continuously distributed polymer-filler bridged structures resulting in the significant increase of modulus. However, a dramatic decrease of modulus was observed from ABPBI/5AM, which should be due to the agglomeration of POSS particles leading to the stress concentration and the enlarged distance of separation of polymer chains. Accordingly, this can also explain the changed rule for tensile stress of composites.

While immersed in water, on one hand, the absorbed water swelled the membranes. Based on the equation 5-1, the increased value of  $V_f$  is from the swelling of water, resulting in the decrease of composite modules and tensile strength. On the other hand, absorbed water molecules separated polymer chains resulting in the reduction of intermolecular reactions, meanwhile acting as plasticisers leading to the increase of elongation.

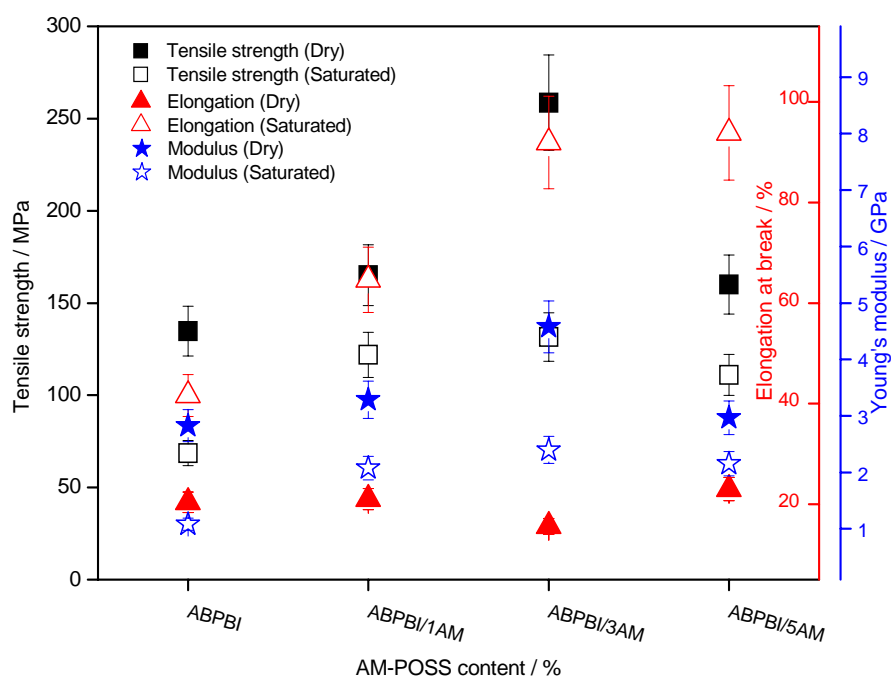


Figure 5-10 Mechanical properties of undoped ABPBI/AM-POSS composite membranes

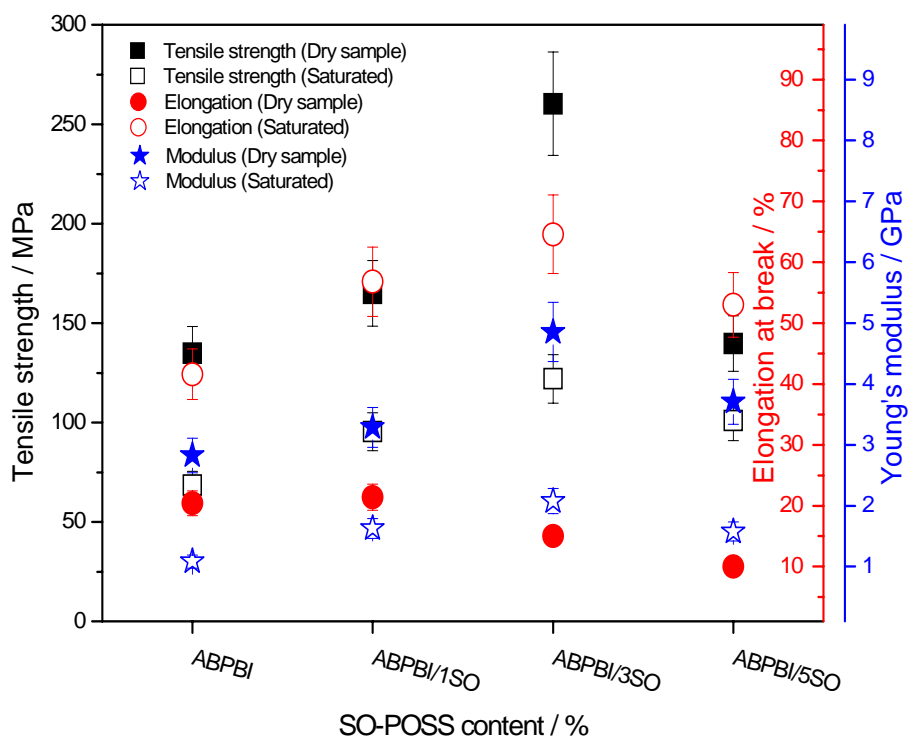
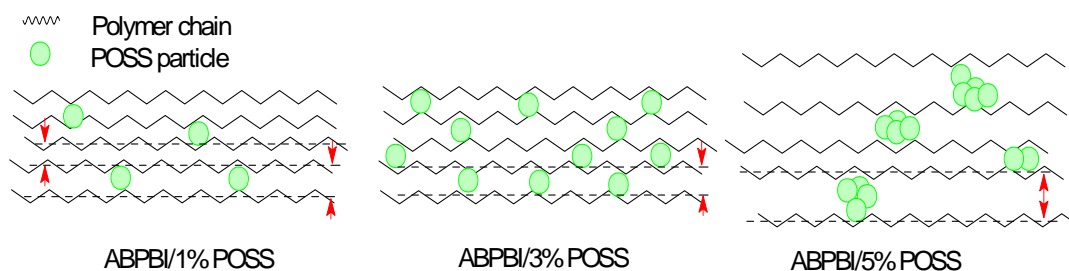


Figure 5-11 Mechanical properties of undoped ABPBI/SO-POSS composite membranes



**Figure 5-12 Schematic drawing showing a polymer matrix bridged by POSS particles**

The quite similar variation tendency of mechanical properties with the various contents of SO-POSS is observed in ABPBI/SO-POSS composite membranes, thereby owing to the same explanations as discussed above. It is noteworthy that the quite approximate values of tensile strength in ABPBI/3SO samples (260MPa) to that of ABPBI/3AM (258MPa) indicate that the significantly increased mechanical strength should be mainly caused by the homogenous dispersion of POSS particles rather than the hydrogen bonding forms between POSS particles and polymer chains since the phenyl groups in SO-POSS could hinder these hydrogen bonding.

### **5.3 Morphologies of ABPBI and Composite Membranes**

#### **5.3.1 Effect of the casting procedure on the morphologies of ABPBI membranes**

The removal of residuals (MSA,  $\text{H}_3\text{PO}_4$  or water) is important for the calculation of water uptake and acid uptake (or doping level) and the evaluation of proton conductivities based on these parameters. From the relevant literature, there are some different conditions of evaporating solvent or water used for membrane casting, e.g. drying at room temperature under reduced pressure<sup>28</sup>, heating at high temperature up to  $200^\circ\text{C}$ <sup>141</sup>, etc. As described in chapter 3, ABPBI and its composite membranes were cast using Petri dishes in this work. The thicknesses of the membranes were varied by controlling the concentration of polymer solutions. The majority of the solvent was evaporated in a wide temperature range (i.e. from synthesis ( $150^\circ\text{C}$ ) or dissolving temperature ( $130^\circ\text{C}$ ) to  $220^\circ\text{C}$ ). Phosphoric acid and the residual solvent were eliminated by neutralisation with NaOH. Subsequently dryness was carried out in an oven. As the boiling point of solvent MSA is  $167^\circ\text{C}$ , the evaporating temperature was set from  $180\sim 220^\circ\text{C}$  with direct heating or gradual heating up to set

temperature. The morphologies of ABPBI membranes prepared by different heating conditions were performed by SEM and shown in Figure 5-13.

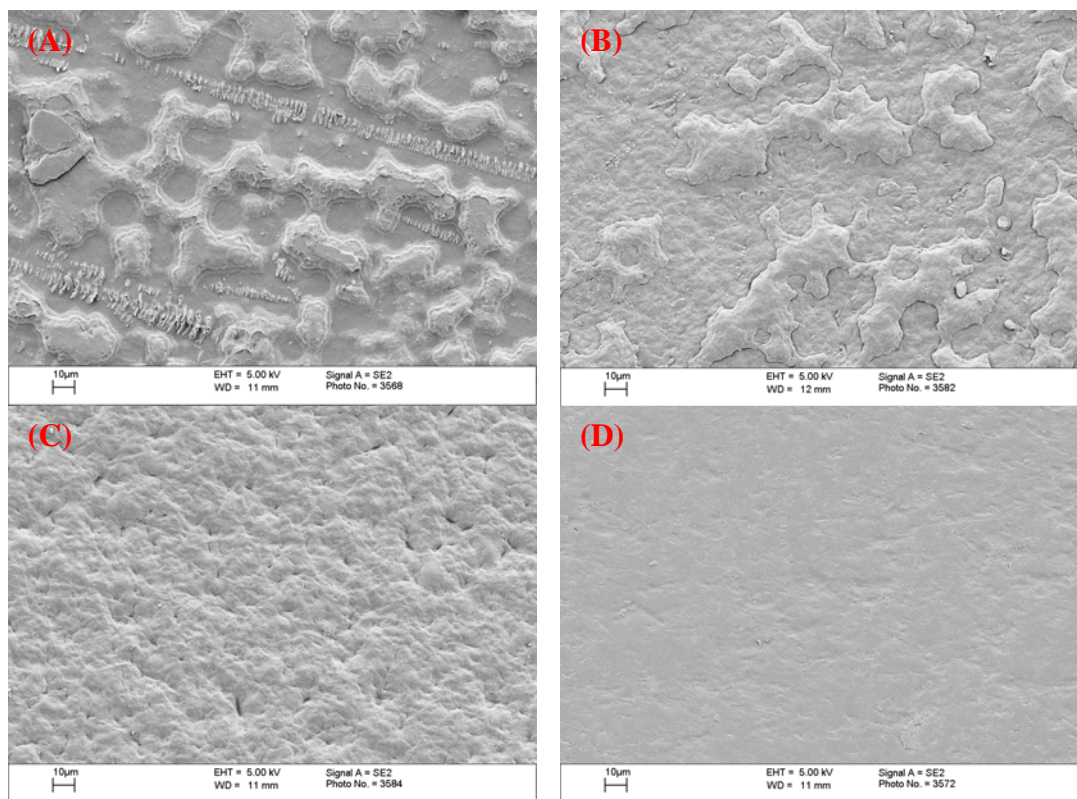


**Figure 5-13 SEM image of ABPBI membrane under the heating conditions of evaporating solvent: A. 180°C for 24 hours, B. 200°C for 24 hours, C. 220°C for 24 hours, D. the temperature varied from 150~220°C with 10°C intervals per hour then hold at 220°C for over 10 hours**

It was found that the membrane qualities were greatly affected by the heating rate when evaporating solvent. As shown in Figure 5-13a, the island-like structures were observed when the membrane was heated at 180°C for 24 hours. The island-like structures shrink at elevated evaporating temperatures i.e. 200°C (as shown in Figure 5-13b) and become unclear or even disappear at 220°C instead of the appearance of pinholes (as shown in Figure 5-13c). By adjusting the heating rate, i.e. increasing the temperature from 150 to 220°C with 10°C intervals per hour then holding at 220°C over 10 hours, a uniform membrane can be achieved (as shown in Figure 5-13d). The island-like structure is likely to be due to the slow and incomplete evaporation of solvent, resulting in the uneven distribution of solvents (acids) in the polymer matrix, whilst the pinhole defects should result from the overquick evaporation of solvent from the viscous mixtures.

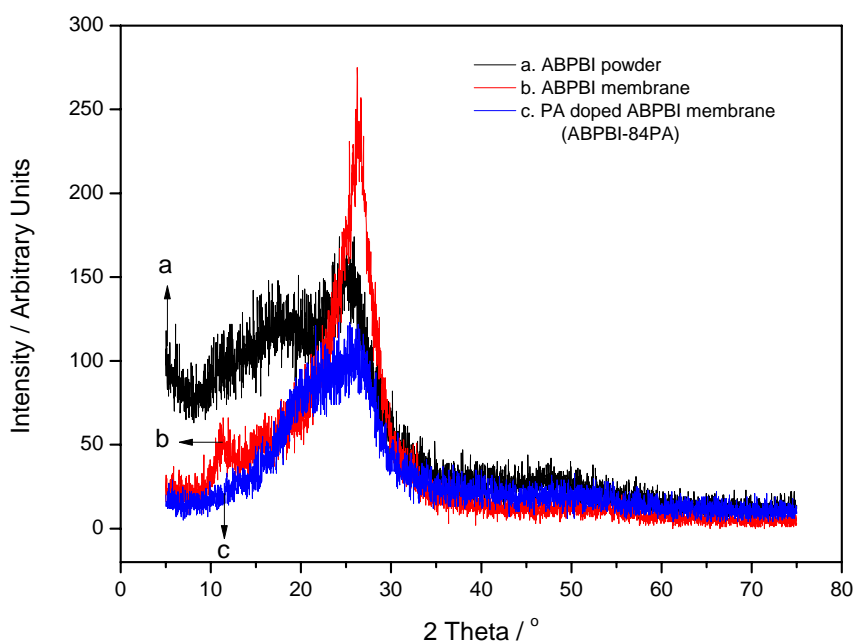


**Figure 5-14 XRD pattern of ABPBI membrane**

The  $\text{H}_3\text{PO}_4$  doped and undoped ABPBI membranes cast from MSA solution were measured by XRD. As shown in Figure 5-14, a sharp peak at  $2\theta=26^\circ$  was observed in the undoped sample, whilst it was found reduced in intensity and broadened when doped from  $\text{H}_3\text{PO}_4$  solution. The scattering angle of  $2\theta$  ( $=26^\circ$ ) corresponds to a  $d$  spacing of  $3.3\text{\AA}$ , characteristic of the stacking of ABPBI chains<sup>212</sup>. Compared to that of ABPBI powder with a semicrystalline structure, this peak becomes sharper, implying a tendency of crystallisation. This is due to benzimidazole rings allowed to stack parallel to the membrane surface during the casting process, showing a greater regularity of polymer chains stacking. After a  $\text{H}_3\text{PO}_4$  doping process, the broadened peak probably centred at  $20\sim 26^\circ$  indicates an expanded stacking spacing due to the presence of absorbed  $\text{H}_3\text{PO}_4$  molecules, whilst the intensively reduced peak shows a more amorphous structure, which was also observed in the work from other group<sup>30</sup>.

### 5.3.2 Evaluation of ABPBI/POSS composite morphology

#### 5.3.2.1 SEM/TEM images

The morphologies of ABPBI/POSS composite membranes were evaluated by inspecting the effects from solvent ethanol, ultrasonication and  $\text{H}_3\text{PO}_4$  doping.



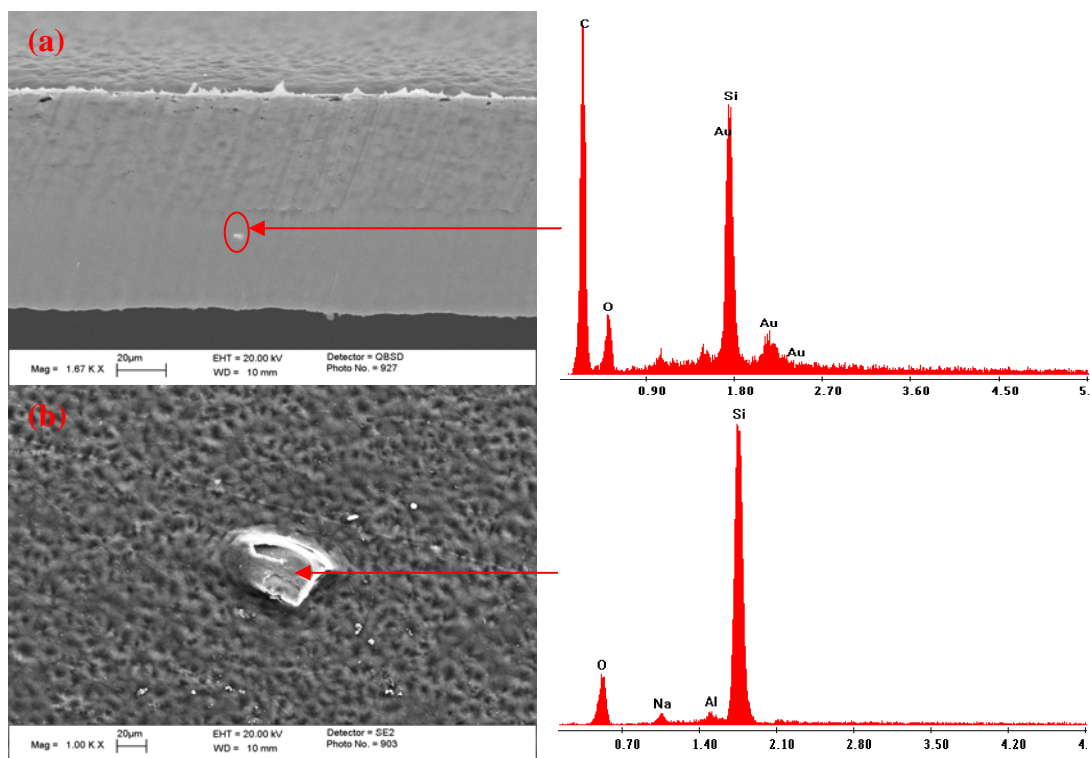


**Figure 5-15 SEM images (left) and EDAX images (right) of samples without treatment of dissolving in ethanol before synthesis in-situ: a. ABPBI/3SO, b. ABPBI/3AM**

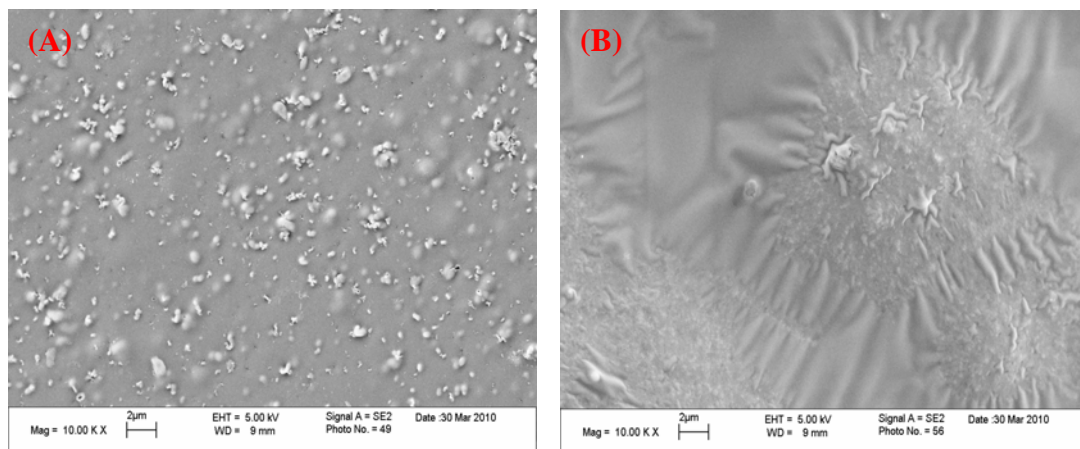


**Figure 5-16 SEM images of samples without ultrasonication treatment before synthesis in-situ: A. ABPBI/3SO, B. ABPBI/3AM**

Figure 5-15 shows the SEM and EDX images of ABPBI/POSS composite membranes without dissolution treatment in ethanol before synthesis in-situ. Agglomerated SO-POSS and AM-POSS particles with large sizes were detected both in the cross-section and the surface of membranes. Figure 5-16 shows the SEM images of the composite membranes without ultrasonic treatment before synthesis in-situ. Although these POSS powder were dispersed in ethanol, the agglomerations were observed. It was found that POSS particles tend to aggregate in the synthesis



medium of MSA, thus, the procedures of dissolution in solvent of ethanol followed by ultrasonic treatment before synthesis in-situ was carried out.

Compared to cases of samples without ultrasonication treatment (in Figure 5-16), the TEM images show uniform surfaces in the membranes cast from the product mixtures after dissolution in ethanol followed by ultrasonic treatment (Figure 5-17, Figure 5-18). With the amount of SO-POSS increasing from 1% to 5%, the surface of composite membrane was tending to become rougher (Figure 5-17), which might indicate the agglomeration occurred in high-percent POSS hybrid composites. The better qualities of surfaces than that of SO-POSS are observed in ABPBI/AM composite membranes (Figure 5-18), which implying a better dispersibility. Based on the FTIR analysis in section 4.3.1.1, there were end-capping reactions occurring between SO-POSS particles and ABPBI polymer chains which might hinder the movement of SO-POSS particles, thus resulting in the rough surfaces.

The  $\text{H}_3\text{PO}_4$  doped membranes were measured by SEM and TEM, respectively. The SEM images and relative EDX maps (Figure 5-19) show a uniform dispersion of either hybrid POSS or absorbed phosphoric acid. It is worth mentioning that the map of silicon (Si) can be clearly seen only when magnified in a certain extent which is due to the maximum of Si in a composite membrane is less than 1%. It is noteworthy that the cracks are observed in ABPBI/5SO and ABPBI/5AM composite membranes after doping in 10M and 12M  $\text{H}_3\text{PO}_4$  solution followed by drying in an oven at  $150^\circ\text{C}$  for 24 hours (Figure 5-20). This might be due to the stress concentration resulted from the agglomerated POSS particles and  $\text{H}_3\text{PO}_4$  accelerates this process.

A TEM was employed to investigate the size of POSS particles dispersed in ABPBI membranes. As shown in Figure 5-21, no visible POSS particle was observed at this resolution level either in undoped pristine ABPBI and ABPBI/5AM composite or in 4M  $\text{H}_3\text{PO}_4$  doped ABPBI/1AM and ABPBI/3AM samples. Additionally, the related EDX images (in Figure 5-21) could not show the signal of silicon in the measured area. As the size of POSS core is around  $0.53\text{nm}^{204}$ , it might be difficult to be traced by our TEM equipment even when the POSS particles were agglomerated. Since the weight percent of silicon is 19.1% in an AM-POSS particle or the maximum weight

percent 0.95% in ABPBI/5AM composite, it would be difficult to be precisely defined by the EDX detection from this TEM equipment.

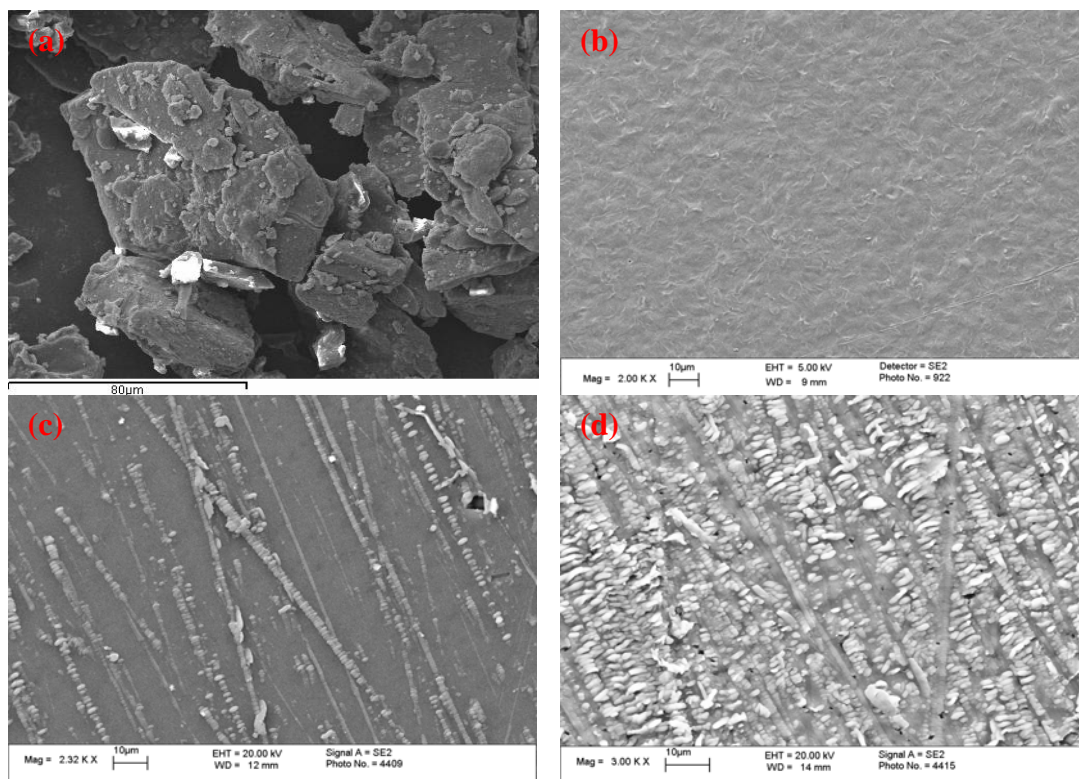


Figure 5-17 SEM images of a. SO-POSS powder, b. ABPBI/ISO, c. ABPBI/3SO, d. ABPBI/5SO

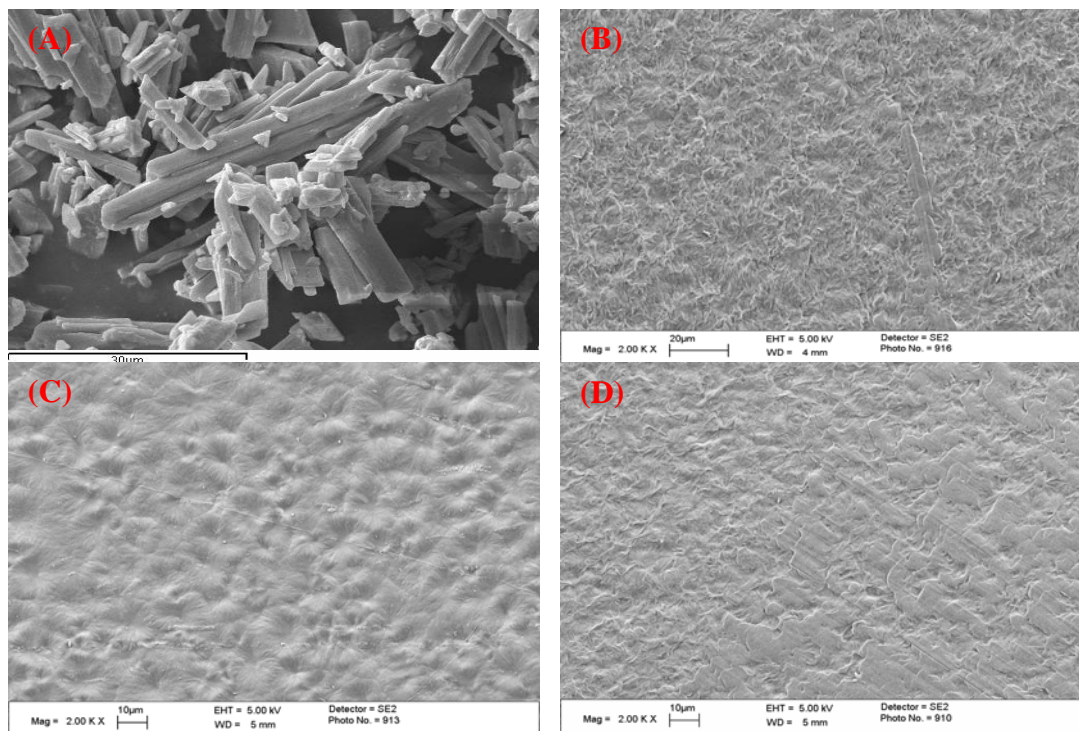


Figure 5-18 SEM images of A. AM-POSS powder, B. ABPBI/1AM, C. ABPBI/3AM, D. ABPBI/5AM



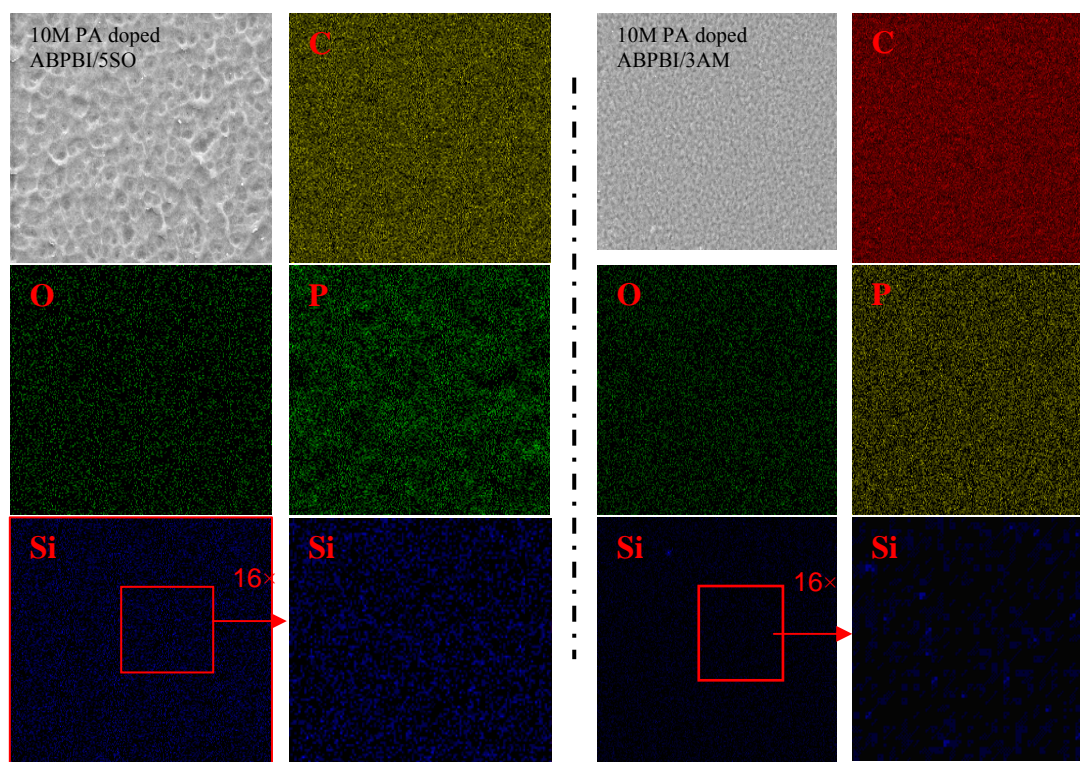


Figure 5-19 EDX map of 10M  $\text{H}_3\text{PO}_4$  doped ABPBI/SSO (left) and ABPBI/3AM (right)

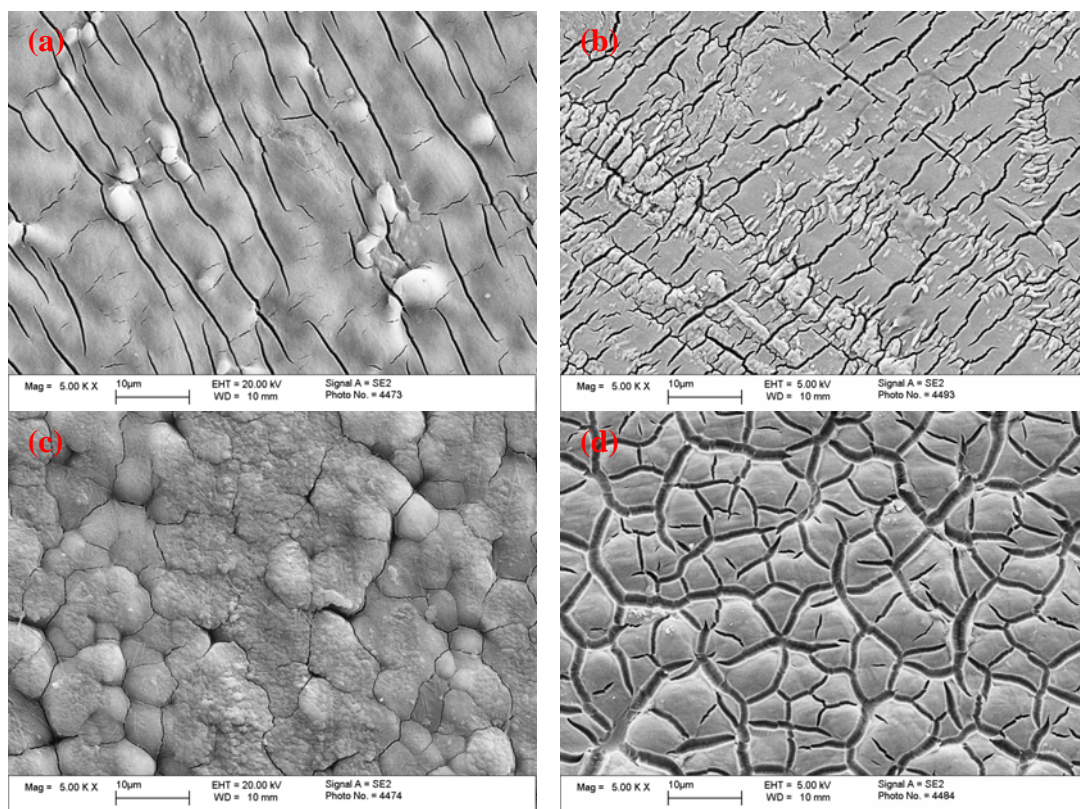


Figure 5-20 SEM images of a. 10M  $\text{H}_3\text{PO}_4$  doped ABPBI/SSO, b. 12M  $\text{H}_3\text{PO}_4$  doped ABPBI/SSO, c. 10M  $\text{H}_3\text{PO}_4$  doped ABPBI/3AM, d. 12M  $\text{H}_3\text{PO}_4$  doped ABPBI/3AM dry membranes

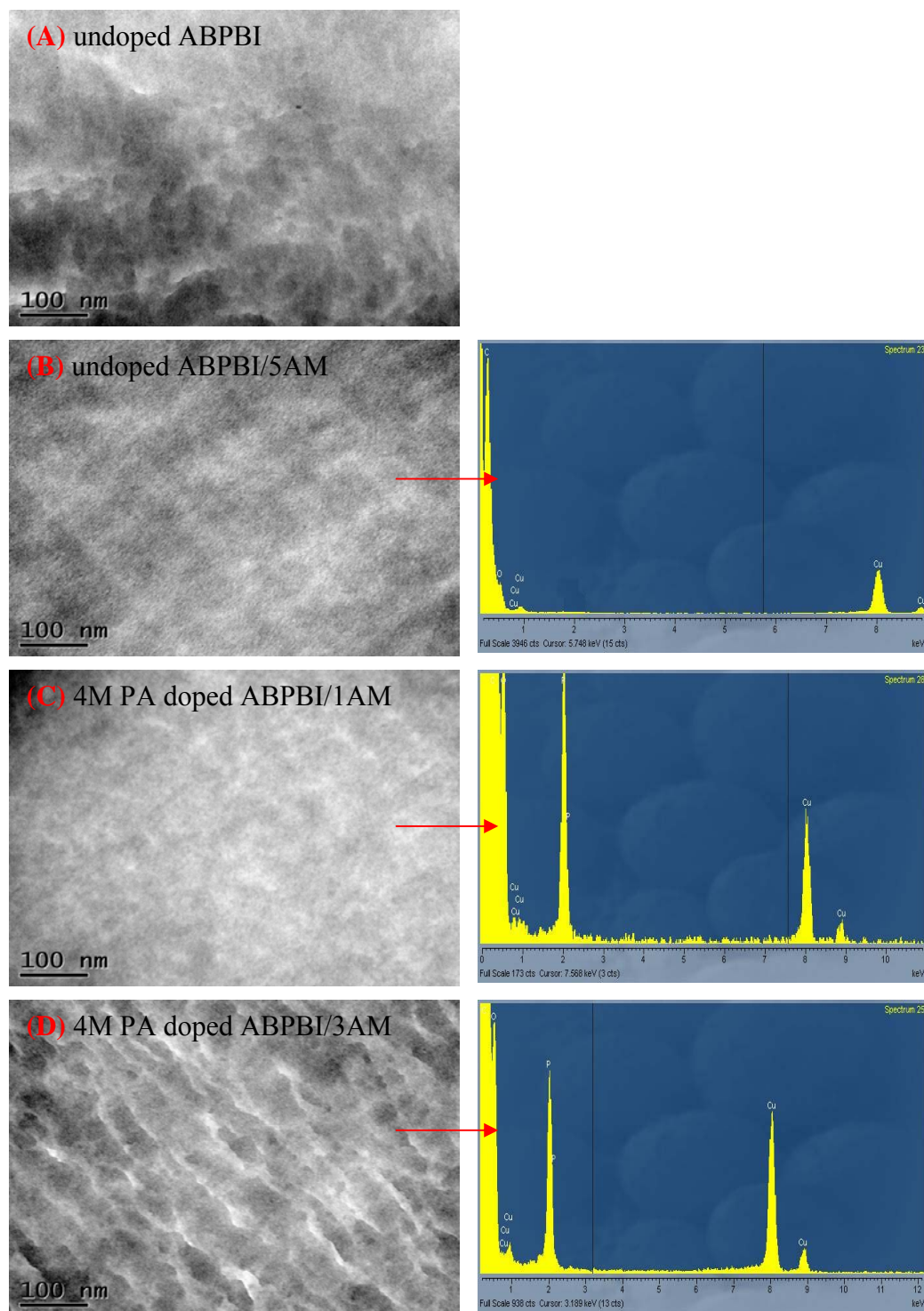


Figure 5-21 TEM images (left) and EDX images (right) of (A) undoped ABPBI, (B) undoped ABPBI/5AM, (C) 4M  $\text{H}_3\text{PO}_4$  doped ABPBI/1AM and (D) 4M  $\text{H}_3\text{PO}_4$  doped ABPBI/3AM

### 5.3.2.2 XRD pattern

The morphologies of ABPBI/POSS composite membranes were recorded by XRD patterns. The XRD patterns of undoped ABPBI/AM composite membranes are shown in Figure 5-22.

It can be seen that a XRD pattern with a peak at  $26^\circ$  similar to that of ABPBI membrane was observed in ABPBI/1AM (Figure 5-22B) and ABPBI/3AM (Figure 5-22C), respectively, whilst a broad shoulder at the range of around  $2\theta=13\sim24^\circ$  and a sharp peak at  $2\theta=26^\circ$  appeared in that of ABPBI/5AM (Figure 5-22D). The similar XRD patterns from ABPBI/1AM and ABPBI/3AM composites show the morphology of ABPBI with a semicrystalline structure didn't change even though 1~3% of AM-POSS was added, which is likely to be owing to the homogeneous dispersion of AM-POSS. The shoulder appeared between  $13\sim24^\circ$  from ABPBI/5AM may overlap that of crystalline AM-POSS since main characteristic peaks of AM-POSS (Figure 5-22E) is at this range. In addition, it implies an expanded stacking spacing which might be due to the agglomeration of embedded POSS particles, resulting in the enlargement of separation of polymer chains.

The  $H_3PO_4$  doped ABPBI/AM composite membranes were measured by XRD. As shown in Figure 5-23, a greater amorphous structure is indicated from the XRD patterns of  $H_3PO_4$  doped ABPBI/AM composite membranes due to the absorbed  $H_3PO_4$ , which was the same as the  $H_3PO_4$  doped ABPBI sample. Additionally, the peak reduced intensity from ABPBI/3AM-241PA (Figure 5-23b) compared to the similar peaks from ABPBI/1AM (Figure 5-23a) and ABPBI/5AM (Figure 5-23c) with similar  $H_3PO_4$  uptake, implies the tendency of amorphousness is enhanced by the increased amount of absorbed PA. Compared to that of ABPBI/AM composites, the quite similar results were measured from the XRD patterns of ABPBI/SO composites and shown in Figure 5-24, which owe to the same reasons as discussed above.

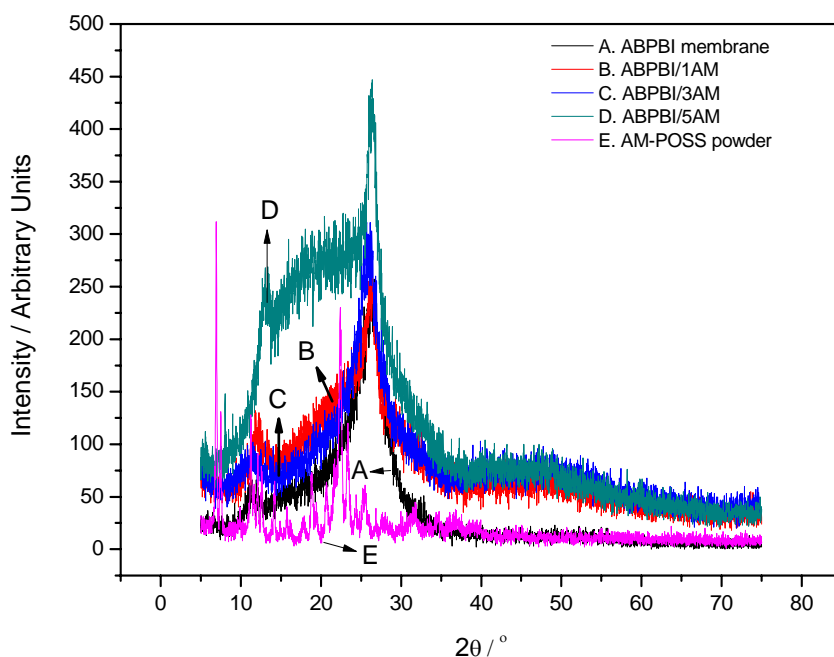


**Figure 5-22 XRD patterns of undoped ABPBI/AM composite membranes: B. ABPBI/1AM, C. ABPBI/3AM, D. ABPBI/5AM (A. ABPBI and E. AM-POSS powder are as references)**

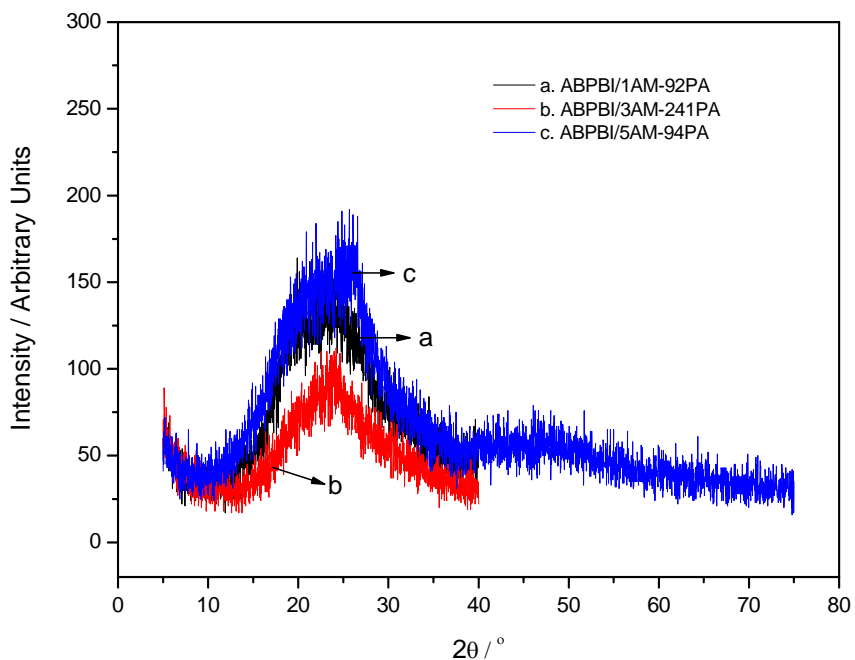


**Figure 5-23 XRD patterns of  $H_3PO_4$  doped ABPBI/AM composite membranes: a. ABPBI/1AM-92PA, b. ABPBI/3AM-241PA and c. ABPBI/5AM-94PA**



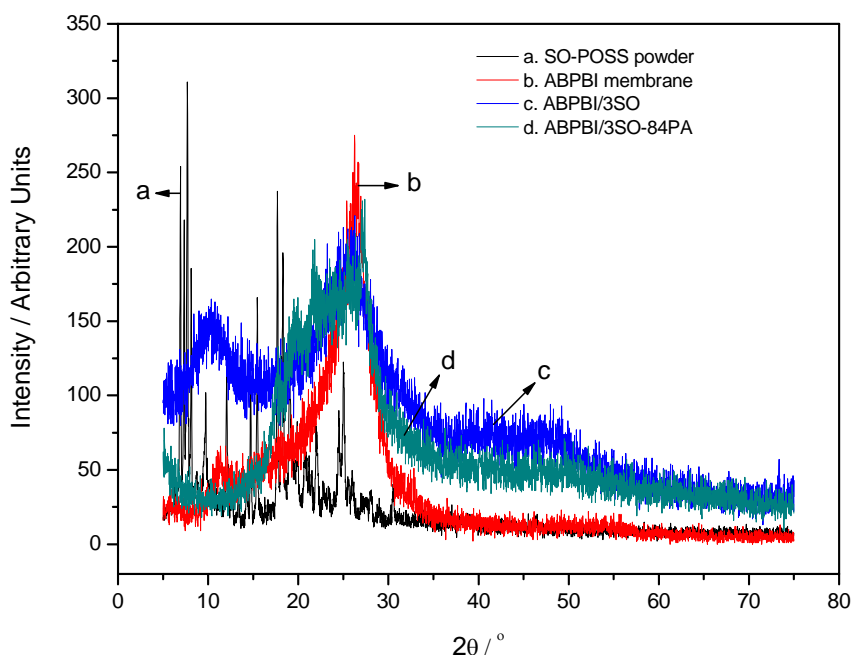


Figure 5-24 XRD patterns of a. SO-POSS powder, c. ABPBI/3SO and d. ABPBI/3SO-84PA

## 5.4 FTIR Analysis

### 5.4.1 FTIR analysis of phosphoric acid doped ABPBI membrane

The FTIR spectra of  $\text{H}_3\text{PO}_4$  solution, pristine and  $\text{H}_3\text{PO}_4$  doped ABPBI membranes are shown in Figure 5-25. Amongst them, the FTIR spectrum of ABPBI (Figure 5-25a) are tentatively assigned in last chapter. The assignment of bonds of hydrous  $\text{H}_3\text{PO}_4$  is made according to the work of Chapman et al.<sup>203</sup> In the IR spectra of phosphoric acid solution (Figure 5-25e), the broad band between  $3600\sim 3300\text{cm}^{-1}$  and the strong absorbance peak at  $1630\text{cm}^{-1}$  are assigned to water. The typical characteristic vibrations of phosphoric acid include (P)O-H, P-O(H) and P=O stretching modes. The asymmetrical and symmetrical stretching modes of O-H in  $\text{H}_3\text{PO}_4$  are seen at  $3000\sim 2000\text{cm}^{-1}$ . The asymmetric vibration of (P)O-H is located at  $3000\sim 2700\text{cm}^{-1}$  and the doubling peak attributed to symmetric vibration is located at the range of  $2390\sim 2280\text{cm}^{-1}$ . In addition, three peaks at the low wave-number region (i.e. below  $1400\text{cm}^{-1}$ ) are regarded as being mainly hydrogen bonded P=O stretching ( $\nu_{as}(\text{PO})\text{H}_3\text{PO}_4$ ) at  $1165\text{cm}^{-1}$ ,  $\text{P}(\text{OH})_3$  asymmetrical P-O stretching ( $\nu_{as}(\text{P}(\text{OH})_3)\text{H}_3\text{PO}_4$ ) at  $1007\text{cm}^{-1}$  and  $\text{P}(\text{OH})_3$  symmetrical P-O stretching ( $\nu_s(\text{P}(\text{OH})_3)\text{H}_3\text{PO}_4$ ) at  $890\text{cm}^{-1}$ .<sup>203</sup>

Due to the alkalinity of benzimidazole groups, once an ABPBI membrane is doped in the phosphoric acid solution, the protonation of benzimidazole groups or nitrogen and absorbance of phosphoric acid are expected to occur. The FTIR spectra of  $\text{H}_3\text{PO}_4$  doped ABPBI membranes with various phosphoric acid uptakes are shown in Figure 5-25b, c and d. In the region  $4000\text{--}2000\text{cm}^{-1}$ , a broad band with a complex structure is observed in agreement with the results from the literature<sup>132</sup>. In the N-H stretching zone ( $3500\text{--}2500\text{cm}^{-1}$ ), an overview of the spectra reveals the evolution of nitrogen protonation by the acid. With elevated  $\text{H}_3\text{PO}_4$  uptakes, the ratio of protonated benzimidazole groups increases. Therefore, the broad band of  $\text{N}^+\text{-H}$  stretching ( $3000\text{--}2500\text{cm}^{-1}$ ) becomes stronger, whilst those of non-associated N-H (centred at  $3415\text{cm}^{-1}$ ) and hydrogen associated N-H (centred at  $3145\text{cm}^{-1}$ ) decrease in intensity or even disappear. As a result, the overlapped C-H stretching at  $3065\text{cm}^{-1}$  becomes apparent due to the decrease in intensity of H associated N-H stretching. The two bands assigned to the O-H asymmetric and symmetric stretching modes in phosphoric acid are also observed in the IR spectra of  $\text{H}_3\text{PO}_4$  doped samples. The asymmetric stretching is observed at about  $2700\text{--}3000\text{cm}^{-1}$  which is partially overlapped by that of the  $\text{N}^+\text{-H}$  stretching, whilst the symmetric mode centred at about  $2350\text{cm}^{-1}$  is most apparent.

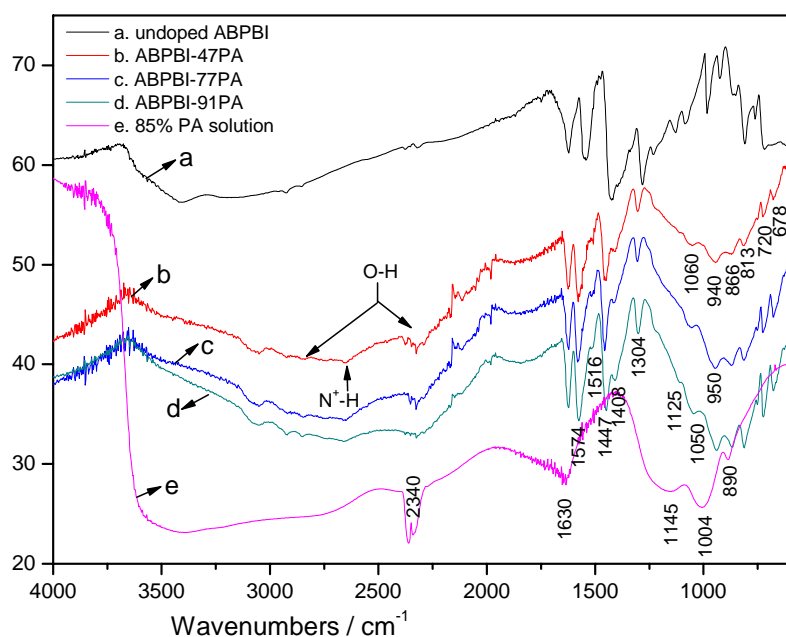


**Figure 5-25** FTIR spectra of a. undoped ABPBI, b. ABPBI-47PA, c. ABPBI-77PA, d. ABPBI-91PA membranes and e. 85%  $\text{H}_3\text{PO}_4$  solution



In the region  $2000\text{--}600\text{cm}^{-1}$ , the interpretation of bonds associated with the complex structures resulted from the protonation reactions between benzimidazole groups and phosphoric acid are tentatively illustrated as follows.

The typical peaks of benzimidazole groups are most apparent at the region  $1650\text{--}1270\text{cm}^{-1}$  in the IR spectra of  $\text{H}_3\text{PO}_4$  doped ABPBI membrane samples, however, at the region below  $1270\text{cm}^{-1}$ , most of them are overlapped by the absorbance of phosphate ion functional groups except the stable peaks assigned to benzene ring vibration and C-H out-of-plane bending at  $813$ ,  $720$  and  $678\text{cm}^{-1}$ , respectively. Compared to that of undoped ABPBI membrane, the bands assigned to the benzimidazole structure in the  $\text{H}_3\text{PO}_4$  doped samples shift to higher wave-number, e.g. that of conjugation mode between benzene ring and imidazole ring shifts from  $1541$  to  $1574\text{cm}^{-1}$ , in-plane deformation of benzimidazole from  $1429$  to  $1447\text{cm}^{-1}$ , breathing mode of benzimidazole ring from  $1281$  to  $1304\text{cm}^{-1}$  etc. This is due to the reduction of polar phosphate ions increasing the frequencies of band vibration, resulting in the shifts to high wave-numbers. It is noteworthy that the peak at  $1429\text{cm}^{-1}$  is assigned to both the imidazole in-plane deformation and C-C stretching. When doped with acid, the band attributed from benzimidazole ring in-plane deformation shifts to a higher wave-number, therefore the stable peak assigned to C-C stretching becomes apparent. Similarly, the weak peak at  $1516\text{cm}^{-1}$  which shifts from  $1541\text{cm}^{-1}$  must be attributed to the conjugation between benzene ring and non-protonated imidazole ring.

Due to the ionic reaction between phosphoric acid and basic benzimidazole, the characteristic peaks of phosphate ions differ from that of hydrous phosphoric acid and is most obvious in the region  $1200\text{--}600\text{cm}^{-1}$  in Figure 5-25b, c and d. In the IR spectra of ABPBI-47PA sample (Figure 5-25b), a shoulder appeared at about  $1060\text{cm}^{-1}$  is assigned to  $\nu_{as}(\text{PO}_3)\text{HPO}_4^{2-}$  (P=O asymmetrical stretching in  $\text{HPO}_4^{2-}$ )<sup>203</sup>, the symmetrical stretching of P=O ( $\nu_s(\text{PO}_3)\text{HPO}_4^{2-}$ ) appears at  $940\text{cm}^{-1}$ ; the peak at  $868\text{cm}^{-1}$  is attributed to  $\text{P}(\text{OH})_2$  symmetrical P-O stretching ( $\nu_s(\text{P}(\text{OH})_2)\text{HPO}_4^{2-}$ )<sup>130, 203</sup>. In the IR spectra of ABPBI-91PA (Figure 5-25d), a shoulder appeared approximately at  $1125\text{cm}^{-1}$  which is due to  $\text{PO}_2$  asymmetrical stretching ( $\nu_{as}(\text{PO}_2)\text{H}_2\text{PO}_4^-$ )<sup>203</sup>. It is noteworthy that a broad peak approximately centred at about  $1810\text{cm}^{-1}$  is considered as the combination mode (Fermi resonance) of

$\nu_s(\text{PO}_3)\text{HPO}_4^{2-}$  at  $940\sim 950\text{cm}^{-1}$  and  $\nu_s(\text{P}(\text{OH})_2)\text{HPO}_4^{2-}$  at  $866\text{cm}^{-1}$ .<sup>203</sup> These FTIR spectra assignments of phosphoric acid and phosphate ions are also summarised in Table 5-6.

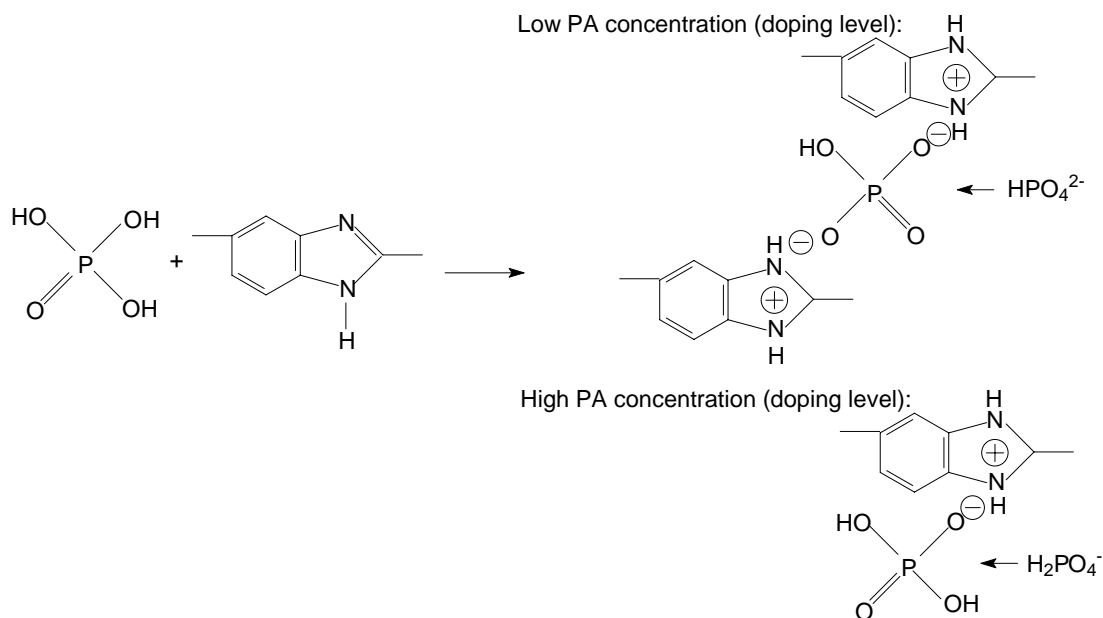


**Figure 5-26 Models proposed for protonation of the benzimidazole group by phosphoric acid**

Based on the above assignment of bands in Figure 5-25b, c and d, the band vibrations assigned to  $\text{HPO}_4^{2-}$  mainly appear in the spectra of sample with low  $\text{H}_3\text{PO}_4$  uptake (i.e. ABPBI-47PA); whilst the  $\text{PO}_2$  vibration from  $\text{H}_2\text{PO}_4^-$  appeared in the spectra of sample with high  $\text{H}_3\text{PO}_4$  uptake (i.e. ABPBI-91PA). This suggests that the protonation reaction between benzimidazole groups and phosphoric acid might occur according to the mechanism proposed in Figure 5-26. At the low level of  $\text{H}_3\text{PO}_4$  absorbance, the concentration of benzimidazole groups is higher than that of phosphoric acid. Therefore, one phosphoric acid molecule could protonate two benzimidazole groups thereby forming  $\text{HPO}_4^{2-}$ . When more  $\text{H}_3\text{PO}_4$  molecules are absorbed, one benzimidazole group protonated by one phosphoric acid molecule occurs, resulting in the form of  $\text{H}_2\text{PO}_4^-$ . This protonation mechanism can also be confirmed by the work of Bouchet et al. In their work, the typical peaks assigned to  $\text{HPO}_4^{2-}$  and  $\text{H}_2\text{PO}_4^-$  respectively, were found in PBI membranes with low and high  $\text{H}_3\text{PO}_4$  doping levels. It was reported that bands of free (or amorphous)  $\text{H}_3\text{PO}_4$  were detected at higher acid doping levels, which should be due to the benzimidazole groups fully protonated by  $\text{H}_3\text{PO}_4$  resulting in the excessive free PA.

### 5.4.2 FTIR analysis of $\text{H}_3\text{PO}_4$ doped ABPBI/SO composite membrane

The FTIR spectra of ABPBI/3SO composite membranes with various  $\text{H}_3\text{PO}_4$  uptakes are shown in Figure 5-27. In the region  $4000\text{--}2000\text{cm}^{-1}$ , the vibration modes of  $\text{N}^+\text{--H}$  stretching at  $3000\text{--}2500\text{cm}^{-1}$ , O-H of  $\text{H}_3\text{PO}_4$  asymmetric and symmetric stretching are observed; the shifts to higher wave-numbers of typical bands of benzimidazole groups due to the  $\text{H}_3\text{PO}_4$  protonation are seen at  $1582$ ,  $1460$  and  $1304\text{cm}^{-1}$ .

In the spectra of region  $2000\text{--}600\text{cm}^{-1}$ , the typical vibration modes of  $\text{HPO}_4^{2-}$  are observed, such as the P=O asymmetrical and symmetrical vibrations at  $1050$  and  $940\text{cm}^{-1}$ , respectively, whilst the P-O symmetrical at  $866\text{cm}^{-1}$ . Additionally, the combination mode of  $\nu_s(\text{PO}_3)\text{HPO}_4^{2-}$  and  $\nu_s(\text{P}(\text{OH})_2)\text{HPO}_4^{2-}$  is found at the region  $1950\text{--}1750\text{cm}^{-1}$ . In addition, the absence of substantiated absorbance bands from  $\text{H}_2\text{PO}_4^-$  and  $\text{H}_3\text{PO}_4$  shows the  $\text{HPO}_4^{2-}$  predominates in the sample.

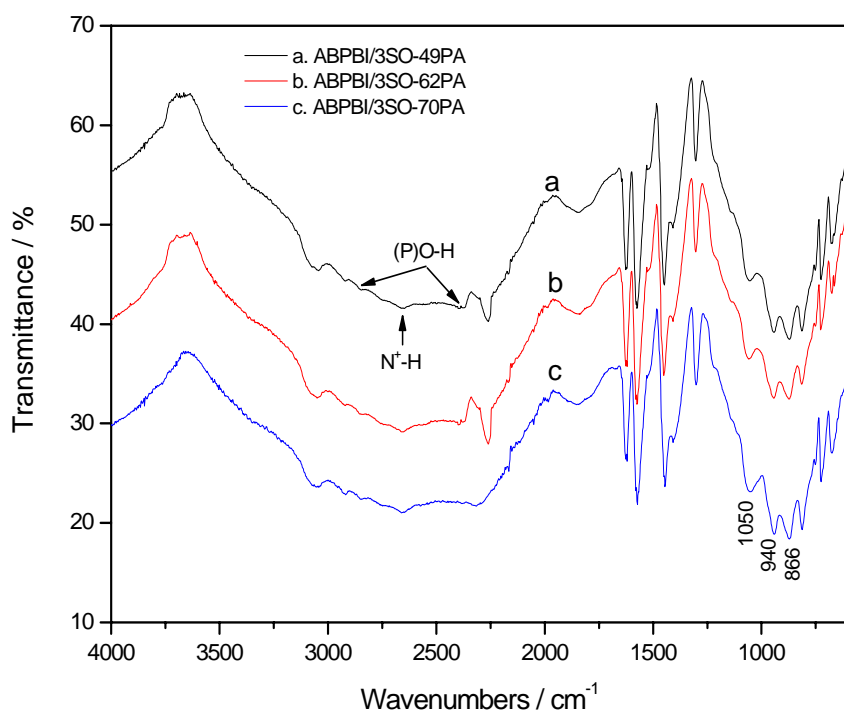
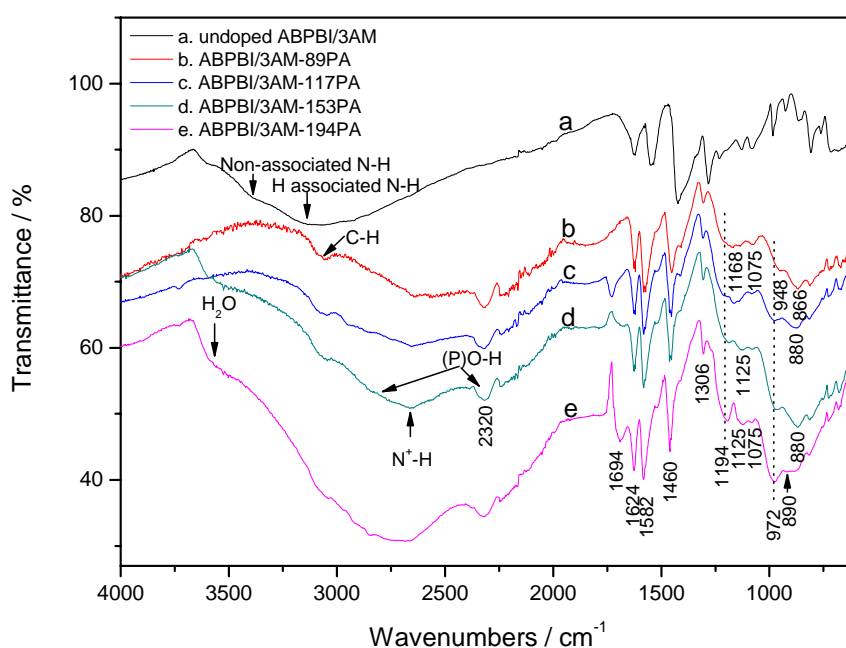


Figure 5-27 FTIR spectra of a. ABPBI/3SO-49PA, b. ABPBI/3SO-62PA and c. ABPBI/3SO-70PA

### 5.4.3 FTIR analysis of $\text{H}_3\text{PO}_4$ doped ABPBI/AM composite membrane

The FTIR spectra of  $\text{H}_3\text{PO}_4$  doped ABPBI/3AM membranes are shown in Figure 5-28. In the region  $4000\text{--}2000\text{cm}^{-1}$ , the IR spectra are similar to that which appeared in the  $\text{H}_3\text{PO}_4$  doped ABPBI and ABPBI/3SO membranes thereby sharing the same interpretations. The main difference is considered from the typical characteristic peaks of phosphate ions at the low wave-number region and is discussed as follows.



**Figure 5-28** FTIR spectra of a. undoped ABPBI/3AM, b. ABPBI/3AM-89PA, c. ABPBI/3AM-117PA, d. ABPBI/3AM-153PA and e. ABPBI/3AM-194PA membranes

In the spectra of ABPBI/3AM-89PA sample, the bands at  $1075$ ,  $948$  and  $866\text{cm}^{-1}$  are assigned to  $\nu_s(\text{PO}_2)\text{H}_2\text{PO}_4^-$ ,  $\nu_{as}(\text{P}(\text{OH})_2)\text{H}_2\text{PO}_4^-$  and  $\nu_s(\text{P}(\text{OH}))\text{HPO}_4^{2-}$ , respectively. The broad peak centred at about  $1168\text{cm}^{-1}$  that appeared in the spectra of ABPBI/3AM-89PA sample shifts into a peak with a shoulder in that of ABPBI/3AM-117PA and ABPBI/3AM-153PA samples, finally splits into two peaks at  $1194$  and  $1125\text{cm}^{-1}$  in that of ABPBI/3AM-194PA sample. These two peaks are attributed to  $\nu_{as}(\text{PO})\text{H}_3\text{PO}_4$  and  $\nu_{as}(\text{PO}_2)\text{H}_2\text{PO}_4^-$ , respectively.<sup>203</sup> The Fermi resonance of  $\text{HPO}_4^{2-}$  is observed at  $1810\text{cm}^{-1}$  in the spectra of ABPBI/3AM-89PA and ABPBI/3AM-117PA samples. The peak at  $972\text{cm}^{-1}$  is observed in the spectra of

ABPBI/3AM with  $\text{H}_3\text{PO}_4$  uptake above 88% which is due to the P-O(H) asymmetrical stretching ( $\nu_{as}(\text{P}(\text{OH})_3\text{H}_3\text{PO}_4)$ )<sup>203</sup>. The vibration of P-O(H) ( $\nu_s(\text{P}(\text{OH})_2\text{H}_2\text{PO}_4^-)$ ) is detected at  $880\text{cm}^{-1}$  in those samples with  $\text{H}_3\text{PO}_4$  uptake above 88%, which is also broadened in that of ABPBI/3AM-194PA by the peak attributed to P-O(H) symmetrical stretching ( $\nu_s(\text{P}(\text{OH})_3\text{H}_3\text{PO}_4)$ ) at  $890\text{cm}^{-1}$ . The peak appeared at  $1694\text{cm}^{-1}$  in the spectra of 8M and 10M  $\text{H}_3\text{PO}_4$  doped composite membranes is due to the Fermi resonance of  $\text{H}_2\text{PO}_4^-$ .<sup>203</sup> The assignment of bands for  $\text{HPO}_4^{2-}$ ,  $\text{H}_2\text{PO}_4^-$  and  $\text{H}_3\text{PO}_4$  is summed up in Table 5-6.

With the increased  $\text{H}_3\text{PO}_4$  uptake from 88% to 153%, the peak for the Fermi resonance of  $\text{HPO}_4^{2-}$  decrease in intensity and disappears in that of ABPBI/3AM-153PA; whilst the peak of the Fermi resonance of  $\text{H}_2\text{PO}_4^-$  increases with the increased  $\text{H}_3\text{PO}_4$  uptake from 153% to 194%. This suggests that  $\text{HPO}_4^{2-}$  predominates in the sample with low  $\text{H}_3\text{PO}_4$  uptake (i.e. 88%). With  $\text{H}_3\text{PO}_4$  uptake increasing (i.e. from 153% to 194%), the associated anion is rather  $\text{H}_2\text{PO}_4^-$ . Also the peak due to the vibration of  $\text{N}^+\text{-H}$  increases with the increase of  $\text{H}_3\text{PO}_4$  uptake, showing the increased degree of protonation results from the enhanced acid absorbance. A shoulder appearing at  $3660\sim 3500\text{cm}^{-1}$  in the spectra of ABPBI/3AM-153PA and ABPBI/3AM-194PA is due to the absorbed moisture. Additionally, the vibrations of amorphous  $\text{H}_3\text{PO}_4$  at  $1194$  and  $972\text{cm}^{-1}$  increase intensively with the elevated  $\text{H}_3\text{PO}_4$  uptakes, indicating a maximum degree of protonation must have been reached during this term. Since one repeat unit of ABPBI or benzimidazole group is protonated theoretically by one phosphoric acid molecule<sup>130</sup>, the excess  $\text{H}_3\text{PO}_4$  exists rather in free form.

**Table 5-6 FTIR spectra assignment of phosphoric acid and phosphate ions (solid state)**

Band	Wavenumbers / Assignment					
	$\text{H}_3\text{PO}_4$		$\text{H}_2\text{PO}_4^-$		$\text{HPO}_4^{2-}$	
(P)O-H	3000-2700	$\nu_{as}(\text{OH})\text{H}_3\text{PO}_4$	3000-2700	$\nu_{as}(\text{OH})\text{H}_2\text{PO}_4^-$	3000-2700	$\nu_{as}(\text{OH})\text{HPO}_4^{2-}$
	2390-2270	$\nu_s(\text{OH})\text{H}_3\text{PO}_4$	2320	$\nu_s(\text{OH})\text{H}_2\text{PO}_4^-$	2390-2700	$\nu_s(\text{OH})\text{HPO}_4^{2-}$
P=O	1194	$\nu_{as}(\text{PO})\text{H}_3\text{PO}_4$	1125	$\nu_{as}(\text{PO}_2)\text{H}_2\text{PO}_4^-$	1050	$\nu_{as}(\text{PO}_3)\text{HPO}_4^{2-}$
			1075	$\nu_s(\text{PO}_2)\text{H}_2\text{PO}_4^-$	940	$\nu_s(\text{PO}_3)\text{HPO}_4^{2-}$
P-O(H)	972	$\nu_{as}(\text{P}(\text{OH})_3)\text{H}_3\text{PO}_4$	948	$\nu_{as}(\text{P}(\text{OH})_2)\text{H}_2\text{PO}_4^-$		
	890	$\nu_s(\text{P}(\text{OH})_3)\text{H}_3\text{PO}_4$	880	$\nu_s(\text{P}(\text{OH})_2)\text{H}_2\text{PO}_4^-$	866	$\nu_s(\text{P}(\text{OH}))\text{HPO}_4^{2-}$

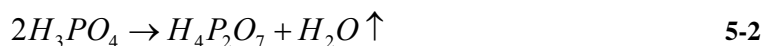
### 5.5 Thermostability of $H_3PO_4$ Doped Membranes

The thermostability of  $H_3PO_4$  doped ABPBI and its composite membranes were investigated by TGA measurement.

The TGA curves of 85.0wt%  $H_3PO_4$  solution are shown in Figure 5-29. It can be seen that there are three stages of weight loss occurring at the range of 20~266°C, 266~506°C and 506~750°C corresponding to 26.4, 10.1 and 61.0% of weight loss.

Since there is 15% of water in the  $H_3PO_4$  solution and the decomposition of  $H_3PO_4$  starts from 158°C, the weight loss before that should owe to the evaporation of water. The found value of 15.9% roughly matches the real water content.

The dimerisation of  $H_3PO_4$  corresponds to different decomposition reactions shown as following<sup>14</sup>:



In theory, the dimerisation of phosphoric acid (or orthophosphoric acid) (in reaction 5-1) produces pyrophosphoric acid and results in 9.2% of weight loss. With the increase of temperature, the continuous dimerisation comes from the dimerisation of pyrophosphoric acid (in reaction 5-2), resulting in 10.1% of weight loss. The final decomposition reaction (reaction 5-3) results in phosphorus pentoxide ( $P_2O_5$ ) and water which both evaporate from the crucible. It can be seen that the found values well match the calculated results.

The TGA curve of ABPBI and ABPBI/POSS doped from 10M  $H_3PO_4$  is respectively shown in Figure 5-30. It can be seen that the weight losses due to water evaporation before 158°C, subsequent continuous release of water, the dimerisation of  $H_3PO_4$  started from 158°C and the decomposition of polymer chains after about 500°C are apparent according to the TGA and the relative DTG curves, indicating that the thermostability of  $H_3PO_4$  doped membranes is limited by the thermostability of PA.

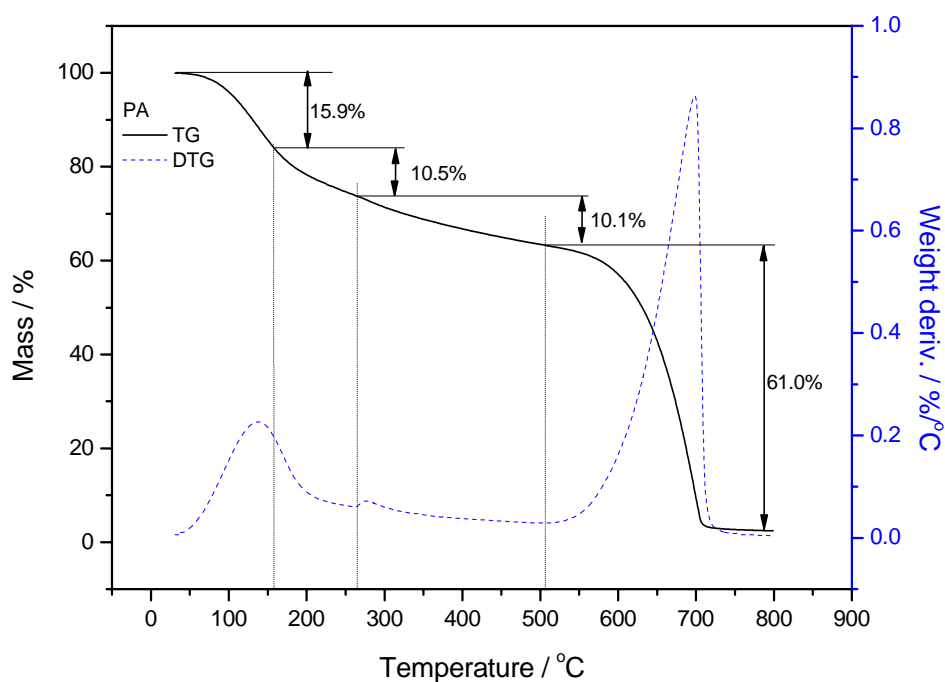


Figure 5-29 TG curve of 85%  $\text{H}_3\text{PO}_4$  solution

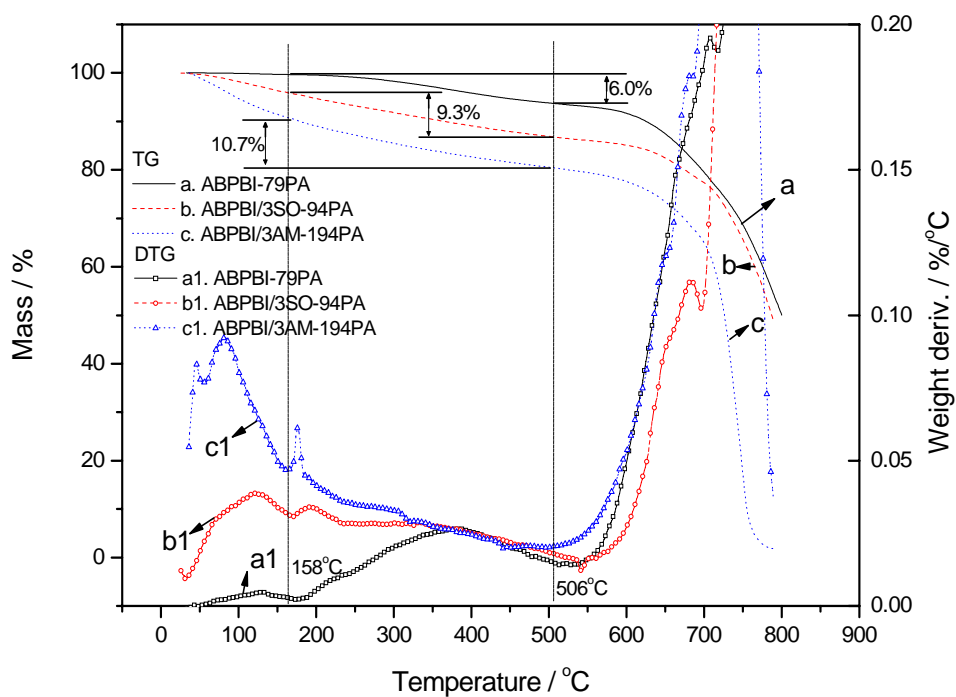


Figure 5-30 TGA curves of 10M  $\text{H}_3\text{PO}_4$  doped membranes: a. ABPBI-79PA, b. ABPBI/3SO-94PA and c. ABPBI/3AM-194PA

As discussed in section 4.1.3.2 in terms of the thermostability of pristine ABPBI, the weight loss before 470°C included the elimination of water and residual low mass polymers, whilst the weight loss of undoped ABPBI/POSS composite samples included the gradual degradation of POSS particles at this range. The decomposition of phosphoric acid also locates at this temperature range. Thus it generates the difficulty to quantitatively analysis the amount of water decomposed from absorbed phosphoric acid in the acid doped samples. However, the weight loss resulted from the degradation of POSS can be neglected since the amount of POSS is less than 5% and the value of weight loss before the decomposition of POSS inorganic core is very small. Thus, it is possible to qualitatively compare the  $\text{H}_3\text{PO}_4$  absorptivity when all samples are treated at the same condition. Figure 5-30 compares the thermostabilities of 10M  $\text{H}_3\text{PO}_4$  doped ABPBI, ABPBI/3SO and ABPBI/3AM membranes. At the decomposition range of  $\text{H}_3\text{PO}_4$  (158~506°C), 6.0% of weight loss happens in 10M  $\text{H}_3\text{PO}_4$  doped ABPBI sample, whilst 9.3% and 10.1% of weight loss in 10M  $\text{H}_3\text{PO}_4$  doped ABPBI/3SO and ABPBI/3AM, respectively. The higher values of weight loss of composite membranes indicate the higher  $\text{H}_3\text{PO}_4$  absorbance, resulting in a higher amount of evaporated water dimerised from PA, which is also confirmed by the values of  $\text{H}_3\text{PO}_4$  uptake measured from the weights before and after the doping process, i.e. 79% of  $\text{H}_3\text{PO}_4$  uptake was found in 10M  $\text{H}_3\text{PO}_4$  doped ABPBI, whilst 94% and 194% of  $\text{H}_3\text{PO}_4$  uptake in 10M  $\text{H}_3\text{PO}_4$  doped ABPBI/3SO and ABPBI/3AM, respectively.



# Chapter 6 RESULTS AND DISCUSSION:

## PROTON CONDUCTIVITY OF ABPBI BASED POLYMER ELECTROLYTE MEMBRANES

### 6.1 Background and Theory of Impedance Spectroscopy

#### 6.1.1 Introduction of impedance spectroscopy

The proton conductivity is generally obtained from the measurement of impedance or resistivity of the proton conductive membrane against the flow of either direct current (*dc*) or alternating current (*ac*).<sup>213</sup> The electrical impedance ( $Z$ ) is defined as the ratio of sinusoidal voltage ( $\tilde{V}$ ) applied to an electrical system to the resulting current ( $\tilde{I}$ ). It is represented as a complex quantity that consists of a real part (resistance,  $Z'$  or  $R$ ) and an imaginary part (reactance,  $Z''$ ) with phase angle  $\theta$  (shown in Figure 6-1).

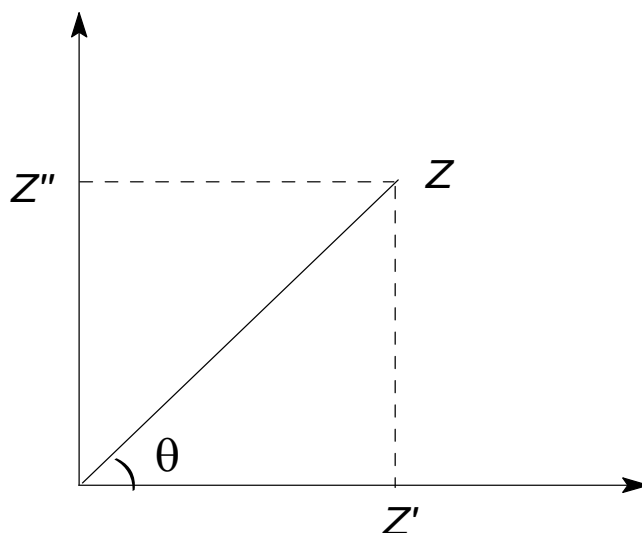


Figure 6-1 A Nyquist plot of imaginary impedance ( $Z''$ ) against real impedance ( $Z'$ ) to define electrical impedance ( $Z$ ) and phase angle ( $\theta$ )

The impedance can be expressed with the rectangular coordinate form (or so-called Nyquist plot):

$$Z = Z' + iZ'' = |Z| \cos \theta + i|Z| \sin \theta = \tilde{V} / \tilde{I} \quad 6-1$$

where, the phase angle,  $\theta = \tan^{-1}(Z'/Z'')$ , degree; the absolute magnitude of total impedance,  $|Z| = \sqrt{Z'^2 + Z''^2}$ , ohm( $\Omega$ );  $i = \sqrt{-1}$ .

If only a pure resistance exists in a cell, the current and potential are in the same phase, so  $Z=Z'=R$ . Whilst a cell contains only a capacitance, the phase difference between the current and potential is 90 degree, thus  $Z=Z''$ . However, the situation in an electrochemical cell is much more complex and often represented by an equivalent circuit as shown in Figure 6-2a.

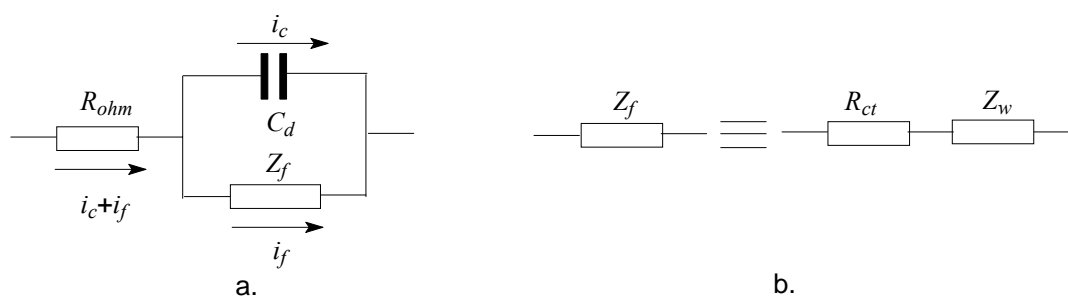


**Figure 6-2 A typical equivalent circuit often used for an electrochemical cell: a. the equivalent circuit, b. the subdivision of the Faradic impedance**

The total current through the electrode interface is the sum of contributions from the faradic current ( $i_f$ ) and double-layer charging current ( $i_c$ ). The double-layer capacitance ( $C_d$ ) is nearly a pure capacitance. The resistance ( $R_\Omega$  or  $R_{ohm}$ ) is representing the ohmic resistance of the cell since the entire current pass through these pure resistors (electrolyte, electrode etc.). The faradic process cannot be represented by simple linear circuit elements like  $R$  and  $C$ , whose values are independent of frequency. Therefore the Faradic impedance ( $Z_f$ ) must be considered as the complex impedance.<sup>214</sup> There are various ways of subdividing Faradic impedance. One of the simplest ways is to subdivide into charge transfer resistance ( $R_{ct}$ ) and mass transfer impedance (or Warburg impedance,  $Z_w$ ).

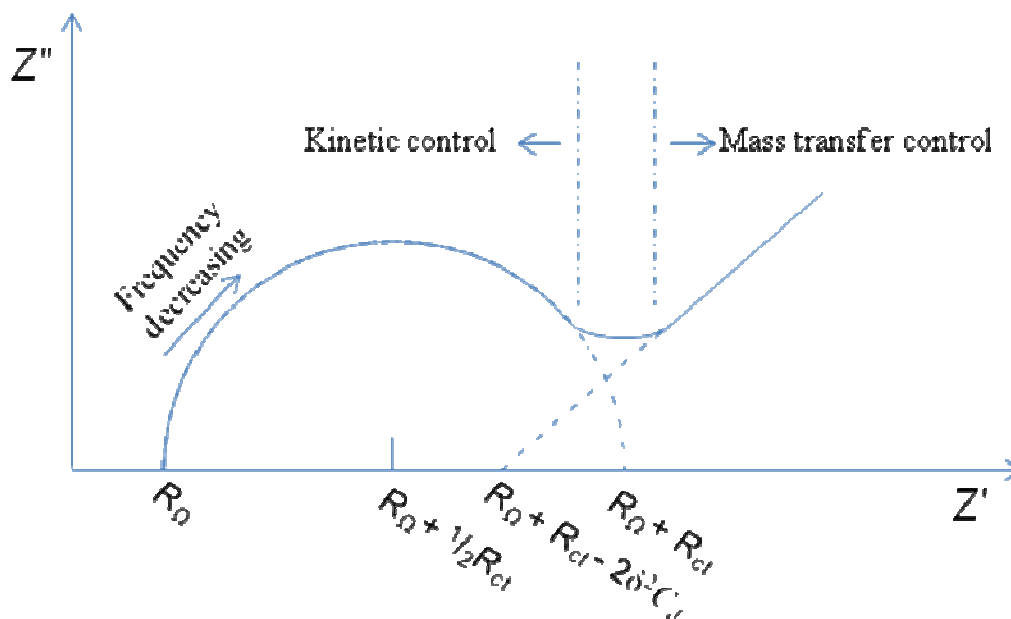


Figure 6-3 A Nyquist plot of the impedance for an electrochemical cell<sup>214</sup>

A Nyquist plot of the equivalent circuit of an electrochemical cell (Figure 6-3) is to explain the relationship between  $Z'$  and  $Z''$  which depends on the frequency<sup>214</sup>.

When the frequency is low, the relationship between  $Z'$  and  $Z''$  adapts to the following equation

$$Z'' = Z' - R_{\Omega} - R_{ct} + 2\delta^2 C_d \quad 6-2$$

where  $\delta$  is the constant of dependent on the diffusion coefficient and concentration of the electro-active species.

As shown in Figure 6-3 (the straight line part), the plot of  $Z''$  against  $Z'$  is a straight line with unit slope and the intercept of this straight line is  $R_{\Omega} + R_{ct} - 2\delta^2 C_d$ . In the low frequency range, the frequency dependence comes only from Warburg impedance, thus the linear correlation of  $Z'$  and  $Z''$  is the characteristic of a diffusion-controlled electrode process.

At high frequency, the impedance is dominated by the charge-transfer resistance and the double-layer capacitance, whilst  $Z_w$  becomes unimportant relative to  $R_{ct}$ . The relationship between  $Z'$  and  $Z''$  can be represented by

$$(Z' - R_\Omega - R_{ct}/2)^2 + Z''^2 = (R_{ct}/2)^2 \quad 6-3$$

Hence the plot of  $Z''$  versus  $Z'$  gives a semicircular centered at  $Z' = R_\Omega + R_{ct}/2$  with a radius of  $R_{ct}$  (the semi-circle part in Figure 6-3).

When the impedance is measured at a wide frequency range, the above two different factors (charge transfer and mass transfer) dominated modes can be combined and shown in Figure 6-3 (solid curve). However, the boundary of the two regions is not well defined and its determining factor is the relation between charge transfer and Warburg impedance. If the electrochemical kinetic is slow, the charge-transfer resistance makes a significant contribution to total impedance, whilst the Warburg impedance is less important, hence the Nyquist plot becomes a semi-circle with a very small mass transfer controlled region. If the kinetics are very fast, the impedance from charge transfer can be ignored compared to Warburg impedance; thus, mass transfer dominates the electrode process, and a straight line is obtained and the semi-circle can hardly be seen.

Although the impedance can be measured by the *dc* and *ac* mode, the *ac* technique still is the most appropriate choice and widely used by many groups<sup>215-217</sup>. As protons are the sole mobile charges in these electrolyte membranes, their conductivity can be measured by a *dc* electrochemical impedance spectroscopy (EIS) technique using only the  $H/H^+$  reversible electrodes, which is expensive and too complex for a routine test. Additionally, when the proton conductivity is measured using irreversible electrodes in the *dc* mode, unfavourable ionic blocking is formed and subsequently results in inaccurate measurement. Therefore, an *ac* EIS technique allowing polarisation effects at the irreversible electrodes (i.e. Pt) to be avoided is commonly considered as the most appropriate method for solid electrolytes.<sup>216</sup>

### 6.1.2 Introduction of measurement techniques of electrochemical impedance spectroscopy (EIS)

When the impedance is measured by the *ac* EIS technique, the auto-balancing bridge method is most favourable for general purpose measurement due to its wide frequency range (i.e. from 5 Hz to 40 MHz) and its high accuracy over a wide impedance measurement range (i.e. from 1 milli ohm to 100 meg ohm).<sup>213</sup> In the

auto-balancing bridge, there are four coaxial terminals, i.e. two reference electrodes (voltage Hi, voltage Lo), one working electrodes (current Hi) and one counter electrode (current Lo). The impedance is computed from the voltage difference between reference electrodes. However, the different connection modes of interconnecting the four terminals (which are relative to different methods) generate different results of sample impedances. Of these methods, the four-probe method and two-probe method is generally used. Basically, the result from four-probe method is more accurate than that from two-probe which is due to the elimination of the extra effects from the lead impedance in the former method.<sup>215</sup>

However, in the four-probe method, the conductivity is measured in the longitudinal direction on a membrane side along a face exposed to environment. Obviously, this method is only suitable for the isotropic membranes with surface properties indistinguishable from the bulk. In the two-probe method, the conductivity is measured in the transverse direction, which is the same as the proton conducting direction in a real fuel cell system, thus it can reflect the virtual membrane proton conducting property. In addition, in the two-probe cell configuration, the interfacial impedance is expected to dominate in the lower frequency range. It is reported that the membrane ionic resistance can be satisfactorily resolved from interfacial impedance only when the frequency is above 100Hz<sup>218</sup>.

## **6.2 Experimental Details**

### **6.2.1 Experimental apparatus**

Since the effect of extra impedance (i.e. interfacial impedance) can be eliminated when measured at above 100Hz as discussed above, and the proton conducting direction is the same as that in a real fuel cell, the two-probe EIS technique is employed in this project.

A Solartron Analytical 1280 Electrochemical Measurement Unit (1280 EMU, Solartron Analytical Ltd.) was used to measure the impedance of membranes (shown in Figure 6-4). The 1280 EMU is composed of an electrochemical interface (ECI), a frequency response analyser (FRA) and a controller of computer system. The controller is responsible to send commands to the ECI and receive impedance data

from the FRA. According to these commands from the controller, the ECI, which is used as a galvanostat or potentiostat, provides a constant current or voltage to maintain the *dc* polarisation of an electrochemical cell and measures the resulting cell behaviour. The FRA, on the one hand, is used as a precision signal generator to generate an *ac* perturbing signal for the cell (which will be added to the *dc* polarisation provided by the ECI) and, on the other hand, is used as a analyzer to analyse the *ac* component of cell polarisation (which is then output as cell impedance data to the controller). Finally, those impedance data returned to the controller are treated with the impedance software of Z-Plot.

The home-made electrochemical cell connected with the 1280 EMU is a simply equipped EMA (electrode-membrane assembly). The electrolyte membrane was sandwiched between two circular platinum (Pt) electrodes (diameter 2.00mm, purity 99.95%, Goodfellow Cambridge Ltd.). The two Pt rods were vertically fixed in the insulator PTFE frame (in Figure 6-4). Two copper wires, respectively welded to two Pt rods, were connected with the 1280 EMU via two-probe EIS mode. It was worth mentioning that each Pt rod must be polished well according to standard electrode polishing guidelines. In details, a Pt rod was initially sanded with Buehler CarbiMet silicon carbide paper of grit numbers 240, 400 and 600 (Buehler Ltd., USA), then carefully polished on a rotating polishing machine using 1 $\mu$ m alumina (Buehler Ltd., USA) first, then 0.05 $\mu$ m diamond (Buehler Ltd., USA) in order on different microcloth pads (no. 40-7208 and 40-7308, Buehler Ltd., USA). The electrode was cooled with deionised water while polishing. The final step was ultrasonic cleaning for about 1 minute in a beaker of ethanol, followed by washing with deionised water. At that point the Pt electrode working face had a shiny, mirror-like appearance. Before each experiment, the polishing step was begun by polishing with 0.05 $\mu$ m diamond.

During the impedance measurement, a 320g mass was placed on the upper electrode while the bottom electrode was fixed. This is to ensure that the electrodes and the membrane were in good contact without significant compression on the membrane. In a two-probe mode, the impedance analyser often works in a potentiostatic mode with a small applied potential perturbation. In this experiment, the 10mV perturbation potential was used.

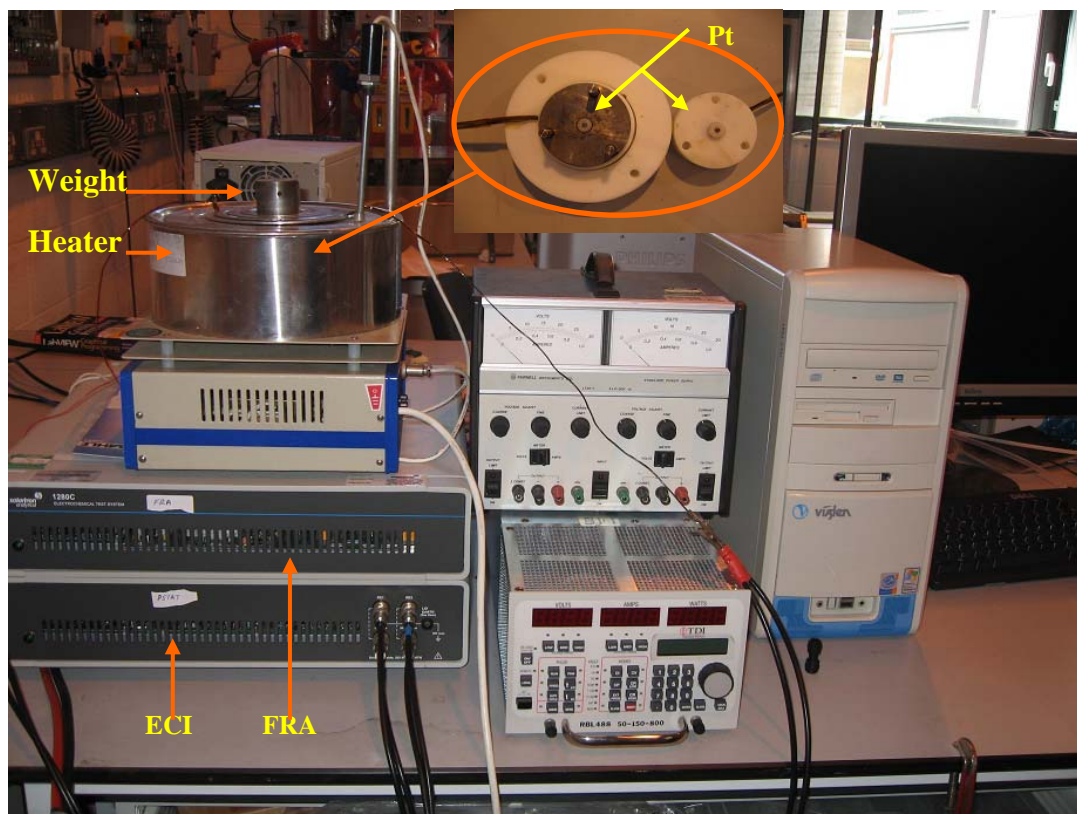


Figure 6-4 Conductivity measurement unit used in this work

### 6.2.2 Calculation of the proton conductivity

The proton conductivity ( $\sigma$ ) of an electrochemical cell can be calculated by the following equation:

$$\sigma = d / (R \times A) \quad 6-4$$

where  $d$  is the distance between two electrodes, i.e. the thickness of a sample membrane, cm;  $A$  is the testing area of a sample membrane, i.e. the area of working face of Pt rod (in this experiment, the diameter of Pt rod is 2.00mm, therefore,  $A=3.14 \times 10^{-2} \text{ cm}^2$ );  $R$  is the bulk resistance of the membrane sample derived from an impedance analyser,  $\Omega$ .

Here the bulk resistance consists of the ohmic resistance, the contact resistance and the intrinsic resistance of Pt electrodes. It is considered that the bulk resistance is the ohmic resistance, because the contact resistance and the resistance of Pt electrodes are small enough to be negligible compared with the ohmic resistance.<sup>215</sup>

Since no bias voltage was applied on the membrane, and the perturbation voltage was very small (10 mV), which was not sufficient to drive any significant electrochemical reactions on the electrodes, thus meaning the charge transfer resistance can be assumed to be infinite, the Faradic impedance (Figure 6-2, a.) can thus be ignored. Double layer capacitance always exists in an electrochemical cell. The equivalent circuit at high frequencies of the electrochemical cell was simplified into the membrane resistance ( $R_m$ ) and the double layer capacitance ( $C_d$ ) (shown in Figure 6-5, a). Accordingly,  $R_m$  was the value of the intercept on the impedance plot at the high frequency region.

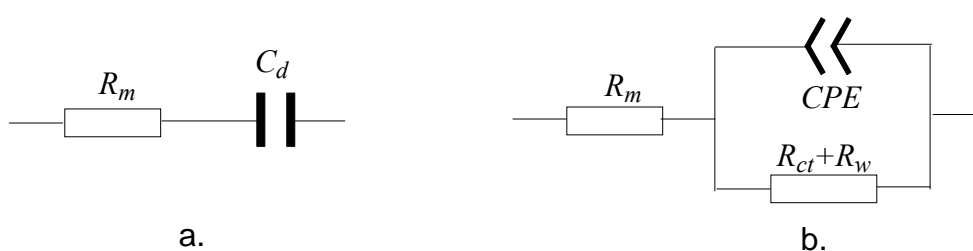


**Figure 6-5** Equivalent circuit of the membrane impedance measurement system (a) at high frequency; (b) in this experiment

However, the highest frequency of Solartron 1280 EMU provided is 20 kHz. It is indicated that the frequency was not high enough to drive the impedance plots to intercept the real part ( $Z'$  axis). In other words,  $R_m$  couldn't be directly obtained from the membrane impedance plot.

In order to ensure that the high frequency intercept on an impedance plot represents the membrane resistance, one of the methods is to generate different bias voltages on the membrane. Li, X's experimental results<sup>219</sup> showed that the applied various bias voltages (from 0 to 1.8V) had almost no effect on the intercept on  $Z'$  axis, which indicated that the membrane resistance did not depend on the bias voltage. However, a high bias voltage could induce the unexpected electrochemical reactions to happen thereby affecting the result of the membrane resistance measurement, since the equivalent circuit was based on the assumption that the Faradic impedance could be ignored when no significant electrochemical reaction was in evidence during the measurement.



Another valuable method is to use an equivalent circuit to fit the measured impedance plots and simulate from a wide frequency range thus obtaining the intercept on  $Z'$  axis. In this experiment, the equivalent circuit was employed including Faradic resistance as the Faradic resistance could not be ignored at this frequency range (from 20 kHz to 100Hz). Additionally, a constant phase element (CPE) was brought in and replaced the double layer capacitor. Often a CPE is used in a model in place of a capacitor to compensate for non-homogeneity in the system. For example, a rough or porous surface can cause a double layer capacitance to appear as a constant phase element. In practice, the membrane surfaces were quite rough compared with the mirror-like Pt electrodes. Hence, the equivalent circuit used in this experiment was illustrated in Figure 6-5, b. Through this equivalent circuit, the membrane impedance was read from the intercept on  $Z$  axis at high frequency. Finally the proton conductivity was calculated through equation 6-4.

### **6.3 Evaluation of Measurement Technology**

#### **6.3.1 Verification of the equivalent circuit and calculation of conductivity**

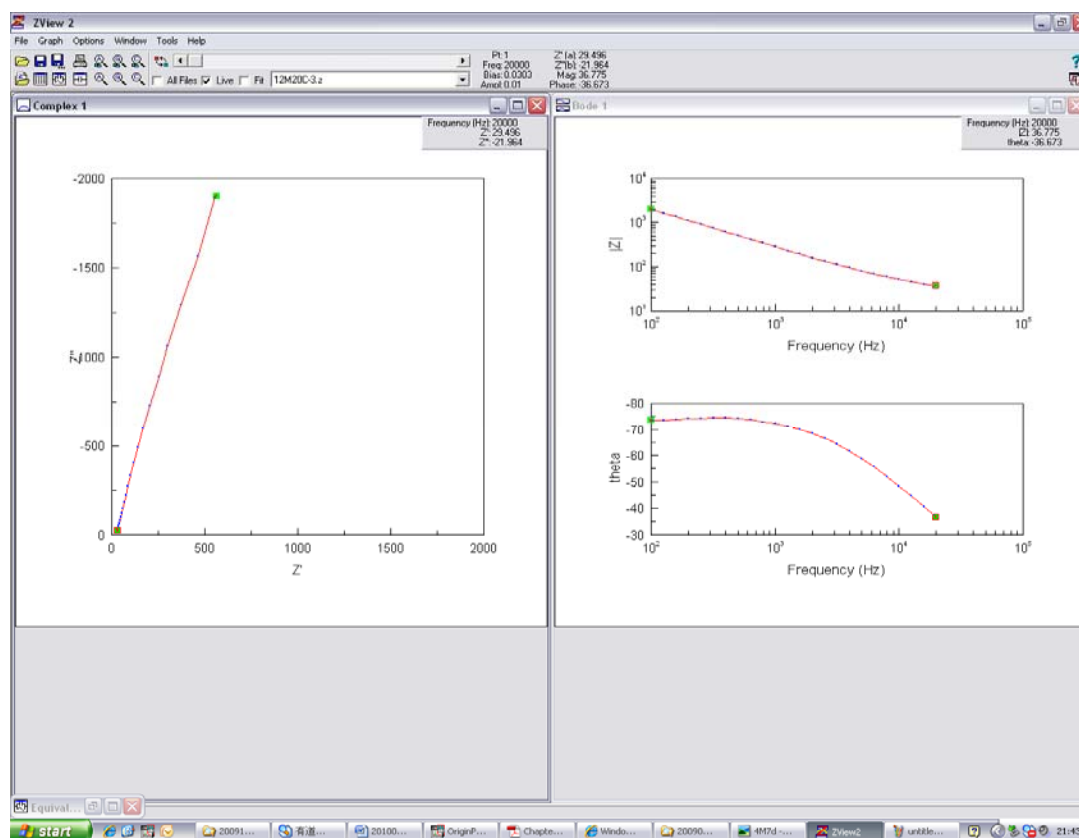
The equivalent circuit was verified by fitting the Nyquist plot output from the EIS equipment with it to check the repeatability of both curves. Both the Nyquist plot of ABPBI-92PA and Nafion 117 samples with the respective thickness of 0.023cm and 0.0178cm were presented here. The fitted Nyquist plot subsequently was simulated in a wide frequency range so that it could intercept the  $Z'$  axis and obtain the membrane resistance.

Figure 6-6 shows the Nyquist plot of water saturated ABPBI-94PA measured in the frequency range of 20 kHz~100Hz at 20°C. The coordinate systems of  $|Z|$  and  $\theta$  against frequency shown in this figure are the Bode plot, different expression form of impedance. The Nyquist plots fitted by the equivalent circuit (as shown in Figure 6-5b) were given in Figure 6-8, whilst a simulated curve of Nyquist plots at the wide frequency range of  $10^{10} \sim 10^{-3}$ Hz was presented in Figure 6-7. With simulation from the wide frequency range of  $10^{10} \sim 10^{-3}$ Hz, a semi-circle was also observed and the intercept on the impedance plot ( $Z'$  axis) or the membrane resistance was achieved at the frequency between  $10^6 \sim 10^5$ Hz, which was 24.9( $\Omega$ ), so that the conductivity

according to equation 6-4 was worked out as  $2.9 \times 10^{-2} \text{ S.cm}^{-1}$ . This was also at the same order of magnitude compared to the results measured at similar conditions from the literature<sup>127</sup>.

Comparing the real and fitted Nyquist plots, the highly congruent curves indicate that the equivalent circuit successfully fitted the real circuit; meanwhile, the semi-circle shape of Nyquist plots simulated from a wide frequency range agreed with Figure 6-3 and the related analysis discussed above. Additionally, it is also indirectly supported by the consistency of calculated conductivity in this work and the results from the literature.

Similarly, the resistance of a commercial Nafion 117 membrane was also worked out with this equivalent circuit and shown in Figure 6-9. The obtained resistance of the membrane of  $51.0 \Omega$  was allowed to work out the proton conductivity with  $1.1 \times 10^{-2} \text{ S.cm}^{-1}$ , which is close to the published results<sup>220</sup>.



**Figure 6-6 Nyquist plot of ABPBI-94PA measured in a frequency range of 20kHz~100Hz at 20°C and saturated condition)**

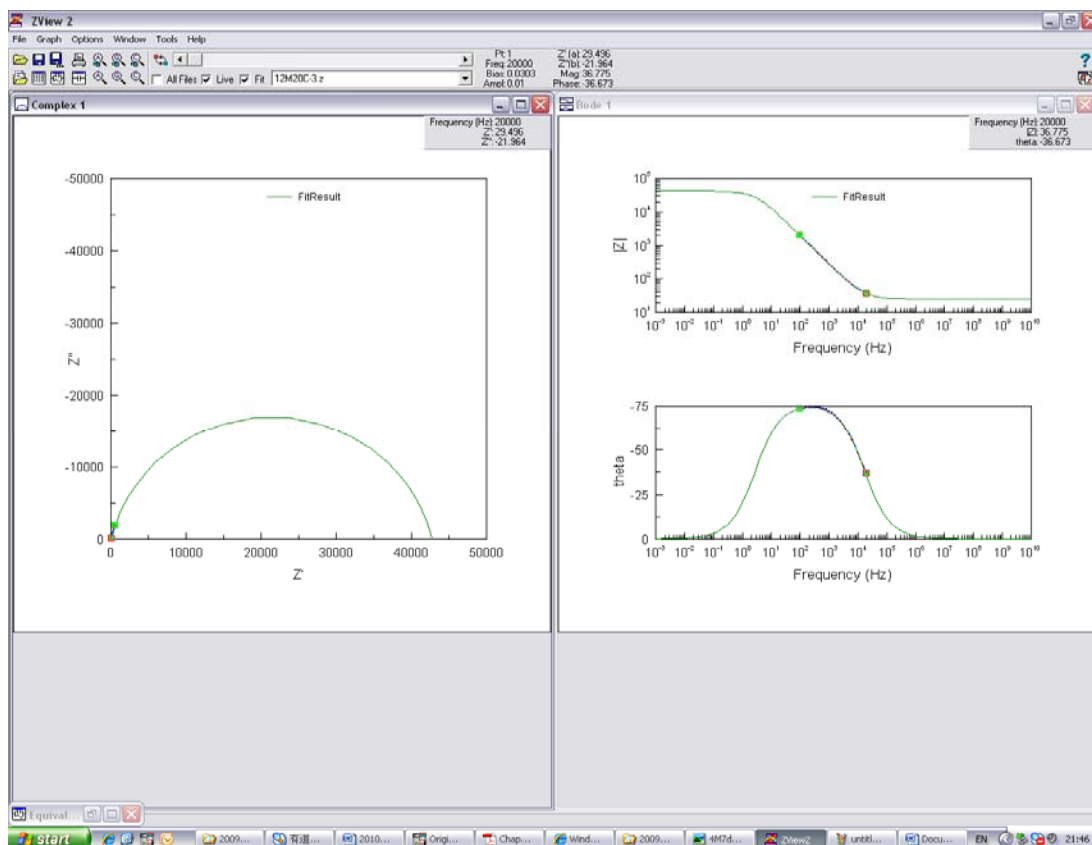
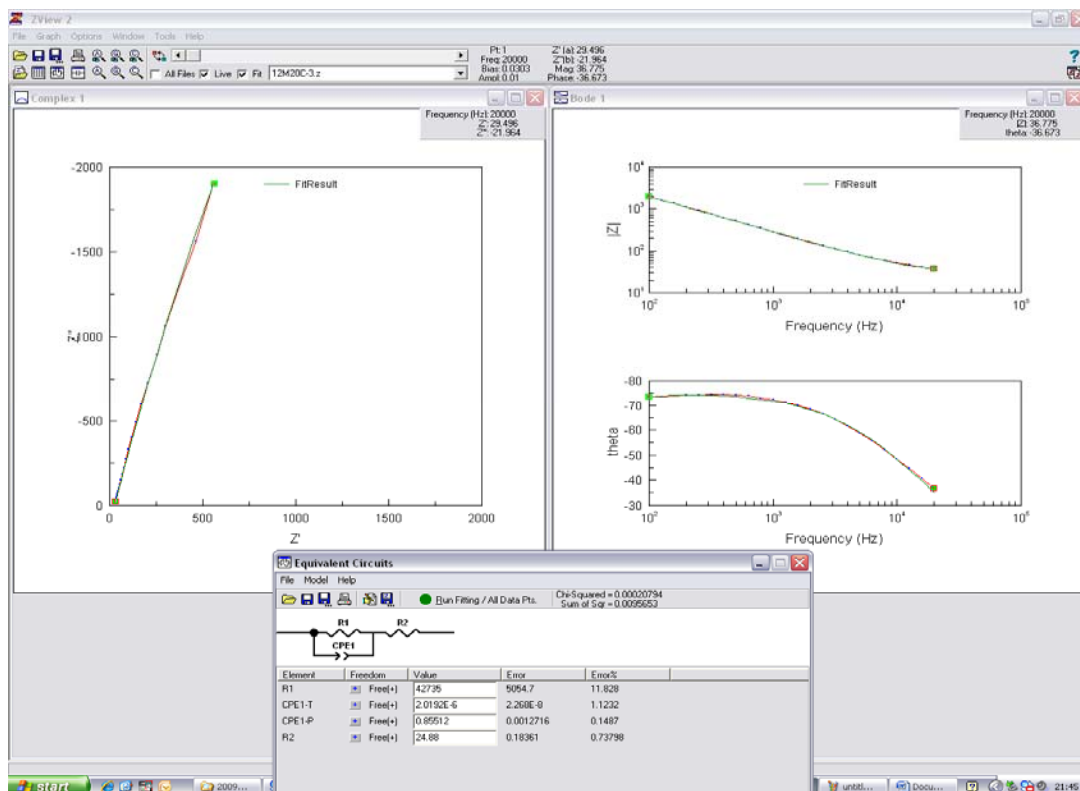
Figure 6-7 Simulated Nyquist plot of ABPBI-94PA in the frequency range of  $10^{10}$  Hz~ $10^{-3}$  Hz

Figure 6-8 Fitted Nyquist plot of ABPBI-94PA in the measuring frequency range (20 kHz~100 Hz)

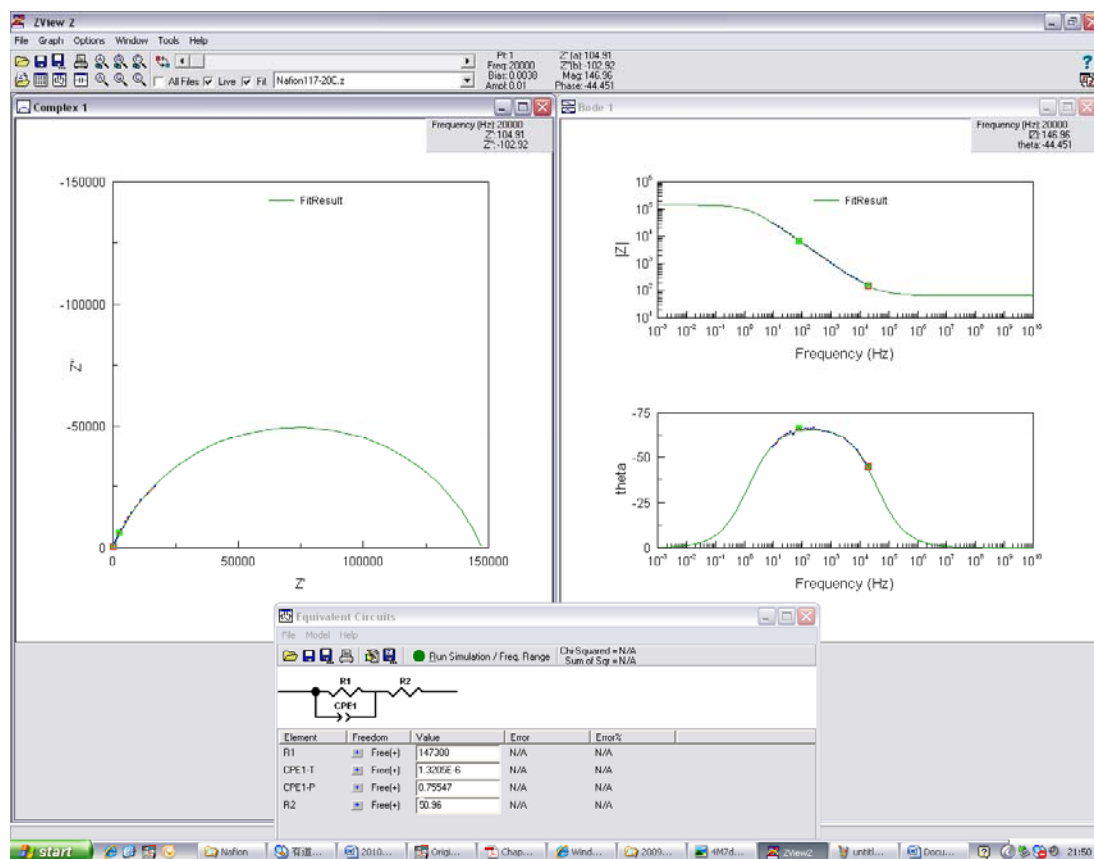
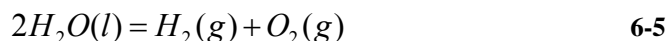


Figure 6-9 Simulated Nyquist plot of Nafion 117 in the frequency range of  $10^{10}$  Hz~ $10^{-3}$  Hz

### 6.3.2 Effect of bias voltage on the proton conductivity

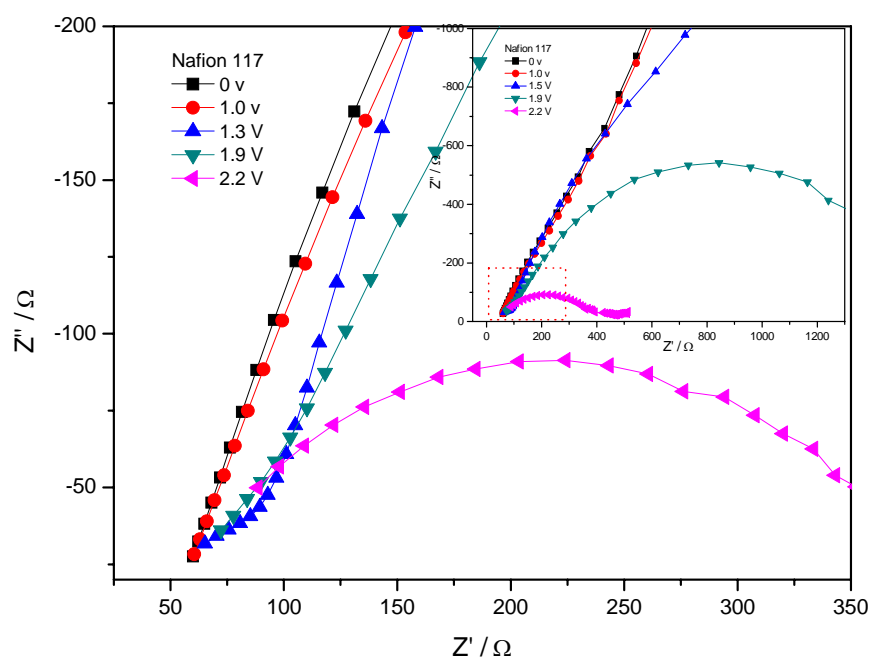
The effect of bias voltage on the proton conductivity was investigated by measuring the membrane resistance with various bias voltages applied on a membrane sample.

Figure 6-10 shows the Nyquist plots of Nafion 117 membrane impedance with various bias voltages applied. It can be seen that, with the bias voltage increased from 0 to 1.0V, the Nyquist plots were almost unchanged, but the shape of the curve changed obviously at the bias voltage of 1.3V. Both the semi-circle and straight line components became evident when the bias voltage of 1.9 and 2.2V were applied respectively. It is also very clear that the various bias voltages have little effect on the high frequency intercept, which suggests that the intercept with the  $Z'$  axis at high frequency indicates the membrane resistance, since the membrane resistance does not depend on the bias voltage. The charge transfer resistance ( $R_{ct}$ ) started to decrease significantly when the bias voltage of 1.3V was applied. It is well known that the standard potential of the water electrolysis cell is 1.23V at 25°C at pH7 and the overall reaction of electrolysis of water is



Therefore, the applied bias voltage of 1.3V would drive this electrolysis reaction to occur on the Pt electrode surface. In fact, bubbles were observed on the electrode surfaces in the experiments at the bias voltage above 1.3V, which was also observed in Li's work<sup>219</sup>. The appeared part of semi-circle for a bias voltage of 1.3V and 1.9V and an intact semi-circle for a bias voltage of 2.2V were clearly observed in Figure 6-10, indicating a parallel R-C element in the electrochemical cell (Figure 6-5a). With the frequency decreasing, the subsequently appearing straight line implies the existence of Warburg impedance (Figure 6-5b). In other words, it means proton transfer is dominated by the mass transfer rather than charge transfer in these conditions.

An anhydrous ABPBI-74PA sample was measured at 160°C with the bias voltage increasing from 0 to 2.2V. The related Nyquist plots are shown in Figure 6-11. It can be seen that, with the bias voltage increasing from 0 to 1.0V, the curvature of the curve increased, whilst slightly increased when the bias voltage increased from 1.4 to 1.6V. Finally, a clear partial semi-circle appeared both at the bias voltage of 2.0 and 2.2V. It is also clear that the membrane impedance at high frequency is not affected by the bias voltage. With the bias voltage increasing, the increased curvature of the membrane impedance curve indicates that charge transfer resistance starts to decrease. Therefore, the equivalent circuit as shown in Figure 6-5b would be adequate rather than that in Figure 6-5a.



**Figure 6-10** Nyquist plot of the impedance of saturated Nafion 117 membrane at various bias voltages

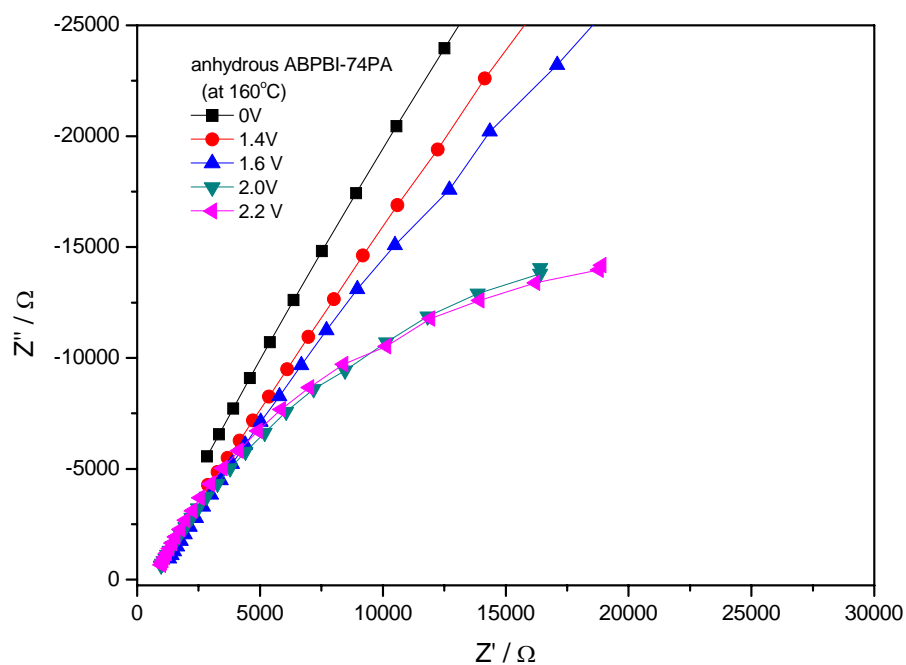


**Figure 6-11** Nyquist plot of the impedance of anhydrous ABPBI-74PA at 160°C and various bias voltages

### 6.3.3 Effect of pressure on the proton conductivity

The effect of the pressure or compression on the proton conductivity was investigated by measuring the membrane resistance under various pressures applied on the membrane surfaces. The Nyquist plots of the impedance of Nafion 117, ABPBI and ABPBI/3SO-92PA are shown in Figure 6-12, Figure 6-13 and Figure 6-14, respectively.

It can be seen that, with the pressure increased from 3.0 to 18.0kPa, the impedance curve moved forward to an imaginary axis. Correspondingly, the obtained resistance of Nafion 117 membrane reduced from 75.5 to 48.6 $\Omega$  (in Figure 6-12). When the pressure continuously increased to 240kPa, the resistance was almost not affected. The increased resistance (65.5 $\Omega$ ) was found when 1.0MPa of pressure was applied.

Normally, the pressure on a membrane is essential for the proton conducting, which makes the electrodes perfectly contact with the membrane therefore reducing the interfacial resistance. Due to owing an essential mechanical property, saturated Nafion 117 membrane endured a pressure up to 1.0MPa in this work; therefore, the membrane resistance almost remained unchanged when the pressure increased from 18 to 240kPa. However, the significant increase of the membrane resistance when the pressure of 1.0MPa was applied must be due to the partial water forced out at this pressure.

It can be seen that, with the pressure increasing to 250kPa, the decreased values of membrane resistances were found in either H<sub>3</sub>PO<sub>4</sub> doped ABPBI (Figure 6-13) or H<sub>3</sub>PO<sub>4</sub> doped ABPBI/POSS membrane (Figure 6-14). Due to the better mechanical property compared to that of Nafion 117, the result of those membrane impedances was not affected although these membranes were bearing a pressure increasing from 250kPa to 1.5MPa. Therefore, the constant pressure of 1.0MPa was applied on any ABPBI or ABPBI/POSS composite membrane during its conductivity measurement.

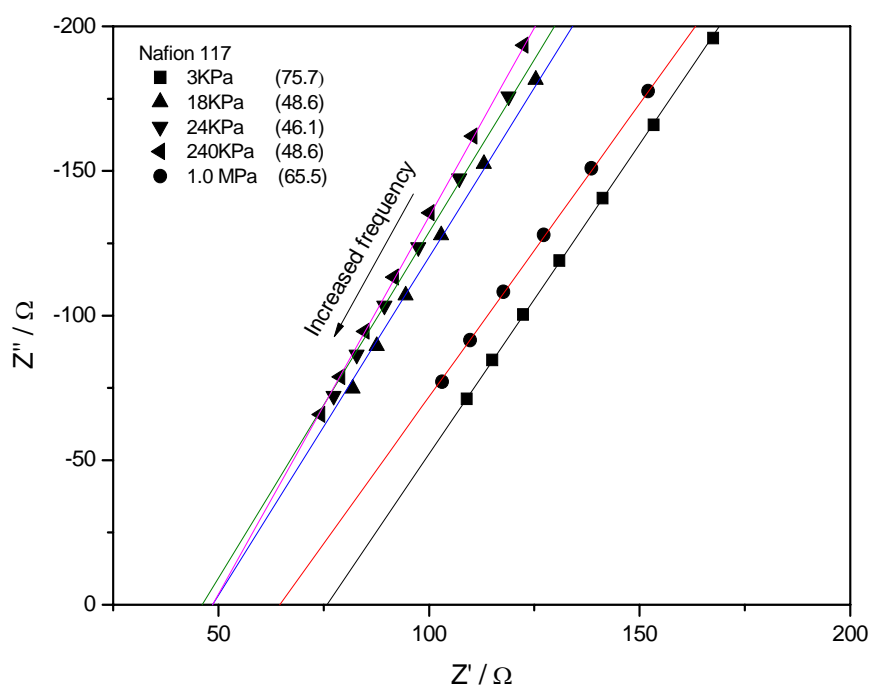


Figure 6-12 Nyquist plot of the impedance of saturated Nafion 117 membrane at 20°C and ambient atmosphere

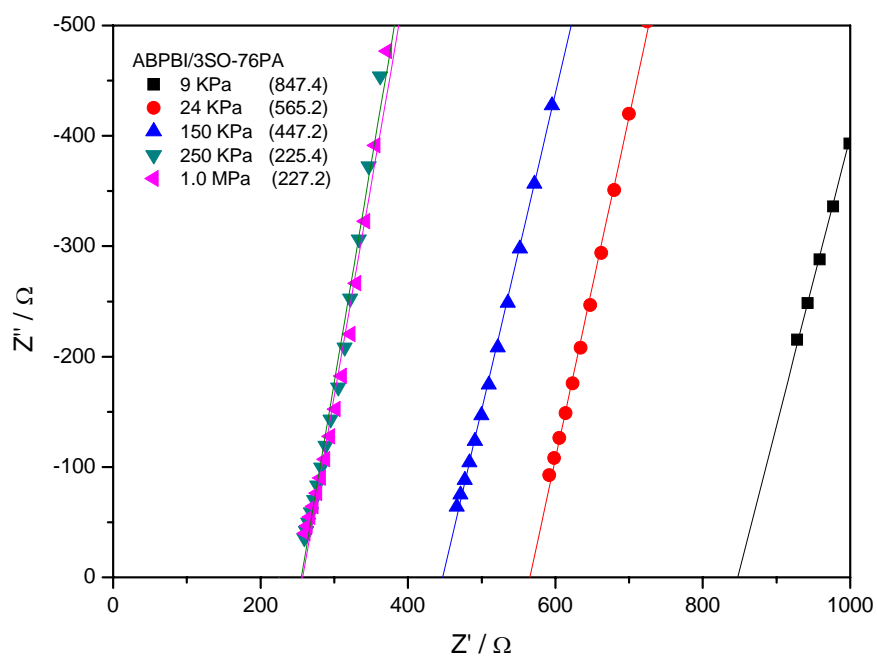


Figure 6-13 Nyquist plot of the impedance of saturated ABPBI-47PA at 20°C and ambient atmosphere



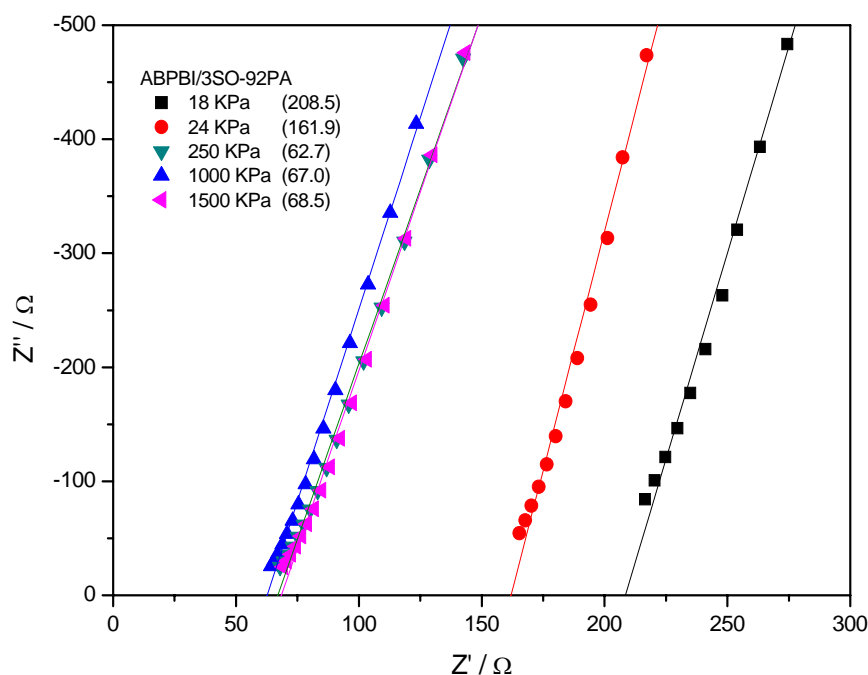


Figure 6-14 Nyquist plot of the impedance of saturated ABPBI/3SO-92PA measured at 20°C and ambient atmosphere

## 6.4 Proton Conductivity of Phosphoric Acid doped Membranes

### 6.4.1 Effect of temperature on proton conductivity

The conductivities of H<sub>3</sub>PO<sub>4</sub> doped anhydrous ABPBI, ABPBI/1AM, ABPBI/3AM, ABPBI/5AM and ABPBI/3SO membranes are shown in Figure 6-15, Figure 6-16, Figure 6-17, Figure 6-18 and Figure 6-19, respectively. The conductivity increased with the rising temperatures and H<sub>3</sub>PO<sub>4</sub> uptake for all anhydrous membranes.

To gain an insight into the motional processes causing nuclear relaxation and conductivity, it is common to construct Arrhenius plots of temperature and the conductivity<sup>100, 116, 130</sup>. The temperature dependence of conductivity can be described by an Arrhenius equation:

$$\frac{\ln(\sigma_T)}{\ln(\sigma_0)} = -\frac{\Delta E_a}{R} \times \frac{1}{T} \quad 6-6$$

where  $E_a$  is activation energy,  $\sigma_0$  is pre-exponential factor,  $R$  is gas constant,  $T$  is absolute temperature, whilst  $\sigma_T$  is the conductivity at temperature  $T$ .

The related Arrhenius plots of  $\ln(\sigma_T)$  against  $10^3/T$  are shown in Figure 6-20, Figure 6-21, Figure 6-22, Figure 6-23 and Figure 6-24, respectively. The activation energy ( $E_a$ ) of proton conducting is derived from these plots and given in Table 6-1, Table 6-3 and Table 6-2, respectively.

As shown in Table 6-1,  $E_a$  increased from 36.6kJ/mol of ABPBI-43PA, to 31.5kJ/mol of ABPBI-60PA then decreased with the increased  $H_3PO_4$  uptake. Similarly,  $E_a$  first increased then decreased with the  $H_3PO_4$  uptake increasing from 67 to 102% (in Table 6-2).  $E_a$  decreasing with the increased  $H_3PO_4$  uptake was observed in ABPBI/AM composite membranes (in Table 6-3). With the similar  $H_3PO_4$  uptake,  $E_a$  of ABPBI was lower than that of ABPBI/POSS composites, i.e.  $E_a$  of 28.0kJ/mol was from ABPBI-41PA and 36.6kJ/mol from ABPBI/5AM-43PA, 19.0kJ/mol from ABPBI-70PA and 31.4kJ/mol from ABPBI/1AM-67PA and 28.0kJ/mol from ABPBI/3SO-74PA.

The activation energy ( $E_a$ ) is the sum of the enthalpies of defect pair (charge carrier) formation ( $\Delta H_f$ ) and defect migration ( $\Delta H$ ), and indicates the ease for proton hopping and rotation of the donor and acceptor<sup>100</sup>. A large value of  $E_a$  indicates the enthalpy required for proton transfer is high, causing low conductivity. The reduction of  $E_a$  with the increased  $H_3PO_4$  uptake indicates the enthalpy required for proton transfer through  $H_3PO_4$  molecules must be lower than that through imidazole groups. The higher  $E_a$  from ABPBI/POSS composite than that of ABPBI with the same or similar  $H_3PO_4$  uptake implies that the POSS core might twist and turn the route of proton transfer, causing more enthalpy required of proton hopping. However, the lower  $E_a$  from ABPBI and ABPBI/3SO with low  $H_3PO_4$  uptake (i.e. before the maximum protonation is reached) might be due to a different dominant proton hopping route which will be discussed in the following section. It is also noteworthy that  $E_a$  of ABPBI/3AM was calculated from the temperature below 140°C due to the slow increase of conductivity from 140 to 160°C in which the Arrhenius plots were not linear against the increased temperature. This should be due to the self-dissociation of anhydrous  $H_3PO_4$  and will be discussed in the following section.

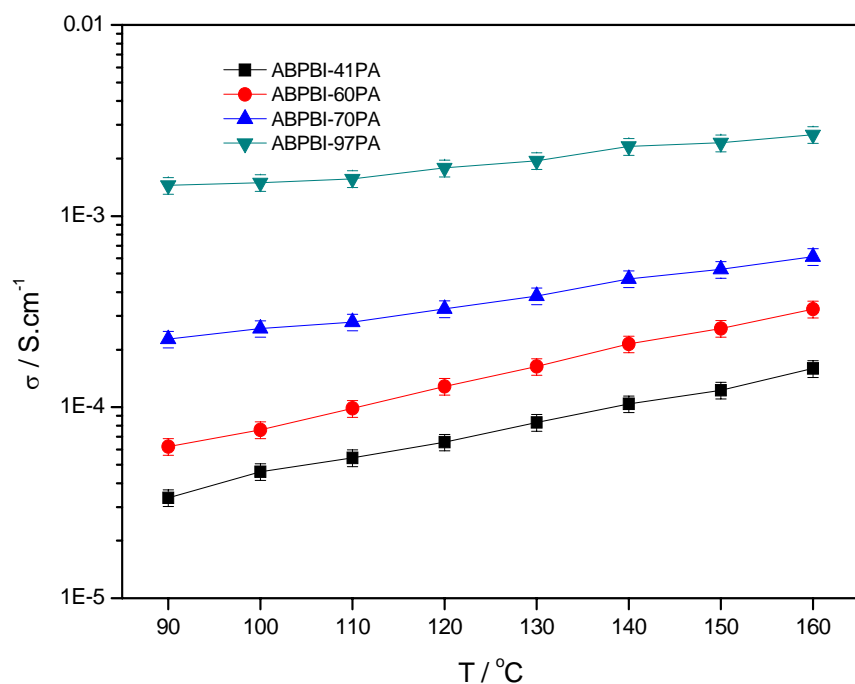


Figure 6-15 Variation of conductivity of anhydrous  $\text{H}_3\text{PO}_4$  doped ABPBI with temperature

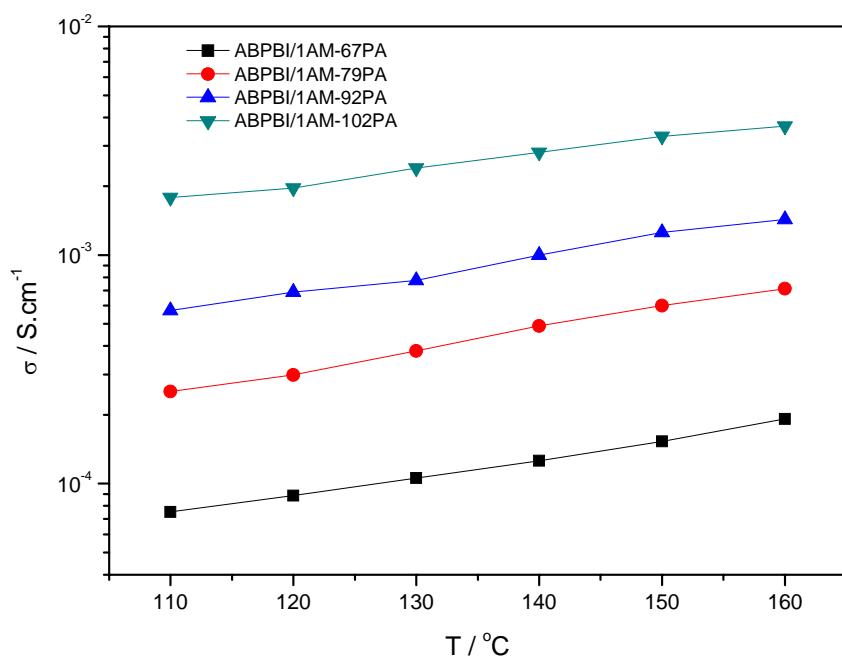


Figure 6-16 Variation of conductivity of anhydrous  $\text{H}_3\text{PO}_4$  doped ABPBI/1AM with temperature

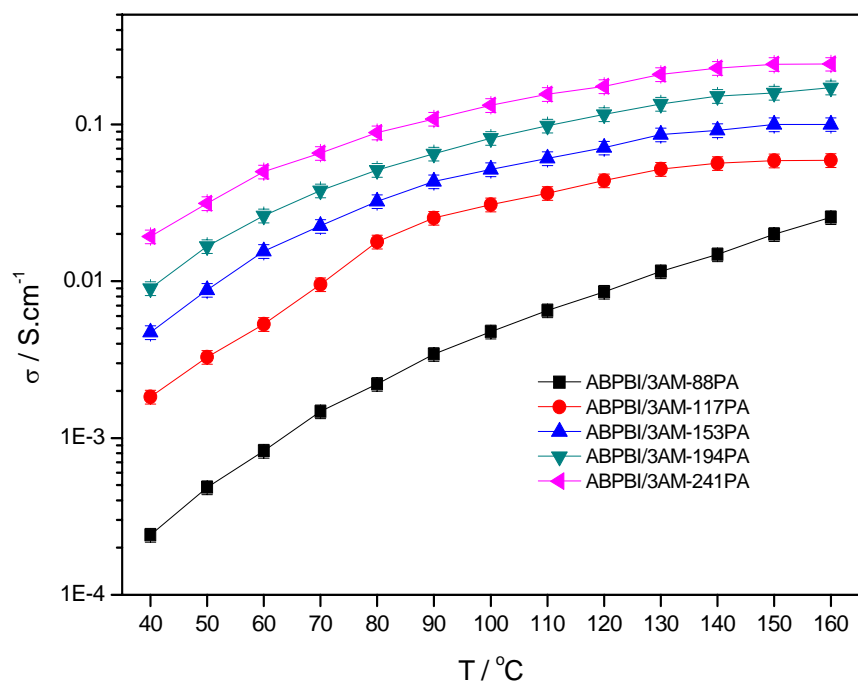


Figure 6-17 Variation of conductivity of anhydrous  $\text{H}_3\text{PO}_4$  doped ABPBI/3AM with temperature

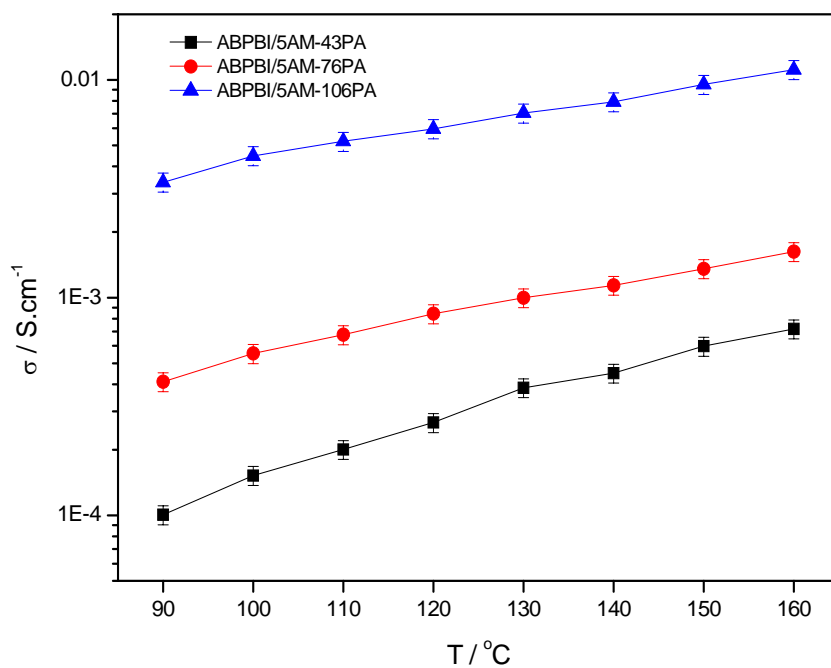


Figure 6-18 Variation of conductivity of anhydrous  $\text{H}_3\text{PO}_4$  doped ABPBI/5AM with temperature

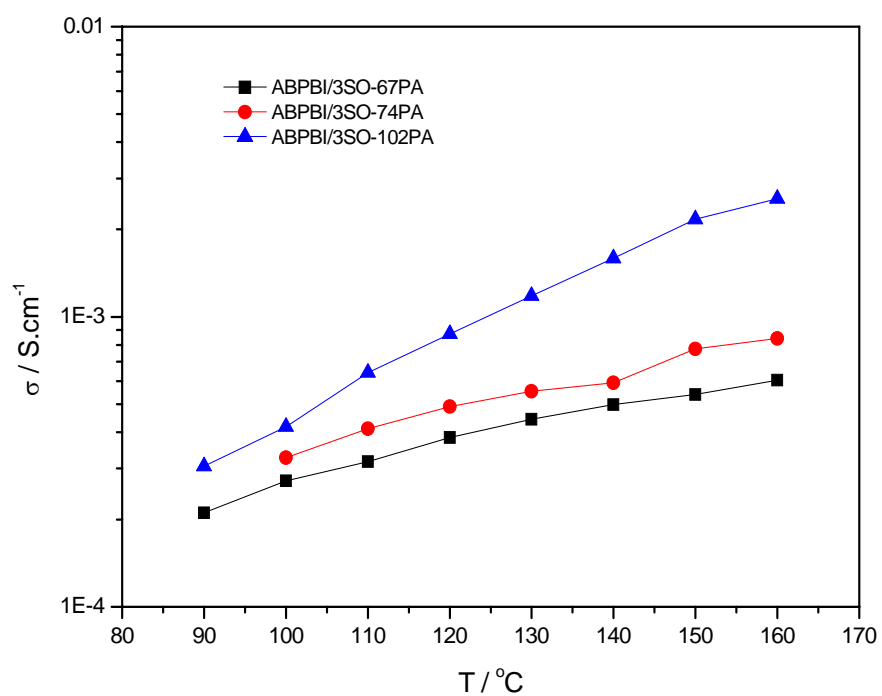


Figure 6-19 Variation of conductivity of anhydrous H<sub>3</sub>PO<sub>4</sub> doped ABPBI/3SO with temperature

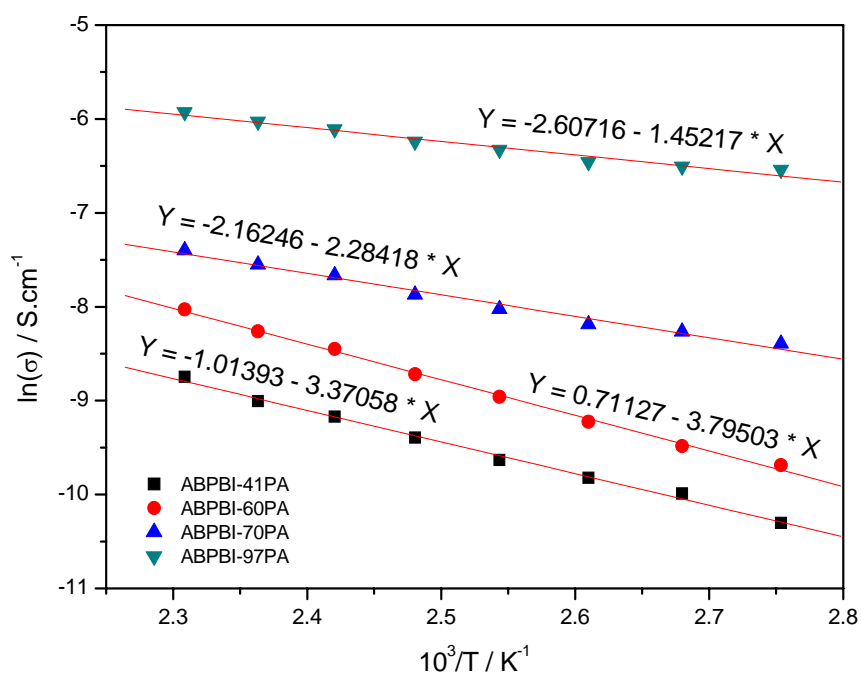
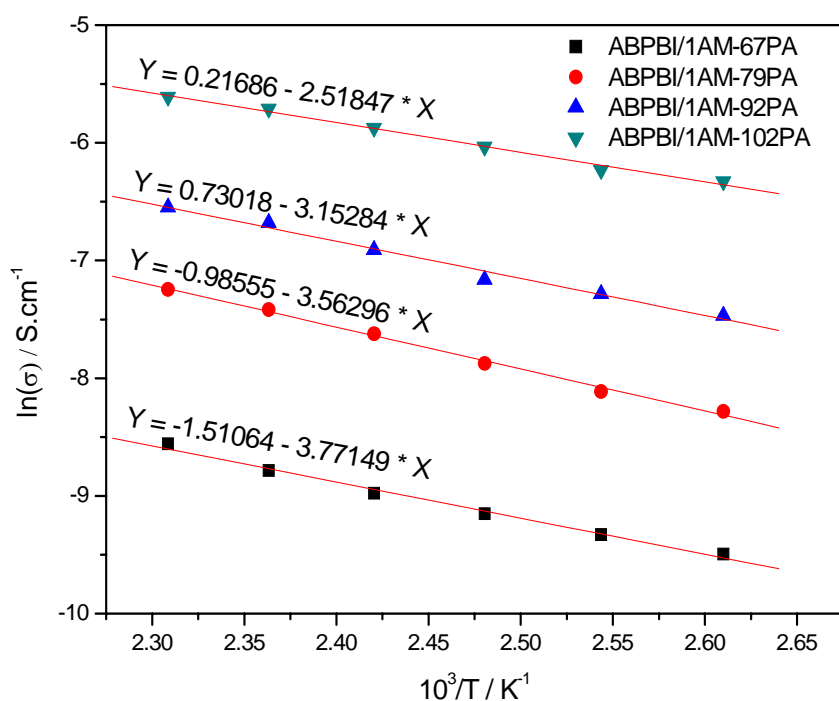
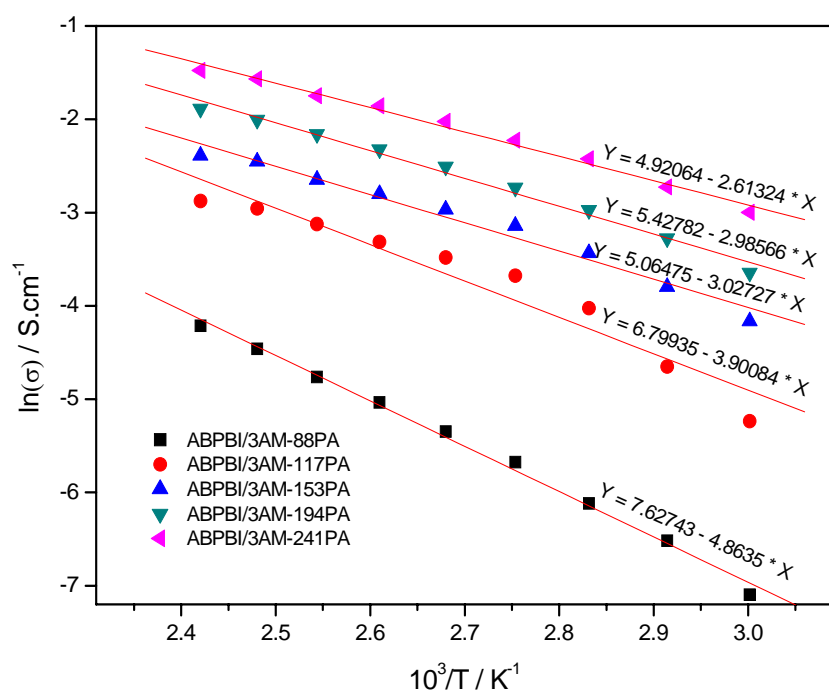
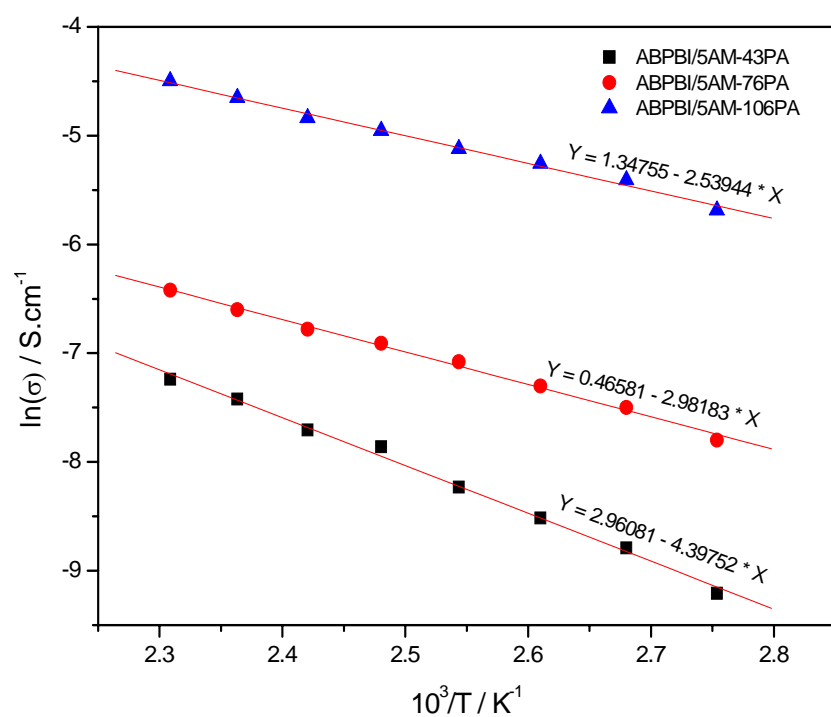
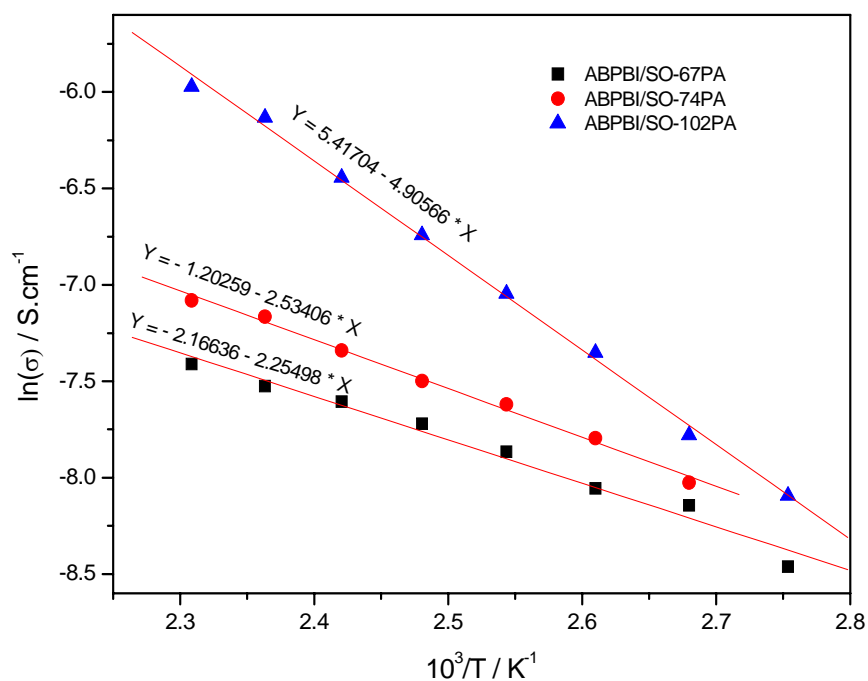


Figure 6-20 Arrhenius plot of conductivity of H<sub>3</sub>PO<sub>4</sub> doped ABPBI

Figure 6-21 Arrhenius plot of conductivity of anhydrous  $\text{H}_3\text{PO}_4$  doped ABPBI/1AMFigure 6-22 Arrhenius plot of conductivity of anhydrous  $\text{H}_3\text{PO}_4$  doped ABPBI/3AM

Figure 6-23 Arrhenius plot of conductivity of anhydrous  $\text{H}_3\text{PO}_4$  doped ABPBI/5AMFigure 6-24 Arrhenius plot of conductivity of anhydrous  $\text{H}_3\text{PO}_4$  doped ABPBI/3SO

**Table 6-1 Activation energy of conductivity of H<sub>3</sub>PO<sub>4</sub> doped ABPBI membrane**

PA doped ABPBI	Activation energy (E <sub>a</sub> ) (kJ/mol)	Temperature range (T) (°C)
ABPBI-41PA	28.0	90~160
ABPBI-60PA	31.5	90~160
ABPBI-70PA	19.0	90~160
ABPBI-97PA	12.1	90~160

**Table 6-2 Activation energy of conductivity of H<sub>3</sub>PO<sub>4</sub> doped ABPBI/3SO composite membrane**

PA doped ABPBI/3SO	Activation energy (E <sub>a</sub> ) (kJ/mol)	Temperature range (T) (°C)
ABPBI/3SO-67PA	28.0	90~160
ABPBI/3SO-74PA	31.5	90~160
ABPBI/3SO-102PA	21.1	90~160

**Table 6-3 Activation energy of conductivity of H<sub>3</sub>PO<sub>4</sub> doped ABPBI/AM composite membrane**

PA doped ABPBI/AM	Activation energy (E <sub>a</sub> ) (kJ/mol)	Temperature range (T) (°C)
ABPBI/1AM-67PA	31.4	110~160
ABPBI/1AM-79PA	29.6	110~160
ABPBI/1AM-92PA	26.2	110~160
ABPBI/1AM-102PA	25.5	110~160
ABPBI/3AM-88PA	40.4	60~160
ABPBI/3AM-117PA	32.4	60~140
ABPBI/3AM-153PA	25.2	60~140
ABPBI/3AM-194PA	24.8	60~140
ABPBI/3AM-241PA	21.7	60~140
ABPBI/5AM-43PA	36.6	90~160
ABPBI/5AM-76PA	24.8	90~160
ABPBI/5AM-106PA	21.1	90~160



### 6.4.2 Effect of H<sub>3</sub>PO<sub>4</sub> on proton conductivity

In a H<sub>3</sub>PO<sub>4</sub> doped membrane, the proton transfer is dominant by a hopping mechanism which can be expressed by the hopping model<sup>10</sup>

$$\sigma_0 = \left( \frac{z^2 F^2}{R} \right) \alpha v_0 d^2 C \exp \left( \frac{\Delta S + \Delta S_f}{R} \right) \quad 6-7$$

where  $z$  is the charge number;  $F$  is the Faraday constant;  $C$  is the concentration of mobile species;  $\alpha$  is the reciprocal number of all possible hopping directions (1/6 for a stereo structure);  $v_0$  is the hopping frequency;  $d$  is the hopping distance between sites;  $\Delta S$  and  $\Delta S_f$  is the activation entropy of migration and formation of proton defect, respectively.

In a H<sub>3</sub>PO<sub>4</sub> doped membrane, imidazole groups in ABPBI polymer, H<sub>3</sub>PO<sub>4</sub> and water can act as both the proton donor and acceptor in the hopping model<sup>100</sup>. The concentration of mobile species,  $C$ , is related to the concentration of proton donors and acceptors which is increased with the increasing H<sub>3</sub>PO<sub>4</sub> and water uptakes. The distance for proton hopping,  $d$ , is related to the type of hydrogen bond. The hydrogen bond can be formed between either two of imidazole group, H<sub>3</sub>PO<sub>4</sub> and water, which is proposed in Figure 6-25. Obviously, different hydrogen bonds owe different proton hopping distances. Increasing H<sub>3</sub>PO<sub>4</sub> and water uptake can change the ratios of different bonds so as to affect  $d$ . The hopping frequency,  $v_0$ , is related to the vibration of hydrogen bonds<sup>63</sup>, similar to  $d$ , is affected by the ratio of different hydrogen bonds. The number of proton charge carriers increases with increasing H<sub>3</sub>PO<sub>4</sub> and water uptake, causing an increase of hydrogen bonds that weakens the original chemical bonds and results in the shift of  $v_0$  to low frequency.  $\Delta S$  and  $\Delta S_f$  are related to the charge of configuration and vibration of the system before and after the proton hopping and the reorientation of the proton carriers.

As mentioned above, the conductivity rose with the H<sub>3</sub>PO<sub>4</sub> uptake increasing in all samples. Although the increased H<sub>3</sub>PO<sub>4</sub> concentration leads to the conductivity increasing, the proton hopping route can be different when different amounts of H<sub>3</sub>PO<sub>4</sub> were absorbed.

At lower  $H_3PO_4$  uptake (<75% or before the maximum protonation is reached),  $H_2PO_4^-$  and  $HPO_4^{2-}$  are the dominant anion over the entire acid concentration which were confirmed by FTIR. Protons transfer mainly along hydrogen bonds which are formed between protonated imidazole groups ( $N^+-H\cdots N$ ) on the neighbouring polymer chains and between imino nitrogen and phosphate ions ( $N^+-H\cdots H_2PO_4^-$  or  $HPO_4^{2-}\cdots N-H$ ). With more  $H_3PO_4$  absorbed, the ratio of proton transfer along  $N^+-H\cdots H_2PO_4^-\cdots N-H$  to  $N^+-H\cdots N$  increased. The proton transfer might occur mainly along  $N^+-H\cdots H_2PO_4^-\cdots N-H$  when the maximum protonation of imidazole groups was reached. The continuously increased  $H_3PO_4$  uptake caused more free (or amorphous<sup>130</sup>)  $H_3PO_4$ . Thereby the proton transfer might occur mainly through hydrogen bonds (shown in Figure 6-25), resulting in the increase of the overall conductivity. It is noteworthy that lower  $E_a$  from those samples with  $H_3PO_4$  uptake under the level of maximum protonation of imidazole groups indicates that the enthalpy required for proton transfer through ionic bonds i.e.  $N^+-H\cdots H_2PO_4^-$  or  $HPO_4^{2-}\cdots N-$  must be lower than through hydrogen bonds, since the dominant route for proton transfer is through ionic bonds below the level of the maximum protonation of imidazole groups and through other hydrogen bonding forms.

At the high  $H_3PO_4$  uptake i.e. about >117% in ABPBI/3AM samples, more  $H_3PO_4$  was present in a  $H_3PO_4$  doped membrane and formed  $H_3PO_4$ -rich domains, behaving like concentrated  $H_3PO_4$  solution. Accordingly, ABPBI polymer acted as a solvent to ionise  $H_3PO_4$  molecules by protonation of the imidazole groups. In pure  $H_3PO_4$  acid, self-dissociation of anhydrous  $H_3PO_4$  is represented by the following reactions<sup>221</sup>:



In section 5.3, it was mentioned that the dimerisation of  $H_3PO_4$  in 85%  $H_3PO_4$  solution occurred at around 158°C and produced pyrophosphoric acid ( $H_4P_2O_7$ , equation 5-2), which is a very strong acid and has two dissociations to  $H_3P_2O_7^-$  and  $H_2P_2O_7^{2-}$ , thus equation 5-2 is always expressed as following



The first equilibrium (Equation 6-8) is labelled fast while the last (Equation 6-9) is labelled slow<sup>100, 221</sup>. Ma<sup>100</sup> found that the formation of  $H_4P_2O_7$  in  $H_3PO_4$  doped PBI membranes under dry conditions started around 140°C, depending on the acid doping level. Thus, the proton transfer path may be different above and below 140°C under dry conditions. It has been shown that  $H_4P_2O_7$  molecule has low mobility due to its large molecule size<sup>222</sup>. Therefore, the more slowly increasing conductivities of ABPBI/3AM with  $H_3PO_4$  uptake above 117% between 140~160°C should be due to the dimerisation of excess  $H_3PO_4$  producing pyrophosphoric acid, which has a slow dissociation reaction (Equation 6-9) and low mobility, leading to requiring higher reaction energy for proton transfer. Similar results were also reported in PBI with high  $H_3PO_4$  doping levels<sup>100</sup>.

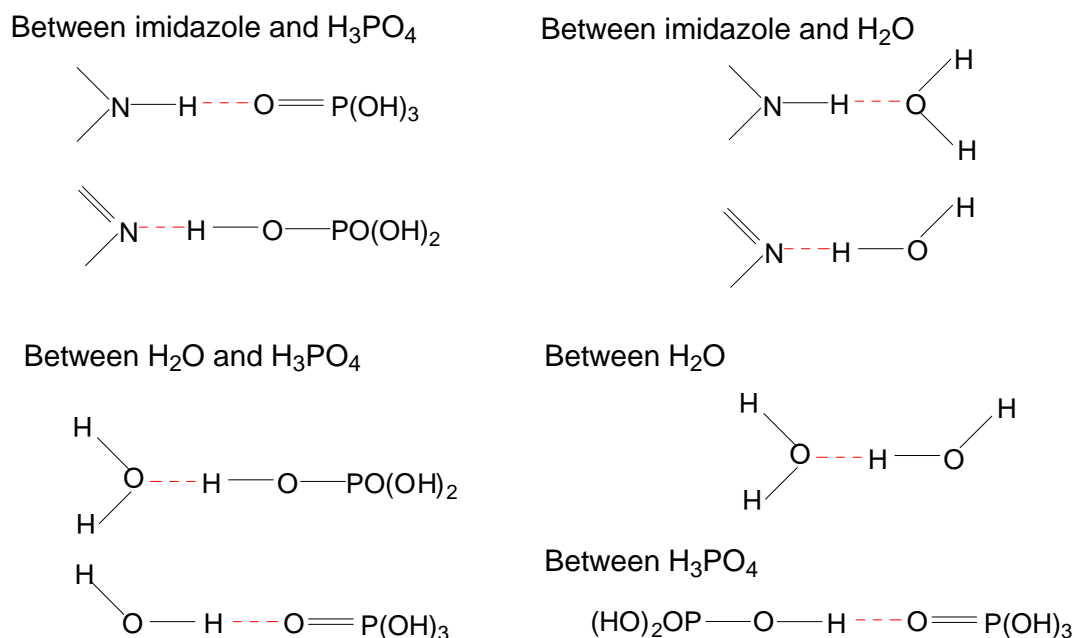


Figure 6-25 Hydrogen bonding forms proposed in a  $H_3PO_4$  doped ABPBI membrane

#### 6.4.3 Effect of water on proton conductivity

Figure 6-26 shows the proton conductivity of  $H_3PO_4$  doped hydrous ABPBI-53PA measured at room temperature and ambient atmosphere with various exposure times. Figure 6-27, Figure 6-28 and Figure 6-29 show the proton conductivities of  $H_3PO_4$  doped hydrous ABPBI, ABPBI/AM and ABPBI/3SO samples measured at ambient atmosphere and various temperatures. The commercial Nafion 117 was measured in the same conditions and the related results are given in Figure 6-26 and Figure 6-27.

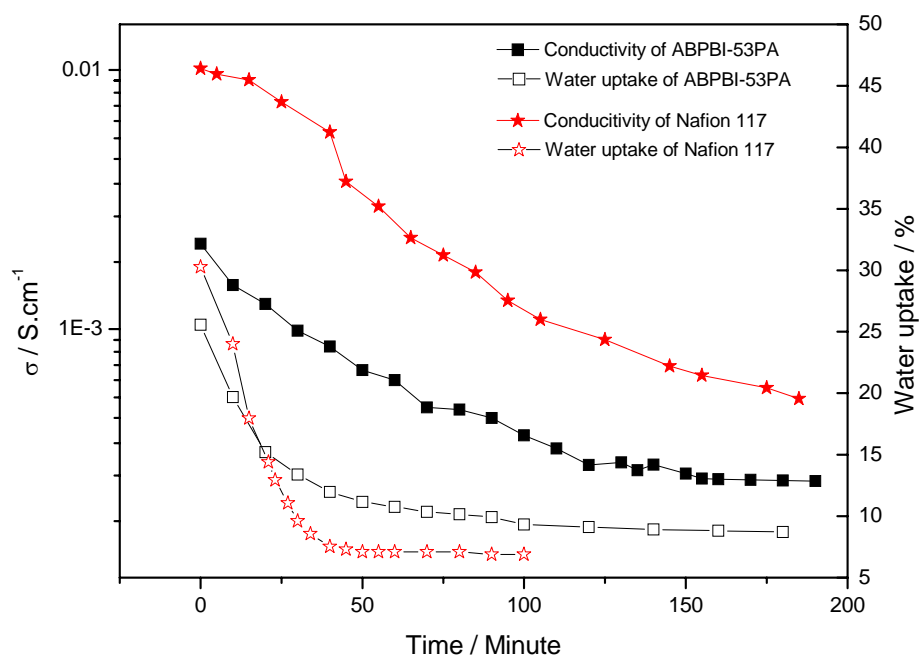


Figure 6-26 Conductivity of ABPBI-53PA and Nafion 117 at 20°C and ambient atmosphere against various exposure times

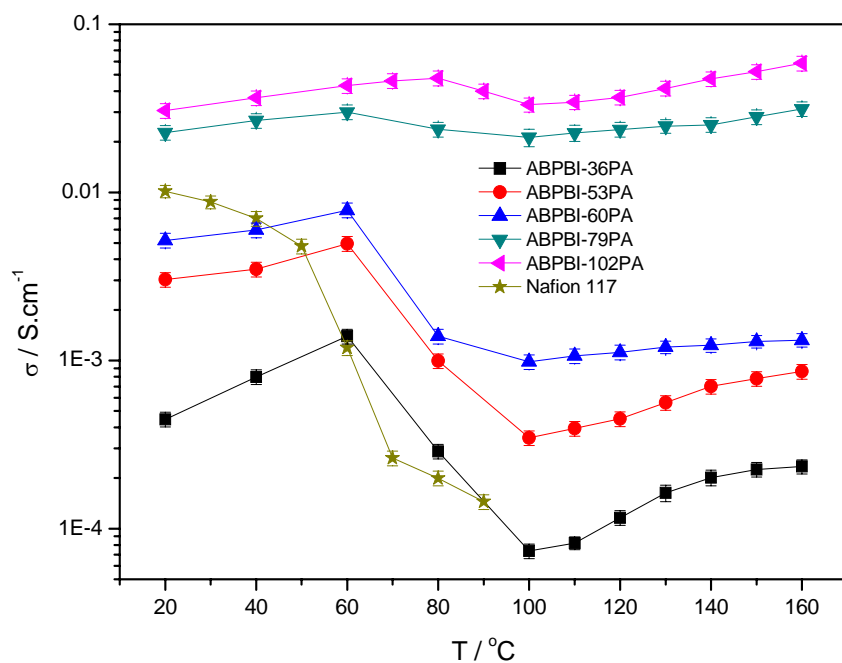


Figure 6-27 Conductivity of H<sub>3</sub>PO<sub>4</sub> doped hydrous ABPBI and Nafion 117 at various temperatures

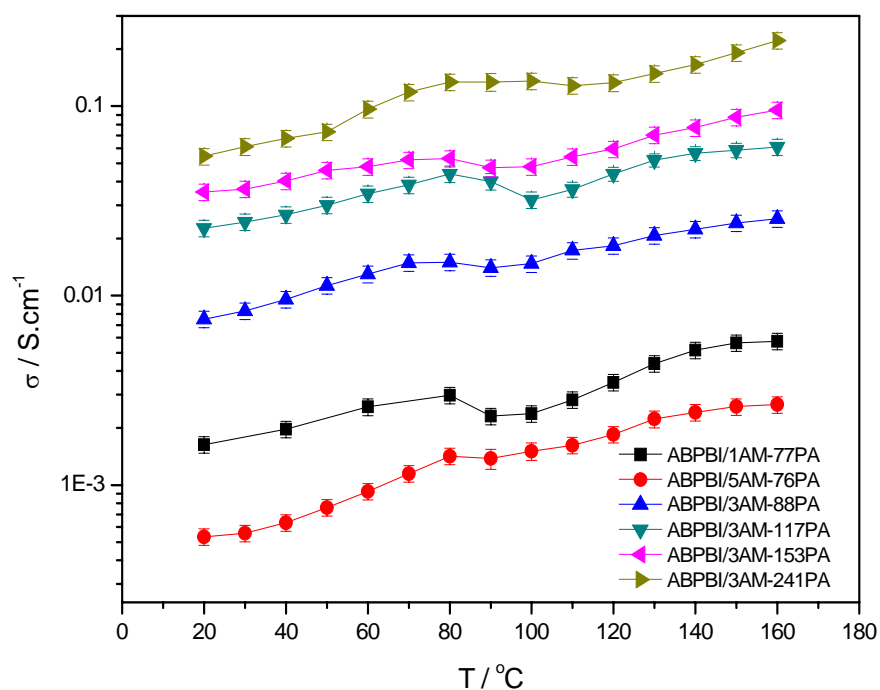


Figure 6-28 Conductivity of  $\text{H}_3\text{PO}_4$  doped hydrous ABPBI/AM composites at various time

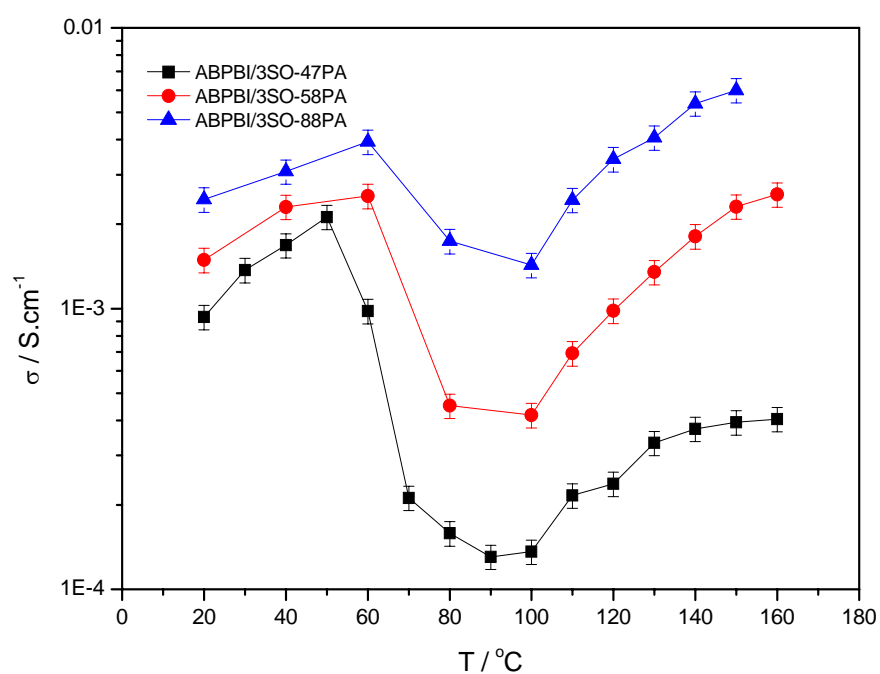


Figure 6-29 Conductivity of  $\text{H}_3\text{PO}_4$  doped hydrous ABPBI/3SO composites at various temperatures

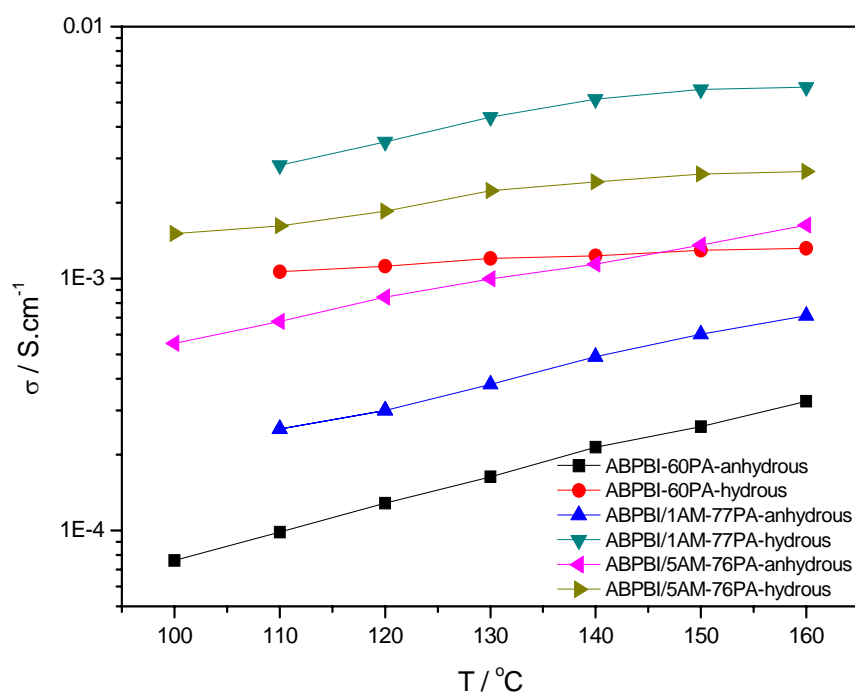


Figure 6-30 Comparison of conductivities of anhydrous and hydrous ABPBI/60PA, ABPBI/1AM-77PA and ABPBI/5AM-76PA samples measured above 100°C

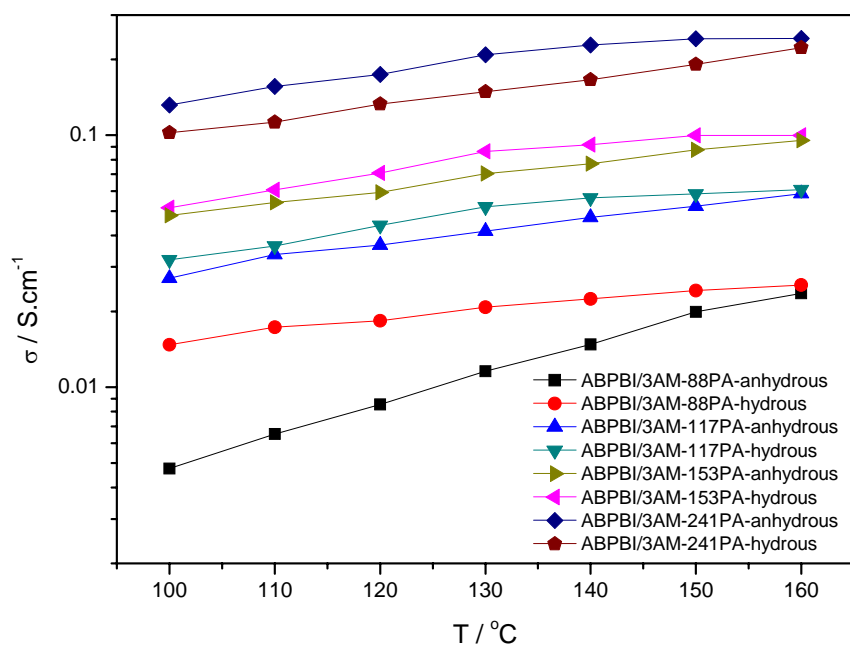


Figure 6-31 Comparison of conductivities of anhydrous and hydrous ABPBI/3AM samples measured above 100°C

As shown in Figure 6-26, the conductivity of hydrous ABPBI-53PA decreased with the elapsed time. In Figure 6-27, the conductivities of  $\text{H}_3\text{PO}_4$  doped ABPBI membranes first increased with the temperature increasing from 20 to 60°C (from 20 to 80°C for ABPBI-102PA), and subsequently dropped down with the temperature increased to 100°C, then increased again with the continuously heightened temperature up to 160°C. It can also be seen that the reduction of conductivity of these  $\text{H}_3\text{PO}_4$  doped ABPBI samples between 60 and 100°C seems to decrease with the increased  $\text{H}_3\text{PO}_4$  uptake. In Figure 6-28, the conductivity increasing with the temperature rising from 20 to 160°C was observed in ABPBI/3AM-241PA sample and also observed in other ABPBI/3AM samples with the exception of a slight fluctuation, which occurred between 80 and 100°C. Quite similar to that of low  $\text{H}_3\text{PO}_4$  absorbed ABPBI samples, the significant reduction of conductivities occurred between 60 and 100°C, which also decreased with the increasing  $\text{H}_3\text{PO}_4$  uptake at this temperature range observed in  $\text{H}_3\text{PO}_4$  doped ABPBI/3SO samples as shown in Figure 6-29. It can also be seen that both the conductivity of hydrous Nafion 117 decreased with the exposure time (Figure 6-26) and the increased temperatures (Figure 6-27).

As discussed in the hopping model (Equation 6-7) in the above section, quite similar to  $\text{H}_3\text{PO}_4$  molecule, water acts as either a proton acceptor or a proton donor and the addition of water increases the number of charge carrier by forming hydrogen bonds (shown in Figure 6-25).

At ambient atmosphere and room temperature i.e. 20°C, the water uptake of hydrous ABPBI-53PA (in Figure 6-26) decreased with the elapsed time due to the water evaporation. The related decreased conductivity with the elapsed time indicates that the decreased water uptake caused the reduction of the number of charge carriers in the membrane, leading to lower mobility and conductivity. In other words, the conductivity depends on the water content significantly in the membrane at low temperature. For example, the conductivity of ABPBI-53PA decreased two orders of magnitude from  $2.1 \times 10^{-3}$  to  $2.6 \times 10^{-5}$  whilst the water uptake dropped down from 25.6 to 8.7%.

It is noted that the water uptake data was not possible to be obtained since the conductivity of hydrous membranes were measured in an oven during a whole heating process. However, from the all DSC and TGA curves shown in the earlier chapters, it can be seen that the free water started to evaporate from 60°C. Therefore, compared to the slight fluctuations at 80~100°C for those membranes with high H<sub>3</sub>PO<sub>4</sub> uptake i.e. ABPBI-79PA and ABPBI-102PA (in Figure 6-26), ABPBI/3AM-88~241PA (in Figure 6-28), and the dramatic drops of conductivities from these membranes with low H<sub>3</sub>PO<sub>4</sub> uptake i.e. ABPBI-36~60PA (in Figure 6-27), ABPBI/3SO-47~58PA (in Figure 6-29), it is indicated that the conductivity depends on water content significantly at low H<sub>3</sub>PO<sub>4</sub> uptake. The higher water absorption in a membrane with low H<sub>3</sub>PO<sub>4</sub> uptake has been illustrated in a model shown in Figure 5-5.

The effect on the conductivity from water was investigated at above 100°C through comparing conductivities of hydrous and anhydrous samples with the same H<sub>3</sub>PO<sub>4</sub> uptake at the same temperature. The results also show that the conductivity depends on water content significantly at low H<sub>3</sub>PO<sub>4</sub> uptake at high temperature. For example, in Figure 6-30, the conductivities of hydrous ABPBI-60PA, ABPBI/1AM-77PA and ABPBI/5AM-76PA were higher by approximately one order of magnitude than those of anhydrous samples at the temperature range of 100~160°C. In Figure 6-31, the conductivities of anhydrous ABPBI/3AM-117~241PA samples were around 75~90% to that of hydrous samples at 100°C and much closed at 160°C, whilst the conductivity of anhydrous ABPBI/3AM-88PA was probably one-third to that of hydrous one at 100°C ( $4.8 \times 10^{-3}$  vs  $1.4 \times 10^{-2} \text{ S.cm}^{-1}$ ) and became closed at 160°C ( $2.4 \times 10^{-2}$  vs  $2.5 \times 10^{-2} \text{ S.cm}^{-1}$ ).

It is interesting to mention that, as shown in Figure 6-27, the conductivity of water saturated ABPBI membrane with H<sub>3</sub>PO<sub>4</sub> uptake above 79% is compatible at a wide temperature range i.e. between 20~160°C compared to that of saturated commercial Nafion 117 at 20°C. Meanwhile, the conductivity of ABPBI/3AM with H<sub>3</sub>PO<sub>4</sub> uptake above 117% whenever at anhydrous or hydrous conditions at a wide temperature range as shown in Figure 6-17 and Figure 6-28, is comparable to saturated Nafion at 20°C.



# Chapter 7 CONCLUSIONS AND RECOMMENDATIONS FOR FUTURE WORK

## 7.1 Conclusions

The following conclusions can be drawn from the work conducted in this project:

1. Poly(2,5-benzimidazole)(ABPBI), polybenzimidazole (poly[2,2'-(*m*-phenylene)-5,5'-bibenzimidazole], PBI) and copolymers of ABPBI and PBI were synthesised using methanesulfonic acid/phosphorus pentoxide (MSA/P<sub>2</sub>O<sub>5</sub>) as the reaction media. Their chemical structures were confirmed by FTIR spectra and elemental analysis. Among them, ABPBI showed the highest crystallinity and the thermal stability. The molecular weights of the polymers synthesised were affected by the reaction temperature and time, the concentration of monomer(s) and stirring conditions. ABPBI with a molecular weight of 18,000g/mol was obtained under the optimised reaction conditions (26.7 mmol of monomer 3,4-diaminobenzoic (DABA) in 40mL of MSA and 6.0g of P<sub>2</sub>O<sub>5</sub> at 150°C for 120 minutes with around 400rpm of the stirring speed), which was adequate for the membrane preparation.
2. By casting from MSA subsequently progressively heating to remove the solvent followed by a phosphoric acid (PA, H<sub>3</sub>PO<sub>4</sub>) solution doping procedure, qualified ABPBI membranes were fabricated and characterised. The tensile test results showed that the anhydrous ABPBI membrane with low H<sub>3</sub>PO<sub>4</sub> uptake i.e. 53% possessed higher tensile strength and modulus probably due to the crosslink-like structures formed between polymer chains through imidazole-HPO<sub>4</sub><sup>2-</sup>-imidazole bonds, in which, the presence of HPO<sub>4</sub><sup>2-</sup> was also confirmed by FTIR. XRD showed that the ABPBI membrane was semi-crystalline, which was reduced by the absorbed H<sub>3</sub>PO<sub>4</sub> molecules. Due to the alkalinity of imidazole groups, ABPBI can be protonated by H<sub>3</sub>PO<sub>4</sub> and absorb water via hydrogen bonding. The water and H<sub>3</sub>PO<sub>4</sub> uptake results showed that, before imidazole groups in ABPBI were fully protonated by H<sub>3</sub>PO<sub>4</sub>, water molecules could be hydrogen

bonded with the unprotonated imidazole groups, but with  $\text{H}_3\text{PO}_4$  molecules when the imidazole groups were fully protonated. The excess free  $\text{H}_3\text{PO}_4$  detected by FTIR was due to the hydrogen bonds formed between  $\text{H}_3\text{PO}_4$  molecules resulting in the increase of  $\text{H}_3\text{PO}_4$  uptake with increase of  $\text{H}_3\text{PO}_4$  concentration as well as water uptake.

3. ABPBI/OctaAmmonium POSS (AM-POSS) (ABPBI/AM) and ABPBI/TriSilanolPhenyl POSS (SO-POSS) (ABPBI/SO) composites were synthesised in situ in MSA/ $\text{P}_2\text{O}_5$  media and direct cast to form membranes. The SEM/TEM micrographs and EDX maps showed that both AM-POSS and SO-POSS uniformly dispersed in polymer matrix through dissolving in selected solvent first followed by ultrasonication bath before synthesis. DSC results showed that the addition of POSS reduced the glass transition temperature of pristine ABPBI from  $420^\circ\text{C}$  to  $300\sim 350^\circ\text{C}$  due to the enlargement of the distance between polymer chains by POSS particles. The significantly improved mechanical properties of 90% in tensile strength ( $>258\text{MPa}$ ) and 60% in Young's modulus ( $>4.5\text{GPa}$ ), respectively for composite membranes were obtained by addition of 3 wt% AM-POSS attributed to the fine and uniform dispersion of the POSS particles in polymer matrix, which was also in favour of water and PA absorptions of the membranes. Both the  $\text{H}_3\text{PO}_4$  and water uptake of ABPBI/AM and ABPBI/SO composites with 1~3 wt% POSS concentration were higher than those of the pristine ABPBI membrane at same conditions due to the hydrogen bonds formed between POSS and  $\text{H}_3\text{PO}_4$  and water molecules, whilst the reduction in  $\text{H}_3\text{PO}_4$  and water absorption for ABPBI/POSS with 5 wt% POSS might result from the agglomeration of POSS particles. The highest  $\text{H}_3\text{PO}_4$  uptake of 241% was achieved for 3 wt% ABPBI/AM membrane.
4. The proton conductivity results showed that the conductivities of  $\text{H}_3\text{PO}_4$  doped membranes increased with the increase of  $\text{H}_3\text{PO}_4$  or water molecule absorbance. When the imidazole groups were fully protonated, the activation energy of proton transfer decreased with the increase of  $\text{H}_3\text{PO}_4$  uptake resulted in the increase of proton conductivities. The ABPBI/3AM composite membrane with  $\text{H}_3\text{PO}_4$  uptake above 117% showed excellent proton conductivity at high temperatures in both hydrous and anhydrous conditions, which was comparable

with commercial Nafion 117 ( $1.1 \text{ S.cm}^{-1}$  measured at  $20^\circ\text{C}$  and the water saturated condition), indicating that  $\text{H}_3\text{PO}_4$  doped ABPBI/3AM composite membrane could be an excellent candidate as a polymer electrolyte membrane for the high temperature fuel cell purpose.

## ***7.2 Recommendations for Future work***

1. It has been reported that both the temperature and humidity affect the proton conductivity of the membranes. Due to the availability of the facilities, the proton conductivity was not measured at the controlled humidity condition. It would be appreciated if these conditions could be controlled in measuring conductivity, which will be very helpful and useful in understanding fully the proton transfer mechanisms in this new composite membrane system.
2. For potential commercialisation of these new composite membranes, it will be necessary to test the conductivity of the membranes using membrane electrolyte assembly (MEA) system. Finally, the thermal stability / degradation of the membranes at high temperature should also be assessed.

## REFERENCES

1. Shafiee, S.; Topal, E., When will fossil fuel reserves be diminished? *Energy Policy* **2009**, 37, (1), 181-189.
2. Fuel Cell Industry Analysis. In RNCOS: **2009**; p 115.
3. Larminie, J.; Dicks, A., *Fuel Cell Systems Explained, 2nd edition*. John Wiley and Sons: England, **2003**.
4. Steele, B. C. H.; Heinzel, A., Materials for fuel-cell technologies. *Nature* **2001**, 414, (6861), 345-352.
5. Kordesch, K.; Simader, G., *Fuel Cells and Their Applications*. VCH: Weinheim, Germany, **1996**.
6. Doyle, M.; Rajendran, G., Perfluorinated Membranes. In *Handbook of Fuel Cells: Fundamentals, Technology, Applications*, Vielstich, W.; Lamm, A.; Gasteiger, H. A., Eds. John Wiley & Sons: Chichester, England, **2003**; Vol. 3, pp 351-395.
7. Mehta, V.; Cooper, J. S., Review and analysis of PEM fuel cell design and manufacturing. *Journal of Power Sources* **2003**, 114, (1), 32-53.
8. Rikukawa, M.; Sanui, K., Proton-conducting polymer electrolyte membranes based on hydrocarbon polymers. *Progress in Polymer Science* **2000**, 25, (10), 1463-1502.
9. Kreuer, K. D., On the development of proton conducting polymer membranes for hydrogen and methanol fuel cells. *Journal of Membrane Science* **2001**, 185, (1), 29-39.
10. Li, Q. F.; Hjuler, H. A.; Bjerrum, N. J., Phosphoric acid doped polybenzimidazole membranes: Physiochemical characterization and fuel cell applications. *Journal of Applied Electrochemistry* **2001**, 31, (7), 773-779.
11. Li, Q. F.; Jensen, J. O.; Savinell, R. F.; Bjerrum, N. J., High temperature proton exchange membranes based on polybenzimidazoles for fuel cells. *Progress in Polymer Science* **2009**, 34, (5), 449-477.
12. Grotthuss, C. J. T., Sur la décomposition de l'eau et des corps q'uelle tient en dissolution à l'aide de l'électricité galvanique. *Ann. Chim. LVIII* **1806**, 20.
13. Kreuer, K. D., Fast proton conductivity: A phenomenon between the solid and the liquid state? *Solid State Ionics* **1997**, 94, (1-4), 55-62.
14. Ma, Y. L.; Wainright, J. S.; Litt, M. H.; Savinell, R. F., Conductivity of PBI membranes for high-temperature polymer electrolyte fuel cells. *Journal of the Electrochemical Society* **2004**, 151, (1), A8-A16.
15. Li, Q.; He, R.; Jensen, J. O.; Bjerrum, N. J., PBI-Based Polymer Membranes for High Temperature Fuel Cells - Preparation, Characteriazation and Fuel Cell Demonstration. *Fuel Cells* **2004**, 4, (3), 147-159.
16. Samms, S. R.; Wasmus, S.; Savinell, R. F., Thermal stability of proton conducting acid doped polybenzimidazole in simulated fuel cell environments. *Journal of the Electrochemical Society* **1996**, 143, (4), 1225-1232.
17. Kerres, J. A., Development of ionomer membranes for fuel cells. *Journal of Membrane Science* **2001**, 185, (1), 3-27.
18. Hughes, C. E.; Haufe, S.; Angerstein, B.; Kalim, R.; Mahr, U.; Reiche, A.; Baldus, M., Probing structure and dynamics in poly[2,2'-(m-phenylene)-5,5'-bibenzimidazole] fuel cells with magic-angle spinning NMR. *Journal of Physical Chemistry B* **2004**, 108, (36), 13626-13631.

19. Fontanella, J. J.; Wintersgill, M. C.; Wainright, J. S.; Savinell, R. F.; Litt, M., High pressure electrical conductivity studies of acid doped polybenzimidazole. *Electrochimica Acta* **1998**, 43, (10-11), 1289-1294.
20. Bouchet, R.; Miller, S.; Duclot, M.; Souquet, J. L., A thermodynamic approach to proton conductivity in acid-doped polybenzimidazole. *Solid State Ionics* **2001**, 145, (1-4), 69-78.
21. Wang, J. T.; Savinell, R. F.; Wainright, J.; Litt, M.; Yu, H., A H<sub>2</sub>/O<sub>2</sub> fuel cell using acid doped polybenzimidazole as polymer electrolyte. *Electrochimica Acta* **1996**, 41, (2), 193-197.
22. Li, Q. F.; He, R. H.; Gao, J. A.; Jensen, J. O.; Bjerrum, N. J., The CO poisoning effect in PEMFCs operational at temperatures up to 200 degrees C. *Journal of the Electrochemical Society* **2003**, 150, (12), A1599-A1605.
23. Petrushina, I. M.; Bandur, V. A.; Cappeln, F.; Bjerrum, N. J.; Sorensen, R. Z.; Refshauge, R. H.; Li, Q. F., Electrochemical promotion of NO reduction by hydrogen on a platinum/polybenzimidazole catalyst. *Journal of the Electrochemical Society* **2003**, 150, (5), D87-D90.
24. Liu, Z. Y.; Wainright, J. S.; Savinell, R. F., High-temperature polymer electrolytes for PEM fuel cells: study of the oxygen reduction reaction (ORR) at a Pt-polymer electrolyte interface. *Chemical Engineering Science* **2004**, 59, (22-23), 4833-4838.
25. Holladay, J. D.; Wainright, J. S.; Jones, E. O.; Gano, S. R., Power generation using a mesoscale fuel cell integrated with a microscale fuel processor. *Journal of Power Sources* **2004**, 130, (1-2), 111-118.
26. Thomas, S.-G.; Georg, F.; Jochen, B.; Jurgen, P.; Rudiger, K. Polymer composition, membrane containing said composition, method for the production and uses thereof. US Patent 6632847, **2003**.
27. Carollo, A.; Quartarone, E.; Tomasi, C.; Mustarelli, P.; Belotti, F.; Magistris, A.; Maestroni, F.; Parachini, M.; Garlaschelli, L.; Righetti, P. P., Developments of new proton conducting membranes based on different polybenzimidazole structures for fuel cells applications. *Journal of Power Sources* **2006**, 160, (1), 175-180.
28. Kim, H. J.; Cho, S. Y.; An, S. J.; Eun, Y. C.; Kim, J. Y.; Yoon, H. K.; Kweon, H. J.; Yew, K. H., Synthesis of poly(2,5-benzimidazole) for use as a fuel-cell membrane. *Macromolecular Rapid Communications* **2004**, 25, (8), 894-897.
29. Krishnan, P.; Park, J. S.; Kim, C. S., Performance of a poly(2,5-benzimidazole) membrane based high temperature PEM fuel cell in the presence of carbon monoxide. *Journal of Power Sources* **2006**, 159, (2), 817-823.
30. Asensio, J. A.; Borro, S.; Gomez-Romero, P., Polymer electrolyte fuel cells based on phosphoric acid-impregnated poly(2,5-benzimidazole) membranes. *Journal of the Electrochemical Society* **2004**, 151, (2), A304-A310.
31. O' Hayre, R.; Cha, S. W.; Colella, W.; Prinz, F. B., *Fuel Cell Fundamentals*. John Wiley & Sons: New Jersey, **2005**.
32. Joon, K., Fuel cells - a 21st century power system. *Journal of Power Sources* **1998**, 71, (1-2), 12-18.
33. Appleby, A. J., From Sir William Grove to Today - Fuel-Cells and the Future. *Journal of Power Sources* **1990**, 29, (1-2), 3-11.
34. Perry, M. L.; Fuller, T. F., A historical perspective of fuel cell technology in the 20th century. *Journal of the Electrochemical Society* **2002**, 149, (7), S59-S67.

35. Carrette, L.; Friedrich, K. A.; Stimming, U., Fuel cells: Principles, types, fuels, and applications. *Chemphyschem* **2000**, 1, (4), 162-193.
36. Sammes, N. M., Fuel Cell Technology: Reaching towards commercialization. *Springer* **2006**.
37. Ogden, J. M.; Steinbugler, M. M.; Kreutz, T. G., A comparison of hydrogen, methanol and gasoline as fuels for fuel cell vehicles: implications for vehicle design and infrastructure development. *Journal of Power Sources* **1999**, 79, (2), 143-168.
38. Simbeck, D. R., CO<sub>2</sub> capture and storage - the essential bridge to the hydrogen economy. *Energy* **2004**, 29, (9-10), 1633-1641.
39. Ogden, J. M., Prospects for building a hydrogen energy infrastructure. *Annual Review of Energy and the Environment* **1999**, 24, 227-279.
40. Barreto, L.; Makihiro, A.; Riahi, K., The hydrogen economy in the 21st century: a sustainable development scenario. *International Journal of Hydrogen Energy* **2003**, 28, (3), 267-284.
41. Yaws, C., *Chemical Properties Handbook: Physical, Thermodynamics, Environmental Transport, Safety & Health Related Properties for Organic & Inorganic Chemical*. McGraw-Hill: New York, **1999**.
42. Caldirola, M., *Physics of High Energy Densities*. Academic Press: Amsterdam, **1961**.
43. Shinnar, R., The hydrogen economy, fuel cells, and electric cars. *Technology in Society* **2003**, 25, (4), 21.
44. Ni, M.; Leung, M. K. H.; Sumathy, K.; Leung, D. Y. C., Potential of renewable hydrogen production for energy supply in Hong Kong. *International Journal of Hydrogen Energy* **2006**, 31, (10), 1401-1412.
45. Dillon, R.; Srinivasan, S.; Arico, A. S.; Antonucci, V., International activities in DMFC R&D: status of technologies and potential applications. *Journal of Power Sources* **2004**, 127, (1-2), 112-126.
46. Apanel, G.; Johnson, E., Direct methanol fuel cells-ready to go commercial? *Fuel Cells Bulletin* **2004**, 11, 12-17.
47. Casalegno, A.; Marchesi, R., DMFC performance and methanol cross-over: Experimental analysis and model validation. *Journal of Power Sources* **2008**, 185, (1), 318-330.
48. Arico, A. S.; Srinivasan, S.; Antonucci, V., DMFCs: From Fundamental Aspects to Technology Development. *Fuel Cells* **2001**, 1, (2), 133-161.
49. Wang, J. T.; Wainright, J. S.; Savinell, R. F.; Litt, M., A direct methanol fuel cell using acid-doped polybenzimidazole as polymer electrolyte. *Journal of Applied Electrochemistry* **1996**, 26, (7), 751-756.
50. Rice, C.; Ha, R. I.; Masel, R. I.; Waszczuk, P.; Wieckowski, A.; Barnard, T., Direct formic acid fuel cells. *Journal of Power Sources* **2002**, 111, (1), 83-89.
51. Rice, C.; Ha, S.; Masel, R. I.; Wieckowski, A., Catalysts for direct formic acid fuel cells. *Journal of Power Sources* **2003**, 115, (2), 229-235.
52. Zhu, Y. M.; Khan, Z.; Masel, R. I., The behavior of palladium catalysts in direct formic acid fuel cells. *Journal of Power Sources* **2005**, 139, (1-2), 15-20.
53. Song, S. Q.; Zhou, W. J.; Liang, Z. X.; Cai, R.; Sun, G. Q.; Xin, Q.; Stergiopoulos, V.; Tsiakaras, P., The effect of methanol and ethanol cross-over on the performance of PtRu/C-based anode DAFCs. *Applied Catalysis B-Environmental* **2005**, 55, (1), 65-72.

54. Song, S. Q.; Tsiakaras, P., Recent progress in direct ethanol proton exchange membrane fuel cells (DE-PEMFCs). *Applied Catalysis B-Environmental* **2006**, 63, (3-4), 187-193.
55. Yamada, K.; Asazawa, K.; Yasuda, K.; Ioroi, T.; Tanaka, H.; Miyazaki, Y.; Kobayashi, T., Investigation of PEM type direct hydrazine fuel cell. *Journal of Power Sources* **2003**, 115, (2), 236-242.
56. Li, Q. F.; He, R. H.; Jensen, J. O.; Bjerrum, N. J., Approaches and recent development of polymer electrolyte membranes for fuel cells operating above 100 degrees C. *Chemistry of Materials* **2003**, 15, (26), 4896-4915.
57. Jalani, N. H. Development of Nanocomposite Polymer Electrolyte Membranes for High Temperature PEM Fuel Cells. PhD Thesis, Worcester Polytechnic Institute, **2006**.
58. Cohen, R. In *Gemini fuel cell system*, Proceedings of the 20th Annual Power Sources Conference, New Jersey, 24-26 May 1966, 1966; New Jersey, **1966**; pp 21-24.
59. Gottesfeld, S.; Zawodzinski, T. A., *Advances in Electrochemical Science and Engineering*. Wiley/VCH: Weinheim, Germany, **1997**; Vol. 5, p 195-301.
60. Costamagna, P.; Srinivasan, S., Quantum jumps in the PEMFC science and technology from the 1960s to the year 2000 Part I. Fundamental scientific aspects. *Journal of Power Sources* **2001**, 102, (1-2), 242-252.
61. Savinell, R.; Yeager, E.; Tryk, D.; Landau, U.; Wainright, J.; Weng, D.; Lux, K.; Litt, M.; Rogers, C., A Polymer Electrolyte for Operation at Temperatures up to 200-Degrees-C. *Journal of the Electrochemical Society* **1994**, 141, (4), L46-L48.
62. Kreuer, K. D.; Rabenau, A.; Weppner, W., Vehicle Mechanism, a New Model for the Interpretation of the Conductivity of Fast Proton Conductors. *Angewandte Chemie-International Edition in English* **1982**, 21, (3), 208-209.
63. Kreuer, K. D., Proton conductivity: Materials and applications. *Chemistry of Materials* **1996**, 8, (3), 610-641.
64. Fischer, S. F.; Hofacker, G. L.; Sabin, J. R., Proton-Phonon Coupling in a Hydrogen Bonded System. *Physik Der Kondensiterten Materie* **1969**, 8, (4), 268-&.
65. Kreuer, K. D., On the complexity of proton conduction phenomena. *Solid State Ionics* **2000**, 136, 149-160.
66. Dippel, T.; Kreuer, K. D.; Lassegues, J. C.; Rodriguez, D., Proton Conductivity in Fused Phosphoric-Acid - a H-1 P-31 Pfg-Nmr and Qns Study. *Solid State Ionics* **1993**, 61, (1-3), 41-46.
67. Kreuer, K. D.; Dippel, T.; Hainovsky, N. G.; Maier, J., Proton Conductivity - Compounds and Their Structural and Chemical Peculiarities. *Berichte Der Bunsen-Gesellschaft-Physical Chemistry Chemical Physics* **1992**, 96, (11), 1736-1742.
68. Bozkurt, A.; Ise, M.; Kreuer, K. D.; Meyer, W. H.; Wegner, G., Proton-conducting polymer electrolytes based on phosphoric acid. *Solid State Ionics* **1999**, 125, (1-4), 225-233.
69. Souzy, R.; Ameduri, B., Functional fluoropolymers for fuel cell membranes. *Progress in Polymer Science* **2005**, 30, (6), 644-687.
70. Hickner, M. A.; Pivovar, B. S., The chemical and structural nature of proton exchange membrane fuel cell properties. *Fuel Cells* **2005**, 5, (2), 213-229.
71. DuPont Fuel Cells-DoPont Nafion PFSA Membranes. In DuPont Co.: **2004**.

72. Fritts, S. D.; Gervasio, D.; Zeller, R. L.; Savinell, R. F., Investigation of H<sub>2</sub> Gas-Transport in Recast Nafion Films Coated on Platinum in Hydrogen Saturated 85-Percent Phosphoric-Acid. *Journal of the Electrochemical Society* **1991**, 138, (11), 3345-3349.
73. Gottesfeld, S.; Raistrick, I. D.; Srinivasan, S., Oxygen Reduction Kinetics on a Platinum Rde Coated with a Recast Nafion<sup>1</sup> Film. *Journal of the Electrochemical Society* **1987**, 134, (6), 1455-1462.
74. Hogarth, W. H. J.; da Costa, J. C. D.; Lu, G. Q., Solid acid membranes for high temperature (> 140 degrees C) proton exchange membrane fuel cells. *Journal of Power Sources* **2005**, 142, (1-2), 223-237.
75. Ianniello, R.; Schmidt, V. M.; Stimming, U.; Stumper, J.; Wallau, A., Co Adsorption and Oxidation on Pt and Pt-Ru Alloys - Dependence on Substrate Composition. *Electrochimica Acta* **1994**, 39, (11-12), 1863-1869.
76. Heinzl, A.; Barragan, V. M., A review of the state-of-the-art of the methanol crossover in direct methanol fuel cells. *Journal of Power Sources* **1999**, 84, (1), 70-74.
77. Alberti, G.; Casciola, M., Composite membranes for medium-temperature PEM fuel cells. *Annual Review of Materials Research* **2003**, 33, 129-154.
78. Zhang, J. L.; Xie, Z.; Zhang, J. J.; Tanga, Y. H.; Song, C. J.; Navessin, T.; Shi, Z. Q.; Song, D. T.; Wang, H. J.; Wilkinson, D. P.; Liu, Z. S.; Holdcroft, S., High temperature PEM fuel cells. *Journal of Power Sources* **2006**, 160, (2), 872-891.
79. Xu, H.; Song, Y.; Kunz, H. R.; Fenton, J. M., Effect of elevated temperature and reduced relative humidity on ORR kinetics for PEM fuel cells. *Journal of the Electrochemical Society* **2005**, 152, (9), A1828-A1836.
80. Wilkinson, D. P.; Thompsett, D., Materials and approaches for CO and CO<sub>2</sub> tolerance for polymer electrolyte membrane fuel cells. In *Proceedings of the Second International Symposium on New Materials For Fuel Cell and Modern Battery Systems*, Ecole Polytechnique de Montreal, Montreal, Canada, **1997**; pp 266-285.
81. Vogel, W.; Lundquist, J.; Ross, P.; Stonehart, P., Reaction Pathways and Poisons .2. Rate Controlling Step for Electrochemical Oxidation of Hydrogen on Pt in Acid and Poisoning of Reaction by Co. *Electrochimica Acta* **1975**, 20, (1), 79-93.
82. Dhar, H.; Kush, A.; Patel, D.; Christner, L., Modeling for Co Poisoning of a Fuel-Cell Anode. *Journal of the Electrochemical Society* **1986**, 133, (8), C299-C299.
83. Li, Q. F.; Hjuler, H. A.; Hasiotis, C.; Kallitsis, J. K.; Kontoyannis, C. G.; Bjerrum, N. J., A Quasi-Direct Methanol Fuel Cell System Based on Blend Polymer Membrane Electrolytes. *Journal of Electrochemical and Solid-State Letters* **2002**, 5, (6), A125-A128.
84. Staiti, P.; Minutoli, M.; Hocevar, S., Membranes based on phosphotungstic acid and polybenzimidazole for fuel cell application. *Journal of Power Sources* **2000**, 90, (2), 231-235.
85. Staiti, P.; Minutoli, M., Influence of composition and acid treatment on proton conduction of composite polybenzimidazole membranes. *Journal of Power Sources* **2001**, 94, (1), 9-13.
86. Staiti, P., Proton conductive membranes based on silicotungstic acid/silica and polybenzimidazole. *Materials Letters* **2001**, 47, (4-5), 241-246.



87. Nunes, S. P.; Ruffmann, B.; Rikowski, E.; Vetter, S.; Richau, K., Inorganic modification of proton conductive polymer membranes for direct methanol fuel cells. *Journal of Membrane Science* **2002**, 203, (1-2), 215-225.
88. Bonnet, B.; Jones, D. J.; Roziere, J.; Tchicaya, L.; Alberti, G.; Casciola, M.; Massinelli, L.; Bauer, B.; Peraio, A.; Ramunni, E., Hybrid organic-inorganic membranes for a medium temperature fuel cell. *Journal of New Materials for Electrochemical Systems* **2000**, 3, (2), 87-92.
89. Zaidi, S. M. J.; Mikhailenko, S. D.; Robertson, G. P.; Guiver, M. D.; Kaliaguine, S., Proton conducting composite membranes from polyether ether ketone and heteropolyacids for fuel cell applications. *Journal of Membrane Science* **2000**, 173, (1), 17-34.
90. Mikhailenko, S. D.; Zaidi, S. M. J.; Kaliaguine, S., Sulfonated polyether ether ketone based composite polymer electrolyte membranes. *Catalysis Today* **2001**, 67, (1-3), 225-236.
91. He, R. H.; Li, Q. F.; Xiao, G.; Bjerrum, N. J., Proton conductivity of phosphoric acid doped polybenzimidazole and its composites with inorganic proton conductors. *Journal of Membrane Science* **2003**, 226, (1-2), 169-184.
92. Boysen, D. A.; Chisholm, C. R. I.; Haile, S. M.; Narayanan, S. R., Polymer solid acid composite membranes for fuel-cell applications. *Journal of the Electrochemical Society* **2000**, 147, (10), 3610-3613.
93. Park, Y.; Nagai, M., Proton exchange nanocomposite membranes based on 3-glycidoxypyrroltrimethoxysilane, silicotungstic acid and alpha-zirconium phosphate hydrate. *Solid State Ionics* **2001**, 145, (1-4), 149-160.
94. Honma, I.; Nakajima, H.; Nishikawa, O.; Sugimoto, T.; Nomura, S., Amphiphilic organic/inorganic nanohybrid macromolecules for intermediate-temperature proton conducting electrolyte membranes. *Journal of the Electrochemical Society* **2002**, 149, (10), A1389-A1392.
95. Nakajima, H.; Honma, I., Proton-conducting hybrid solid electrolytes for intermediate temperature fuel cells. *Solid State Ionics* **2002**, 148, (3-4), 607-610.
96. Nakajima, H.; Nomura, S.; Sugimoto, T.; Nishikawa, S.; Honma, I., High temperature proton conducting organic-inorganic nanohybrids for polymer electrolyte membrane - Part II. *Journal of the Electrochemical Society* **2002**, 149, (8), A953-A959.
97. Honma, I.; Nomura, S.; Nakajima, H., Protonic conducting organic/inorganic nanocomposites for polymer electrolyte membrane. *Journal of Membrane Science* **2001**, 185, (1), 83-94.
98. Lasségues, J. C., Mixed inorganic-organic systems: the acid/polymer blends. In *Proton Conductors: Solids, Membranes and Gels - Materials and Devices*, Colomban, P., Ed. Cambridge Univ. Press: New York, **1992**; pp 311-328.
99. Gillespie, R. J.; Robinson, E. A., *Nonaqueous Solvent Systems*. Academic Press: New York, **1965**; p 117-210.
100. Ma, Y. The Fundamental Studies of Polybenzimidazole/Phosphoric Acid Polymer Electrolyte for Fuel Cells. PhD Thesis, Case Western Reserve University, Cleveland, Ohio, **2004**.
101. Senadeera, G. K. R.; Careem, M. A.; Skaarup, S.; West, K., Enhanced ionic conductivity of poly(ethylene imine) phosphate. *Solid State Ionics* **1996**, 85, (1-4), 37-42.

102. Lassegues, J. C.; Grondin, J.; Hernandez, M.; Maree, B., Proton conducting polymer blends and hybrid organic inorganic materials. *Solid State Ionics* **2001**, 145, (1-4), 37-45.
103. Mader, J.; Xiao, L.; Schmidt, T. J.; Benicewicz, B. C., Polybenzimidazole/Acid Complexes as High-Temperature Membranes. *Fuel Cells li* **2008**, 216, 63-124.
104. Powers, E. J.; Serad, G. A., History and Development of Polybenzimidazoles. In *HIGH PERFORMANCE POLYMERS: THEIR ORIGIN AND DEVELOPMENT*, Seymour, R. B.; Kirshenbaum, G. S., Eds. Elsevier Applied Science: New York, **1986**; pp 355-373.
105. Musto, P.; Karasz, F. E.; Macknight, W. J., Fourier-Transform Infrared-Spectroscopy on the Thermooxidative Degradation of Polybenzimidazole and of a Polybenzimidazole Polyetherimide Blend. *Polymer* **1993**, 34, (14), 2934-2945.
106. Chung, T. S.; Chen, P. N., Film and Membrane-Properties of Polybenzimidazole (Pbi) and Polyarylate Alloys. *Polymer Engineering and Science* **1990**, 30, (1), 1-6.
107. Wainright, J. S.; Wang, J. T.; Weng, D.; Savinell, R. F.; Litt, M., Acid-Doped Polybenzimidazoles - a New Polymer Electrolyte. *Journal of the Electrochemical Society* **1995**, 142, (7), L121-L123.
108. Weng, D.; Wainright, J. S.; Landau, U.; Savinell, R. F., Electro-osmotic drag coefficient of water and methanol in polymer electrolytes at elevated temperatures. *Journal of the Electrochemical Society* **1996**, 143, (4), 1260-1263.
109. Wainright, J.; Litt, M.; Savinell, R., High Temperature Polymer Electrolyte for PEM Fuel Cells. In *Handbook of Fuel Cells: Fundamentals, Technology, Applications*, Vielstich, W.; Lamm, A.; Gasteiger, H. A., Eds. John Wiley & Sons: New York, **2003**; Vol. 3, pp 436-446.
110. Wang, J. T.; Wasmus, S.; Savinell, R. F., Real-time mass spectrometric study of the methanol crossover in a direct methanol fuel cell. *Journal of the Electrochemical Society* **1996**, 143, (4), 1233-1239.
111. Litt, M.; Ameri, R.; Wang, Y.; Savinell, R.; Wainright, J. S., Polybenzimidazoles/Phosphoric Acid Solid Polymer Electrolytes: Mechanical and Electrical Properties. In *Materials Research Society Symposium Proceeding*, Warrendale, PA, **1999**; Vol. 548, pp 313-323.
112. Wasmus, S.; B. A. Dauch; Moaddel, H.; Rinaldi, P. L.; Litt, M. H.; Rogers, C.; Valeriu, A.; Mateescu, G. D.; Tryk, D. A.; Savinell, R. F., Solid-state NMR characterization of H<sub>3</sub>PO<sub>4</sub>-doped polybenzimidazole polymer electrolyte fuel cell membranes. In *Proceedings of the 187th Electrochemical Society Meeting Extended Abstracts*, Reno, Nevada, **1995**; p 716.
113. Schechter, A.; Savinell, R. F.; Wainright, J. S.; Ray, D., H-1 and P-31 NMR Study of Phosphoric Acid-Doped Polybenzimidazole under Controlled Water Activity. *Journal of the Electrochemical Society* **2009**, 156, (2), B283-B290.
114. Glipa, X.; Bonnet, B.; Mula, B.; Jones, D. J.; Roziere, J., Investigation of the conduction properties of phosphoric and sulfuric acid doped polybenzimidazole. *Journal of Materials Chemistry* **1999**, 9, (12), 3045-3049.
115. Kawahara, M.; Morita, J.; Rikukawa, M.; Sanui, K.; Ogata, N., Synthesis and proton conductivity of thermally stable polymer electrolyte: poly(benzimidazole) complexes with strong acid molecules. *Electrochimica Acta* **2000**, 45, (8-9), 1395-1398.

116. Pu, H. T.; Meyer, W. H.; Wegner, G., Proton transport in polybenzimidazole blended with H<sub>3</sub>PO<sub>4</sub> or H<sub>2</sub>SO<sub>4</sub>. *Journal of Polymer Science Part B-Polymer Physics* **2002**, 40, (7), 663-669.
117. Vogel, H.; Marvel, C. S., Polybenzimidazoles, New Thermally Stable Polymers. *Journal of Polymer Science* **1961**, 50, (154), 511-539.
118. Iwakura, Y.; Imai, Y.; Uno, K., Polyphenylenebenzimidazoles. *Journal of Polymer Science Part a-General Papers* **1964**, 2, (6), 2605-2615.
119. Imai, Y.; Uno, K.; Iwakura, Y., Polybenzazoles. *Makromolekulare Chemie* **1965**, 83, (Apr), 179-187.
120. Choe, E. W.; Conciatori, A. B. (1) Synthesis of high molecular weight polybenzimidazole with arylhalo phosphorus compound catalyst, US Patent US4535144 (**1985**); (2) High molecular weight polybenzimidazole production, European Patent EP0122735 (**1984**); (3) Two stage high molecular weight polybenzimidazole production with phosphorus containing catalyst, US Patent US4506068 (**1985**); (4) High molecular weight polybenzimidazole preparation with phosphorus containing catalyst, US Patent US4452967 (**1984**); (5) Synthesis of high molecular weight polybenzimidazole with arylhalo phosphorus compound catalyst, US Patent US4533725 (**1985**); (6) High molecular weight polybenzimidazole preparation with phosphorus containing polymerisation catalyst, US Patent US4414383 (**1983**).
121. Choe, E. W. Single-stage melt polymerisation process for the production of high molecular weight polybenzimidazole. US Patent US4312976, **1982**.
122. Lobato, J.; Canizares, P.; Rodrigo, M. A.; Linares, J. J.; Manjavacas, G., Synthesis and characterisation of poly[2,2-(m-phenylene)-5,5-bibenzimidazole] as polymer electrolyte membrane for high temperature PEMFCs. *Journal of Membrane Science* **2006**, 280, (1-2), 351-362.
123. Xiao, L.; Zhang, H.; Jana, T.; Scanlon, E.; Chen, R.; Choe, E. W.; Ramanathan, L. S.; Yu, S.; Benicewicz, B. C., Synthesis and characterization of pyridine-based polybenzimidazoles for high temperature polymer electrolyte membrane fuel cell applications. *Fuel Cells* **2005**, 5, (2), 287-295.
124. Xiao, L. X.; Zhang, H. F.; Scanlon, E.; Ramanathan, L. S.; Choe, E. W.; Rogers, D.; Apple, T.; Benicewicz, B. C., High-temperature polybenzimidazole fuel cell membranes via a sol-gel process. *Chemistry of Materials* **2005**, 17, (21), 5328-5333.
125. Kim, H. J.; An, S. J.; Kim, J. Y.; Moon, J. K.; Cho, S. Y.; Eun, Y. C.; Yoon, H. K.; Park, Y.; Kweon, H. J.; Shin, E. M., Polybenzimidazoles for high temperature fuel cell applications. *Macromolecular Rapid Communications* **2004**, 25, (15), 1410-1413.
126. Wolfe, J. F.; Sybert, P. D.; Sybert, J. R. Process for the synthesis of polybenzazole polymers. US Patent 4533693, **1985**.
127. Asensio, J. A.; Gomez-Romero, P., Recent developments on proton conducting poly(2,5-benzimidazole) (ABPBI) membranes for high temperature polymer electrolyte membrane fuel cells. *Fuel Cells* **2005**, 5, (3), 336-343.
128. Akita, H.; Ichikawa, M.; Iguchi, M.; Katsutoshi, N.; Hiroyuki, O. Solid polymer electrolytes. European Patent 0967674A1 **1999**.
129. Aharoni, S. M.; Litt, M. H., Synthesis and Some Properties of Poly-(2,5-Trimethylene Benzimidazole) and Poly-(2,5-Trimethylene Benzimidazole Hydrochloride). *Journal of Polymer Science Part a-Polymer Chemistry* **1974**, 12, (3), 639-650.

130. Bouchet, R.; Siebert, E., Proton conduction in acid doped polybenzimidazole. *Solid State Ionics* **1999**, 118, (3-4), 287-299.
131. Ameri, R. Polybenzimidazole film containing phosphoric acid as proton exchange membrane (PEM). PhD Thesis, Case Western Reserve University, Cleveland, **1997**.
132. Asensio, J. A.; Borros, S.; Gomez-Romero, P., Proton-conducting membranes based on poly(2,5-benzimidazole) (ABPBI) and phosphoric acid prepared by direct acid casting. *Journal of Membrane Science* **2004**, 241, (1), 89-93.
133. Mecerreyes, D.; Grande, H.; Miguel, O.; Ochoteco, E.; Marcilla, R.; Cantero, I., Porous polybenzimidazole membranes doped with phosphoric acid: Highly proton-conducting solid electrolytes. *Chemistry of Materials* **2004**, 16, (4), 604-607.
134. Jayakody, J. R. P.; Chung, S. H.; Durantino, L.; Zhang, H.; Xiao, L.; Benicewicz, B. C.; Greenbaum, S. G., NMR studies of mass transport in high-acid-content fuel cell membranes based on phosphoric acid and polybenzimidazole. *Journal of the Electrochemical Society* **2007**, 154, (2), B242-B246.
135. Uchida, H.; Yamada, Y.; Asano, N.; Watanabe, M.; Litt, M., Properties of ab-PBI membranes for fuel cells. *Electrochemistry* **2002**, 70, (12), 943-945.
136. Xing, B. Z.; Savadogo, O., The effect of acid doping on the conductivity of polybenzimidazole (PBI). *Journal of New Materials for Electrochemical Systems* **1999**, 2, (2), 95-101.
137. Jones, D. J.; Roziere, J., Inorganic/organic composite membranes. In *Handbook of fuel cells*, Vielstich, W.; Lamm, A.; Gasteiger, H. A., Eds. John Wiley & Sons Ltd.: **2003**; Vol. 3, pp 447-463.
138. Herring, A. M., Inorganic-polymer composite membranes for proton exchange membrane fuel cells. *Polymer Reviews* **2006**, 46, (3), 245-296.
139. Staiti, P., Proton conductive membranes constituted of silicotungstic acid anchored to silica-polybenzimidazole matrices. *Journal of New Materials for Electrochemical Systems* **2001**, 4, (3), 181-186.
140. Li, M. Q.; Shao, Z. G.; Scott, K., A high conductivity Cs<sub>2.5</sub>H<sub>0.5</sub>PMo<sub>12</sub>O<sub>40</sub>/polybenzimidazole (PBI)/H<sub>3</sub>PO<sub>4</sub> composite membrane for proton-exchange membrane fuel cells OPE-rating at high temperature. *Journal of Power Sources* **2008**, 183, (1), 69-75.
141. Asensio, J. A.; Borros, S.; Gomez-Romero, P., Enhanced conductivity in polyanion-containing polybenzimidazoles. Improved materials for proton-exchange membranes and PEM fuel cells. *Electrochemistry Communications* **2003**, 5, (11), 967-972.
142. Gomez-Romero, P.; Asensio, J. A.; Borros, S., Hybrid proton-conducting membranes for polymer electrolyte fuel cells phosphomolybdic acid doped poly(2,5-benzimidazole)-(ABPBI-H<sub>3</sub>PMo<sub>12</sub>O<sub>40</sub>). *Electrochimica Acta* **2005**, 50, (24), 4715-4720.
143. Kim, T. H.; Lim, T. W.; Park, Y. S.; Shin, K.; Lee, J. C., Proton-conducting zirconium pyrophosphate/poly(2,5-benzimidazole) composite membranes prepared by a PPA direct casting method. *Macromolecular Chemistry and Physics* **2007**, 208, (21), 2293-2302.
144. Kuder, J. E.; Chen, J. C. Chemical modification of preformed polybenzimidazole semipermeable membrane. US Patent 4634530, **1987**.

145. Staiti, P.; Lufrano, F.; Arico, A. S.; Passalacqua, E.; Antonucci, V., Sulfonated polybenzimidazole membranes - preparation and physico-chemical characterization. *Journal of Membrane Science* **2001**, 188, (1), 71-78.
146. Ariza, M. J.; Jones, D. J.; Roziere, J., Role of post-sulfonation thermal treatment in conducting and thermal properties of sulfuric acid sulfonated poly(benzimidazole) membranes. *Desalination* **2002**, 147, (1-3), 183-189.
147. Gieselman, M. B.; Reynolds, J. R., Aramid and Imidazole Based Polyelectrolytes - Physical-Properties and Ternary Phase-Behavior with Poly(Benzobisthiazole) in Methanesulfonic-Acid. *Macromolecules* **1993**, 26, (21), 5633-5642.
148. Glipa, X.; ElHaddad, M.; Jones, D. J.; Roziere, J., Synthesis and characterisation of sulfonated polybenzimidazole: A highly conducting proton exchange polymer. *Solid State Ionics* **1997**, 97, (1-4), 323-331.
149. Gieselman, M. B.; Reynolds, J. R., Water-Soluble Polybenzimidazole-Based Polyelectrolytes. *Macromolecules* **1992**, 25, (18), 4832-4834.
150. Roziere, J.; Jones, D. J.; Marrony, M.; Glipa, X.; Mula, B., On the doping of sulfonated polybenzimidazole with strong bases. *Solid State Ionics* **2001**, 145, (1-4), 61-68.
151. Kawahara, M.; Rikukawa, M.; Sanui, K.; Ogata, N., Synthesis and proton conductivity of sulfopropylated poly(benzimidazole) films. *Solid State Ionics* **2000**, 136, 1193-1196.
152. Bae, J. M.; Honma, I.; Murata, M.; Yamamoto, T.; Rikukawa, M.; Ogata, N., Properties of selected sulfonated polymers as proton-conducting electrolytes for polymer electrolyte fuel cells. *Solid State Ionics* **2002**, 147, (1-2), 189-194.
153. Asensio, J. A.; Borros, S.; Gomez-Romero, P., Proton-conducting polymers based on benzimidazoles and sulfonated benzimidazoles. *Journal of Polymer Science Part a-Polymer Chemistry* **2002**, 40, (21), 3703-3710.
154. Qing, S. B.; Huang, W.; Yan, D. Y., Synthesis and characterization of thermally stable sulfonated polybenzimidazoles obtained from 3,3'-disulfonyl-4,4'-dicarboxyldiphenylsulfone. *Journal of Polymer Science Part a-Polymer Chemistry* **2005**, 43, (19), 4363-4372.
155. Qing, S. B.; Huang, W.; Yan, D. Y., Synthesis and characterization of thermally stable sulfonated polybenzimidazoles. *European Polymer Journal* **2005**, 41, (7), 1589-1595.
156. Qing, S. B.; Huang, W.; Yan, D. Y., Synthesis and properties of soluble sulfonated polybenzimidazoles. *Reactive & Functional Polymers* **2006**, 66, (2), 219-227.
157. Kang, S.; Zhang, C. J.; Xiao, G. Y.; Yan, D. Y.; Sun, G. M., Synthesis and properties of soluble sulfonated polybenzimidazoles from 3,3'-disulfonate-4,4'-dicarboxylbiphenyl as proton exchange membranes. *Journal of Membrane Science* **2009**, 334, (1-2), 91-100.
158. Bai, H.; Ho, W. S. W., New Carbon Dioxide-Selective Membranes Based on Sulfonated Polybenzimidazole (SPBI) Copolymer Matrix for Fuel Cell Applications. *Industrial & Engineering Chemistry Research* **2009**, 48, (5), 2344-2354.
159. Kerres, J.; Ullrich, A.; Meier, F.; Haring, T., Synthesis and characterization of novel acid-base polymer blends for application in membrane fuel cells. *Solid State Ionics* **1999**, 125, (1-4), 243-249.

160. Kerres, J.; Hein, M.; Zhang, W.; Graf, S.; Nicoloso, N., Development of new blend membranes for polymer electrolyte fuel cell applications. *Journal of New Materials for Electrochemical Systems* **2003**, 6, (4), 223-229.
161. Kerres, J.; Ullrich, A.; Haring, T.; Baldauf, M.; Gebhardt, U.; Preidel, W., Preparation, characterization and fuel cell application of new acid-base blend membranes. *Journal of New Materials for Electrochemical Systems* **2000**, 3, (3), 229-239.
162. Kerres, J.; Zhang, W.; Jorissen, L.; Gogel, V., Application of different types of polyaryl-blend-membranes in DMFC. *Journal of New Materials for Electrochemical Systems* **2002**, 5, (2), 97-107.
163. Kerres, J. A., Blended and cross-linked ionomer membranes for application in membrane fuel cells. *Fuel Cells* **2005**, 5, (2), 230-247.
164. Xing, D.; Kerres, J., Improvement of synthesis procedure and characterization of sulfonated poly(arylene ether sulfone) for proton exchange membranes. *Journal of New Materials for Electrochemical Systems* **2006**, 9, (1), 51-60.
165. Kerres, J.; Ullrich, A., Synthesis of novel engineering polymers containing basic side groups and their application in acid-base polymer blend membranes. *Separation and Purification Technology* **2001**, 22-3, (1-3), 1-15.
166. Lee, J. K.; Kerres, J., Synthesis and characterization of sulfonated poly(arylene thioether)s and their blends with polybenzimidazole for proton exchange membranes. *Journal of Membrane Science* **2007**, 294, (1-2), 75-83.
167. Wycisk, R.; Lee, J. K.; Pintauro, P. N., Sulfonated polyphosphazene-polybenzimidazole membranes for DMFCs. *Journal of the Electrochemical Society* **2005**, 152, (5), A892-A898.
168. Deimede, V.; Voyiatzis, G. A.; Kallitsis, J. K.; Qingfeng, L.; Bjerrum, N. J., Miscibility behavior of polybenzimidazole/sulfonated polysulfone blends for use in fuel cell applications. *Macromolecules* **2000**, 33, (20), 7609-7617.
169. Kerres, J. A.; Xing, D. M.; Schonberger, F., Comparative investigation of novel PBI blend ionomer membranes from nonfluorinated and partially fluorinated poly arylene ethers. *Journal of Polymer Science Part B-Polymer Physics* **2006**, 44, (16), 2311-2326.
170. Schonberger, F.; Hein, M.; Kerres, J., Preparation and characterisation of sulfonated partially fluorinated statistical poly(arylene ether sulfone)s and their blends with PBI. *Solid State Ionics* **2007**, 178, (7-10), 547-554.
171. Schonberger, F.; Chromik, A.; Kerres, J., Synthesis and characterization of novel (sulfonated) poly(arylene ether)s with pendent trifluoromethyl groups. *Polymer* **2009**, 50, (9), 2010-2024.
172. Li, Q.; Jensen, J. O.; Pan, C.; Bandur, V.; Nilsson, M. S.; Schonberger, F.; Chromik, A.; Hein, M.; Haring, T.; Kerres, J.; Bjerrum, N. J., Partially Fluorinated Arylene Polyethers and their Ternary Blends with PBI and H<sub>3</sub>PO<sub>4</sub>. Part II. Characterisation and Fuel Cell Tests of the Ternary Membranes (vol 8, pg 188, 2008). *Fuel Cells* **2008**, 8, (5), 374-374.
173. Acar, O.; Sen, U.; Bozkurt, A.; Ata, A., Proton conducting membranes based on Poly(2,5-benzimidazole) (ABPBI)-Poly(vinylphosphonic acid) blends for fuel cells. *International Journal of Hydrogen Energy* **2009**, 34, (6), 2724-2730.
174. Akbey, U.; Graf, R.; Chu, P. P.; Spiess, H. W., Anhydrous Poly(2,5-benzimidazole)-Poly(vinylphosphonic Acid) Acid-Base Polymer Blends: a Detailed Solid-State NMR Investigation. *Australian Journal of Chemistry* **2009**, 62, (8), 848-856.

175. Acar, O.; Sen, U.; Bozkurt, A.; Ata, A., Blend membranes from poly(2,5-benzimidazole) and poly(styrene sulfonic acid) as proton-conducting polymer electrolytes for fuel cells. *Journal of Materials Science* **2010**, 45, (4), 993-998.
176. Zhang, W.; Gogel, V.; Friedrich, K. A.; Kerres, J., Novel covalently cross-linked poly(etheretherketone) ionomer membranes. *Journal of Power Sources* **2006**, 155, (1), 3-12.
177. Kerres, J.; Zhang, W.; Haering, T., Covalently cross-linked ionomer (blend) membranes for fuel cells. *Journal of New Materials for Electrochemical Systems* **2004**, 7, (4), 299-309.
178. Kerres, J., Covalent-ionically cross-linked poly(etheretherketone)-basic polysulfone blend ionomer membranes. *Fuel Cells* **2006**, 6, (3-4), 251-260.
179. Choi, J.; Harcup, J.; Yee, A. F.; Zhu, Q.; Laine, R. M., Organic/inorganic hybrid composites from cubic silsesquioxanes. *Journal of the American Chemical Society* **2001**, 123, (46), 11420-11430.
180. Gómez-Romero, P.; Sanchez, C., *Hybrid Materials, Functional Applications. An Introduction*. WILEY-VCH Verlag GmbH & Co. KGaA: **2004**; p 1-14.
181. Choi, J.; Kim, S. G.; Laine, R. M., Organic/inorganic hybrid epoxy nanocomposites from aminophenylsilsesquioxanes. *Macromolecules* **2004**, 37, (1), 99-109.
182. Schwab, J. J.; Lichtenhan, J. D., Polyhedral oligomeric silsesquioxane (POSS)-based polymers. *Applied Organometallic Chemistry* **1998**, 12, (10-11), 707-713.
183. Pittman, C. U.; Li, G. Z.; Ni, H. L., Hybrid inorganic/organic crosslinked resins containing polyhedral oligomeric silsesquioxanes. *Macromolecular Symposia* **2003**, 196, 301-325.
184. Scott, D. W., Thermal Rearrangement of Branched-Chain Methylpolysiloxanes. *Journal of the American Chemical Society* **1946**, 68, (3), 356-358.
185. Fina, A.; Tabuani, D.; Carniato, F.; Frache, A.; Boccaleri, E.; Camino, G., Polyhedral oligomeric silsesquioxanes (POSS) thermal degradation. *Thermochimica Acta* **2006**, 440, (1), 36-42.
186. Ni, Y.; Zheng, S. X.; Nie, K. M., Morphology and thermal properties of inorganic-organic hybrids involving epoxy resin and polyhedral oligomeric silsesquioxanes. *Polymer* **2004**, 45, (16), 5557-5568.
187. Liu, H. Z.; Zheng, S. X.; Nie, K. M., Morphology and thermomechanical properties of organic-inorganic hybrid composites involving epoxy resin and an incompletely condensed polyhedral oligomeric silsesquioxane. *Macromolecules* **2005**, 38, (12), 5088-5097.
188. Lichtenhan, J. D., Polyhedral Oligomeric Silsesquioxanes - Building-Blocks for Silsesquioxane-Based Polymers and Hybrid Materials. *Comments on Inorganic Chemistry* **1995**, 17, (2), 115-130.
189. Eshel, H.; Dahan, L.; Dotan, A.; Dodiuk, H.; Kenig, S., Nanotailoring of nanocomposite hydrogels containing POSS. *Polymer Bulletin* **2008**, 61, (2), 257-265.
190. Subianto, S.; Mistry, M. K.; Choudhury, N. R.; Dutta, N. K.; Knott, R., Composite polymer electrolyte containing ionic liquid and functionalized polyhedral oligomeric silsesquioxanes for anhydrous PEM applications. *Acs Applied Materials & Interfaces* **2009**, 1, (6), 1173-1182.

191. Zawodzinski, T. A.; Neeman, M.; Sillerud, L. O.; Gottesfeld, S., Determination of Water Diffusion-Coefficients in Perfluorosulfonate Ionomeric Membranes. *Journal of Physical Chemistry* **1991**, 95, (15), 6040-6044.
192. Smith, B. C., *Fundamentals of Fourier Transform Infrared Spectroscopy*. Second ed.; CRC: Massachusetts, **2009**.
193. Kojima, T. J., Studies of molecular aggregation of a polybenzimidazole in solution by fluorescence spectroscopy. *Journal of Polymer Science Part B-Polymer Physics* **1980**, 18, (8), 1685-1695.
194. Kojima, T.; Yokota, R.; Kochi, M.; Kambe, H., Dilute solution properties of a polybenzimidazole. *Journal of Polymer Science Part B-Polymer Physics* **1980**, 18, (8), 1673-1683.
195. Wang, Y. The synthesis and properties of poly(2,5-benzimidazole). M.S, Case Western Reserve University, Cleveland, Ohio, **1998**.
196. Sundaraganesan, N.; Joshua, B. D.; Meganathan, C.; Meenashi, R.; Cornard, J. P., Vibrational spectra and quantum chemical calculations of 3,4-diaminobenzoic acid. *Spectrochimica Acta Part a-Molecular and Biomolecular Spectroscopy* **2008**, 70, (2), 376-383.
197. Cordes, M. M.; Walter, J. L., Infrared and Raman Studies of Heterocyclic Compounds .2. Infrared Spectra and Normal Vibrations of Benzimidazole and Bis-(Benzimidazolato)-Metal Complexes. *Spectrochimica Acta Part a-Molecular Spectroscopy* **1968**, A 24, (9), 1421-&.
198. Meyer, T.; Keurentjes, J., *Handbook of Polymer Reaction Engineering*. **2005**; Vol. 1, p 1137.
199. Young, R. J., *Introduction to polymers*. Chapman and Hall: New York, **1981**; p 368.
200. Kulkarni, M.; Potrekar, R.; Kulkarni, R. A.; Vernekar, S. P., Synthesis and characterization of novel polybenzimidazoles bearing pendant phenoxyamine groups. *Journal of Polymer Science Part a-Polymer Chemistry* **2008**, 46, (17), 5776-5793.
201. Krause, S. J.; Haddock, T.; Lenhert, P. G.; Obrien, J. F.; Helminiak, T. E.; Adams, W. W., Morphology of a Phase-Separated and a Molecular Composite Pbt Abpbi Polymer Blend. *Journal of Polymer Science Part B-Polymer Physics* **1986**, 24, (9), 1991-2016.
202. Wereta, A.; Gehatia, M. T.; Wiff, D. R., Morphological and Physical Property Effects for Solvent Cast Films of Poly-2, 5(6) Benzimidazole. *Polymer Engineering and Science* **1978**, 18, (3), 204-209.
203. Chapman, A. C.; Thirlwell, L. E., Spectra of Phosphorus Compounds .1. The Infra-Red Spectra of Orthophosphates. *Spectrochimica Acta* **1964**, 20, (6), 937-947.
204. Fina, A.; Abbenhuis, H. C. L.; Tabuani, D.; Frache, A.; Camino, G., Polypropylene metal functionalised POSS nanocomposites: A study by thermogravimetric analysis. *Polymer Degradation and Stability* **2006**, 91, (5), 1064-1070.
205. Launer, P. J., Infrared analysis of organosilicon compounds: spectra-structure correlations. In *Silicon Compounds, Register, and Review*, Anderson, R.; Arkles, B.; Larson, G. L., Eds. Petrarch System: New York, **1987**; pp 47-53.
206. Liu, Y. R.; Huang, Y. D.; Liu, L., Effects of TriSilanollisobutyl-POSS on thermal stability of methylsilicone resin. *Polymer Degradation and Stability* **2006**, 91, (11), 2731-2738.



207. Bellamy, L. J., *The Infrared Spectra of Complex Molecules*. 2nd ed.; Chapman and Hall: London, **1980**; Vol. 2.
208. Zhang, X.; Tay, S. W.; Hong, L.; Liu, Z., In situ implantation of PolyPOSS blocks in Nafion matrix to promote its performance in direct methanol fuel cell. *Journal of Membrane Science* **2008**, 320, 310-318.
209. Tay, S. W.; Zhang, X.; Liu, Z.; Hong, L.; Chan, S. H., Composite Nafion (R) membrane embedded with hybrid nanofillers for promoting direct methanol fuel cell performance. *Journal of Membrane Science* **2008**, 321, (2), 139-145.
210. Stevens, M. P., *Polymer Chemistry: An Introduction*. 3rd ed.; Oxford University Press: New York, **1998**.
211. He, R. H.; Li, Q. F.; Bach, A.; Jensen, J. O.; Bjerrum, N. J., Physicochemical properties of phosphoric acid doped polybenzimidazole membranes for fuel cells. *Journal of Membrane Science* **2006**, 277, (1-2), 38-45.
212. Savadogo, O.; Xing, B., Hydrogen/oxygen polymer electrolyte membrane fuel cell (PEMFC) based on acid-doped polybenzimidazole (PBI). *Journal of New Materials for Electrochemical Systems* **2000**, 3, (4), 343-347.
213. Honda, M., A Guide to Measurement Technology and Techniques. In *The Impedance Measurement Handbook*, Yokogawa-Hewlett-Packard Ltd: Tokyo, Japan, **1989**.
214. Bard, A. J.; Faulkner, L. R., *Electrochemical Methods: Fundamentals and Applications*. 2nd ed.; John Wiley and Sons: New York, **2001**.
215. Lee, C. H.; Park, H. B.; Lee, Y. M.; Lee, R. D., Importance of proton conductivity measurement in polymer electrolyte membrane for fuel cell application. *Industrial & Engineering Chemistry Research* **2005**, 44, (20), 7617-7626.
216. Mikhailenko, S. D.; Guiver, M. D.; Kaliaguine, S., Measurements of PEM conductivity by impedance spectroscopy. *Solid State Ionics* **2008**, 179, (17-18), 619-624.
217. Xie, Z.; Song, C. J.; Andreaus, B.; Navessin, T.; Shi, Z. Q.; Zhang, J. J.; Holdcroft, S., Discrepancies in the measurement of ionic conductivity of PEMs using two- and four-probe AC impedance Spectroscopy. *Journal of the Electrochemical Society* **2006**, 153, (10), E173-E178.
218. Cahan, B. D.; Wainright, J. S., Ac-Impedance Investigations of Proton Conduction in Nafion(Tm). *Journal of the Electrochemical Society* **1993**, 140, (12), L185-L186.
219. Li, X. Development of Composite Membranes for Direct Methanol Fuel Cell. PhD Thesis, The University of Manchester, Manchester, **2006**.
220. Savett, S. C.; Atkins, J. R.; Sides, C. R.; Harris, J. L.; Thomas, B. H.; Creager, S. E.; Pennington, W. T.; DesMarteau, D. D., A comparison of bis[(perfluoroalkyl)sulfonyl]imide ionomers and perfluorosulfonic acid ionomers for applications in PEM fuel-cell technology. *Journal of the Electrochemical Society* **2002**, 149, (12), A1527-A1532.
221. Greenwood, N. N.; Thompson, A., The Mechanism of Electrical Conduction in Fused Phosphoric and Trideuterophosphoric Acids. *Journal of the Chemical Society* **1959**, (Nov), 3485-3492.
222. Chung, S. H.; Bajue, S.; Greenbaum, S. G., Mass transport of phosphoric acid in water: A H-1 and P-31 pulsed gradient spin-echo nuclear magnetic resonance study. *Journal of Chemical Physics* **2000**, 112, (19), 8515-8521.

## PUBLICATIONS

1. X.Bao and Q.Liu, Poly(2,5-benzimidazole) Based Polymer Electrolyte Membranes for High Temperature Fuel Cell Applications, Proceedings of Nanotech 2010, NSTI, USA, June, 2010, pp765-768 (Ref. No. 476)

2.Q.Liu and X.Bao, Novel POSS Hybrid Poly(2,5-benzimidazole) for High Temperature Polymer Electrolyte Membrane Fuel Cell Applications, 2010 Fuel Cell Seminar & Exposition, October, 2010, San Antonio, TX, USA (Ref. No: 337)